



Technische Universität München
TUM School of Engineering and Design

**Sensorless Internal Temperature Estimation for
Lithium-Ion Batteries:**
A Pulse Resistance Method with Adaptation to Aging

Sebastian Peter Ludwig, M.Sc.

Vollständiger Abdruck der von der TUM School of Engineering and Design der Technischen Universität München zur Erlangung eines

Doktors der Ingenieurwissenschaften (Dr.-Ing.)

genehmigten Dissertation.

Vorsitz: Prof. Malte Jaensch, Ph.D.
Prüfer*innen der Dissertation: 1. Prof. Dr.-Ing. Andreas Jossen
2. Prof. Dr.-Ing. Jan Philipp Schmidt

Die Dissertation wurde am 24.02.2023 bei der Technischen Universität München eingereicht und durch die TUM School of Engineering and Design am 18.07.2023 angenommen.

Abstract

A long service life, high performance and safety are three of the most important key properties of lithium-ion batteries. All three are strongly dependent on temperature, which is why temperature monitoring is a key task of a battery management system. However, conventional monitoring with temperature sensors on each individual cell proves increasingly difficult as system size increases. The effort for wiring and the required measurement electronics increase with the number of cells and thus also the cost, weight and complexity of the battery management system. For these reasons, research explores new approaches that enable sensorless temperature estimation and make use of existing resources in the battery management system. One promising approach is to utilize the temperature dependence of the impedance of lithium-ion batteries. Many approaches in the literature rely on electrochemical impedance spectroscopy as a measurement method in the frequency domain for this purpose. Although this measurement method uses the existing voltage and current measurements in the battery management system, it is complex and requires additional hardware for a defined sinusoidal measurement excitation. As a result, only a part of the resources can be saved compared to the measurement with temperature sensors. Therefore, the object of this study is to develop a method for sensorless temperature estimation, which is also based on cell impedance, but does not require any further resources. Instead of an artificial excitation for the impedance measurement, as in the case of electrochemical impedance spectroscopy, the load fluctuations that occur during operation are used in this work to calculate a resistance in the time domain. Using this resistance, the cell temperature can be determined for different cell formats and chemistries. By comparison with a thermal cell model, it is shown that this temperature corresponds most closely to the average internal cell temperature. Thus, the temperature determined by the resistance offers added value compared to the measurement with temperature sensors, which only determine the surface temperature. Furthermore, a method for temperature determination from the load profile is developed and validated in a battery module. By studying the effects of temperature differences on battery module aging, the need for temperature monitoring of even small temperature differences is reinforced. Due to the changing impedance and capacity over the lifetime of the module, a methodology is additionally developed to adapt the resistance-based temperature estimation to the aging state of the cells. In summary, this results in a sensorless method for estimating the internal cell temperature that can be applied over the entire lifetime of a lithium-ion battery without adapting the existing hardware of the battery management system.

Kurzfassung

Eine lange Lebensdauer, eine hohe Leistungsfähigkeit und Sicherheit sind drei der wichtigsten Kerneigenschaften von Lithium-Ionen-Batterien. Alle drei hängen stark von der Temperatur ab, weshalb die Überwachung der Temperatur eine zentrale Aufgabe eines Batteriemanagementsystems ist. Eine konventionelle Überwachung mit Temperatursensoren jeder einzelnen Zelle gestaltet sich jedoch mit steigender Systemgröße immer schwieriger. Der Verkabelungsaufwand und die benötigte Messelektronik steigen mit der Anzahl der Zellen an und damit auch die Kosten, das Gewicht und die Komplexität des Batteriemanagementsystems. Aus diesen Gründen wird in der Forschung nach neuen Ansätzen gesucht, die eine sensorlose Temperaturbestimmung ermöglichen und auf bestehende Ressourcen im Batteriemanagementsystem zurückgreifen. Ein vielversprechender Ansatz ist die Nutzung der Temperaturabhängigkeit der Impedanz von Lithium-Ionen-Batterien. Viele Ansätze in der Literatur greifen dafür auf die elektrochemische Impedanzspektroskopie als Messmethode im Frequenzbereich zurück. Dieses Messverfahren nutzt zwar die bestehenden Spannungs- und Strommessungen im Batteriemanagementsystem, ist jedoch komplex und benötigt zusätzliche Hardware für eine definierte sinusförmige Messanregung. Dadurch lässt sich nur ein Teil der Ressourcen gegenüber der Messung mit Temperatursensoren einsparen. In dieser Arbeit wird deshalb das Ziel verfolgt eine Methode zur sensorlosen Temperaturbestimmung zu entwickeln, die ebenfalls auf der Zellimpedanz beruht, jedoch keine weiteren Ressourcen in Anspruch nimmt. Anstelle einer künstlichen Anregung für die Impedanzmessung, wie bei der elektrochemischen Impedanzspektroskopie, werden in dieser Arbeit die Lastfluktuationen, die im Betrieb vorkommen genutzt, um einen Widerstand im Zeitbereich zu berechnen. Mit Hilfe dieses Widerstandes kann eine Zelltemperatur für verschiedene Zellformate und Chemien bestimmt werden. Über den Vergleich mit einem thermischen Zellmodell kann gezeigt werden, dass diese Temperatur am ehesten der mittleren internen Zelltemperatur entspricht. Damit bietet die aus dem Widerstand ermittelte Temperatur einen Mehrwert gegenüber der Messung mit Temperatursensoren, die nur die Oberflächentemperatur bestimmen. Außerdem wird eine Methode zur Temperaturbestimmung aus dem Lastverlauf entwickelt und in einem Batteriemodul validiert. Durch die Untersuchung der Auswirkung von Temperaturunterschieden auf die Alterung des Batteriemoduls konnte die Notwendigkeit der Temperaturüberwachung von selbst kleinen Temperaturunterschieden bekräftigt werden. Aufgrund der sich ändernden Impedanz und Kapazität über die Lebensdauer des Moduls wird zusätzlich eine Methodik entwickelt, um die bestehende Methode zur Temperaturbestimmung an den Alterungszustand der Zellen anzupassen. Zusammengefasst wird so eine sensorlose Methode zur Bestimmung der internen Zelltemperatur entwickelt, die sich ohne Anpassung der bestehenden Batteriemanagementsystem Hardware und auf die gesamte Lebensdauer einer Lithium-Ionen-Batterie anwenden lässt.

Contents

Abstract	c
Kurzfassung	e
List of Publications	III
Abbreviations	V
Formula Symbols	VII
1 Introduction	1
1.1 Motivation for Sensorless Temperature Estimation	3
1.2 Scope and Outline	4
2 Fundamentals and Methodology	7
2.1 Fundamentals of Lithium-Ion Batteries	7
2.1.1 Components of Lithium-Ion Batteries	7
2.1.2 Cell Format and Size	11
2.1.3 Functional Principle of Lithium-Ion Batteries	12
2.2 Temperature-dependent Processes in Lithium-Ion Batteries	13
2.2.1 Open-Circuit-Voltage	14
2.2.2 Overpotentials	14
2.2.3 Summary and Conclusion on Temperature-dependent Processes in Lithium-Ion Batteries	22
2.3 Effects of Temperature on Lithium-Ion Batteries	23
2.3.1 Low Temperatures	24
2.3.2 High Temperatures	24
2.3.3 Other Influencing Factors than Temperature	25
2.4 Impedance Measurement Techniques for Lithium-Ion Batteries	25
2.4.1 Frequency Domain	26
2.4.2 Time Domain	28
2.4.3 Factors Influencing the Impedance Determination for Lithium-Ion Batteries	32
2.5 Review on the State of the Art Temperature Estimation Methods for Lithium-Ion Batteries	33
2.5.1 Estimation Methods	33
2.5.2 Investigated Systems	36
2.5.3 Validation	38
3 Relation between Cell Temperature and Pulse Resistance	41
3.1 Internal Cell Temperature in Relation to Pulse Resistance and the Influence of Cell Dimension and Chemistry	41
3.2 Relation between Average Cell Temperature, Temperature Gradients and Pulse Resistance	70

4	Sensorless Online Pulse Resistance Temperature Estimation - Method Development	75
5	Effects of Temperature Inhomogeneities on Battery Modules under Cyclic Aging	93
6	Sensorless Online Pulse Resistance Temperature Estimation - Aging Compensation	107
7	Conclusion and Outlook	121
	References	125
	List of Figures	145
	List of Tables	147
	Acknowledgment	149

List of Publications

Peer-reviewed journal paper contributions (lead author)

- a Ludwig S., Zilberman I., Horsche M. F., Wohlers T., Jossen A.: *Pulse resistance based online temperature estimation for lithium-ion cells*, in: *Journal of Power Sources* 490, 229523, 2021, <https://doi.org/10.1016/j.jpowsour.2021.229523>
- b Ludwig S., Zilberman I., Oberbauer A., Rogge M., Fischer M., Rehm M., Jossen A.: *Adaptive method for sensorless temperature estimation over the lifetime of lithium-ion batteries*, in: *Journal of Power Sources* 521, 230864, 2022, <https://doi.org/10.1016/j.jpowsour.2021.230864>
- c Ludwig S., Steinhardt M., Jossen A.: *Determination of Internal Temperature Differences for Various Cylindrical Lithium-ion Batteries Using a Pulse Resistance Approach*, in: *Batteries* 8, no. 7: 60, 2022, <https://doi.org/10.3390/batteries8070060>

Self-written sections of peer-reviewed lead author journal paper contributions are partially contained in this doctoral thesis without further reference in the text.

Peer-reviewed journal paper contributions (co-author)

- a Sturm J., Ludwig S., Zwirner J., Ramirez-Garcia C., Heinrich B., Horsche M. F., Jossen A.: *Suitability of physicochemical models for embedded systems regarding a nickel-rich, silicon-graphite lithium-ion battery*, in: *Journal of Power Sources* 436, 226834, 2019, <https://doi.org/10.1016/j.jpowsour.2019.226834>
- b Zilberman I., Ludwig S., Jossen A.: *Cell-to-cell variation of calendar aging and reversible self-discharge in 18650 nickel-rich, silicon-graphite lithium-ion cells*, in: *Journal of Energy Storage* 26, 100900, 2019, <https://doi.org/10.1016/j.est.2019.100900>
- c Zilberman I., Ludwig S., Schiller M., Jossen A.: *Online aging determination in lithium-ion battery module with forced temperature gradient*, in: *Journal of Energy Storage* 28, 101170, 2020, <https://doi.org/10.1016/j.est.2019.101170>
- d Zilberman I., Schmitt J., Ludwig S., Naumann M., Jossen A.: *Simulation of voltage imbalance in large lithium-ion battery packs influenced by cell-to-cell variations and balancing systems*, in: *Journal of Energy Storage* 32, 101828, 2020, <https://doi.org/10.1016/j.est.2020.101828>
- e Schindler M., Sturm J., Ludwig S., Schmitt J., Jossen A.: *Evolution of Initial Cell-to-Cell Variations During a Three-Year Production Cycle*, in: *eTransportation* 8, 100102, 2021 <https://doi.org/10.1016/j.etrans.2020.100102>
- f Pra F., Al Koussa J., Ludwig S., De Servi C. M.: *Experimental and Numerical Investigation of the Thermal Performance of a Hybrid Battery Thermal Management System for an Electric Van*, in: *Batteries* 7, 27, 2021, <https://doi.org/10.3390/batteries7020027>
- g Jocher P., Steinhardt M., Ludwig S., Schindler M., Martin J., Jossen A.: *A novel measurement technique for parallel-connected lithium-ion cells with controllable interconnection resistance*, in: *Journal of Power Sources* 503, 230030, 2021, <https://doi.org/10.1016/j.jpowsour.2021.230030>

- h Schindler M., Sturm J., **Ludwig S.**, Durdel A., Jossen A.: *Comprehensive Analysis of the Aging Behavior of Nickel-Rich, Silicon-Graphite Lithium-Ion Cells Subject to Varying Temperature and Charging Profiles*, in: *Journal of The Electrochemical Society* 168, 060522, 2021, <https://doi.org/10.1149/1945-7111/ac03f6>
- i Zhao Y., Kumtepelı V., **Ludwig S.**, Jossen A.: *Investigation of the distribution of relaxation times of a porous electrode using a physics-based impedance model*, in: *Journal of Power Sources* 530, 231250, 2022, <https://doi:10.1016/j.jpowsour.2022.231250>

Conference contributions (lead author)

- a **Ludwig S.**, Schmitt J., Zilberman I., Wendel S., Jossen A.: *New Method for Analyzing Ultrasonic based Measurements for Lithium-ion Batteries*, in: *Advanced Battery Power - Kraftwerk Batterie 2019*, lecture, 2019
- b **Ludwig S.**, Zilberman I., Wohlers T., Jossen A.: *Data Driven Approach for Sensorless Temperature Estimation for Lithium-Ion Cells based on Pulse Resistance Measurements*, in: *Advanced Battery Power - Kraftwerk Batterie 2021*, poster [online], 2021
- c **Ludwig S.**, Zilberman I., Jossen A.: *Sensorless Cell Temperature Estimation over the Lifetime of Lithium-Ion Batteries*, in: *240th ECS Meeting*, poster [online], 2021
- d **Ludwig S.**, Jossen A.: *Sensorlose Temperaturbestimmung für Lithium-Ionen Zellen mit Hilfe von Pulswiderständen*, in: *Battery World 2022*, lecture [online], 2022
- e **Ludwig S.**, Jossen A.: *Detecting internal and external temperature inhomogeneities with a pulse resistance approach*, in: *Battery Modeling Webinar Series*, lecture [online], 2022

Conference contributions (co-author)

- a Zilberman I., **Ludwig S.**, Jossen A.: *Online Aging Determination with Dissipative Balancing Circuits*, in: *Advanced Battery Power - Kraftwerk Batterie 2019*, lecture, 2019
- b Sturm J., **Ludwig S.**, Zwirner J., Ramirez-Garcia C., Heinrich B., Zilberman I., Frie F., Jossen A.: *Suitability of physicochemical models in microcontroller systems for monitoring lithium-ion batteries*, in: *ModVal 2019*, lecture, 2019
- c Jocher P., Steinhardt M., **Ludwig S.**, Schindler M., Martin J., Jossen A.: *Experimental Validation of Parallel-Connected Lithium-Ion Cells with Controllable Interconnection Resistance*, in: *Advanced Battery Power - Kraftwerk Batterie 2021*, poster [online], 2021

Abbreviations

Please note that the list below is based on the main part of this thesis and does not fully cover the abbreviations used in the papers. Each paper itself includes an individual list.

R_{DC}	direct current resistance
T_{int}	internal cell temperature
$t_{r/f}$	pulse rise/fall time
ANN	artificial neural networks
ARTEMIS	assessment and reliability of transport emission models and inventory systems
BEV	battery electric vehicle
BMS	battery management system
CC	constant-current
DC	direct current
DEC	diethyl carbonate
DMC	dimethyl carbonate
DOD	depth of discharge
DVA	differential voltage analysis
EC	ethylene carbonate
ECM	equivalent circuit model
EES	Institute for Electrical Energy Storage Technology
EIS	electrochemical impedance spectroscopy
EMC	ethyl methyl carbonate
EV	electric vehicle
FEC	fluoroethylene carbonate
FT	Fourier transform
GEIS	galvanostatic electrochemical impedance spectroscopy
Gr	graphite
KF	Kalman filter
LCO	lithium cobalt oxide
LFP	lithium iron phosphate
$LiMO_2$	lithium-metal oxide

LIB	lithium-ion battery
LMO	lithium manganese oxide
LTI	linear time-invariant
LTO	lithium titanate
LUT	look-up table
NCA	lithium nickel cobalt aluminum oxide
NEDC	new European driving cycle
NLEIS	non-linear electrochemical impedance spectroscopy
NLS	nonlinear least-squares solver
NMC	lithium nickel manganese cobalt oxide
OCV	open-circuit-voltage
PC	propylene carbonate
PEIS	potentiostatic electrochemical impedance spectroscopy
PHEV	plug-in hybrid electric vehicle
RMSE	root mean square error
SEI	solid electrolyte interphase
Si	silicon
SNR	signal-to-noise ratio
SOC	state of charge
SOH	state of health
SPI	solid permeable interface
SPM	single particle model
STD	standard deviation
TR	thermal runaway
TUM	Technical University of Munich
UDDS	urban dynamometer driving schedule
USABC	United States advanced battery consortium
VDA	Verband der Automobilindustrie
VTF	Vogel-Tamman-Fulcher

Formula Symbols

Please note that the list below is based on the main part of this thesis and does not fully cover the symbols used in the papers. Each paper itself includes an individual list or description.

$E_{A,b}$	activation energy per particle in J
$E_{A,r}$	activation energy in J mol^{-1}
E_c	conduction band energy in eV
E_d	doped/impure valence band energy in eV
E_v	valence band energy in eV
f	frequency in Hz
F	Faraday constant, $96\,485.332\,123\,310\,018\,4\text{ As mol}^{-1}$
k_B	Boltzmann constant, $1.380\,649 \times 10^{-23}\text{ J K}^{-1}$
N_A	Avogadro constant, $6.022\,140\,76 \times 10^{23}\text{ mol}^{-1}$
ω	angular frequency in Hz
η_{cont}	overpotential related to contact losses in V
$\eta_{\text{ct,a}}$	overpotential related to the charge-transfer at the anode in V
$\eta_{\text{ct,c}}$	overpotential related to the charge-transfer at the cathode in V
$\eta_{\text{diff,a}}$	overpotential related to diffusion losses in the solid phase at the anode in V
$\eta_{\text{diff,c}}$	overpotential related to diffusion losses in the solid phase at the cathode in V
$\eta_{\text{diff,l}}$	overpotential related to diffusion losses in the liquid phase in V
$\eta_{\text{diff,s}}$	overpotential related to diffusion losses in the solid phase in V
η_{elec}	overpotential related to electronic losses in V
η_{IND}	overpotential related to inductive losses in V
η_{ion}	overpotential related to ionic losses in V
η_{Ω}	overpotential related to ohmic losses in V
p	amount of cells connected in parallel
R	universal gas constant, $8.314\,462\,618\,153\,24\text{ J K}^{-1}\text{ mol}^{-1}$
s	amount of cells connected in serial
SOC	state of charge
T_a	absolute temperature in K
U_{OCV}	open-circuit-voltage in V
U_S	standard cell potential in V

1 Introduction

Lithium-ion batteries (LIBs) became an integral part of everyday life since they were commercialized in the 1990s [1]. LIBs pervade every area of life from consumer electronics, such as smart phones, laptops, or power tools, over stationary battery applications for home storage or for grid stabilization, up to battery packs for mobile applications reaching from electric bikes and scooters to plug-in hybrid electric vehicles (PHEVs) and battery electric vehicles (BEVs) [2–4]. The worldwide demand for LIBs in stationary and mobile applications, as well as consumer electronics is steadily increasing and predicted to grow beyond 2000 GWh by the year 2030 as Fig. 1.1 shows [5]. The growth is further fueled by the desire for a climate-neutral future and the corresponding legislation, as well as an increasing price and supply uncertainty in the fossil energy market [6; 7]. As Fig. 1.1 shows, the mobility sector plays a decisive role in this development. The increasing sales figures from 7780 vehicles in 2010 to 6.6 million

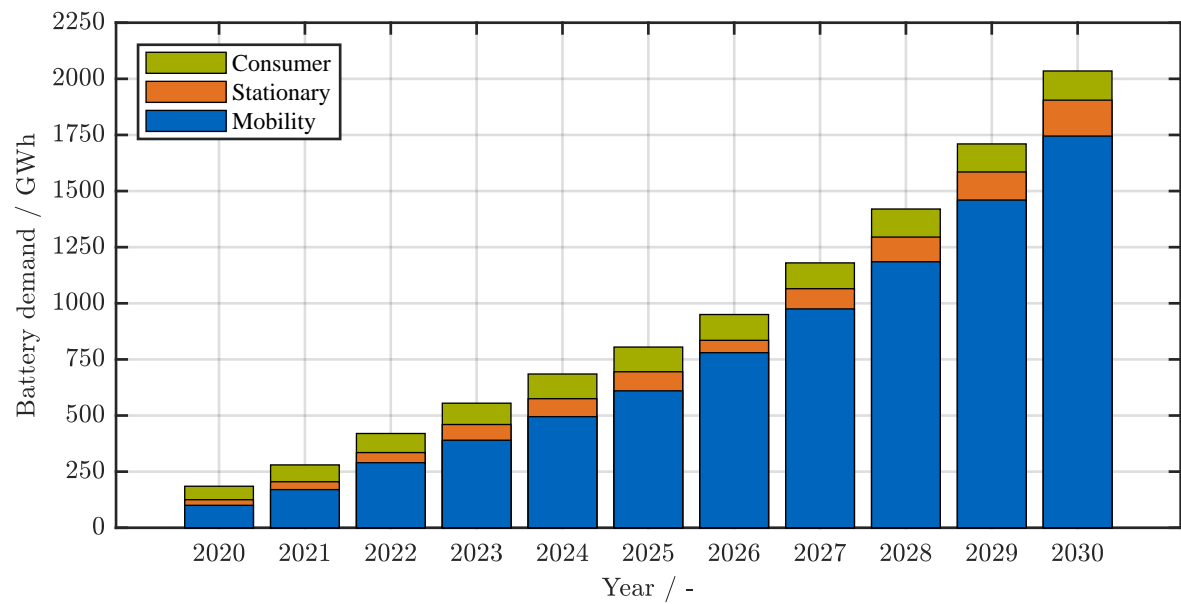


Figure 1.1: Projected global battery demand in GWh from 2020 to 2030 by application. [5]

vehicles in 2021 in Fig. 1.2a and the forecast of 27.7 million vehicles by 2030 in Fig. 1.2b, illustrate that the market for BEVs and PHEVs is a crucial application area for LIBs worldwide, especially in China followed by Europe and the USA. Compared to existing competing technologies, such as combustion engines or lead-acid batteries, LIBs are still a relatively young technology. As with any new technology that seeks to replace an established one, there are challenges and obstacles to overcome.

Electromobility in particular faces a number of challenges: the still disadvantageous driving range [9; 10] and charging times [11; 12] compared to internal combustion vehicles, the charging infrastructure that is still under development [13], the high vehicle prices [14], or uncertainties regarding the residual value of the vehicles, to name just a few. The temperature of LIBs plays a crucial role in many of these challenges and is therefore an important aspect in the system design and for the operation of

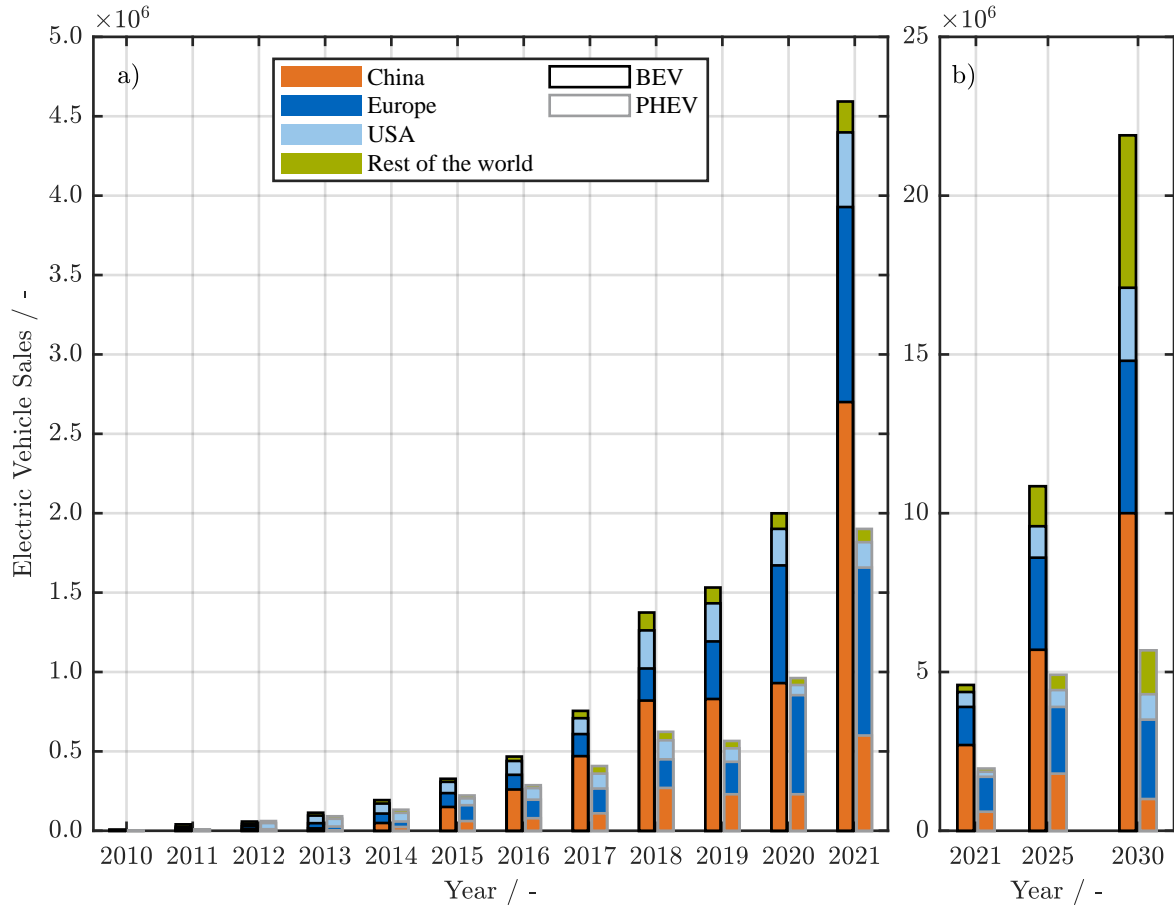


Figure 1.2: BEVs and PHEVs sales by market: a) current figures from 2010 to 2021 and b) forecast for 2025 and 2030 compared to 2021. [8]

battery packs. For example, the charging time, the range, and the performance of **electric vehicles (EVs)** essentially depend on the temperature of the battery pack. The temperature also influences the aging behavior and thus the lifetime and residual value of **EVs**. One more aspect that keeps drawing attention is the safety of **LIBs**. In particular, the focus is on the hazard posed by a thermal runaway, which can occur from several forms of mechanical, electrical, and thermal abuse of the **LIB** [10]. The continuous rise in temperature due to a thermal runaway results in the release of large amounts of flammable gases, which in turn leads to an increase in pressure in the **LIB** and can ultimately lead to explosion and fire [15–17]. In addition to the absolute temperature of a battery system, non-uniform temperature distribution between cells within a battery pack and likewise within each cell can lead to non-uniform current distribution, poor battery performance, capacity fade and power degradation [18–21]. The non-uniform current distribution due to non-uniform temperature distribution within the cell can further cause localized aging [18; 22–25]. In summary, it can be said that temperature is a major influencing factor on the safety [10; 18; 26–29], aging [18; 28–32], and performance [18; 28; 29; 33] of a **LIB**. For these reasons, monitoring and if possible controlling the temperature is an essential task of the **battery management system (BMS)** for any **LIB**-based system.

In general, the temperatures of cells within a battery pack differ during operation [34; 35], simply caused by the spatial location of the cells, which leads to varying thermal boundary conditions among the cells. Consequently, homogeneous cooling or heating of each cell poses a challenging task [36; 37].

As previously mentioned, the resulting temperature inhomogeneity within the battery pack may cause safety issues and facilitate inhomogeneous aging. Thermal simulations of the battery pack are capable of detecting systematic design flaws causing the inhomogeneous temperature distribution within a battery pack [38; 39]. Nevertheless, simulations cannot take all events into account, such as deviations during pack assembly, abnormal heating due to poor electrical contacting, or intrinsic cell parameter variations [40]. Also a shift of the pack temperature distribution during operation, for instance induced by non-uniform cell aging, is difficult to model. Therefore, monitoring the temperature of each cell in the battery pack is of high interest for a **BMS**. Most frequently, conventional temperature sensors, such as thermocouples or thermistors, which are mounted on the housing of the cell, are used for temperature monitoring [41]. Since a battery system can be composed of several hundred cells, such as a Nissan Leaf or Renault Zoe with 192 cells, where 2 parallel cells are 96-times serially connected (2p96s), up to thousands of cells, such as a Tesla Model 3 with 4416 cells (46p96s) or a Tesla Model S with 7104 cells (74p96s) [42; 43], monitoring each cell poses a difficult task. The consequences, if temperature sensors are used on each individual cell, are increased wiring effort, more weight due to the additional hardware, and rising **BMS** costs [44]. As a trade-off, sensors are only installed at strategic important positions in the battery pack, possibly leaving the majority of cells unmonitored. Moreover, external sensors barely deliver a overall picture of the cell temperature. In case of high load currents applied to the cell or an external temperature change, for example introduced by a thermal management system, the internal temperature can differ significantly from the surface temperature. The difference in temperature can only be detected with a time-shift or requires extensive thermal models, due to the thermal mass and limited heat transfer of a cell [41; 45; 46]. Approaches using instrumented cells with an internal temperature sensor circumvent this problem. However, inserting the sensor into the cell results in increased costs, manufacturing complexity and negative effects on cell aging [28; 41; 47]. Furthermore, a temperature sensor covers only a limited area on the surface of the cell and their accuracy is bound to the quality of the thermal contact to the cell and the position on the cell [41; 45; 48].

1.1 Motivation for Sensorless Temperature Estimation

Although individual cell temperature monitoring is desirable, it cannot be realized with conventional temperature sensors for systems with many cells, as described above, without considerable resource investment and the associated disadvantages. For this reason, new approaches have been explored in research to achieve sensorless temperature monitoring using existing resources of the **BMS**. One promising approach is to utilize the temperature dependence of the impedance of **LIBs**. For this purpose, many approaches in the literature [44; 45; 47; 49–53] make use of **electrochemical impedance spectroscopy (EIS)** as a measurement method in the frequency domain to determine the impedance of a **LIB**. By utilizing the relation of a cell's temperature and certain features within the impedance spectrum, the temperature can be estimated without the use of an external temperature sensor. Using **EIS**-based methods does not increase the wiring effort, since the existing connections for voltage and current monitoring can be utilized, but the additional effort and cost for the hardware, which performs the sinusoidal excitation for the **EIS** measurement, remains. Wang et al. [54] developed an approach using the instant current changes and the corresponding voltage response in the time domain as input for a wavelet transformation to calculate the cell impedance. With the transformed result, they build on the findings of the **EIS**-based methods to estimate the temperature. Using pulses in the time domain is also used for estimating other critical battery states. For instance, Mathew et al. [55] have already

shown that using only sharp current pulses for direct resistance estimation can be utilized for **state of health (SOH)** estimation. Their approach significantly reduces the required computational complexity compared to model-based solutions. With the pulse-based approach in the time domain, the need for additional hardware for **EIS** measurements can be eliminated as shown by [54]. Furthermore, the complex transformation to the frequency domain to calculate the impedance as in [54] is not necessary, if the pulse response is directly used to calculate a resistance in the time domain for the estimation as shown by [55]. Load changes, which naturally occur during the operation of battery powered devices, such as acceleration or braking of an **EV** can be used as an excitation. These considerations gave rise to the idea for this thesis with the aim of investigating the relationship between cell temperature and cell resistance in the time domain. A detailed breakdown of the research questions and the structure of the thesis follow in the next section.

1.2 Scope and Outline

The scope of this thesis is the investigation of the relation between a **LIB**'s temperature and its time domain pulse resistance, also referred to from here on as **direct current resistance (R_{DC})**, with the goal to answer four central research questions:

- Q1 What is the relation of temperature and R_{DC} in a general and spatial sense?
- Q2 Can the R_{DC} be calculated from load changes in an application and under what boundary conditions can it be utilized for estimating the temperature of a cell?
- Q3 How does aging affect the R_{DC} and therefore the approach developed in Q2?
- Q4 And consequently, how can the approach developed in Q2 be adapted to aging?

To answer these four central research questions, the thesis is structured as shown in Fig. 1.3. The figure also indicates which content was published in a paper. After the introduction in this chapter and before focusing on the central aspects of the thesis, the fundamentals and the relevant methodology are presented in Chapter 2. This includes the basic functional principle and components of a **LIB**, the theoretical relation between temperature (T) and the conduction phenomena in a **LIB**, and the effects of temperature in terms of safety, performance, and aging. Furthermore, Chapter 2 deals with general impedance measurement principles and the state of the art for impedance-based temperature estimation for **LIBs**. In Chapter 3, the focus lies on question Q1, pinpointing at the relation between spatial internal temperature distribution in the cell (T_{int}) and the temperature indicated by the R_{DC} , and the influence of the cell's dimension and chemistry. Chapter 4 answers question Q2 by investigating temperature estimation with the R_{DC} in a module under an external enforced temperature gradient (ΔT). A general approach for the parametrization of a temperature estimation function from current pulses and the boundary condition for its online application with load profiles are discussed as well. The next two chapters deal with the topic aging and hence with Q3 and Q4, whereby Chapter 5 focuses on temperature gradients on module level and analyzes their effects on the R_{DC} and capacity under cyclic aging. Chapter 6 focuses on the effects of aging on the method presented in Chapter 4 and how to compensate these effects in order to maintain a stable temperature estimation over the lifetime of the module. The final chapter Chapter 7 of the thesis briefly summarizes the key conclusions and closes with an outlook on open topics.

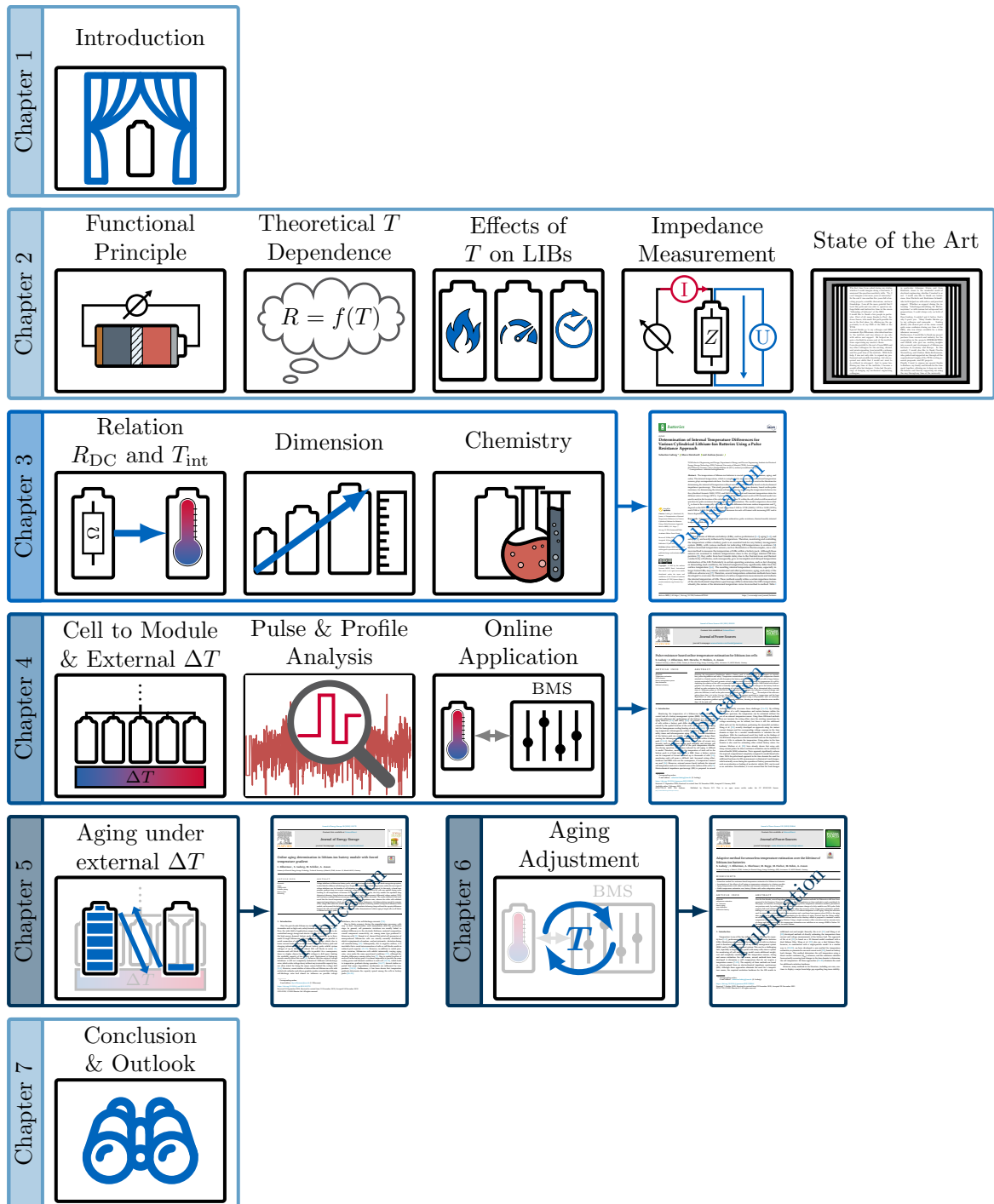


Figure 1.3: Scope and outline of this thesis structured by chapters and with indication on involved publications.

2 Fundamentals and Methodology

Before addressing the actual research questions of this thesis, this chapter deals with the required fundamentals and methodology. Fig. 2.1 visualizes the focus of the individual sections. First, the structure and functional principle of a LIB are explained in Section 2.1, followed by the theoretical basics with focus on temperature dependency in Section 2.2 and the impact on safety, performance and lifetime of a LIB in Section 2.3. Section 2.4 covers the basic methods for determining the cell impedance in the frequency and time domain. Finally, Section 2.5 summarizes the state of the art for sensorless temperature estimation for LIBs.

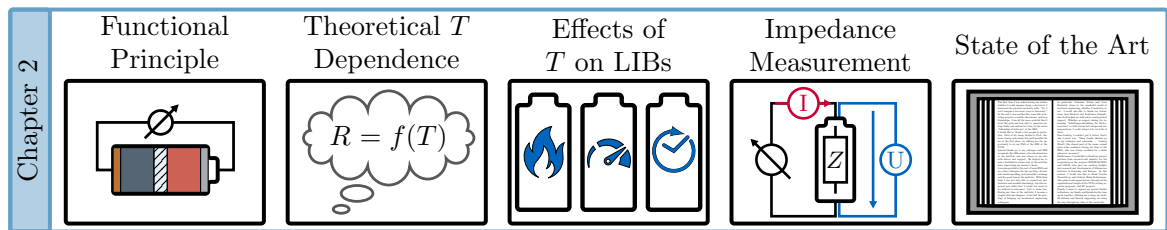


Figure 2.1: Scope of Chapter 2.

2.1 Fundamentals of Lithium-Ion Batteries

In order to understand the temperature-dependent processes and their effects on a LIB, a basic understanding of the structure and functional principle of a LIB is required. For this purpose, Fig. 2.2 shows the schematic representation of the fundamental electrochemical cell.

2.1.1 Components of Lithium-Ion Batteries

In general, the main components of a LIB are two porous electrodes, which are separated by a separator and soaked in a liquid electrolyte enabling ion exchange between the two electrodes. The individual components are explained in more detail below.

2.1.1.1 Electrode

In chemistry, the designation of the electrode depends on whether it is oxidized (anode) or reduced (cathode). Since LIBs are operated in both charging and discharging direction, the electrode designation would change with the operating mode, which can easily lead to confusion. For this reason, the convention to specify the designation of the electrodes based on the discharging process prevailed in battery research, implying that the negative electrode is the anode and the positive electrode is the cathode. Each electrode consists of a current collector coated with a composite material. The current

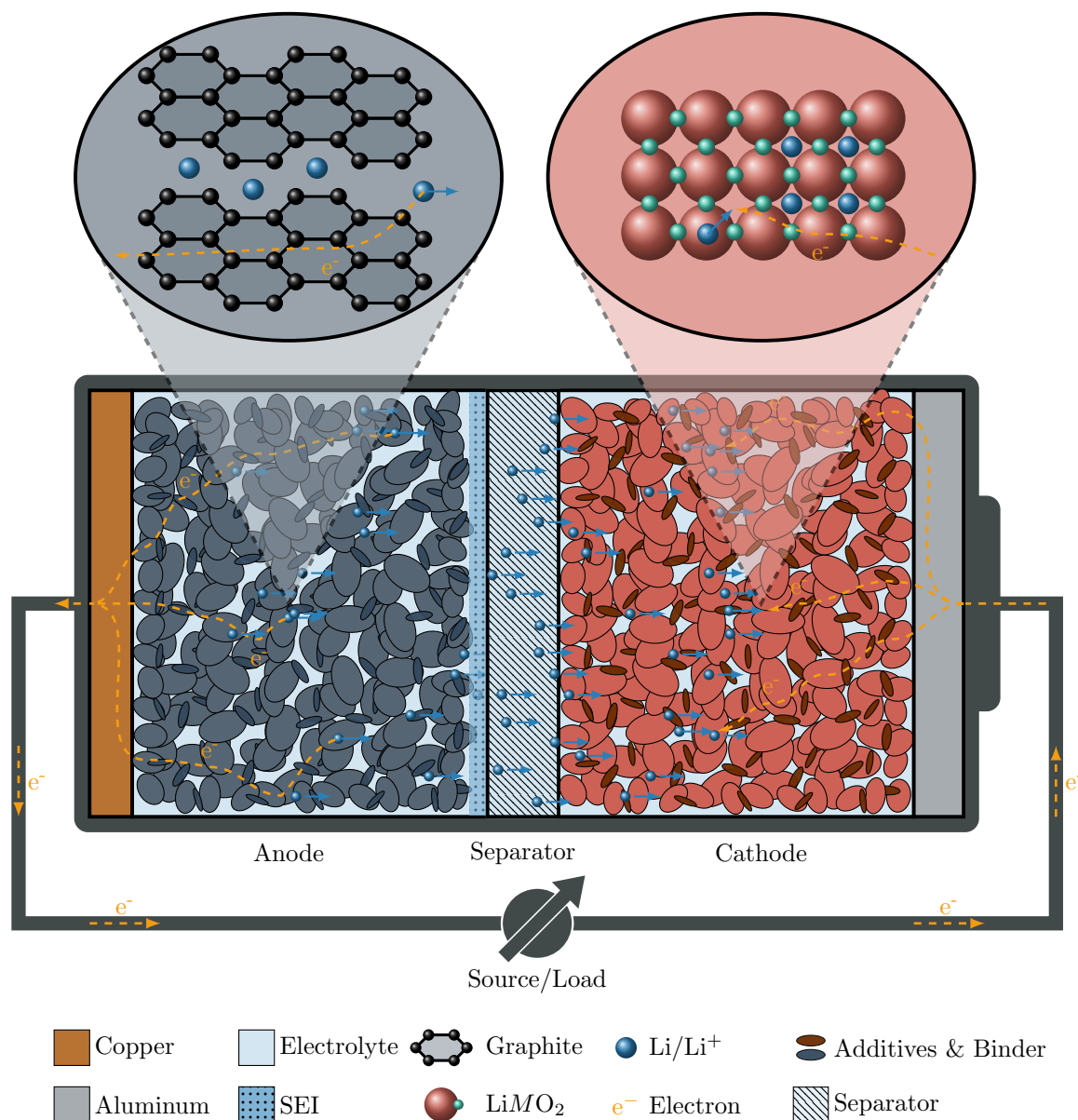


Figure 2.2: Schematic representation of the components of a lithium-ion cell and the current and ion flow during the discharge process. Above the cell, the structure of an anode particle made from graphite (left) and a cathode particle made from lithium-metal oxide (LiMO₂) (right) is illustrated. The solid electrolyte interphase (SEI) is shown only simplified at the interface between the anode and the separator.

collectors are usually made of copper at the anode and aluminum at the cathode, as shown in Fig. 2.2. From a functional point of view, the choice of current collector materials is based on their high electrical conductivity and electrochemical stability in the presence of the remaining cell materials, which ensures long term functionality and safe operation of the cell, provided the cell is operated within its current, voltage and temperature limits [56–59]. The electrode composite consist of an active material, holding the lithium inventory, a binder, ensuring mechanical stability [60], and optional additives such as carbon black to increase the electronic conductivity of the composite [61].

Various active materials are used for commercial LIBs, differing in their physical properties, such as

structure, potential, specific capacity and cycle stability. Furthermore, economical, social and ecological aspects, such as costs, mining conditions, and environmental friendliness, play a part in the selection of active materials. Fig. 2.3 shows the specific capacity and potentials of commonly used active materials for the cathode (Fig. 2.3a) and the anode (Fig. 2.3b).

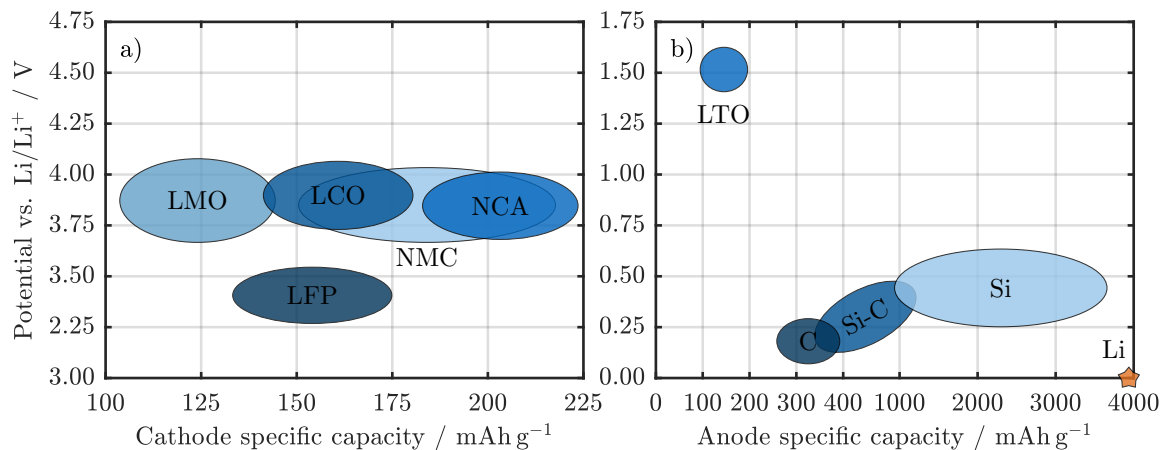


Figure 2.3: Overview of common active materials for a) cathodes and b) anodes with regard to their approximate discharge potentials vs. Li/Li⁺ over the specific capacity. Derived from [62–69].

Cathode Active Materials The most common cathode active materials for commercial LIBs are layered transition metal oxides [66; 70], such as lithium cobalt oxide (LCO), lithium nickel manganese cobalt oxide (NMC), and lithium nickel cobalt aluminum oxide (NCA). LCO was the first commercialized cathode active material, is still used for portable electronic devices [3; 65; 71], and has an advantageous cycle life. However, it comes with high economical cost, due to the large share of cobalt, and a low thermal stability [3; 67; 69; 72]. NMC has a good energy density, power capability, thermal stability and cycle life and is therefore used in many application areas from portable electronics to power tools and EVs [3; 73]. The large variation in specific capacity for NMC in Fig. 2.3a reaching from about 160 mAh g⁻¹ to 200 mAh g⁻¹ and above is related to the ratio of nickel, cobalt, and manganese in the active material, whereby the nickel-rich version NMC-811 is at the upper end and NMC-111 at the lower end [66; 68; 71]. In addition to the increase in energy density of the NMC-811 system, the price advantage due to the reduction in the cobalt content also plays a role. Another layered transition metal oxide is NCA, which has a comparable good energy density, power capability, and cycle life as NMC. Areas of application are premium electronics and EVs [3; 73; 74].

In addition to the layered transition metal oxides, there are spinel transition metal oxides such as lithium manganese oxide (LMO) and systems using poly-anionic compounds such as lithium iron phosphate (LFP). Both, LMO and LFP are cost-efficient due to the lack of cobalt and nickel, show a very good thermal stability, but have a lower specific capacity. Moreover, LMO has a very good power capability and is therefore mostly used in high power applications [3]. However, it shows only a moderate cycle life [3]. LFP on the other hand has a very good cycle life, but an adverse energy density due to the comparably low potential of 3.45 V against Li/Li⁺ [65]. For this reason, the main area of application have been stationary energy storage applications, for which the energy density is not as important as for EVs [3; 4; 32; 75]. Despite the disadvantageous energy density and thus shorter driving range, many manufacturers, such as Tesla, Chevrolet, BMW, and BYD, are opting for BEVs

powered by LFP batteries [76; 77]. This is mainly driven by the lower prices, the cycle stability and the safety of LFP [76; 77].

Anode Active Materials On the anode side, graphite (Gr) has been asserting itself as the go to intercalation material for more than 20 years, although the theoretical specific capacity of 372 mAh g^{-1} is rather small compared to other anode active materials [32; 67; 78; 79]. Advantageous are the long cycle life, its cost-efficiency, low volume expansion and safety [18; 67; 69]. A side effect of graphite as an anode active material is the formation of a passivation layer on the surface of the graphite particles, the solid electrolyte interphase (SEI). The SEI is displayed in a simplified way at the interface between anode and the separator in Fig. 2.2. It is formed from electrolyte decomposition products mainly during the first few cycles and it is permeable to lithium-ions [78–80]. Just as the oxide layer on aluminum prevents the underlying aluminum from corroding, so does the SEI prevent further reductive electrolyte decomposition and adverse solvent co-intercalation [78; 79]. Apart from graphite, there is also lithium titanate (LTO) as another intercalation material. The advantages of LTO are long cycle life, high rate capability, and very good thermal stability [67; 69]. Figure 2.3b shows the disadvantages of LTO: a rather low specific capacity of about 175 mAh g^{-1} and a relatively high potential of 1.55 V with respect to Li/Li^+ [65; 67; 69]. In recent years, anodes with alloying type materials, such as silicon (Si) and silicon oxides, have been investigated. The appeal of these materials lies in their very high specific capacity of 3579 mAh g^{-1} , which, however, comes at the price of very high volume changes of up to 300% [65; 67; 69; 81]. This excessive change in volume leads to strong mechanical stress and chemical degradation of the active material [65]. There are two approaches to circumvent this negative property. One approach reduces the effectively used proportion of available silicon, which also reduces the change in volume and thereby increases the cycle stability [81]. This case is represented in Fig. 2.3b by the lower range of the specific capacity of silicon of about 1000 mAh g^{-1} . The other approach relies on blended electrodes, combining silicon and graphite, and thereby increasing the specific capacity of the anode and limiting the volume expansion [79; 82; 83]. This case represents the transition from graphite to silicon anode materials in Fig. 2.3b. LIBs with blended electrodes are commercially available [84–86] and are already used in EVs [73; 74]. Seen from an energetic perspective, the theoretically optimal anode active material for LIBs is pure lithium itself with a specific capacity of 3860 mAh g^{-1} and the lowest potential of 0V compared to Li/Li^+ . However, in such a cell, the anode is constantly being dissolved and built up again during cycling, which leads to mechanical stability problems. In addition, lithium dendrites may form during cycling, which can lead to safety-critical internal short circuits [69; 87].

2.1.1.2 Electrolyte

The electrolyte ensures the ionic transport of lithium-ions between the active materials through the pores of the separator and is crucial for the safety, performance and lifetime of a LIB [88; 89]. Non-aqueous liquid electrolytes consisting of organic solvents, conducting salts and various additives are widely used for LIBs [90]. LiPF_6 is the most commonly used conducting salt, although a large variety of other salts, such as LiBF_4 , LiAsF_6 , LiClO_4 , LiDFOB , LiBOB , or LiTFSI , are known [89–91]. A large number of carbonate derivatives such as ethylene carbonates (ECs), propylene carbonates (PCs), ethyl methyl carbonates (EMCs), diethyl carbonates (DECs), dimethyl carbonates (DMCs), or fluoroethylene carbonates (FECs) and combinations of these are used as a solvent [88; 90; 92].

2.1.1.3 Separator

The main purpose of the porous separator for LIBs using liquid electrolytes is to prevent an internal electronic short circuit between the electrodes and at the same time to provide a passage for the lithium-ions to cross between the electrodes [93; 94]. Ideally, separators therefore have very low electronic and very high ionic conductivity, whereby the electronic conductivity is dependent on the used separator material and the ionic conductivity on the electrolyte and structural features, such as porosity and tortuosity, of the separator. Another relevant property of separators is thermal stability to avoid shrinking or melting of the separator during elevated temperatures, which could lead to safety critical short circuits [94; 95].

2.1.2 Cell Format and Size

As large as the number of applications with LIBs as energy source is, as large is the number of different LIB formats and sizes [96–98]. The optimal format and design of LIBs strongly depend on the application and its system related constrains. The basic design of an electrochemical cell as shown in Fig. 2.2 can be scaled up to commercial LIBs in different ways. In order to increase the energy density, both sides of the current collector foil are usually coated with composite materials as shown in Fig. 2.4a [99]. The double-sided coated electrode sheets are then wound or stacked as shown in Fig. 2.4b, whereby the winding can be either spiral or flat. Due to winding or stacking, a second separator layer as shown in Fig. 2.4a is needed to prevent a short circuit between neighboring layers. The wound or stacked electrodes are assembled into a casing. The three most common casing formats are cylindrical, prismatic and pouch as shown in Fig. 2.4c. Cylindrical and prismatic cells have a hard casing typically made from stainless steel or an aluminum alloy respectively. Pouch cells on the other hand are enclosed by a flexible aluminum foil, which is laminated with plastics on both sides to ensure electrical insulation and electrochemical stability against the encapsulated cell materials [100]. Cylindrical casings typically contain the spiral wound electrodes, prismatic casings can either be equipped with flat wound or stacked electrodes, and the pouch format generally uses stacked electrodes [101–103].

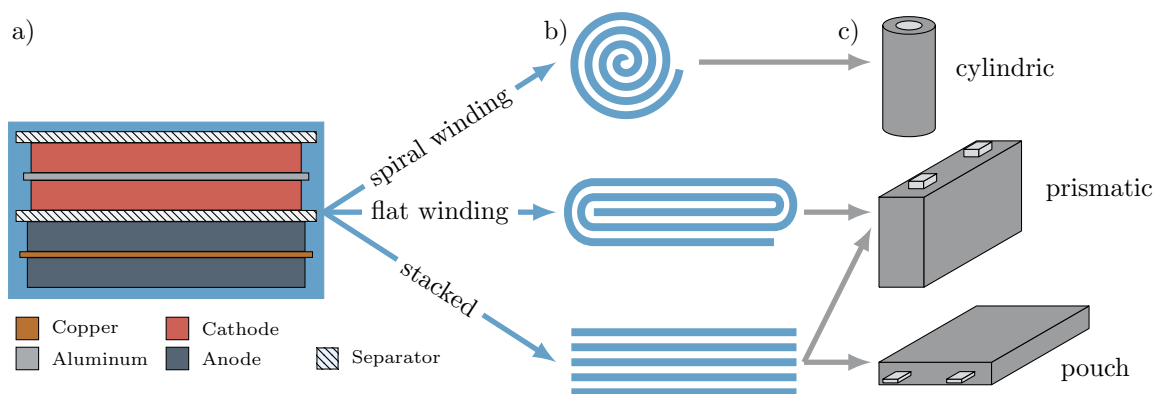


Figure 2.4: a) Stacking of a double-sided coated electrodes for anode and cathode isolated by separator layers. b) Winding methods for the stacked electrodes and c) integration in corresponding cell casings. Adapted from [96].

The individual casing formats each have different advantages and disadvantages. Prismatic cells, for instance, are mechanically stable [104; 105] and are often equipped with additional safety devices,

such as fuses and vents [106], but at the expense of increased weight and volume. The casing foils of pouch cells on the other hand are thin and thereby reduce weight and volume, but at the cost of mechanical stability. Cylindrical cells are mechanically stable, due to the metal casing and the round shape and include several safety features. Additionally, they have affordable prices, due to the highly industrialized and standardized production in large numbers such as the 18650 format (18 mm diameter, 65 mm height) [84; 107; 108]. For systems with high energy requirements in a small space such as EVs, cylindrical cells are disadvantageous at first glance, since the cylindrical casing means that the packaging density is lower than for prismatic or pouch cells. Since standardized cylindrical cells come in relatively small formats and therefore capacity, many cells are needed to achieve corresponding capacities, leading to a more complex battery pack with more cell interconnections and thus potential fault sources [109]. However, the low packaging density and the large number of cylindrical cells are not only disadvantages, but also offer design advantages. The free space between the cells can be used for a cooling/heating system and the effects of a defective cell are more manageable than with large-format cells, due to the lower capacity of the cylindrical cells. For these and other reasons, Tesla was one of the first EV manufacturers, who incorporated cylindrical cells into their models [73; 74; 109; 110]. Other EV manufacturers, such as Lucid, Rivian, or BMW, follow the trend and already offer or plan to produce EVs with cylindrical cells [111; 112]. With larger formats, such as 21700 or 46800, the energy content per cell is improved and manufacturing costs can be decreased [73; 74; 107; 113]. However, the larger cell formats also lead to internal inhomogeneities in temperature and current distribution [96; 97; 113].

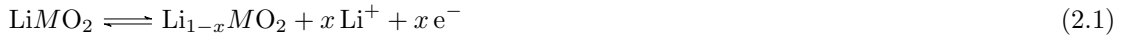
Overall, cylindrical cells are most appropriate for addressing the research questions Q1 to Q4 from Section 1.2 in this thesis for several reasons:

They are of high production quality and widely available in different chemistries and sizes, which is favorable for the comparison of different chemistries and the investigation of internal temperature inhomogeneities. They have a relatively low capacity, which is convenient for laboratory-scale investigations, and they are in line with the current trend of EV manufacturers. Consequently, the focus of this thesis is on the investigation of cylindrical cells. The specific cells that are actually investigated in this thesis is covered separately in Chapter 3.

2.1.3 Functional Principle of Lithium-Ion Batteries

After the introduction to the main components of a LIB follows a brief description of the main chemical reactions in an electrochemical cell. The cell in Fig. 2.2 shows the external current and internal ion flow during discharging. This means that the anode is oxidized and lithium-ions deintercalate from the graphite host lattice (C_6) as shown in the closeup above the anode in Fig. 2.2. The released lithium-ions diffuse/migrate over the electrolyte through the separator towards the cathode where they intercalate in the host lattice of the cathode active material, which is shown in the closeup above the cathode in Fig. 2.2. As mentioned in Section 2.1.1, the active material of the cathode is usually a lithium-metal oxide ($LiMO_2$) with M representing the metals nickel, cobalt and/or manganese. Simultaneously, the path of the electrons lead from the active material of the anode via the anode current collector (Cu) and the external load to the cathode current collector (Al) and finally into the active material of the cathode. During charging the process is reversed. This redox reaction can be described with two equations [114–117]:

Eq. (2.1) at the cathode



and Eq. (2.2) at the anode



where x represents the level of lithiation of the host lattice in the theoretical range of $0 \leq x \leq 1$. In practice, the reversible delithiation range for cathode materials is limited and reaches for instance $x \leq 0.5$ for metal oxides with nickel, cobalt or manganese [117].

2.2 Temperature-dependent Processes in Lithium-Ion Batteries

The ionic and electronic current flow paths, as just described in Section 2.1.3, are dependent on the material properties and underlying transport mechanisms in the cell, causing losses that manifest in different overpotentials and at different time scales. Among other factors, these losses and consequently the cell impedance are strongly dependent on temperature, which is the reason why an impedance-based temperature estimation is possible in the first place. For this reason, this section discusses the theory behind the individual loss processes. A special focus is put on their temperature dependence and the relation to the cell impedance.

$$U_{\text{cell}} = U_{\text{OCV}} - \eta_{\text{IND}} - \underbrace{(\eta_{\text{elec}} + \eta_{\text{ion}} + \eta_{\text{cont}})}_{\eta_{\Omega}} - \underbrace{(\eta_{\text{ct,a}} + \eta_{\text{ct,c}})}_{\eta_{\text{CT}}} - \underbrace{(\eta_{\text{diff,l}} + \eta_{\text{diff,a}} + \eta_{\text{diff,c}})}_{\eta_{\text{DIFF}}} \quad (2.3)$$

The cell voltage U_{cell} in Eq. (2.3) can be broken down to five parts [18; 33; 118–121]:

1. the open-circuit-voltage (OCV) U_{OCV} ,
2. the inductive overpotential η_{IND} ,
3. the ohmic overpotential η_{Ω} related to electronic η_{elec} and ionic η_{ion} losses also including contact losses η_{cont} ,
4. the overpotential η_{CT} related to interface losses between the anode/cathode $\eta_{\text{ct,a}}/\eta_{\text{ct,c}}$ and the electrolyte,
5. as well as the overpotential η_{DIFF} related to diffusion losses in the liquid phase $\eta_{\text{diff,l}}$ and the solid phase $\eta_{\text{diff,s}}$, whereby a further differentiation can be made between diffusion in the active material of the anode $\eta_{\text{diff,a}}$ and the cathode $\eta_{\text{diff,c}}$.

A more detailed discussion of the individual voltage shares follows in the upcoming sections. The discussion is confined to the acceptable temperature operating range of LIBs, which is approximately -20 to 60 °C [2; 122]. This temperature range is also covered by the majority of all methods discussed later in the context of Table 2.5 and is thus also the range in which the method developed in Chapter 4 is intended to operate. Continuous operation near the lower or upper temperature limit of the operating range can have a severe negative impact on the lifetime, performance and safety of a LIB [18; 29]. For instance, operation at elevated temperatures has a negative effect on aging and can lead to thermal runaway of the LIB [10; 18]. At very low temperatures, in contrast, the performance of a LIB is severely limited and the risk of lithium plating rises [18; 123; 124]. A more detailed discussion of the effects of temperature on LIBs is provided in Section 2.3. Due to the negative effects, the temperature range of

a LIB should be further restricted to approximately between 15 °C and 35 °C for optimal operation [2].

2.2.1 Open-Circuit-Voltage

The OCV describes the cell voltage in equilibrium when there is no external load applied to the cell. Since impedance measurements are always based on differential values in voltage and current, the temperature dependency of the OCV is of no further concern for this work and is only mentioned for the sake of completeness. The OCV is described by the Nernst equation in Eq. (2.4) [125].

$$U_{\text{OCV}} = U_S + \frac{RT_a}{nF} \ln \left(\frac{\alpha_{\text{ox}}}{\alpha_{\text{red}}} \right) \quad (2.4)$$

Its potential is dependent on the standard cell potential U_S which is the difference between the half-cell potentials of the cathode and anode material under standard conditions, the absolute temperature T_a , the number of electrons transferred in the cell reaction n , and the ratio of the chemical activities α_{red} and α_{ox} . The other parameters are the universal gas constant R and the Faraday constant F . The Nernst equation and consequently the OCV have three temperature dependent parts. The directly proportional part comes with the prefactor of the logarithm. Two indirectly proportional parts are concealed in the chemical activities, which themselves are dependent on temperature [126; 127], and the standard cell potential. The standard potential is defined at a reference temperature, for example at room temperature (25 °C), but changes with temperature due to the reaction entropy [128; 129].

2.2.2 Overpotentials

By applying a current to a cell, it leaves its electrical equilibrium and the overpotentials from Eq. (2.3) build up related to different losses at different time scales as shown in Fig. 2.5. The scale below the example of the pulse response in Fig. 2.5 focuses on the overpotentials relevant for temperature estimation from μs to s. However, it also includes effects occurring at load durations beyond that scale, such as a change in the OCV due to a change in state of charge (SOC) and aging as a long term effect. The losses/overpotentials can be related to different conduction phenomena, which in turn can be expressed as a conductivity or resistivity. The following sections discuss the relation of the conductivity/resistivity expressions to temperature. The result and the corresponding equations are summarized in the table at the bottom of Fig. 2.5. In this table, all proportionalities refer to the overpotential of the cell and thus to the resistivity. Note that the individual equations referenced in the table do not always do so. In the literature, conductivity, the reciprocal of resistivity, is often used when considering the temperature dependence of processes and is therefore also used in the corresponding equations.

2.2.2.1 Ohmic Overpotential

Since both, ohmic and inductive overpotentials occur almost instantaneously after a current change, it is difficult to separate the two at first. However, the inductive behavior of LIBs decays quickly after the current has settled at a new constant level and is in general beyond the measuring ability of a BMS. The ohmic overpotential η_Ω is influenced by the electronic (η_{elec}) and ionic (η_{ion}) conductivity of the materials used in the cell and the contact resistance (η_{cont}) between anode/cathode and current collector, as well as particle to particle contact at anode/cathode as indicated in Fig. 2.5 [33; 120].

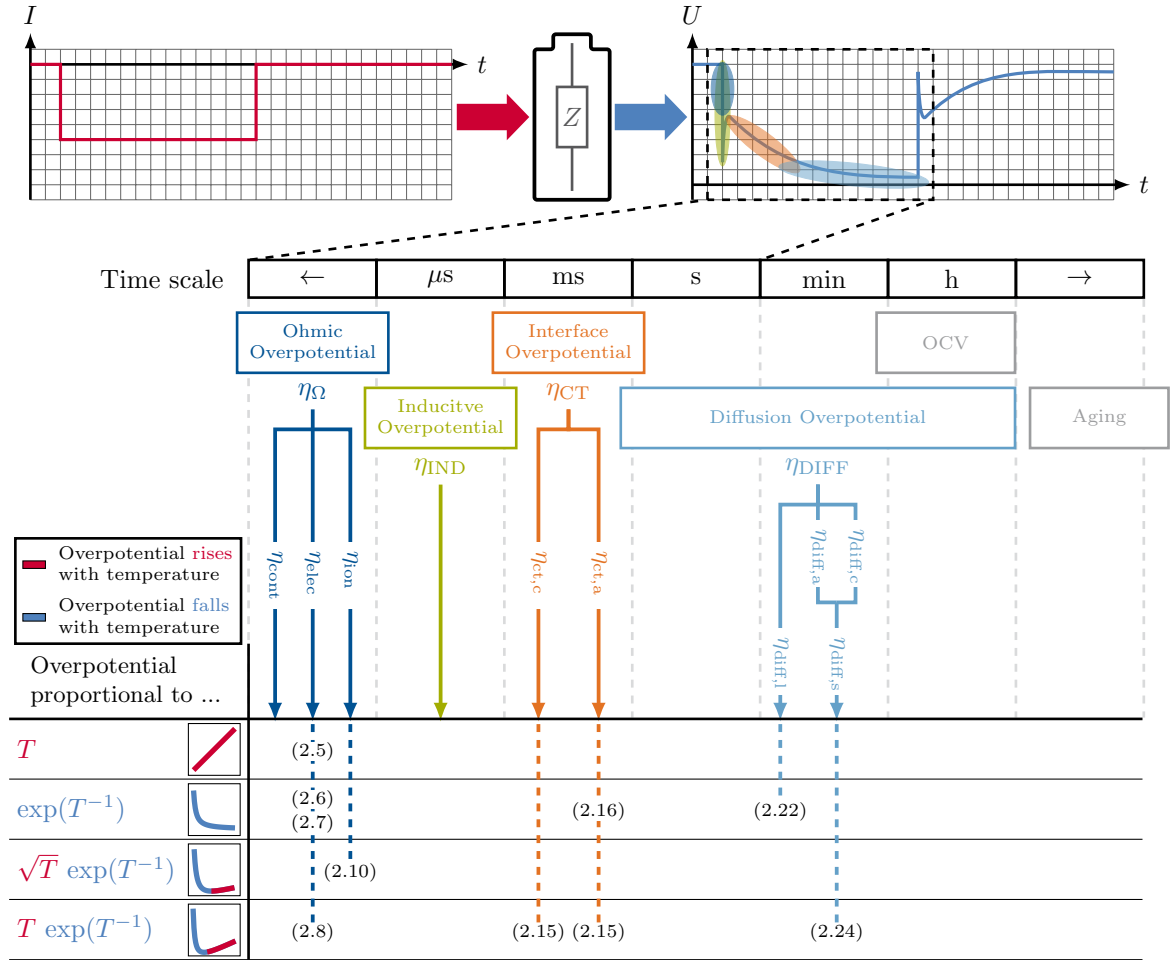


Figure 2.5: Exemplary voltage response of a LIB to a current pulse excitation and classification into the corresponding overpotentials. Below the approximate time intervals in which the overpotentials occur as well as the corresponding dependencies to temperature with reference to the associated equations. Based on [33; 118; 120].

Contact Losses A LIB is not made from a homogeneous block and therefore the transition between materials causes a contact resistance leading to the overpotential η_{cont} . The contact losses between anode/cathode and current collector and between anode/cathode particles are evident in measurements at high frequencies and are superimposed by the inductive behavior of the cell [119; 120]. However, Illig et al. [130] showed with a specially prepared experimental cell that the contact resistance between the cathode and the current collector is independent of both, the SOC and the temperature. Rattanaweeranon et al. [131] studied the influence of mechanical pressure and temperature on the conductivity of bulk graphite samples. The conductivity increased with pressure due to the improved electrical contact between the particles. The general temperature behavior was not changed by the pressure. This suggests that the contact resistance between particles does not depend on temperature. Together with the results of Illig et al. [130], it can be assumed that the contact losses are independent of the temperature.

The electronic overpotential η_{elec} is determined by the electronic conductivity of the materials in a cell. This includes the electronic conductivity of the active material particles, the conductive additives, the current collector, and the cell taps [33; 120], which are discussed next.

Current Collectors Current collectors and cell taps are made from metals, which in general show an increasing resistance with increasing temperature. The most comprehensive description of the resistance behavior of metals over a large temperature range is provided by the Bloch-Grüneisen formula [132–134]. However, the discussion is limited to the acceptable temperature range of approximately -20 to 60 °C [2; 122]. In this temperature range, the resistance behavior of metals is almost linear. For this reason, the linear approximation in Eq. (2.5) for the relationship between temperature and resistance is often used

$$\rho_M(T_a) = \rho_0 [1 + \alpha (T_a - T_0)], \quad (2.5)$$

where T_a is the absolute temperature, ρ_0 is the resistivity measured at the reference temperature T_0 , and α is the temperature coefficient of resistivity. This empirical fitted values describe the resistivity change due to temperature in the region of the reference temperature T_0 . The values of α may vary depending on T_0 . For the LIB relevant materials of the current collectors, copper and aluminum, the values for ρ_0 and α are given in Table 2.1 along with the conductivity σ_0 . The values in Table 2.1 and in all following tables in this section refer to the reference temperature of $T_0 = 20$ °C, which is exactly in the center of the considered temperature range between -20 °C and 60 °C.

Table 2.1: Resistivity ρ_M , conductivity σ_M , and temperature coefficient α for the reference temperature $T_0 = 20$ °C for the current collector metals copper and aluminum.

Ref.	Material	resistivity $\rho_M / \Omega \text{ cm}$	conductivity $\sigma_M = \frac{1}{\rho_M} / \text{S cm}^{-1}$	temperature coefficient α / K^{-1}
[133]	copper	1.68×10^{-6}	5.96×10^5	4.04×10^{-3}
[135]	aluminum	2.65×10^{-6}	3.77×10^5	3.90×10^{-3}

Active Materials Active materials of a LIB are made from several different materials, as discussed in Section 2.1.1. At the anode, graphite and increasingly more silicon and silicon-oxides are used, whereas at the cathode metal-oxides are dominant. The active materials serve as electronic and ionic conductor in a LIB.

Graphite is a crystalline form of carbon and consists of stacked layers of graphene. It is known as a semi-metal [33; 136] with an electronic conductivity in the range of 10^3 to 10^4 S cm^{-1} [33; 137], which is still good but already at least a magnitude less than that of the current collector metals in Table 2.1. Due to loose bonding between the graphene layers, the conductivity of graphite differs with direction [33; 138]. The conductivity along each graphene layer is about 100 times better than the conductivity perpendicular to it [139]. The literature offers different statements on the temperature dependence of the electric conductivity of graphite, whereby different temperature ranges and specimens were investigated. Dutta [140] determined a roughly exponential behavior for single graphite crystals between 80 to 500 K. He found a rising conductivity with temperature parallel to the graphene layers and a falling conductivity perpendicular to the graphene layers. On particle/bulk level several studies showed an increasing conductivity with increasing temperature [131; 141–143], suggesting that the conductivity parallel to the graphene dominates on this level. Iwashita et al. [143] described the temperature-conductivity relation for graphite with an Arrhenius behavior as stated in Eq. (2.6)

$$\sigma_{Gr}(T_a) = \sigma_0 \exp\left(-\frac{E_{A,b}}{k_B T_a}\right), \quad (2.6)$$

where σ_0 is a pre-exponential conductivity factor and k_B is the Boltzmann constant. In this case, the activation energy $E_{A,b}$ is related to a particle due to the representation of the Arrhenius behavior by means of the Boltzmann constant and thus has the unit [J]. Using the Avogadro constant N_A and the relation $R = k_B N_A$, the Arrhenius behavior can also be represented with reference to the general gas constant R . Thus, the activation energy $E_{A,r}$ refers to the amount of substance and has the unit [J mol⁻¹]. In the literature, both variants are used and are distinguished in this work with the respective index in $E_{A,b}$ and $E_{A,r}$. The temperature behavior in Eq. (2.6) applies to the above mentioned practical temperature range between -20°C and 60°C for LIBs [2; 122]. In the case of semi-metals such as graphite, the conductivity decreases again as the temperature rises above 500°C [131; 139; 141–143]. In addition, the electrical conductivity of a graphite anode is SOC dependent. With increasing SOC the lithium content in the anode rises and thus the conductivity due to the electron donor nature of the lithium [33; 144].

Because of its extremely high specific capacity as shown in Fig. 2.3b, silicon is considered as a promising anode material for LIBs. It is mostly used in graphite composite electrodes to increase the energy density [79]. As a semiconductor, silicon has a relatively poor intrinsic electronic conductivity of about $10^{-3} \text{ S cm}^{-1}$ [145], which is eight orders of magnitude lower than the conductivity of the current collector metals in Table 2.1 and at least six magnitudes less than graphite.

The conductivity of semiconductors depends on the number of electrons transferred from the valence band to the conduction band. The required energy ΔE depends on the type of semiconductor and its doping or impurity. For a pristine semiconductor ΔE corresponds to the difference between the conduction band energy E_c , which lies higher in energy, and the valence band energy E_v at a lower level. This energy difference decreases by doping or impurity to $\Delta E = E_c - E_d$, where $E_d > E_v$. The number of electrons, and hence the conductivity, depends on temperature as given in Eq. (2.7).

$$\sigma_{\text{Si}}(T_a) = \sigma_0 \exp\left(-\frac{\Delta E}{k_B T_a}\right) \quad (2.7)$$

The pre-exponential factor σ_0 is an empirically determined value, which depends on the temperature range. For low temperatures, for which $k_B T_a \ll (E_c - E_v)$ holds, σ_0 is proportional to the doping or impurity density, since most of the electrons originate from the doping atoms or impurities. At higher temperatures, the electrons originating from the valence band of the semiconductor into the conduction band dominate. [146]

The increasing conductivity with increasing temperature was already demonstrated for amorphous silicon [147; 148], silicon dioxide [149], and silicon carbide [150]. In addition to the temperature dependency, Pollak et al. [148] report that, as with graphite, the conductivity depends on the inserted lithium content. However, there is no monotonous relation to the SOC and an additional relation to the extraction and insertion of lithium.

After considering the anode materials, the cathode materials follow. These are mainly composed of metal-oxides, which still have semiconductor features [33; 151], but with more insulating properties as the conductivity values in Table 2.2 show. As with silicon, the electron conductivity of cathode active materials σ_{CAM} is a thermally activated phenomenon and generally follows an Arrhenius-like trend [18; 33; 158; 159]:

$$\sigma_{\text{CAM}}(T_a) = \frac{\sigma_0}{T_a} \exp\left(-\frac{E_{A,b}}{k_B T_a}\right) \quad (2.8)$$

Due to their poor electron conductivity, additives are used in cathodes to improve conductivity, often

Table 2.2: Resistivity ρ_{CAM} and conductivity σ_{CAM} values of common cathode and anode active materials at 20 °C.

Ref.	Material	resistivity $\rho_{\text{CAM}} / \Omega \text{ cm}$	conductivity $\sigma_{\text{CAM}} = \frac{1}{\rho_{\text{CAM}}} / \text{S cm}^{-1}$
[33; 137]	Graphite	$\sim 10^{-3}$ to 10^{-4}	$\sim 10^3$ to 10^4
[145]	Silicon	$\sim 10^3$	$\sim 10^{-3}$
[33; 137; 152]	LCO	$\sim 10^3$ to 10^4	$\sim 10^{-3}$ to 10^{-4}
[33; 137; 153]	LMO	$\sim 10^5$ to 10^6	$\sim 10^{-5}$ to 10^{-6}
[33; 90; 137; 154]	LFP	$\sim 10^9$	$\sim 10^{-9}$
[155; 156]	NMC	$\sim 10^3$ to 10^6	$\sim 10^{-3}$ to 10^{-6}
[157]	NCA	$\sim 10^4$	$\sim 10^{-4}$

in the form of conductive carbon black (amorphous carbon) [33; 137; 160]. The temperature behavior of amorphous carbon can be approximated with [161]

$$\sigma_{\text{CB}}(T_{\text{a}}) = \sigma_0 \exp\left(-\frac{T_0}{T_{\text{a}}}\right)^{\beta}, \quad (2.9)$$

where T_0 is a reference temperature and β is a conduction process dependent factor with $\beta \in [\frac{1}{4}, \frac{1}{3}, 1]$. The conductivity always increases with temperature, regardless of the value of β . In addition to temperature, the conductivity of cathode materials is dependent on the lithiation level. Amin and Chiang [156] showed in their study that the electrical conductivity of different NMC materials increases with increasing delithiation. Other studies showed that this fact is also true for NCA [157] and LCO [152]. The fraction of different materials in the cathode can also affect the conductivity, as indicated by the relatively large conductivity range for NMC in Table 2.2. For instance, Wang et al. [155] showed that the conductivity of NMC improves with increasing nickel content.

Electrolyte In addition to the ohmic overpotential caused by electronic conductivity of the active materials, additives, and the current collectors, an ionic overpotential occurs, which is caused by the ionic current flow through the cell and is essentially determined by the ionic conductivity of the electrolyte [18; 33; 120; 162]. For the ohmic conductivity, the time scale of consideration in Fig. 2.5 is in the range of a few microseconds and less. For this reason, effects such as diffusion and convection, which arise later in the electrolyte, can be neglected in this context. Without considering diffusion and convection, the overpotential η_{ion} and the absolute ionic current is directly proportional to the ionic conductivity κ of the electrolyte [18]. The ionic conductivity of the electrolyte depends strongly on the temperature. It increases monotonically in a Arrhenius-like manner with temperature up to very high temperatures, where the ionic conductivity is more dominantly affected by the dielectric constants of the solvent mixture [163]. A frequently used fitting function to describe this convex behavior is derived from the Vogel-Tamman-Fulcher (VTF) equation [18; 33; 163]

$$\kappa(T_{\text{a}}) = \frac{\kappa_0}{\sqrt{T_{\text{a}}}} \exp\left(-\frac{E_{\text{A,r}}}{R(T_{\text{a}} - T_{\text{g}})}\right), \quad (2.10)$$

where T_{g} is the theoretical glass transition temperature in Kelvin [33]. The constant κ_0 , the activation energy $E_{\text{A,r}}$, and T_{g} are fitted parameters.

In addition to the temperature, the initial salt concentration influences the conductivity, whereby the relationship is also convex. Thus, the conductivity increases with increasing salt concentration up to

a certain point, and then decreases again, since at too high salt concentration ions of opposite charges can become associated or paired, and thereby cease to contribute to the overall conductivity [163; 164]. Moreover, it should be mentioned that the separator used also has an influence on the overall ionic conductivity of the cell, yet preserving the Arrhenius-like behavior [165]. Table 2.3 summarizes the ionic conductivity of several electrolytes.

Table 2.3: Ionic conductivity of lithium salt solution at 20 °C. All samples referenced are 1 mol dm⁻³ solutions of their respective salts. Table adapted from [33].

Salt	Solvent	Ionic conductivity κ / S cm ⁻¹
Lithium perchlorate (LiClO ₄)	PC EC/DMC	5.6 8.4
Lithium hexafluoroarsenate (LiAsF ₆)	PC EC/DMC	5.7 11.1
Lithium tetrafluoroborate (LiBF ₄)	PC EC/DMC	3.4 4.9
Lithium trifluoromethanesulfonate (LiTf)	PC	1.7
Lithium bis(trifluoromethanesulfonyl)imide (Lilm)	PC EC/DMC	5.1 9.0
Lithium hexafluorophosphate (LiPF ₆)	PC EC/DMC	5.8 10.7

2.2.2.2 Inductive Overpotential

The fastest effect, beside the instantaneous ohmic voltage drop, contributing to the overpotential of the cell shown in Fig. 2.5 in the microseconds regime is dominated by the inductance of the cell. In this time domain, the cell geometry and electrode design, including tab number and positioning, affect the overpotential behavior [166; 167]. Landinger et al. [166] showed that the impedance of LIBs is temperature dependent in the frequency range beyond 10 MHz. However, the Arrhenius-like temperature dependency was attributed to resistive losses, caused by ionic current flow [166]. Due to the high measurement frequency in the MHz regime and the specially adapted measurement setup using a vector network analyzer to measure the inductive effects, temperature estimation relying on inductance is out of the scope for a temperature estimation method running on a BMS.

2.2.2.3 Interface Overpotential

After the instantaneous ohmic and the inductive voltage drop, losses due to the charge transfer between the electrolyte and the anode/cathode active material, including the SEI, build up in a time domain from milliseconds to seconds as shown in Fig. 2.5 [118; 120; 168]. The time delay compared to the ohmic overpotential is caused by the double layer capacitance, which is formed at the interface between the electrolyte and the electrode. Although the double layer capacitance does not cause a direct overpotential, its capacitance causes the interface potential to behave like a first-order timing element.

Charge Transfer Resistance The charge transfer resistance of a LIB is related to the reaction kinetics from the Butler-Volmer equation and can be linearized for relatively small currents and notably fast

electrode kinetics [18; 169; 170]:

$$R_{\text{ct}} = \frac{RT_{\text{a}}}{F i_0}. \quad (2.11)$$

Temperature and SOC dependence of the charge transfer resistance R_{ct} in Eq. (2.11) are linked to the exchange current density i_0

$$i_0 = FA k_{\text{s}} c^{\delta}, \quad (2.12)$$

where k_{s} is the standard rate constant, A is the electrode area, c is the concentration of lithium-ions in the solid phase, and δ is the transfer coefficient [18; 169]. The dependence on SOC related to the electrode is given by

$$c = \text{SOC} \cdot c_{\text{s,max}}, \quad (2.13)$$

with the maximum accessible lithium concentration in the solid phase $c_{\text{s,max}}$ [18; 169]. The dependence on temperature is related to the Arrhenius behavior of the standard rate constant

$$k_{\text{s}} = k_0 \exp\left(\frac{-E_{\text{A,r}}}{RT_{\text{a}}}\right), \quad (2.14)$$

with the pre-exponential factor k_0 [18; 169]. By replacing the exchange current density in Eq. (2.11) with Eq. (2.12) and substituting k_{s} and c in Eq. (2.12) with the corresponding dependencies of Eq. (2.13) and Eq. (2.14), a resistance can be derived which describes the dependence of the charge transfer on temperature and SOC [18; 169]

$$R_{\text{ct}} = \frac{R}{F^2 A k_0 (\text{SOC} \cdot c_{\text{s,max}})^{\delta}} T_{\text{a}} \exp\left(\frac{E_{\text{A,r}}}{RT_{\text{a}}}\right). \quad (2.15)$$

With k_{s} from Eq. (2.14) inserted in the denominator of Eq. (2.15), the sign in the exponent changes from minus to plus. As with the electrolyte, the temperature dependence of the charge transfer resistance can be divided into two regions: A region for moderate temperatures with an Arrhenius-like behavior, where the charge transfer resistance decreases with temperature, and an elevated-temperature region, where the charge transfer resistance increases again with temperature. Gantenbein et al. [120] showed via EIS measurements that the charge transfer resistance at the cathode increases at the SOC boundaries, whereas the charge transfer resistance at anode is almost independent of SOC. Another impact of the Butler-Volmer equation on the charge transfer resistance is the non-linear behavior of its overpotential at increased current densities, causing the charge transfer resistance to decrease as the current density increases [171].

Surface Film Resistance As discussed in Section 2.1.1, a SEI forms at the anode during cycling. The SEI is often expressed as a temperature-dependent surface film resistance R_{SEI} following the Arrhenius equation [18; 120; 169]

$$R_{\text{SEI}} = R_1 \exp\left(\frac{E_{\text{A,b}}}{k_{\text{B}} T_{\text{a}}}\right), \quad (2.16)$$

where R_1 is a pre-exponential factor. In addition, R_{SEI} is SOC-dependent, but the dependency is only marginal and occurs at low temperatures according to [120; 169].

2.2.2.4 Diffusion Overpotential

The transport of lithium-ions associated with diffusion and migration can be attributed to various gradients caused by particle concentration, chemical potential, and electric fields [137]. The overpotential losses $\eta_{\text{diff},l}$ and $\eta_{\text{diff},s}$ due to concentration gradients have the slowest time constants and take effect after a few seconds [118; 120; 168] as Fig. 2.5 shows. They are diffusion-driven processes, which are governed by Fick's first and second law [33; 137].

$$\text{Fick's first law: } j = -D\nabla c \quad (2.17)$$

$$\text{Fick's second law: } \frac{\partial c}{\partial t} = D\nabla^2 c \quad (2.18)$$

The diffusivity or diffusion coefficient D is the proportionality factor relating the spatial gradient of the ion concentration c to the ionic flux j in Eq. (2.17) and linking the temporal change in concentration to the spatial change in concentration in Eq. (2.18). In liquids and solids, diffusion is the result of random motions of atoms or ions, which results in an exchange of positions with their neighbors. The process itself shows an Arrhenius-like temperature dependency, whereby the diffusion in the solid phase (active material) is much more temperature-dependent than in the liquid phase (electrolyte). [33; 137]

In the works of Park et al. [33] and Wu et al. [137], a link between ionic conductivity and diffusivity is provided. The connection is obtained by describing the motion of charged particles, which includes lithium-ions, in a medium caused by the two following forces. The first force is generated by an externally applied electric field and the related motion is described using the mobility μ of ions. The second force arises from a concentration gradient and the related motion is described by the diffusivity D of the ions. Using the Nernst-Einstein equation, the relationship between ionic conductivity and diffusivity in Eq. (2.19) can be obtained [33; 137]

$$\sigma_{\text{Diff}} = \frac{q_{\text{ion}}^2 c_{\text{ion}}}{k_{\text{B}} T_{\text{a}}} D, \quad (2.19)$$

where q_{ion} is the charge of the solute of a certain species and c_{ion} is the concentration of the species. The relation in Eq. (2.19) is linked to the temperature-dependent description of the diffusivity in the liquid and the solid phase in the following paragraphs.

Liquid Phase The Einstein-Stokes relation in Eq. (2.20) is often used to describe the diffusivity in the liquid phase D_l , since there is no successful first-principles calculation for diffusivity in liquids yet [33].

$$D_l = \frac{k_{\text{B}} T_{\text{a}}}{6\pi \mu_l r_{\text{p}}} \quad (2.20)$$

Here, spherical particles with radius r_{p} are assumed to move through a liquid with the viscosity μ_l . Viscosity itself is temperature dependent as well and can be described using the empirical Andrade equation [172]

$$\mu_l = b_0 \exp\left(\frac{b_1}{T_{\text{a}}}\right), \quad (2.21)$$

with the fitting parameters $b_0 > 0$ and $b_1 > 0$. By substituting Eq. (2.21) in Eq. (2.20) and consequently in Eq. (2.19), a temperature-dependent description for the ionic conductivity in the liquid phase $\sigma_{\text{Diff},l}$ can be gained.

$$\sigma_{\text{Diff},l}(T_a) = \frac{q_{\text{ion}}^2 c_{\text{ion}}}{6\pi r_p b_0} \exp\left(-\frac{b_1}{T_a}\right) \quad (2.22)$$

The increasing conductivity with rising temperatures in Eq. (2.22) is caused by the change in viscosity, since the temperature dependent terms in Eq. (2.20) and Eq. (2.19) cancel each other out.

Solid Phase For the solid phase, the diffusivity shows an Arrhenius behavior [137; 173].

$$D_s = D_0 \exp\left(-\frac{E_{A,b}}{k_B T_a}\right) \quad (2.23)$$

In Eq. (2.23), D_0 denotes the pre-exponential factor, also called frequency factor [173]. A temperature-dependent description for the conductivity in the solid phase $\sigma_{\text{Diff},s}$ is obtained by substituting D in Eq. (2.19) by the expression for the diffusivity in the solid phase from Eq. (2.23).

$$\sigma_{\text{Diff},s}(T_a) = \frac{q_{\text{ion}}^2 c_{\text{ion}} D_0}{k_B T_a} \exp\left(-\frac{E_{A,b}}{k_B T_a}\right) \quad (2.24)$$

The resulting expression in Eq. (2.24) has the same structure as the equations for charge transfer resistance in Eq. (2.15) or the electronic conductivity of cathode materials in Eq. (2.8). A first exponentially dominated part, in which the conductivity increases with increasing temperatures, and a second part, in which the conductivity decreases again with temperature.

2.2.3 Summary and Conclusion on Temperature-dependent Processes in Lithium-Ion Batteries

In summary, the theoretical considerations in this chapter show that all materials and processes that contribute to the overpotential of a LIB, except for the metals of the current collectors, have an increasing conductivity with increasing temperature for the temperature range between -20°C and 60°C in which LIBs can be reasonably operated [2; 122]. Due to the comparatively high conductivity of the current collectors (see Table 2.1), their contribution to the overall overpotential is relatively small and therefore their inverse temperature behavior can be neglected [45; 120]. The general temperature behavior of the overpotential is primarily characterized by exponential dependencies as Eqs. (2.6) to (2.10), (2.15), (2.16), (2.22) and (2.24) emphasize. This results in an explicit relationship between temperature and overpotential in the reasonable temperature operation range for LIBs, which can be exploited for a temperature estimation method. It should be mentioned that at elevated temperatures some processes, such as in Eq. (2.8), Eq. (2.10), Eq. (2.15), and Eq. (2.24), tend to exhibit the inverse temperature behavior where the conductivity decreases with rising temperatures. Due to that there is probably no explicit relation between impedance and temperature, if temperatures beyond the reasonable operating range of LIBs are considered. In the study by Spinner et al. [174], this effect was apparent in the impedance ($-\text{Im}\{Z\}$ at 300 Hz) at temperatures above 60°C . The impedance decreases progressively less with increasing temperature and levels out. Above 90°C , there is even an indication of an increasing impedance in their study.

2.3 Effects of Temperature on Lithium-Ion Batteries

After considering the dependence of the internal processes of a LIB on temperature, this section is devoted to the effects of temperature on a LIB. The various effects of temperature on a LIB, as described in this section, emphasize the importance of monitoring and controlling the temperature of a LIB-based energy storage system with a BMS. This is of interest not only because the crucial properties of lifetime, performance, and safety depend on temperature, but also because, as shown in Chapter 5, the resistance of a LIB changes permanently due to temperature-induced effects and thus any impedance-based method for determining temperature faces the challenge of finding a way to adapt to these changes.

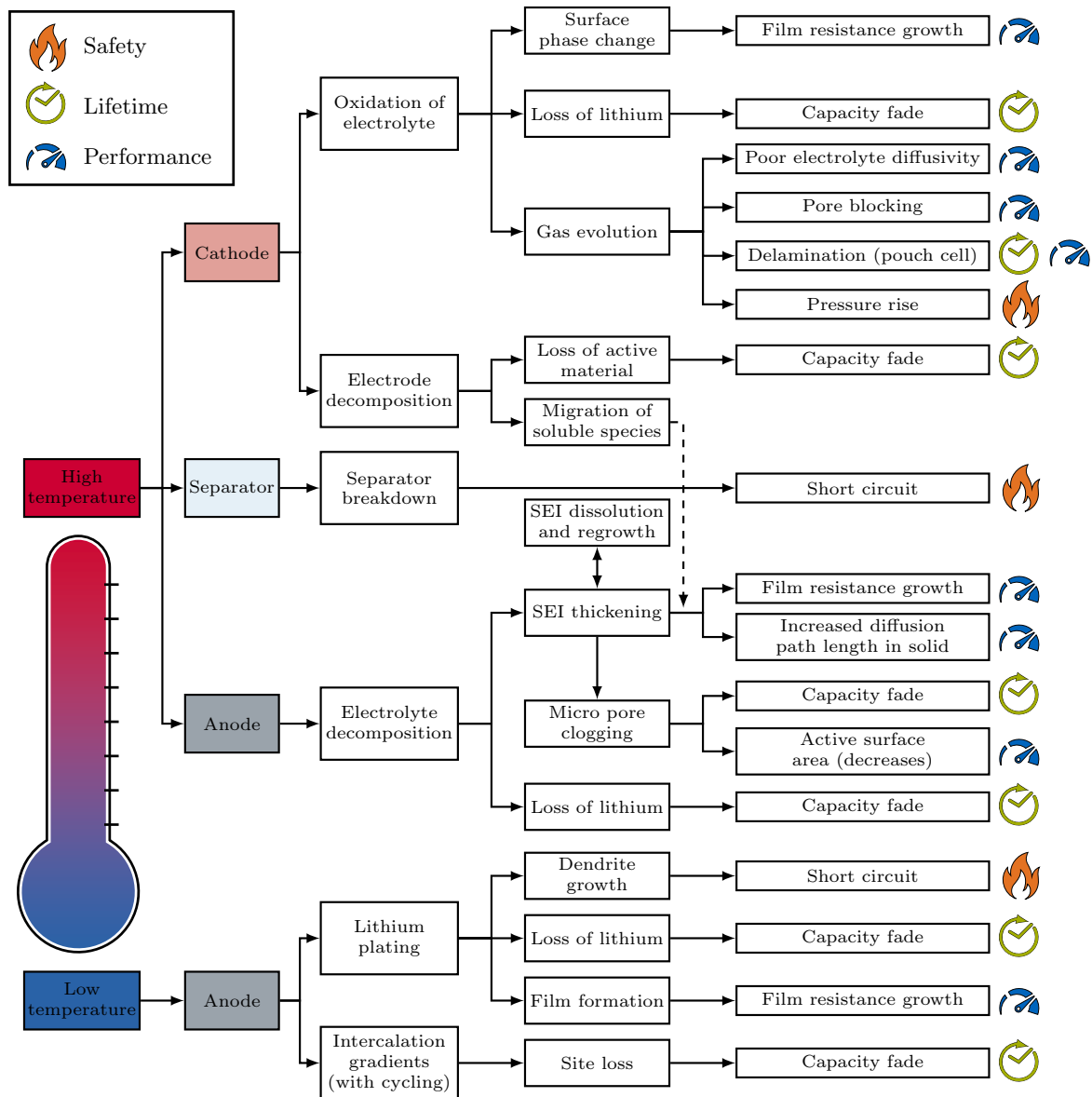


Figure 2.6: Effects of low and high temperatures on the anode, cathode, and separator and their impact on the lifetime, safety, and performance of LIBs. Adapted from [18; 175].

Fig. 2.6 illustrates the main effects of temperature on the two electrodes and the separator of a LIB,

whereby interaction with the electrolyte is regarded as a part of the corresponding electrode and is not discussed separately [18]. The following sections give a brief review on the effects of temperature with respect to Fig. 2.6. The effects considered here are classified into the two temperature categories low and high, in which they occur to a greater extent. However, the effects can also be observed in the other category.

2.3.1 Low Temperatures

Anode Especially the aging mechanisms of the anode are strongly affected by temperatures in the subzero range. Low temperatures in combination with high charging currents foster lithium plating [123; 124] and increase intercalation gradients [18; 175]. The consequence of lithium plating is the loss of lithium inventory resulting in a reduced capacity [30; 176]. The film that the plated lithium forms on the anode also influences the SEI resistance of the anode and therefore has an effect on the performance of the LIB [177]. Eventually, the plated lithium forms dendrites, which deteriorate the thermal stability of the SEI layer, thereby reducing the temperature of the thermal runaway of the LIB [38]. In the worst case, the dendrites pierce the separator and cause a short circuit leading to severe safety hazards [38; 177–179]. The other consequence of the combination of low temperatures and high charging currents are increased intercalation gradients, which can cause a mechanical strain in the anode particles, eventually resulting in particle cracks and even site loss of particles [18; 180–182]. These particles are electrically disconnected from the rest of the electrode and therefore the capacity of the LIB is reduced, because the lithium inventory of these particles is no longer available for cycling.

Cathode and Separator Compared to the number of effects of low temperatures on the anode, there are rarely reports on the effects of low temperatures on the cathode and the separator. In many studies [175; 183; 184], no effects are reported. However, according to the study of Wu et al. [185], low temperatures (10 °C) can lead to an increase in the charge transfer resistance at the cathode.

2.3.2 High Temperatures

Anode The main effect of high temperatures at the anode is the decomposition of the electrolyte, mainly due to the formation and growth of the SEI on the electrode surface, which is accompanied by the loss of lithium and thus reducing the capacity [18; 78–80]. As the SEI layer thickness increases, the diffusion path length in the solid phase becomes longer and the SEI resistance increases, resulting in reduced performance of the LIB. The SEI layer is not thermally stable and increasingly decomposes with increased temperature [18; 186]. The collapsed SEI layer is then regenerated and lithium-ions are consumed again, leading to an ongoing capacity fade. Furthermore, the parts of the collapsed SEI fill the free space between the particles, resulting in a reduced available reaction surface on the active material and thus reducing the performance and available capacity [18; 187; 188].

Separator Separators can melt and breakdown at high temperatures, which can lead to a short circuit between the two electrodes and thus pose a significant safety risk. However, the melting point of common separators starts between 135 °C and 220 °C, which is already far outside the acceptable operating range of LIBs. With multilayer separators, a lower melting point of one of the layers may also be intentional. The melted layer blocks the pores of the other separator layers which stops the

ion flow and thus the current flow. The aim of this safety measure is to prevent a thermal runaway due to abnormal heating of the LIB caused by too high current loads. [46; 189]

Cathode The effects on the cathode at high temperatures in Fig. 2.6 can be categorized in oxidation of the electrolyte and the decomposition of the cathode. The oxidation of the electrolyte at the cathode electrolyte interface leads to the formation of the **solid permeable interface (SPI)** on the surface of the cathode [18], a surface film that is similar to the **SEI** at the anode [89]. The thickness of the **SPI** layer increases with rising temperature, indicating the stronger electrolyte oxidation at higher temperatures [190], which is accompanied by a loss of lithium. For **LCO** electrodes, the growth of the **SPI** layer at high temperatures is accompanied by structural changes in the cathode. Both effects reduce the reaction rate of lithium-ion (de)intercalation and the charge transfer rates [18; 20], which ultimately reduces the performance of the LIB. The oxidation of the electrolyte further generates gases on the cathode side, such as CO_2 and CO [178; 191; 192]. According to Ohsaki et al. [192], the exothermic oxidation reaction of the electrolyte accelerates at temperatures above 60°C and increased gas generation occurs with increasing temperature. More gas generation leads to an increase in the internal pressure of the LIB. As soon as the pressure reaches a critical value, the casing can burst open, which is however prevented in many LIBs with a safety valve [178]. In addition to the safety hazard, the gas generation also degrades the LIB's performance and lifetime, as the gas can block pores, reduces the electrolyte diffusivity and causes delamination of layers in pouch cells [18; 175]. At high temperatures and high **SOC**, the transition metals of the cathode, such as Mn, Ni, or Co, can dissolve in the electrolyte, thus losing active material at the cathode and consequently reducing the accessible storage capacity of the cathode. This phenomenon, also referred to as cross-talk, not only affects the cathode structure, but also changes the composition of the **SEI** layer on the anode surface [18; 193; 194]. After dissolution in the electrolyte, the transition metals diffuse/migrate via the electrolyte through the separator to the anode, where they are deposited. The transition metals accumulate in the anode's **SEI** layer and subsequently block the lithium diffusion path or they react with the **SEI** layer to form new compositions [18; 195]. This in turn leads to an increase in impedance and loss of capacity, thus aggravating the performance and lifetime of the LIB. In several studies [195–198], a descending order of transition metals in terms of dissolution in electrolytes was found, with Ni being the most stable one, followed by Co, and finally Mn.

2.3.3 Other Influencing Factors than Temperature

In addition to temperature, other factors such as the **depth of discharge (DOD)** [199–201], the number of cycles, the applied current during the cycles [26; 199; 202], the storage **SOC** [21; 32; 203], as well as the general design and the materials used for the cell have an influence on the lifetime, safety, and performance. Further information on their impact can be found in several review articles in the literature, such as in Alipour et al. [18], Uddin et al. [175], and Birkl et al. [184].

2.4 Impedance Measurement Techniques for Lithium-Ion Batteries

The field of impedance measurement methods for LIBs can be divided into two branches: a frequency and a time domain approach. Both approaches are used for various purposes, including the parametrization of **equivalent circuit models (ECMs)** [114; 120], state estimation [114; 204; 205] or the

characterization of LIBs [31; 206–209]. The measurement methods are also the basis for the state of the art temperature estimation methods presented in Section 2.5 and the one developed in this thesis. Since both measurement techniques, in the frequency domain and in the time domain, determine the impedance of a LIB, it is an obvious step to compare the calculated values with each other. Barai et al. [210] make this attempt by comparing the results of the EIS with pulse measurements. They conclude that the results are comparable but not identical. However, the results of both measurement techniques are dependent on temperature and can therefore be used for the development of a temperature estimation method. In the following sections, the underlying measurement principles of the two techniques are briefly explained and evaluated in terms of their relevancy in an application.

2.4.1 Frequency Domain

Electrochemical impedance spectroscopy is a common method to investigate the dynamic behavior of a LIB. It is used to measure the frequency-dependent impedance of a cell. The two measurement methods galvanostatic and potentiostatic can be distinguishing. Fig. 2.7a shows the measurement setup. For the galvanostatic electrochemical impedance spectroscopy (GEIS), the cell is excited with a sinusoidal current $i(t)$ as in Eq. (2.25)

$$i(t) = i_0 \sin(\omega t + \varphi_i) \quad (2.25)$$

and the corresponding voltage response of the cell $u(t)$ is measured as in Eq. (2.26)

$$u(t) = u_0 \sin(\omega t + \varphi_u). \quad (2.26)$$

For the potentiostatic electrochemical impedance spectroscopy (PEIS), excitation and measurement signals are inverse. The condition for an EIS is that a causal, linear time-invariant (LTI) system is measured, which is only true for LIBs under equilibrium conditions, where no load except for the perturbation of the EIS is applied [211]. At a first glance, this more or less limits EIS to laboratory use.

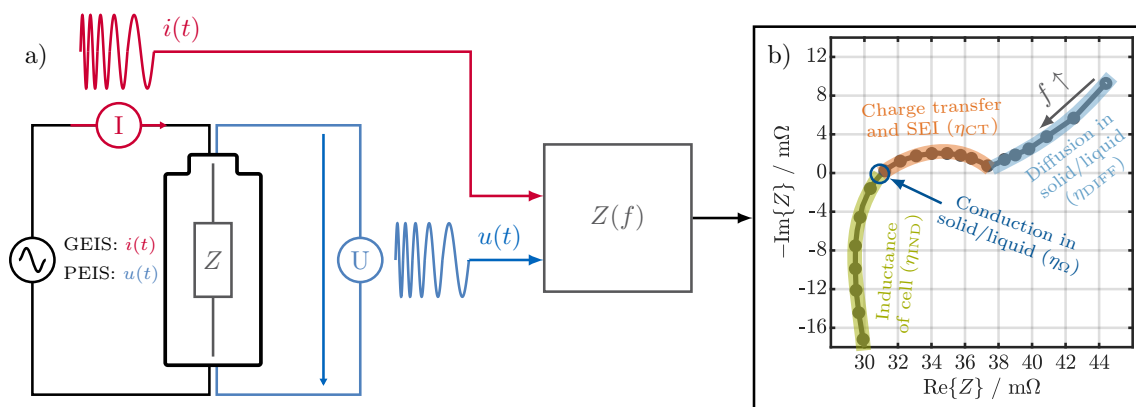


Figure 2.7: a) Measurement principle for EIS and b) exemplary Nyquist diagram of a 18650 cell (see Table 3.1) between 10 mHz and 10 kHz at 20 °C and a SOC of 45%.

Two competing objectives apply to both measurement methods. On the one hand it is the objective to keep the excitation amplitude (i_0 in the case of a GEIS) as small as possible in order to maintain

the small-signal behavior and satisfy linearity of the cell at the respective operating point (the angular frequency $\omega = 2\pi f$). On the other hand it is the objective to generate a large enough excitation to ensure a correspondingly high response signal (u_0 in the case of a [GEIS](#)), mainly to guarantee a high enough [signal-to-noise ratio \(SNR\)](#) and therefore measurement quality. Using the complex representation $I(j\omega) = i_0 \exp(j(\omega t + \varphi_i))$ and $U(j\omega) = u_0 \exp(j(\omega t + \varphi_u))$ of equations Eq. (2.25) and Eq. (2.26), the complex impedance of the cell $Z(j\omega)$ can be calculated

$$Z(j\omega) = \frac{U(j\omega)}{I(j\omega)} = \frac{u_0}{i_0} \exp(j(\varphi_u - \varphi_i)) = Z_0 \exp(j\varphi) = \text{Re}\{Z(\omega)\} + j\text{Im}\{Z(\omega)\}, \quad (2.27)$$

where $\varphi = \varphi_u - \varphi_i$ is the phase shift between excitation and response signal and Z_0 is the absolute value of the impedance. In the field of battery research, the resulting complex impedance is usually visualized in a Nyquist plot. Fig. 2.7b showcases the spectrum of one 18650 cell investigated in this thesis at 20 °C and a [SOC](#) of 45%. The impedance spectrum can be divided in some characteristic areas and points, which roughly describe the dynamic behavior of a [LIB](#) [114; 120; 209]:

- The highest frequency parts in Fig. 2.7b (green) describe the inductance of the cell and can thus be assigned to η_{IND} . However, they can also be influenced by the wiring and the measurement setup.
- The point at which the capacitive and inductive effects of the cell eliminate each other and $\text{Im}(Z) = 0$ is often referred to as ohmic resistance and associated with η_{Ω} .
- In the subsequent frequency range, a semicircle appears in Fig. 2.7b (orange), which represents the impedance of the charge transfer reaction combined with the double layer capacitance, as well as the [SEI](#), and thus is associated it with η_{CT} . Depending on the cell, measurement conditions, such as temperature and [SOC](#), and the time constants of the processes, two semicircles may also be visible in the spectrum, where the semicircle with the higher frequencies reflects the impedance of the [SEI](#) and the semicircle with the lower frequencies reflects the charge transfer reaction and the double layer capacitance of the cell.
- After the semicircle in Fig. 2.7b, the spectrum reaches a local minimum and turns into a rising branch with capacitive behavior. The effects measured at these low frequencies can be related to diffusion in the solid and liquid phase and thus to η_{DIFF} .

By specifically determining single or multiple temperature-dependent characteristics of the spectrum, a wide variety of (online) methods for temperature estimation using [EIS](#) have emerged since 2010. These methods are presented and discussed in Section 2.5. At first glance, this does not seem practically realizable, since the [EIS](#) is a measurement technique developed for a lab environment and not for use in a commercial application. The commercially available [EIS](#) measurement devices are designed as standalone devices and are very expensive. Integration would add additional cost and weight to the system. Also, the desired conditions ([LTI](#)) for a [EIS](#) measurement do not prevail during operation of the [LIB](#), due to the superimposed load currents. Nevertheless, there are already approaches to solve some of these challenges by the following measures:

- (A) Several studies developed examples of low-cost circuits with the goal of integrating them into a [BMS](#) and making [EIS](#) measurements in operation viable [51; 212–214].
- (B) The use of existing power electronics to generate the excitation for [EIS](#) measurements is also feasible [215].
- (C) To avoid any additional hardware effort, a transformation of the current and voltage measurements from the time domain to the frequency domain can be implemented [216].

However, all solution attempts are either still associated with an increase in weight and costs (A), with an intervention in the system behavior (B), or with complex and therefore possibly error-prone software (C). For these reasons, a simple time-domain based approach for temperature estimation is pursued in Chapter 4, which does not require any additional hardware or excitation signals.

In addition to the EIS measurement method just described, there are more advanced EIS-based approaches, such as non-linear electrochemical impedance spectroscopy (NLEIS) or multi-sine EIS. With NLEIS, the LIB is excited with an increased amplitude, which allows better characterization of non-linear effects of the LIB and improves the SNR [217]. With the help of multi-sine EIS, the measurement time can be shortened by exciting the LIB not sequentially with one frequency after the other, but with several superimposed frequencies. This is also a step towards the applicability of the EIS under normal operation conditions in an application. Normally, a conventional EIS measurement is not suitable for use in operation, since under load the SOC and the temperature change during the rather long EIS measurement, thus violating the requirement of a LTI system. The multi-sine EIS minimizes the change during the measurement and allows it to be used under regular operation conditions. [120; 211] However, the measurement quality is reduced, the frequency range is limited, and the complexity of the measurement is increased [120].

2.4.2 Time Domain

In comparison to the quite uniform determination of the impedance in the frequency domain, there is a large number of variants to determine the resistance of a cell in the time domain. The following sections give a brief introduction to a selection of methods for calculating a time domain based resistance in the field of battery research. A more detailed overview on determining the resistance of LIBs can be found in the work of Schweiger et al. [218].

2.4.2.1 Resistance calculated from Voltage Curve Difference

Several authors [219–221] propose the calculation of a voltage curve difference resistance R_{VCD} at a given SOC by using the difference between two voltage curves U_{I_1} and U_{I_2} of a cell recorded at different constant current rates I_1 and I_2 as shown in Fig. 2.8. The quotient of the voltage and the current difference in Eq. (2.28) then results in a SOC-dependent resistance

$$R_{\text{VCD}}(\text{SOC}) = \left| \frac{U_{I_1}(\text{SOC}) - U_{I_2}(\text{SOC})}{I_1 - I_2} \right|. \quad (2.28)$$

By setting one of the currents to a very small charge/discharge rate such as 0.01 C and the other to higher charge/discharge rates, a R_{DC} is obtained, which relates a pseudo equilibrium thermodynamic charge/discharge curve to a fully polarized cell. On the one hand, the method is easy and fast to apply. On the other hand, it is unsuitable for model parametrization as the cell temperature changes over discharge/charge and the SOC accuracy is low. [219; 221]

In terms of temperature estimation in an application, this method can only be applied in applications with constant current loads, which disqualifies it for BEVs during most driving scenarios.

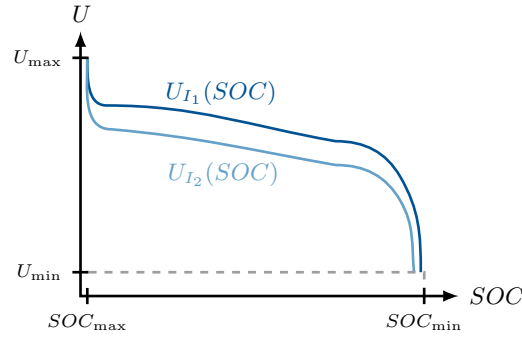


Figure 2.8: Example of discharge voltage curves to calculate the R_{VCD} with the voltage curve difference method. Based on [221].

2.4.2.2 Energy Loss Method

This rather complex method calculates a resistance considering the heat loss of a cell [218; 222]. By measuring the heat loss Q_{HL} , for example with a calorimeter, generated by a current $I(t)$ in an interval t_1 to t_2 , the resistance R_{HL} can be calculated using Eq. (2.29).

$$R_{HL} = \frac{Q_{HL}}{\int_{t_1}^{t_2} (I(\tau))^2 d\tau} \quad (2.29)$$

Since the effort to determine the heat loss Q_{HL} in an application is difficult to justify, this method is not suitable for BEVs and the method development in this work.

2.4.2.3 Resistance calculated from Direct Current Pulses

The most common method to obtain the resistance of a LIB in the time domain uses a **direct current (DC)** pulse as an excitation [114; 168; 209; 223; 224]. Due to the excitation with **direct current**, this resistance is often called R_{DC} [209]. However, there are different methods and boundary conditions to determine the R_{DC} from the current pulse, which also lead to different results. The **DC** pulse itself can be specified with the following parameters: base current I_0 , height of current change ΔI from I_0 to I_1 , and pulse duration t_p as shown in Fig. 2.9a. For most methods I_0 is equal to 0 A. However, there are also methods such as in the **United States advanced battery consortium (USABC)** manual appendix I where I_0 is not equal to 0 A [210; 218; 221; 223]. In general, the pulse duration varies between 1 s and 30 s depending on purpose and applied measurement standard [210]. In the procedure of the **Verband der Automobilindustrie (VDA)** for example, a pulse duration of 18 s is prescribed [218]. Furthermore, the **pulse rise/fall time** ($t_{r/f}$) for the duration of the current change can be defined. Ideally, $t_{r/f}$ would be zero, which is not possible due to physical limitations of the test equipment. However, the **pulse rise/fall time** for characterization pulses is often neglected since it is very small in relation to the pulse duration. If consecutive pulses are used for characterization, the break duration t_b between the pulses also matters in order to avoid the pulses influencing each other. For instance, a break of 40 s is mandatory between pulses in the procedure of the **VDA** [218]. However, equalization processes in a cell due to local inhomogeneities can also take several hours and influence the measurement result [209; 225].

In general, there are the six current pulse types marked P_1 to P_6 in Fig. 2.9a and Fig. 2.9c that are

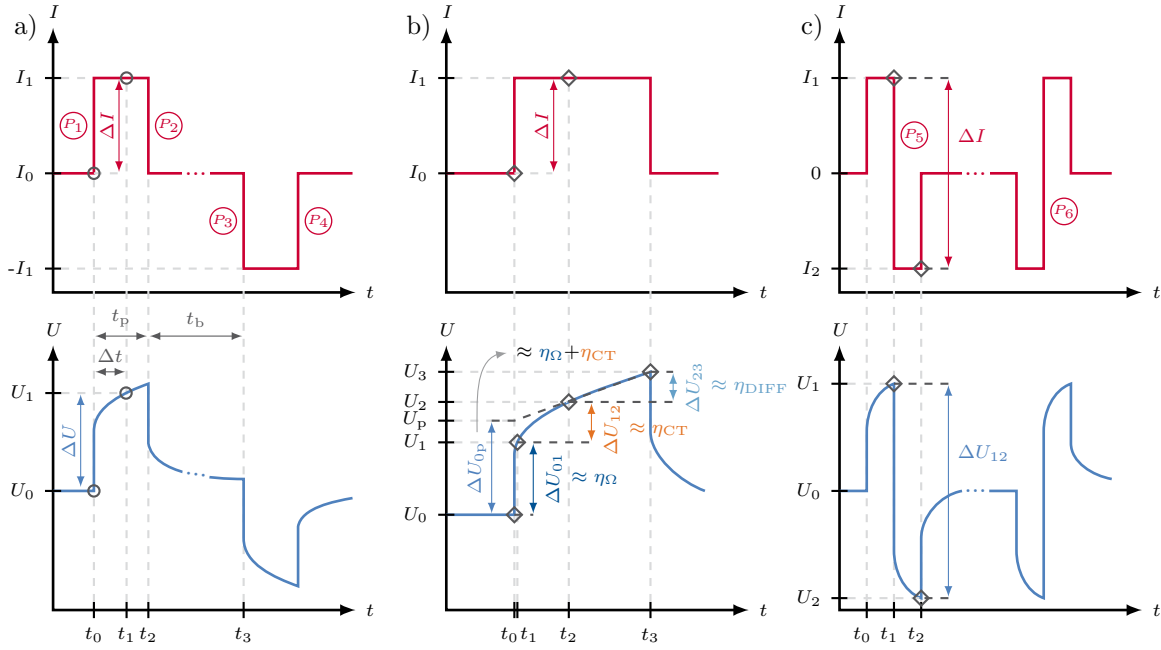


Figure 2.9: Current and voltage profiles for the characterization of the resistance of a LIB with methods based on a direct current pulse. a) The four different current change types P_1 to P_4 suitable for resistance calculation and definition of the pulse duration t_p , pulse break t_b , and the duration Δt between current change and resistance calculation. b) Example of different base lines and Δt for resistance calculation and their relation to the overpotentials in Fig. 2.5. c) Voltage and current signals for the current switch method for determining the R_{DC} and the current change types P_5 and P_6 .

suitable for the characterization of a LIB with a R_{DC} . They are distinguished by the base current and the direction of the current change:

P_1 Starting from $I_0 \geq 0$ and increasing to a current $I_1 > I_0$.

P_2 Starting from $I_1 > 0$ and decreasing to a current $I_0 \geq 0$.

P_3 Starting from $I_0 \leq 0$ and decreasing to a current $I_1 < I_0$.

P_4 Starting from $I_1 < 0$ and increasing to a current $I_0 \leq 0$.

P_5 Starting from $I_1 > 0$ and decreasing to a current $I_2 < 0$.

P_6 Starting from $I_1 < 0$ and increasing to a current $I_2 > 0$.

For the resistance calculation itself, two current and voltage values are required at defined points in time. These values and their time stamps are shown as an example for a P_1 current change in Fig. 2.9a. At the first time stamps t_0 , the base current I_0 and the corresponding voltage U_0 are measured. At the second time stamp t_1 , specified by the time $t_0 < \Delta t \leq t_p$, the pulse current I_1 and the corresponding voltage U_1 are measured. In the VDA procedure for instance, Δt is set to the values 2 s, 10 s, and 18 s. With the four values, the pulse resistance can be calculated according to Eq. (2.30).

$$R_{DC,\Delta t} = \frac{U(t_0) - U(t_0 + \Delta t)}{I(t_0) - I(t_0 + \Delta t)} = \frac{U_0 - U_1}{I_0 - I_1} = \frac{\Delta U}{\Delta I} \quad (2.30)$$

The method can be applied in the most flexible way and also allows the determination of a resistance with different current directions and base currents, which corresponds to a change in driving speed

or braking with recuperation in a BEV. Depending on the choice of Δt different overpotentials, as discussed with Fig. 2.5, contribute to $R_{\text{DC},\Delta t}$. However, the resistance calculated by this method always describes the sum of all effects occurring up to Δt [210]. Moving the baseline for the calculation away from U_0 to other reference points, such as U_1 or U_2 in Fig. 2.9b, partially remedies this. Keeping U_0 as the baseline, the voltage U_{01} and a resistance according to Eq. (2.31) can be obtained with very short Δt , which most likely corresponds to the ohmic resistance $R_{\text{DC},\Omega}$ of the cell.

$$R_{\text{DC},\Omega} = \frac{U_0 - U_1}{I_0 - I_1} = \frac{\Delta U_{01}}{\Delta I} \quad (2.31)$$

The timing for Δt is not standardized. Zhao et al. [223] set the time for the calculation to 10 ms after the current change. Anseán et al. [221] and Barai et al. [210] specify 100 ms for Δt . Waag et al. [209] and Wang et al. [114] refer to the instantaneous voltage drop and do not specify a concrete time for Δt . Ultimately Δt is limited by the sampling time of the test device or the BMS measurement hardware respectively.

If the base value for the calculation is shifted to U_1 , as shown in Fig. 2.9b, an overpotential U_{12} can be determined with a Δt in the millisecond to a few seconds range [209; 210; 221], which corresponds approximately to the interface overpotential in Fig. 2.5. The resulting resistance $R_{\text{DC,int}}$ can be calculated with Eq. (2.32) analog to $R_{\text{DC},\Omega}$.

$$R_{\text{DC,int}} = \frac{U_1 - U_2}{I_0 - I_1} = \frac{\Delta U_{12}}{\Delta I} \quad (2.32)$$

Repeating this scheme and taking U_2 as the reference point, Eq. (2.33) and the voltage difference U_{23} can be used to calculate a resistance $R_{\text{DC,diff}}$ for Δt in the seconds to minutes regime [221] that approximately reflects the diffusion overpotential in Fig. 2.5.

$$R_{\text{DC,diff}} = \frac{U_2 - U_3}{I_0 - I_1} = \frac{\Delta U_{23}}{\Delta I} \quad (2.33)$$

The issue in calculating $R_{\text{DC},\Omega}$, $R_{\text{DC,int}}$, and $R_{\text{DC,diff}}$ with this methodology is that the voltage response in the time domain does not have specific characteristics like the spectrum of an EIS, and thus the determination of the precise reference points and values for Δt is not possible [210].

Waag et al. [209] and Barai et al. [210] used another current pulse-based method, which compensates for both the influence of changing OCV and the influence of diffusion as the pulse duration t_p increases. The method is demonstrated in Fig. 2.9b and uses the two voltages U_2 and U_3 measured at t_2 and t_3 . The voltages are linearized and extrapolated to the point t_0 to calculate the voltage U_p . The voltage drop U_{0p} and the current change ΔI are then used to calculate a polarization resistance $R_{\text{DC,p}}$ according to Eq. (2.34).

$$R_{\text{DC,p}} = \frac{U_0 - U_p}{I_0 - I_1} = \frac{\Delta U_{0p}}{\Delta I} \quad (2.34)$$

Waag et al. [209] propose $t_2 = 5$ s and $t_3 = 10$ s, but also mention that the points may vary with conditions, such as aging state or temperature, and depend on the investigated battery. Therefore, they suggest to consider the frequency behavior when selecting t_2 and t_3 for the linearization.

The last current pulse based method presented here is shown in Fig. 2.9c and is called current switch method. The cell is first charged with a pulse and then discharged with a counter pulse without

a break. The reverse pulse sequence is also possible, starting with a discharge pulse. Finally, the resistance $R_{\text{DC,cs}}$ is calculated with the help of Eq. (2.35).

$$R_{\text{DC,cs}} = \frac{U_1 - U_2}{I_1 - I_2} = \frac{\Delta U_{12}}{\Delta I} \quad (2.35)$$

The procedure has two advantages. First, the SOC is not changed by the procedure because the same amount of charge is charged and discharged, if the same pulse durations and currents are used for charging and discharging. Second, the current change is doubled compared to the other methods and the corresponding voltage is increased as well, which improves the SNR. A disadvantage is the sign change in current at time t_1 in Fig. 2.9c, which is demanding for the measurement equipment. [218]

2.4.3 Factors Influencing the Impedance Determination for Lithium-Ion Batteries

The effect of temperature on the processes in a LIB, discussed in Section 2.2, affect the impedance calculation in the time and frequency domain. Several studies [120; 168; 209; 226] show that both $Z(f)$ for a wide frequency range and $R_{\text{DC},\Delta t}$ for various Δt depend on temperature. In addition to temperature, other influencing factors, such as SOC or current, which affect the impedance of a LIB were already mentioned in Section 2.2.

Several studies [120; 168; 209; 210; 223; 224] show that the spectrum of an EIS and also the resistance in the time domain changes with magnitude of the current excitation and also with SOC. Both effects have often been attributed to the SOC and current dependence of the charge transfer reaction [120; 168; 209], regardless of the method for resistance determination. The impedance decreases with increased current due to the nonlinear behavior of the Butler-Volmer kinetics and increases at the SOC boundaries due to the limiting electrode.

Schweiger et al. [218] additionally showed that at high currents and long pulse durations ($t_p = 18$ s) the resistance values calculated with Eq. (2.30) increase and attributed this to the additional voltage drop due to the SOC change during the pulse. In contrast, at low currents and pulse durations ($t_p \leq 2$ s), their study showed only minor difference in the calculated resistance values.

Ratnakumar et al. [168] showed that the type of current change also affects the resistance result in the time domain. For current changes from the resting state to a state under load, such as P_1 and P_3 in Fig. 2.9a, they found an increased resistance compared to current changes from a state under load returning to the resting state, such as P_2 and P_4 in Fig. 2.9a. They attributed this effect to diffusion polarization, which is already present for the pulse types P_2 and P_4 , since these pulses start from a state under load. Zhao et al. [223] also compared the resistance for the different pulse types P_1 to P_4 and showed that differences between the pulse types P_1 and P_4 emerged especially for long pulse durations ($t_p = 30$ s).

All of these effects just mentioned, along with the desired temperature dependence, must be considered when developing a method for temperature estimation. Furthermore, it cannot be assumed that every current change in an application complies with the pulse profiles shown in Fig. 2.9. Therefore, a dedicated investigation on the influence of pulse parameters and shape is conducted in Chapter 4.

2.5 Review on the State of the Art Temperature Estimation Methods for Lithium-Ion Batteries

As mentioned in the introduction, a large variety of methods for estimating the temperature of a LIB from its impedance values exist in the literature. The goal of this chapter is to give an overview on the state of the art in the literature and to address the questions summarized in the following three tables. The first, Table 2.4, focuses on the estimation method itself and addresses the questions:

- a) Which temperature is estimated?
- b) What kind of measurement technique is needed for the estimation?
- c) How is the temperature estimated?
- d) Which impedance features are used for the estimation?

The second, Table 2.5, focuses on the investigated system and addresses the questions:

- e) What are the properties (capacity, chemistry, format) of the investigated cell(s)?
- f) At which system level (cell, module, or pack) is the investigation conducted?
- g) In which temperature range is the system investigated?
- h) Is aging investigated/considered in the study?

The third, Table 2.6, focuses on the method validation and addresses the questions:

- i) How is the developed method validated?
- j) Which metric is used to evaluate the method?
- k) And how accurate is the estimation result?

The reference numbering for the studies under investigation with #1 to #25 remains identical across the three tables and for the remainder of the thesis. The following discussion also pursues the goal to identify the weak spots and unresolved issues in the literature, finally motivating and identifying the topics investigated in this thesis. Detailed reviews on impedance-based temperature and other state estimators can be found in [114; 204; 205; 227].

2.5.1 Estimation Methods

Estimated Temperature In the literature at least the 25 methods listed in Table 2.4 have been conducted from 2011 to 2021. All methods provide information about the internal temperature behavior of the cell. In the majority of the studies in Table 2.4, the impedance is used to determine an internal or core temperature, with two studies (#2 and #17) even examining an electrode-specific temperature. Some studies determine the internal distribution of temperature (#5, #8, #14, and #23) and the average temperature (#2, #13, and #20), or additionally provide the cell's surface temperature (#8, #19, and #25).

Method Inputs Depending on the study, different inputs are required to determine the temperatures just mentioned. A majority of twenty studies relies on measuring the impedance in the frequency domain by means of EIS, whereas two studies (#8 and #14) use the load profile (U & I) as a supplementary input variable for the method. In two studies (#16 and #20) a frequency spectrum is generated from the load profile in the time domain by means of Fourier transform (FT) and in only

Table 2.4: State of the art impedance-based temperature estimation methods: Type of estimated temperature, utilized inputs, estimation method, and used impedance features.

#	Reference	Year	Estimated Temperature				Input			Estimation Method				Feature						
			Internal/Core	Internal Distribution	Average/Integral	Surface	EIS	U & I	T-Sensor	Look-up Table (modified) Arrhenius	Polynomial	Exponential	Cell Model and/or Solver	Thermal Model	$ Z $	$\arg\{Z\}$	$\text{Re}\{Z\}$	$\text{Im}\{Z\}$	f	
1	[51]	2011	x				x			M					40 Hz					
2	[52]	2012	A				x		x						40 Hz					
3	[45]	2013		x			x			M					10.3 kHz					
4	[49]	2014	x				x			x									$\text{Im}\{Z\} = 0$	
5	[47]	2014		x			x	x		(M) 2 nd (1)			1D		215 Hz		(215 Hz)			
6	[228]	2015	x				x		x						50 Hz		50 Hz			
7	[44]	2015	x				x			3 rd				42 Hz	100 Hz	42 Hz	420 Hz		$\arg\{Z\} = 3^\circ$	
8	[229]	2015		x	x		x	x		2 nd (1)	(D)EKF	1D			215 Hz					
9	[174]	2015	x				x			M							300 Hz			
10	[230]	2015	x					x	x				KF	1D					N.A.	
11	[53]	2015	x				x			x				(<17 Hz)	10 Hz to 100 Hz					
12	[214]	2015	x				x			2 nd									$\text{Im}\{Z\} = 0$	
13	[50]	2016		x			x			x									$\text{Im}\{Z\} = Z_0$	
14	[231]	2016		x			x	x		2 nd	EKF	2D					215 Hz			
15	[232]	2017	x				x			1 st					10 Hz					
16	[233]	2017	x					DFT			x				500 Hz					
17	[212]	2018	C A				x						unspecified fitting function		10 Hz 70 Hz					
18	[234]	2018	x				x			M				(5 Hz)	5 Hz					
19	[29]	2018	x		x		x	x		2 nd	ECM	1D		(1 kHz)	1 kHz					
20	[54]	2019		x				FFT			x				10 Hz					
21	[235]	2020	x				x		x						133 Hz/ 630 Hz	133 Hz/ 630 Hz				
22	[38]	2020	x				x			M					10 Hz to 100 Hz					
23	[236]	2020		x				x			KF+ ECM	1D							N.A.	
24	[41]	2021	x				x				ANN				10 Hz to 10 kHz	10 Hz to 10 kHz				
25	[114]	2021			x			x			SPM + DEnKF									N.A.

A Anode
ANN Artificial Neural Network
C Cathode
D Dimensional
DEKF Dual Extended Kalman Filter
DEnKF Dual Ensemble Kalman Filter
DFT Discrete Fourier Transform
ECM Equivalent Circuit Model
EKF Extended Kalman Filter
FFT Fast Fourier Transform
KF Kalman Filter
M Modified Arrhenius
N.A. Not applicable
SPM Single Particle Model
⁽¹⁾ Method uses admittance ($Y = \frac{1}{Z}$)

three publications (#10, #23, and #25) the voltage and current profile is used directly. In addition, temperature sensors are used for the methods in #5 and #10.

Estimation Method Numerous approaches exist to establish a relationship between the input parameters and the cell temperature. Most of the methods rely on functions based on the Arrhenius law or a variation of it to obtain a relation between temperature and an impedance feature Z_f . In this context, the Arrhenius law can be expressed as in Eq. (2.36).

$$Z_f(T_a) = Z_1 \exp\left(\frac{E_{A,b}}{k_B T_a}\right) \quad (2.36)$$

The modified variations of the Arrhenius law either have an additional temperature-independent constant Z_0 , as in Eq. (2.37) (#3, #5, #9, and #22), or there is a linear temperature dependence in addition to the pre-exponential factor Z_1 , as in Eq. (2.38) (#1 and #18).

$$Z_f(T_a) = Z_0 + Z_1 \exp\left(\frac{E_{A,b}}{k_B T_a}\right) \quad (2.37)$$

$$Z_f(T_a) = T_a \cdot Z_1 \exp\left(\frac{E_{A,b}}{k_B T_a}\right) \quad (2.38)$$

All function variations introduced with Eqs. (2.36) to (2.38) coincide with the theoretical relations of the ohmic overpotential in Eqs. (2.6) to (2.8) and the interface overpotential in Eqs. (2.15) and (2.16) of a LIB with temperature as discussed in Section 2.2.2. The functions would also be consistent with the diffusion overpotential in Eqs. (2.22) and (2.24). However, the frequency range used in the studies, which lies above 5 Hz, excludes these effects to a large extent. Furthermore, look-up tables (LUTs), first to third degree polynomials, and exponential functions independent of the Arrhenius law are used as estimation functions. All functions have in common that they describe an impedance that decreases with increasing temperature. In addition, some methods use different variations of a Kalman filter (KF) and supporting cell models such as ECMs (#19 and #23) or even physics based models such as a single particle model (SPM) (#25). In study #24, an artificial neural networks (ANN) based approach is explored. Six papers use thermal cell models that represent the thermal behavior of the cell one-dimensional (1D), except for the two-dimensional (2D) approach in #14. The thermal models are mainly used in studies that estimate the internal temperature distribution in a cell.

Features Almost all methods use at least one specific feature from the impedance spectrum at a specific frequency or the frequency at a specific condition such as $\text{Im}\{Z\} = 0$ in #4 and #12. The only exception are the studies #10, #23, and #25, which use no specific EIS feature, but the load profile as input and are therefore marked with N.A. The frequencies of interest range between 5 Hz and 10.3 kHz, which approximately corresponds to the time domain of the ohmic and interface overpotentials in Fig. 2.5.

Conclusion - Estimation Methods In summary, the majority of methods in Table 2.4 determine an internal cell temperature and require an additional excitation for an EIS measurement as described in Section 2.4.1, thus increasing complexity, weight, and cost of the BMS in use. Those methods that operate with the load profile in the time domain and thus avoid the additional EIS measurement either use complex models, as in #23 or #25, still need a temperature sensor, as in #10, or rely on computationally intensive calculations for an BMS, as the FT in #16 and #20. The majority of the estimation methods rely on an exponential relationship, often but not exclusively related to the Arrhenius law, and are fitted with features from the frequency spectrum with frequencies above 5 Hz. From this review of the literature, the following points can be derived for the succeeding chapters with reference to the research questions from Section 1.2:

- The relationship between temperature and resistance in the time domain for the method to be developed can be expected to be described by an exponential relationship (Chapters 3 and 4) and describes an internal cell temperature (Chapter 3). → Q1
- For the previous point to hold, the computation time Δt of the resistance R_{DC} (see Eq. (2.30))

must be in a range corresponding to the processes above 5 Hz in the frequency spectrum, which is addressed in Chapters 3 and 4. → Q1

- Chapter 4 addresses the fact that there is yet no method in the time domain that uses a resistance calculation as in Section 2.4.2 with load profiles as input and does not increase complexity, weight, or cost. → Q2

2.5.2 Investigated Systems

Table 2.5: State of the art impedance-based temperature estimation methods: Investigated LIB systems, temperature range, and consideration of aging effects.

#	Reference	Cell			System	Temperature Range	Aging
		Capacity	Format	Chemistry Cathode Anode			
1	[51]	53 Ah	prismatic	LCO Gr	cell	−20 to +66 °C	excluded
		2.3 Ah	26650	LFP Gr	cell		
		4.4 Ah	18650	? Gr	1s2p		
2	[52]	53 Ah	prismatic	LCO Gr	cell	−10 to +50 °C	not considered
3	[45]	2 Ah	pouch	LCO+NCA Gr	cell	−40 to +40 °C	not considered
4	[49]	2.3 Ah	26650	LFP Gr	cell	−20 to +50 °C	considered, but no/minor effect on method; NCA Gr cell aged for 600 cycles to SOH of 75%
		7.5 Ah	cylindrical	NCA Gr	cell		
5	[47]	2.3 Ah	26650	LFP Gr	cell	−20 to +45 °C	not considered
6	[228]	90 Ah	?	LFP ?	cell	−20 to +50 °C	not considered, but mentioned
7	[44]	60 Ah	pouch	NMC Gr	cell	+15 to +45 °C	not considered
8	[229]	2.3 Ah	26650	LFP Gr	cell	−20 to +45 °C	excluded with reference to #1
9	[174]	2.6 Ah	18650	LCO ?	cell	−10 to +95 °C	not considered
10	[230]	40 Ah	pouch	LFP Gr	cell	+25 to +46 °C	not considered, but mentioned
11	[53]	8 Ah	prismatic	?	cell	−20 to +50 °C	considered, but no/minor effect on method; aged for 400 cycles to SOH of 75%
12	[214]	20 Ah	?	LTO	cell	+0 to +40 °C	excluded with reference to #4
13	[50]	90 Ah	prismatic	LFP ?	3s1p	−20 to +50 °C	excluded with reference to #4
14	[231]	4.4 Ah	cylindrical 32113	LFP Gr	cell	+10 to +25 °C	excluded
15	[232]	30 Ah	pouch	LFP Gr	cell	−20 to +40 °C	excluded with reference to #4 and #11
16	[233]	20 Ah	prismatic	LMO+NMC ?	cell	+0 to +40 °C	considered and compensation suggested; aged 12 months at three temperatures
17	[212]	5.3 Ah	18650	?	1s2p	ca. +21 to +26 °C	not considered
18	[234]	50 Ah	prismatic	LCO Gr	cell	+14.3 °C to TR (>+128 °C)	not considered
		5.3 Ah	18650	?	1s2p		
		3 Ah	18650	NMC ?	cell		
19	[29]	34 Ah	prismatic	NMC ?	cell	+21 °C	not considered
20	[54]	8 Ah	prismatic	LFP ?	cell	+0 to +45 °C	excluded with reference to #11
		40 Ah	pouch	LFP ?			
21	[235]	23.3 Ah	prismatic	NMC ?	2s1p	−20 to +50 °C	not considered, but mentioned
22	[38]	1.3 Ah	18650	LFP ?	cell	+0 to +55 °C	considered, but no/minor effect on method; aged to SOH of 93%, 86%, 75%, and 59%
23	[236]	3.2 Ah	18650	?	cell	+0 to +60 °C	not considered
24	[41]	1.5 Ah	18650	NMC Gr	cell	+0 to +60 °C	not considered, but aged for other reason; aged from SOH of 99 to 83%
		3.0 Ah		NCA Gr			
25	[114]	2.35 Ah	prismatic	NCA Gr	cell	+20 to +35 °C	not considered
4.85 Ah	21700	NMC Gr+Si					

TR Thermal Runaway
? unknown or not specified

Format & Capacity Reviewing Table 2.5, it is apparent that every common cell format from Section 2.1.2 is examined in the state of the art studies. A total of ten prismatic, five pouch, and sixteen cylindrical cell types are examined. However, in two studies, no information about the cell format is provided. The capacities of the examined cells cover a range of 1.3 to 90 Ah. In most cases, however, the capacity is in the single-digit Ah range, since common cylindrical cells in 18650, 21700, and 26650 format are often examined, which are also investigated in this thesis.

Chemistry The chemistries of the investigated cells cover all common systems for LIBs shown in Fig. 2.3. With eleven cells, LFP is studied most frequently, followed by NMC with seven, LCO with five, and NCA with two cells. The blend electrodes in #3 and #16, and the LTO cell in #12 are the exception, but show the versatility of the applicability of the impedance-based temperature estimation methods. On the anode side, graphite dominates as active material. Only in study #25 silicon is additionally used in a blend electrode. In several studies, no statement is made about the cell chemistry at all or about individual electrodes.

System Except for the parallel-connected systems in #1, #17, and #18, and the series-connected systems in #13 and #21, only individual cells are examined. The scaling from cell to module and system level is thus often left out in the studies.

Temperature Range The temperature range examined in the studies essentially corresponds to the reasonable operating range between -20 to 60 °C [2; 122]. Only in #3 lower temperatures down to -40 °C are studied. Much higher temperatures than 60 °C are studied only in #9, with up to 95 °C, and in #18, where a thermal runaway (TR) is induced.

Aging An often neglected part of the studies is aging. Fourteen studies do not mention aging at all or mention it only in passing, although it can have a significant effect on impedance as discussed in Section 2.3 and thus on the methods. In seven studies, aging effects are excluded, referring either to a relevant reference in the literature or to another study from Table 2.5. However, the cells and methods differ between studies, often not ensuring that aging can truly be excluded. In #4, #11, and #22 aging studies are performed with the result that there is no or a minor effect on the method. The corresponding methods use either the phase $\arg\{Z\}$ or the frequency at a specific condition. Aging seems to affect mainly the magnitude of the impedance in the corresponding studies. For this reason, these methods are thus more independent of aging. Only in #16 an adjustment to the method is suggested to compensate aging effects.

Conclusion - Investigated Systems The existing methods in Table 2.5 show that impedance-based temperature estimation is suitable for all common cell formats, cell chemistries, and in the reasonable temperature operating range of -20 to 60 °C. Fewer studies, however, address elevated temperature ranges above 60 °C, interconnected systems, cells with graphite-silicon blend anodes, or the effect of aging on the methods. From the conclusion of the literature, the following unresolved points are addressed in this work, excluding the behavior at elevated temperatures:

- A 18650 cylindrical cell with NMC cathode and graphite-silicon anode is part of each study in this work to address the trend of silicon as anode blend material (see Table 3.1).

- In Chapter 4 both single cells and a module in 6s1p configuration are investigated. The transferability of the method from one cell to unknown cells of the same type in the module is also a part of the investigation. Unknown cell in this case means that there is no previous characterization of the resistance behavior of the specific cell. → Q2
- Aging and adaptation of the method to aging are discussed in Chapters 5 and 6. → Q3 and Q4

2.5.3 Validation

One of the most relevant aspects of method development is the validation. Table 2.6 shows an overview of the validation and accuracy of the methods in the literature. Overall, four studies do not carry out a validation of the method and in another four studies a validation is carried out, but without giving a quantitative statement on the accuracy of the method.

Validation Scenarios The validation scenarios are divided into six categories for the evaluation. In eight studies, and thus most frequently, drive cycles (D) are used. The drive cycles range from validation in a true EV (#13) to standardized cycles, such as the new European driving cycle (NEDC) (#20), cycles derived from the assessment and reliability of transport emission models and inventory systems (ARTEMIS) project [237] (#5, #8, and #14), or the urban dynamometer driving schedule (UDDS) (#19). On second place, with seven studies, are constant current loads (CC). These include pulses or entire charge and discharge cycles with constant currents. Coming up next are alternating current pulses (AC), with four studies, followed by evaluations based on function or method parametrization errors (PE), with three studies. Also represented with three studies are validation scenarios that evaluate the accuracy of the method under temperature changes due to external heating (H). The validation of a single study (#6) is based on results of Monte-Carlo simulations (S).

Evaluation Measure Three quantities are used as a measure for evaluating the accuracy of the methods: the root mean square error (RMSE), the maximum error, and the average error. With thirteen studies, the most common evaluation measure is the RMSE, which is calculated as in Eq. (2.39) for a number of n measurement points x and the corresponding estimated values \hat{x} :

$$RMSE = \sqrt{\frac{1}{n} \sum_{i=1}^n (x_i - \hat{x}_i)^2} \quad (2.39)$$

In some studies, the standard deviation (STD) is also given, which is calculated as in Eq. (2.40) using the mean of the measurement points μ .

$$STD = \sqrt{\frac{1}{n} \sum_{i=1}^n (\hat{x}_i - \mu)^2} \quad (2.40)$$

Depending on the validation scenario and estimation method, the RMSE ranges from 0.1085 K (#25) to 4.94 K (#9). The average error across all studies in Table 2.6 reporting a RMSE is 0.858 K. Second most frequently, the maximum error is used in ten studies as an evaluation measure. Across all studies, accuracy can be narrowed to a maximum error range between -7.9 K (#7) and $+11.4$ K (#9). The average over the absolute values of all maximum errors is 2.242 K. In five studies, the average error is reported as evaluation measure. It ranges from 0.2767 K (#23) to 4.8059 K (#23) and its average

across all studies is 1.509 K.

Table 2.6: State of the art impedance-based temperature estimation methods: Method validation and accuracy.

#	Reference	Validation	Accuracy		
			RMSE	Maximum error	Average Error
1	[51]	-	no values given		
2	[52]	CC, AC	1.0 K (STD: 3.4 K) ^(I)		
3	[45]	PE, H	0.6 K (STD: 3.4 K) ^(I)	PE SOC known: ± 0.17 K PE SOC unknown: ± 2.5 K	
4	[49]	-	0.9 K (STD: 3.2 K) ^(I)		
5	[47]	AC, D	0.6 K (STD: 1.9 K) ^(I)	± 10 A load: ± 0.4 K ± 20 A load: ± 0.9 K	drive cycle ^(III) : 0.6 K
6	[228]	S	0.4 K (STD: 0.7 K)		
7	[44]	CC		150 A charge discharge: Z : -7.8 K $+3.6$ K arg{Z}: -4.6 K $+1.8$ K Re{Z}: -7.9 K $+3.5$ K Im{Z}: -2.3 K $+1.5$ K f: -4.6 K $+2.1$ K	
8	[229]	D ^(III)	EKF + Re{Z}: T _{core} : 2.04 K T _{surf} : 2.06 K DEKF + Re{Z}: T _{core} : 1.43 K T _{surf} : 1.24 K		
9	[174]	H	T < 68 °C: 0.67 K ^(II) T ≥ 68 °C: 4.94 K ^(II)	T < 68 °C: 2.1 K ^(II) T ≥ 68 °C: 11.4 K ^(II)	
10	[230]	CC	40 A charge discharge: 0.287 K 0.503 K 60 A charge discharge: 0.294 K 0.243 K 80 A charge discharge: 0.301 K 0.362 K	≈ 1 K	
11	[53]	CC	no values given		
12	[214]	PE			SOC known: 2.08 K SOC unknown: 2.48 K
13	[50]	D	real EV drive cycle with STD of ± 1 K		
14	[231]	D ^(III)	Insulated, RMSE < 0.659 K Uninsulated, RMSE < 0.458 K		
15	[232]	CC		T _{amb} = 10 °C: 0.76 to 1.58 K T _{amb} = 20 °C: 0.91 to 2.07 K	
16	[233]	D, H	no values given		
17	[212]	-	no values given		
18	[234]	-	no values given		
19	[29]	D ^(V)	no values given		
20	[54]	AC, D	± 20 A load: 0.43 K	± 20 A load: 1.45 K	drive cycle ^(IV) : 0.5 K ± 20 A load: 0.33 K
21	[235]	D	drive cycle: ± 1 K		
22	[38]	PE	-2.3 to $+2.06$ K		
23	[236]	AC	0.2767 to 4.8059 K		
24	[41]	CC	1.5 Ah cell: 1.0 K 3.0 Ah cell: 0.5 K 2.35 Ah cell: 0.7 K		
25	[114]	CC	1 C discharge: 0.1085 K 2 C discharge: 0.2550 K 3 C discharge: 0.3224 K	1 C discharge: 0.6 K 2 C discharge: 2.0 K 3 C discharge: 0.6 K	

AC Alternating current pulses
 CC Constant current load
 D Drive cycles
 H External heating
 PE Function/Method parametrization error
 S Simulation result
 DEKF Dual Extended Kalman Filter
 EKF Extended Kalman Filter

STD standard deviation
^(I) Values calculated as benchmark in #6 using Monte-Carlo simulations
^(II) Calculated from Table 3 in #9
^(III) [assessment and reliability of transport emission models and inventory systems \(ARTEMIS\)](#)
^(IV) [new European driving cycle \(NEDC\)](#)
^(V) [urban dynamometer driving schedule \(UDDS\)](#)

Conclusion - Validation In summary, it is not possible to make a straight comparison between the studies because the validation scenarios and their boundary conditions, as well as the validation measure used, differ significantly. Nevertheless, the following conclusions can be drawn for this thesis:

- The **RMSE** is the most common evaluation measure and is also used in Chapters 3, 4 and 6.
- Three validation scenarios (PE, H, and D) of the six introduced with Table 2.6 are used in this work.
- While a straight comparison of the results from Chapters 3, 4 and 6 with the values in Table 2.6 is difficult to realize, the accuracy of the method developed in this thesis can still be ranked using Table 2.6.

After reviewing the state of the art in the literature with reference to the research questions of this thesis, the next three chapters are devoted to investigating and answering the individual research questions Q1 to Q4 of Section 1.2 on the basis of four publications that were published as part of this dissertation.

3 Relation between Cell Temperature and Pulse Resistance

Chapter 3 focuses on the goal to gain a general understanding of the relationship between the R_{DC} and the temperature of a LIB. The scope of Chapter 3 is once more highlighted in Fig. 3.1 for content guidance. The three thematic priorities:

- determination of the functional relation between R_{DC} and the internal cell temperature (T_{int}),
- influence of the cell dimension,
- and influence of the cell chemistry

are discussed in Section 3.1. The relation between the average cell temperature and the temperature determined from the measured cell resistance is covered as fourth topic in a subsequent discussion in Section 3.2. The section addresses the aspect that only the superimposed resistance of a cell can be measured and investigates the question of whether the average value of the internal cell temperature corresponds to the temperature determined from the superimposed resistance.

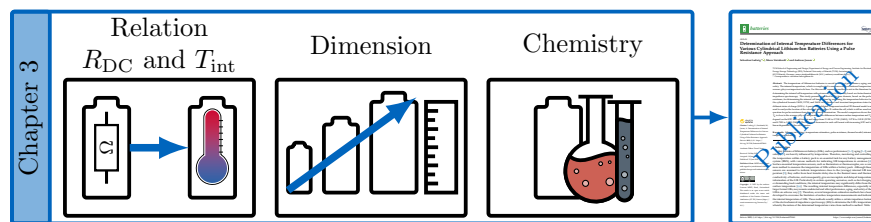


Figure 3.1: Scope of Chapter 3.

3.1 Internal Cell Temperature in Relation to Pulse Resistance and the Influence of Cell Dimension and Chemistry

The results in this section were published in the study *Determination of Internal Temperature Differences for Various Cylindrical Lithium-ion Batteries Using a Pulse Resistance Approach* [238]. The three cylindrical cells in Table 3.1 with different dimensions and chemistry were examined in the study. The 18650 and 21700 cells have the same chemistry with NMC on cathode and a silicon-graphite composite on anode side. The 18650 cell serves as a bridge between the individual studies of this thesis and is used as object of study in all subsequent chapters. The 26650 cell is the largest cell and has a different chemistry with a LMO cathode and a graphite anode. All three cells in Table 3.1 underwent the same test procedure.

In the first step, the R_{DC} of the cells was characterized using pulses at the SOC levels 10%, 50%, and 90%. At each SOC, charge and discharge pulses were applied at ambient temperatures from 5 to 45 °C

Table 3.1: General information and parameters of the investigated cells. Adapted from [238].

	18650	21700	26650
Identifier	INR18650-MJ1	INR21700-M50T	IMR26650-V1
Manufacturer	LG Chem	LG Chem	Efest
Dimensions (d h) / mm	18.1 65.1 [239]	21.1 70.2 [239]	26.5 65.2 [240]
Chemistry (Cathode Anode)	NMC Gr/Si ^(I)	NMC Gr/Si ^(II)	LMO Gr ^(III)
Capacity (C_{nom})	3.35 Ah	4.85 Ah	5.00 Ah

^(I) $\text{Li}(\text{Ni}_{0.84}\text{Co}_{0.11}\text{Mn}_{0.05})\text{O}_2$ | Graphite + 1 wt% Silicon [84]

^(II) $\text{Li}(\text{Ni}_{0.84}\text{Co}_{0.10}\text{Mn}_{0.06})\text{O}_2$ | Graphite + 1 wt% Silicon [84]

^(III) LiMn_2O_4 [241; 242] | Graphite

in 5 K steps. The determined isothermal relation between measured temperature and R_{DC} was mapped with Eq. (3.1), which is the corresponding time domain equation to the modified Arrhenius law used in Eq. (2.37).

$$R_{\text{DC}}(T_{\text{a}}) = R_0 + R_1 \exp\left(\frac{E_{\text{A,b}}}{k_{\text{B}} T_{\text{a}}}\right) \quad (3.1)$$

The resistance values to parametrize Eq. (3.1) were optimized regarding the period Δt for the estimation and the pulse type (see Section 2.4.2.3). For the purpose of estimating the temperature, the inverse of Eq. (3.1) was taken, resulting in the estimation function in Eq. (3.2).

$$T_{\text{R}} = f(R_{\text{DC}}) = \frac{E_{\text{A,b}}}{k_{\text{B}} \cdot [\ln(R_{\text{DC}} - R_0) - \ln(R_1)]} \quad (3.2)$$

The estimation function was applicable to all three cell types, although the function parameters differed with cell format, chemistry, and SOC.

In the second step, pulses were continuously applied to the cells at each SOC and used for temperature estimation while externally increasing the ambient temperature from 10 to 40 °C. This resulted in a SOC and cell format dependent temperature difference ΔT_{R} between the measured cell surface temperature and the temperature T_{R} determined by Eq. (3.2). With increasing cell dimensions and thus increasing heat capacity, the heating of the cell interior slowed down. Consequently and as expected, the temperature difference increased with increasing cell dimension from 2.14 to 2.70 K for the 18650 cell, 3.07 to 3.85 K for the 21700 cell, and 4.74 to 5.45 K for the 26650 cell, whereby ΔT_{R} decreased with increasing SOC by about 0.5 K.

In the third step, the temperature difference was further investigated using the existing 2D thermal model from Steinhardt et al. [239], which was already parametrized for the 18650 and 21700 cell. The comparison with the simulation results revealed that T_{R} was closest to the averaged jelly roll temperature, but could not explain the SOC-dependent change in ΔT_{R} . The difference between simulation and calculated ΔT_{R} could be traced back to two possible reasons: model parameter uncertainties and missing mechanical dependencies of the model on pressure and thermal contact resistance.

Authors Contribution

Sebastian Ludwig developed the idea of the study, conducted the experiments and evaluated the experimental data. Marco Steinhardt created the models and performed the thermal simulations. The manuscript was written by Sebastian Ludwig with the help of Marco Steinhardt, who contributed to

the modeling part. Andreas Jossen supervised the work and reviewed the manuscript. All authors discussed the data and commented on the results.

Determination of Internal Temperature Differences for Various Cylindrical Lithium-ion Batteries Using a Pulse Resistance Approach

Ludwig S., Steinhardt M., Jossen A.

Batteries 8 , no. 7: 60, 2022

Permanent web link:

<https://doi.org/10.3390/batteries8070060>



Reproduced under the terms of the Creative Commons Attribution 4.0 License (CC BY, <http://creativecommons.org/licenses/by/4.0/>), which permits unrestricted reuse of the work in any medium, provided the original work is properly cited.



Article

Determination of Internal Temperature Differences for Various Cylindrical Lithium-Ion Batteries Using a Pulse Resistance Approach

Sebastian Ludwig ^{*}, Marco Steinhardt and Andreas Jossen

TUM School of Engineering and Design, Department of Energy and Process Engineering, Institute for Electrical Energy Storage Technology (EES), Technical University of Munich (TUM), Arcisstrasse 21, 80333 Munich, Germany; marco.steinhardt@tum.de (M.S.); andreas.jossen@tum.de (A.J.)

* Correspondence: sebastian.ludwig@tum.de

Abstract: The temperature of lithium-ion batteries is crucial in terms of performance, aging, and safety. The internal temperature, which is complicated to measure with conventional temperature sensors, plays an important role here. For this reason, numerous methods exist in the literature for determining the internal cell temperature without sensors, which are usually based on electrochemical impedance spectroscopy. This study presents a method in the time domain, based on the pulse resistance, for determining the internal cell temperature by examining the temperature behavior for the cylindrical formats 18650, 21700, and 26650 in isothermal and transient temperature states for different states of charge (SOCs). A previously validated component-resolved 2D thermal model was used to analyze the location of the calculated temperature T_R within the cell, which is still an unsolved question for pulse resistance-based temperature determination. The model comparison shows that T_R is close to the average jelly roll temperature. The differences between surface temperature and T_R depend on the SOC and cell format and range from 2.14 K to 2.70 K (18650), 3.07 K to 3.85 K (21700), and 4.74 K to 5.45 K (26650). The difference decreases for each cell format with increasing SOC and is linear dependent on the cell diameter.

Keywords: lithium-ion battery; temperature estimation; pulse resistance; thermal model; internal temperature difference



Citation: Ludwig, S.; Steinhardt, M.; Jossen, A. Determination of Internal Temperature Differences for Various Cylindrical Lithium-Ion Batteries Using a Pulse Resistance Approach. *Batteries* **2022**, *8*, 60. <https://doi.org/10.3390/batteries8070060>

Academic Editor: Pascal Venet

Received: 24 May 2022

Accepted: 16 June 2022

Published: 23 June 2022

Publisher's Note: MDPI stays neutral with regard to jurisdictional claims in published maps and institutional affiliations.



Copyright: © 2022 by the authors. Licensee MDPI, Basel, Switzerland. This article is an open access article distributed under the terms and conditions of the Creative Commons Attribution (CC BY) license (<https://creativecommons.org/licenses/by/4.0/>).

1. Introduction

Key features of lithium-ion batteries (LIBs), such as performance [1–3], aging [1–3], and safety [1,2], are heavily influenced by temperature. Therefore, monitoring and controlling the temperature within a battery pack is an essential task for any battery management system (BMS), with various methods for indicating LIB temperatures in existence [4]. Surface-mounted temperature sensors, such as thermistors or thermocouples, are a common method to measure the temperature of LIBs within a battery pack. Although these sensors are assumed to indicate temperatures close to the (average) internal LIB temperature [5], they suffer from heat transfer delay due to the thermal mass and thermal conductivity of batteries, and consequently, give an incomplete and delayed temperature information of the LIB. Particularly in certain operating scenarios, such as fast charging or demanding load conditions, the internal temperature may significantly differ from the surface temperature [4,6]. The resulting internal temperature differences, especially in larger format LIBs, may remain undetected and affect performance, aging, and safety of the LIB in an adverse way [7]. Therefore, several temperature estimation methods have been developed to overcome the limitation of surface temperature measurements and indicate the internal temperature of LIBs. These methods usually utilize a certain impedance feature of the electrochemical impedance spectroscopy (EIS) to determine the LIB's temperature, whereby the nature of the determined temperature varies from method to method. Table 1

summarizes the statements on the determined temperature from existing methods in the literature, which range from electrode-specific temperatures [8,9], internal/core temperature [2,5,10–19] to average/integral [20–22], and internal temperature distribution [6,23–25]. The cells examined in the studies of Table 1 cover a wide variety of chemistries and casing types, including various cylindrical, prismatic, and pouch cells with capacities reaching from 2.3 Ah to 90 Ah. Mainly individual cells were studied. Only [5,9,10,18,20] considered interconnected systems. Depending on the thermal boundary conditions, heating scenario, and cell format, the observed differences between internal cell temperature and surface temperature range from about 2 K to 3 K [11,21], over 5 K to 7 K [2,11,23], and up to 10 K [24,26].

Table 1. Overview of impedance-based temperature estimation methods in the literature.

#	Reference	Temperature			Cell		System
		Internal Core	Internal Distribution	Average Integral	Capacity	Format	
1	[8]	A			53 Ah	prismatic	LCO Gr cell
2	[9]	C A			5.3 Ah	18650	? 1s2p
3	[2]	x			34 Ah	prismatic	NMC ? cell
4	[5]	x			23.3 Ah	prismatic	NMC ? 2s1p
5	[10]	x			53 Ah 2.3 Ah 4.4 Ah	prismatic 26650 18650	LCO Gr LFP Gr ? cell cell 1s2p
6	[11]	x			2 Ah	pouch	LCO+NCA Gr cell
7	[12]	x			2.3 Ah 7.5 Ah	26650 cylindrical	LFP Gr NCA Gr cell cell
8	[13]	x			90 Ah	?	LFP ? cell
9	[14]	x			2.6 Ah	18650	LCO ? cell
10	[15]	x			40 Ah	pouch	LFP Gr cell
11	[16]	x			8 Ah	prismatic	? cell
12	[17]	x			30 Ah	pouch	LFP Gr cell
13	[18]	x			50 Ah 5.3 Ah 3 Ah	prismatic 18650 18650	LCO Gr ? NMC ? cell 1s2p cell
14	[19]	x			1.3 Ah	18650	LFP ? cell
15	[20]			x	90 Ah	prismatic	LFP ? 3s1p
16	[22]			x	8 Ah 40 Ah	prismatic pouch	LFP ? LFP ? cell cell
17	[23]	(x)	x		2.3 Ah	26650	LFP Gr cell
18	[24]	(x)	x		2.3 Ah	26650	LFP Gr cell
19	[6]	x	x		20 Ah	prismatic	LMO/NMC ? cell
20	[25]		x		3.2 Ah	18650	? cell

A = Anode, C = Cathode, ? = unknown or not specified by reference.

In our previous work [27] we developed a temperature estimation method, which is not dependent on a certain impedance feature from the EIS, but directly relates the pulse resistance or direct current resistance (R_{DC}) to the LIB's temperature. Since the pulse resistance can be calculated from load fluctuations generated by the application

itself, the method does not require excitation hardware to generate the specific sinusoidal signal required for an EIS or complex filters and transformations to extract the frequency spectrum from the current and voltage time-domain measurements of the BMS. Thereby, our method reduces the complexity and cost of an online sensorless temperature indication. In our previous studies, we avoided discrepancies between the measured surface and internal LIB temperature, since the focus was placed on method development [27] and aging behavior [28]. This was achieved by applying a controlled surface temperature with Peltier elements to a module of small cylindrical (18650) battery cells and moderate load conditions. For a better understanding and the differentiation of this work, the key results of the two previous publications are briefly summarized below.

The first publication [27] focused on the development and applicability of the method. For this purpose, the influence of different pulse parameters on the R_{DC} and the relation to SOC and temperature for three individual 18650 cells (same type as in Table 2) was examined. The parameters examined were the pulse amplitude, pulse duration, pulse current direction, and pulse shape. The pulse shape was varied by changing the pulse rise and fall time from instant (40 μ s) to 4.0 s. In the next step, a resistance-based temperature estimation method was developed and its accuracy was evaluated for various parametrization and validation scenarios. Subsequently, the transferability of the method from individual cells to a module consisting of six cells connected in series was examined. The cells of the module were of the same type, but different from those used for the original parametrization. To adjust the differences between the individual cells and the module, only an offset correction of the R_{DC} values was necessary. Finally, the applicability of the method was validated. For this purpose, the module was discharged with a dynamic load profile and the temperature was estimated using the developed method. The root mean square error (RMSE) for the validation ranged between 0.65 K and 1.11 K. Since aging has a major impact on the resistance of a cell, this topic was investigated in the second publication [28]. For this purpose, exactly the same module as in [27] was examined and aged with constant current and dynamic load profiles until the first cell in the module reached a state of health (SOH) of 80%. The influence of aging on the accuracy of the method was investigated and an extension of the method to adapt to capacity loss and resistance change was developed. By adapting the method to the effects of aging, the RMSE could be reduced from a maximum of 15 K to 3.78 K.

With cylindrical battery cell formats reaching from 18650, over 21700 to 26650 and even larger formats, such as Tesla's 4680 cell, internal temperature discrepancies and their influence on LIBs vary significantly [29]. For instance, fast charging poses the risk of severe battery damage [30] if the battery temperature is not controlled correctly by the BMS and/or thermal management system, especially under harsh environmental conditions, such as extreme heat or cold. Therefore, this study focuses on the relation of a LIB's pulse resistance, which was used for temperature estimation in our previous study [27], and the internal temperature of the three common cylindrical battery cell formats: 18650, 21700, and 26650. The study focuses on analyzing the relationship between the surface and the internal cell temperature in relation to the temperature indicated by the R_{DC} (T_R). The aim is to determine to what extent the pulse resistance from our previous study [27] is suitable for monitoring the internal cell temperature and thus contributes to increasing the safety, performance, and lifetime of LIBs. For this purpose, three representative cylindrical cells are experimentally investigated under isothermal conditions and in a transient temperature state by applying an external temperature change similar to Haussmann and Melbert [21]. A validated 2D thermal model is utilized to analyze the internal temperature behavior of the cells and additionally serves as a reference for comparison with the pulse resistance-based temperature.

The remainder of this study is structured as follows. Section 2 describes the investigated cells, the utilized equipment as well as the test procedures. Section 3 briefly introduces the 2D thermal model used to analyze the relationship between the temperature indicated by the pulse resistance and the internal temperature of the investigated cells. Section 4

presents the results for the R_{DC} to temperature relation under isothermal conditions and the function to relate the R_{DC} to the cell temperature. Subsequently, the results for the temperature indicated by the $R_{DC}(T_R)$ under an external temperature change and the surface temperature are compared and discussed. At the end of Section 4, the spatial relation of T_R and the internal temperature simulated by the 2D thermal model are addressed. Section 5 summarizes the results, presents the key conclusions of the study, and gives an outlook on possible future work.

Table 2. General information and parameters of the investigated cells, including the nominal capacity (C_{nom}), the average capacity (\bar{C}) and resistance (\bar{R}_Ω) as well as the corresponding relative standard deviations $\sigma_{C,rel}$ and $\sigma_{R,rel}$ of the five cell batches used for the cell selection.

	18650	21700	26650	
Identifier	INR18650-MJ1	INR21700-M50T	IMR26650-V1	
Manufacturer	LG Chem	LG Chem	Efest	
Dimensions (d h) / mm	18.1 65.1 [31]	21.1 70.2 [31]	26.5 65.2 [32]	
Chemistry (Cathode Anode)	NMC Gr/Si ^(a)	NMC Gr/Si ^(b)	LMO Gr ^(c)	
Capacity (C_{nom})	3.35 Ah	4.85 Ah	5.00 Ah	
Batch				
Capacity	\bar{C}	3.424 Ah	4.885 Ah	5.511 Ah
	$\sigma_{C,rel}$	0.483%	0.124%	0.233%
Impedance	\bar{R}_Ω	31.079 m Ω	22.657 m Ω	16.097 m Ω
	$\sigma_{R,rel}$	0.379%	0.868%	0.618%

^(a) Li(Ni_{0.84}Co_{0.11}Mn_{0.05})O₂|Graphite + 1 wt% Silicon [33]; ^(b) Li(Ni_{0.84}Co_{0.10}Mn_{0.06})O₂|Graphite + 1 wt% Silicon [33]; ^(c) LiMn₂O₄ [34,35]|Graphite (see Appendix A).

2. Experiment

2.1. Investigated Cells

For this study, the three cylindrical cells listed in Table 2 were selected. The 18650 and the 21700 cells were selected since they represent the latest nickel manganese cobalt oxide (NMC) chemistry with silicon content in the anode composite and a nickel-rich cathode material [33]. Furthermore, the 18650 was investigated in our previous studies [27,28] and the 2D thermal model of both cells (18650 and 21700) was already implemented and validated in the study of Steinhardt et al. [31]. The 26650 cell's LiMn₂O₄ (LMO) chemistry [34,35] was chosen to investigate if the relation of the R_{DC} and temperature is altered by different chemistry. To verify the cell chemistries, the open-circuit voltages (OCVs) of the cells were analyzed using differential voltage analysis (DVA). The results are briefly presented in Appendix A. For each cell format, a batch of five sample cells was initially cycled for ten cycles according to the manufacturer's standard charge and discharge procedure.

Subsequently, a representative cell was selected for this study from each batch, which showed the least deviation in resistance and capacity from the average batch parameters listed in Table 2. The cells were fully charged with a constant current (CC) followed by a constant voltage (CV) protocol until reaching the upper cut-off voltage, with I_{CC} equal to the manufacturer's standard charging current and $I_{CV} = 0.01$ C. The capacity of each cell in the batches was determined by discharging the fully charged cell with 0.033 C to the lower cut-off voltage. The resistance of each cell was determined with a galvanostatic EIS from 10 kHz to 10 mHz at a state of charge (SOC) of 50%, whereby R_Ω represents the real part of the impedance at the zero-crossing of the imaginary part.

2.2. Experimental Setup

Figure 1 shows the experimental setup used in this study. Three PT100 temperature sensors were distributed over the cells' surface: one sensor to measure the temperature

at the positive terminal (T_p), one sensor to measure the temperature at the center of the cell (T_c), and one sensor to measure the temperature at the negative terminal (T_n). The temperature sensors were bonded to the cells' surface with superglue and monitored in a 4-wire connection with a cell measurement unit (CMU) from BaSyTec. An additional negative temperature coefficient (NTC) thermistor connected to a cell test system (CTS) from BaSyTec was used to measure the ambient temperature (T_{amb}) close to the cells' surface. All temperature sensors were initially gain and offset calibrated using a Fluke 1524 reference thermometer and a platinum resistance probe with an accuracy of ± 0.012 K. A potentiostat (VMP3) from BioLogic was used to electrically characterize the cells, which were connected via clipboards with gold contact pins in a 4-wire connection. Only the data acquisition of CTS and CMU were synchronized by integrating the CMU in the CTS test protocol. To synchronize the electrical measurements of the VMP3 and the temperature data of the CTS and CMU, the unused sense wires of the CTS were connected with the sense wires of the VMP3. Thereby, the pulses generated by the VMP3 were also measured from the CTS and served as a means of data synchronization. The thermal boundary conditions were set with a Binder KT 115 climatic chamber, achieving a temperature fluctuation of less than 0.1 K.

2.3. Test Procedures

Two test procedures were conducted in this study. The first one is depicted in Figure 1b, showing the isothermal characterization of the R_{DC} . The second test procedure in Figure 1c shows the transient temperature characterization under an external change in temperature. Both test procedures are presented in detail in the following sections.

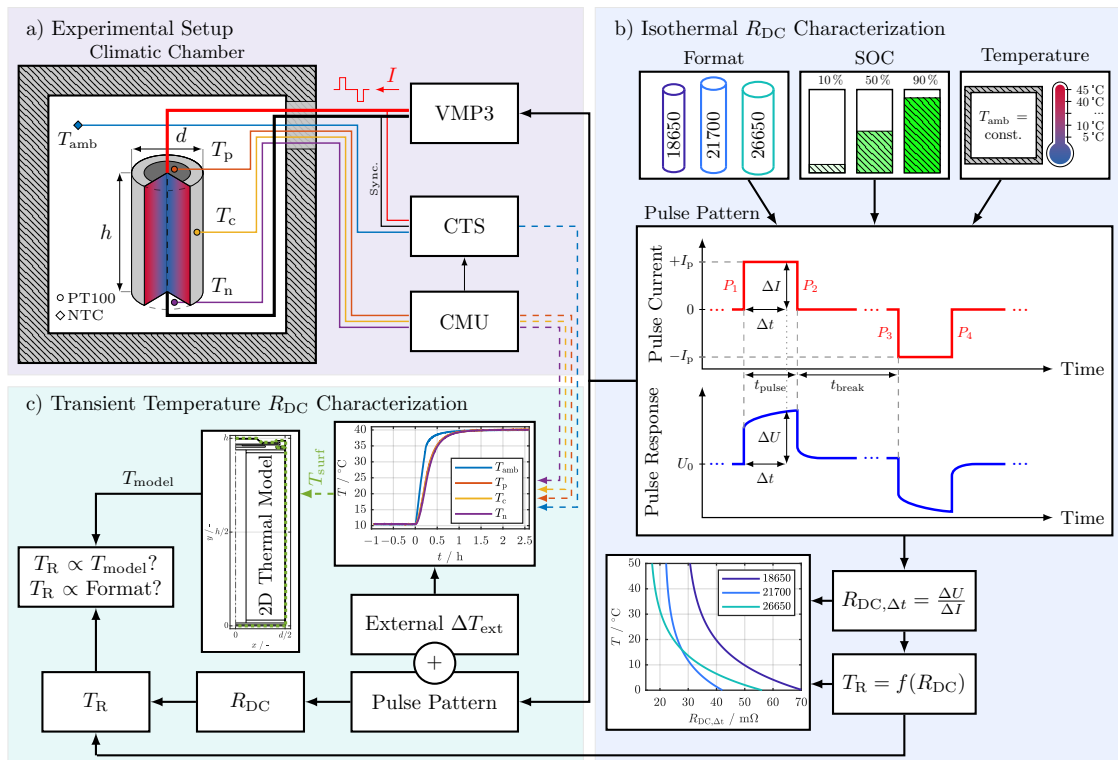


Figure 1. Study overview. (a) Experimental setup: climatic chamber for temperature control, temperature sensor placement on investigated cells (temperature at the positive terminal (T_p), temperature

at the center of the cell (T_c), and temperature at the negative terminal (T_n), ambient temperature (T_{amb}), and measurement equipment as follows: Potentiostat (VMP3) from BioLogic, cell test system (CTS) and cell measurement unit (CMU) from BaSyTec. (b) R_{DC} characterization (flowchart from top to bottom): investigated cell formats, SOCs, and temperature range followed by the pulse pattern used for the characterization of the investigated cells, the equation for the R_{DC} calculation (Equation (1)), and an exemplary result for the temperature estimation function. (c) Internal temperature characterization: flowchart for the investigation of the relation between the internal temperature calculated by the 2D thermal model and the temperature calculated from R_{DC} values during an external change in temperature (ΔT_{ext}) by increasing the ambient temperature (T_{amb}) from 10 °C to 40 °C.

2.3.1. Isothermal R_{DC} Characterization

The different cell formats from Table 2 were characterized at a SOC of 10%, 50%, and 90% in the temperature range of 5 °C to 45 °C in 5 K increments to gain the R_{DC} characteristics at isothermal conditions. The resistance of a cell is usually relatively constant over the middle SOC range, but can increase sharply at the edges of the SOC range [27,36]. In order to investigate the influence at the SOC fringe, the SOCs 10% and 10% were chosen, for the middle range a SOC of 50%. The R_{DC} of each cell at each SOC and temperature was calculated from the pulse pattern shown in Figure 1b. The cells rested for at least 6 h at each temperature before the pulse pattern was applied to ensure that the cells were thermally and electrically equilibrated. For a continuous temperature estimation, continuous R_{DC} values and therefore continuous pulses were needed. To avoid a change in SOC, the pulse pattern contained one charging pulse followed by an equivalent discharging pulse to maintain an even charge balance. The individual pulse parameters listed in Table 3 were carefully selected to fulfill the following requirements:

- (P.1) Our previous analysis in [27] revealed that the optimal evaluation time Δt for the R_{DC} for temperature estimation is in the region of 10 ms to approximately 100 ms. To cover this range with margin, the pulse duration (t_{pulse}) was set to 150 ms. However, the exact evaluation time (Δt) is determined in Section 4.1 with the results listed in Table 4.
- (P.2) The continuous pulses may affect each other since LIBs are time-variant systems. The pause between the charging and discharging pulses (t_{break}) was set to 5 s, which proved to be long enough to avoid the preceding pulse to affect the following one (see Section 4.1).
- (P.3) To analyze the transient temperature behavior (see Section 2.3.2), the cell temperature is changed by externally heating the cell and simultaneously applying current pulses. Internal temperature changes due to heating of the cells through ohmic losses [37] caused by the continuous application of the pulses had to be avoided. Therefore, the pulse current and duration had to be small. The pulse duration with 150 ms selected in (P.1) is already relatively short. Nevertheless, the current had to be large enough to induce a voltage response with a sufficient signal-to-noise ratio (SNR) to avoid inaccurate measurements. The trade-off resulted in a pulse current I_p of ± 0.1 C. Taking the resistance values for \bar{R}_Ω from Table 2 into account, the resulting heat generation of the applied pulses is less than 5.329 mW for each cell.

Table 3. Parameters for the pulses depicted in Figure 1b used for the R_{DC} characterization. The C-rate for the pulse current is related to the nominal capacity (C_{nom}) from Table 3.

Parameter	Value
Pulse Current (I_p)	± 0.1 C
Pulse Duration (t_{pulse})	150 ms
Break Duration (t_{break})	5 s

Table 4. Minimal fitting RMSE from Figure A6 for the different cell formats and SOC with the corresponding pulse current types P_x and Δt , which were used for the parametrization of the estimation function in Equation (4).

SOC	Format	RMSE / K	P_x	Δt / ms
90%	18650	0.223	3	149
	21700	0.378	1	130
	26650	0.162	1	145
50%	18650	0.248	1	149
	21700	0.423	1	90
	26650	0.158	1	145
10%	18650	0.208	1	25
	21700	0.367	1	25
	26650	0.106	1	145

To test the validity of the properties (P.1) to (P.3), the pulse pattern was repeated for over an hour (360 times) at each temperature, and SOC of the isothermal R_{DC} characterization. The pulses in Figure 1b were used to calculate the R_{DC} according to Equation (1), where $R_{DC,\Delta t}$ is the resistance calculated from the current change ΔI and the corresponding voltage change ΔU after the time Δt has passed. Only $\Delta t < t_{pulse}$ between 1 ms and 149 ms were evaluated.

$$R_{DC,\Delta t} = \frac{\Delta U}{\Delta I} \quad (1)$$

Since the pulse pattern contains four different current changes, marked with P_1 to P_4 in Figure 1b, four different R_{DC} were calculated from the pattern. The final goal of the isothermal R_{DC} characterization was the derivation, parametrization, and analysis of the temperature estimation function $T_R = f(R_{DC})$ for the different pulse current types (P_1 to P_4) and evaluation times (Δt), exemplarily depicted at the bottom of Figure 1b. The corresponding results are presented and discussed in Section 4.1.

2.3.2. Transient Temperature R_{DC} Characterization

The test procedure for the transient temperature characterization in Figure 1c was realized by simultaneously generating an ΔT_{ext} from 10 °C to 40 °C with the climatic chamber and continuously applying the pulse pattern from Figure 1b to the cells. Before heating the cells with the maximum heating rate to 40 °C, the cells rested at least for 6 h at 10 °C to ensure that they start from a thermally equilibrated state. The resulting temperature behavior is exemplarily shown in the upper right corner of Figure 1c. The pulses were used to continuously calculate R_{DC} values, which in turn were used to estimate the temperature T_R with the function determined in Section 4.1. The data of T_p , T_c , and T_n was used during the external temperature change to determine the relation between the estimated temperature T_R and the averaged surface temperature (T_{surf}) for the different cylindrical cell formats. Here, T_{surf} is the average of T_p , T_c , and T_n . Additionally, the surface temperature served as input for the 2D thermal model [31] for the 18650 and 21700 cells to identify the internal cell temperature distribution (T_{model}) during the external temperature change and investigate the relation between T_R and T_{Model} . The corresponding results are presented and discussed in Section 4.2. The model itself is briefly described in the upcoming section.

3. 2D Thermal Model

A previously validated 2D thermal model was used to relate T_R to the internal temperature distribution for the 18650 and 21700 cells. This model was developed and parameterized by Steinhardt et al. [31] for the same cell types as used in this work. The model is a component-resolved model, which means that components such as the steel case and the current interrupt device in the positive cell pole are resolved separately. Overall, the

axisymmetric model geometry in Figure 1c defines seven domains with no heat source term, since the cells are not operated in this study. The dimensions of the geometry were either measured in [31] with a micrometer screw or taken from computed tomography scans of the cell. All simulations were run in COMSOL Multiphysics 5.4 with an adiabatic boundary in the inner core of the cell and a defined temperature for the rest of the boundaries.

Every material parameter in the model is considered isotropic except for thermal conductivity, which is defined by the in-plane and through-plane directions of the cell's jelly roll. In the study by [31], the thermal conductivity and the specific heat capacity of the electrode-separator stack were measured at three different SOCs. The measured thermal parameters at the lowest, middle, and highest SOC by [31] were used in this work for the SOC of 10%, 50%, and 90%, respectively. Since the dependence of the thermal model parameters on temperature is less than $0.2\% \text{ K}^{-1}$, a dependence on temperature in the model is omitted and all parameters were set to their 300 K value, which also helped to reduce the model complexity. For example, for the 18650 cell at a SOC of 50%, a specific heat capacity for the jelly roll of $1004 \text{ J kg}^{-1} \text{ K}^{-1}$ and a through-plane conductivity of $1.29 \text{ W m}^{-1} \text{ K}^{-1}$ were taken from [31] and used for the simulation in this work. For all further details, we refer the interested reader to the work of Steinhardt et al. [31].

4. Results & Discussion

4.1. Isothermal R_{DC} Characterization

In our previous works [27,28], we used a general exponential equation, such as [21,22], to describe the relationship between resistance and temperature. However, in the literature, the relation between resistance for different cell internal processes and temperature is frequently described with a (modified) Arrhenius relation [8,10–12,14,18–20,23]. Since the Arrhenius relation is a more commonly used and physics-based approach, the goal of this chapter is to deduce and parameterize an Arrhenius-based function describing the relation between the R_{DC} values, derived from the characterization pulses, and the cell temperature in thermal equilibrium. First, the processes that make up the overpotential during the 150 ms pulse need to be identified. Subsequently, a function in the time domain is derived to map the resistance-temperature behavior. The current pulse duration of 150 ms limits the effects, building up the voltage response to the following processes [36,38,39]:

- (E.1) Ohmic losses, due to limiting electronic/ionic conductivity of the current collectors, the electrolyte, the active materials of the electrodes, and additives, such as carbon black.
- (E.2) Contact losses, attributed to contact resistance between one of the electrodes and the current collector, as well as from particle-to-particle contacts.
- (E.3) Interface losses, related to the charge transfer at the electrodes, as well as the contribution of the solid electrolyte interface (SEI).

The contribution of slower processes, such as diffusion, to the voltage response of the characterization pulses, was assumed to be negligibly small within 150 ms and is therefore neglected.

After identifying the processes building up the voltage response and consequently the R_{DC} , a functional description of the relation between the processes and cell temperature is needed. The ohmic and contact losses are dominated by the ionic conductivity of the electrolyte [36]. Schmidt et al. [11] used the general Arrhenius relation in Equation (2) to describe the functional relation between temperature and the electrolyte impedance of a LIB from EIS measurements.

$$R_{\text{arr}}(T_a) = R_1 \cdot \exp\left(\frac{E_A}{k_B \cdot T_a}\right) \quad (2)$$

To account for the influence of temperature-independent resistances, such as the current collectors and contact resistances, in the impedance spectra Schmidt et al. [11]

expanded the general Arrhenius to Equation (3) by adding the temperature-independent term R_0 .

$$R_{\text{exp}}(T_a) = R_0 + R_1 \cdot \exp\left(\frac{E_A}{k_B \cdot T_a}\right) \quad (3)$$

Although the electronic resistance of the current collector increases with temperature, the authors assumed the resistance to be almost constant in the investigated temperature region between 0 °C to 30 °C [11]. The remaining variables are the activation energy E_a , the Boltzmann constant k_B , a pre-exponential factor R_1 representing the hypothetical resistance at an infinite temperature, and the absolute temperature T_a . Gantenbein et al. [36] confirmed the results of Schmidt et al. [11] for Equation (3) and additionally used Equation (2) to describe the temperature dependence of the resistance related to the charge transfer and SEI process using EIS measurements and analyzing the distribution of relaxation times. Barai et al. [40] showed that different resistance characterization methodologies, such as R_{DC} and EIS, can be aligned if the time scales match. Therefore, a parametrization of Equations (2) and (3) with R_{DC} values comparable to Schmidt et al. [11] and Gantenbein et al. [36] should be achievable. Since the R_{DC} is calculated in the time domain, it is difficult to assign a particular Δt to an individual process, such as ionic electrolyte conductivity or charge transfer, in contrast to analysis making use of impedance spectra as in [11,36]. Consequently, at least the sum of Equations (2) and (3) would be required to describe the temperature behavior of the R_{DC} , although a meaningful parametrization is hardly feasible, since, as mentioned above, no clear separation of the processes in the time domain is possible. However, the aim of the study is not to describe the temperature dependence of the individual processes (E.1) to (E.3) separately, but to describe them in total. For this reason, the authors assume that a single temperature-independent term (R_0) and one temperature-dependent exponential term ($R_1 \cdot \exp\left(\frac{E_A}{k_B \cdot T_a}\right)$), as in Equation (3), are sufficient to represent the overall behavior of the R_{DC} over temperature. For the finally needed description of temperature as a function of resistance, the inverse function of Equation (3) is formed, resulting in Equation (4).

$$T_R = f(R_{\text{DC}}) = \frac{E_A}{k_B \cdot [\ln(R_{\text{DC}} - R_0) - \ln(R_1)]} \quad (4)$$

The function of Equation (4) was parameterized for the four current changes P_1 to P_4 of the pulse pattern in Figure 1b for each cell format and Δt in the range of 1 ms to 149 ms. Figure 2 serves as a representative fitting result for $\Delta t = 100$ ms to discuss the results of the parametrization. The results of the parameters E_A (see Figure A2), R_0 (see Figure A3), and R_1 (see Figure A4) for all Δt are depicted in Appendix B. Although a physical interpretation of the parameters is not the aim of this work, it is worth noting that the results for the activation energy in Figure A2 are in a reasonable range of 0.1 eV to 0.6 eV for Δt between 1 ms and 149 ms. The E_A values for $\Delta t < 5$ ms tend towards common literature values for the activation energy related to the ionic conductivity of the electrolyte with 0.09 eV [39], 0.10 eV [36], and 0.155 eV [41]. With increasing Δt the activation energy rises to almost 0.6 eV, covering common literature values related to the interface processes between the anode, including the SEI, and the electrolyte with 0.35 eV to 0.45 eV [42], 0.52 eV [36], 0.55 eV to 0.62 eV [43], and 0.66 eV [44], and also related to the charge transfer at the cathode with 0.68 eV [36] and 0.64 eV to 0.69 eV [43]. The values for the temperature-independent resistance R_0 in Figure A3 are close to the initially measured \bar{R}_Ω in Table 2, which was determined with EIS measurements.

Each subfigure in Figure 2 shows one of the investigated SOCs: 90%, 50%, and 10%. The fitting results for different cell formats are distinguished by color and the current changes by line and marker type, whereby the marker type represents the averaged value from the repeated pulse pattern (360 values) at each temperature point. No trend in R_{DC} could be observed over the 360 pulses for a specific temperature. Therefore, the break of 5 s between pulses proved to be long enough to prevent the repeating pulses

from significantly interfering with each other (P.2) or heating the cells internally (P.3). As assumed, Equation (4) can reflect the temperature behavior of the R_{DC} values, despite the fact that the resistance values represent the superposition of several processes. Similar to [19,22], who used the R-Square (R^2) as a criterion for assessing the fitting quality for their temperature estimation method, the adjusted R-Square (R^2_{adj}) [45] was used for a quantitative assessment of the fitting results in this work. The R^2 and R^2_{adj} are statistical measures for the goodness of a curve fitting result, whereby values closer to one indicate a better fit quality. In contrast to the R^2 , the number of fitted variables is taken into account with the R^2_{adj} to avoid over-fitting. As the number of fitted variables increases, R^2 will also increase. However, the fitting quality may not improve in a practical sense. To avoid such over-fitting, the R^2_{adj} statistic can be utilized. The overall R^2_{adj} above 0.98 for all Δt (see Figure A5), strongly indicates the validity of Equation (4) as the proposed fitting function.

Assessing the fitting results in Figure 2 for any of the three cells over the SOC range, the expected dependency on the SOC can be seen. The dependency becomes apparent by comparing the x -axis values where the fitting function exceeds 45 °C. For example, this value for the 26650 cell is around 32 mΩ at a SOC of 90% in Figure 2a, then drops slightly in Figure 2b at a SOC of 50% to around 31 mΩ and rises in Figure 2c at a SOC of 10% to about 35 mΩ. These SOC-dependent fluctuations can also be observed in the 18650 and 21700 cell and are consistent with previous studies [27,36]. The difference in the curves, parameterized with P_1 and P_3 , compared to the curves, parameterized with P_2 and P_4 , is particularly evident at temperatures below 25 °C and the SOC of 10% in Figure 2c. At a first glance, there is no difference in the fitting results for the different current changes for the SOC 90% and 50% in Figure 2a,b. However, the close-ups in Figure 2a,b reveal that there is a difference in the curves, albeit a small one. In our previous study [27], we already noticed this difference in R_{DC} for the 18650 cell for different current changes, which is probably caused by the initial condition of the cells at the start of the pulse. For P_1 and P_3 the cells start from an almost equilibrated state, where no current is applied. On the other hand, P_2 and P_4 start from a already polarized state, since current was already flowing for 150 ms, creating a small Li-ion concentration gradient [46]. With the current changes at P_2 and P_4 , the system returns to the equilibrium state and the concentration gradients decrease. This difference in Li-ion concentration at the start of $P_{2/4}$ compared to $P_{1/3}$ results in a small overpotential difference and might be the cause for the difference in R_{DC} [40].

For the determination of the cell temperature behavior during the external temperature change in Section 4.2, a Δt and current change type (P_1 to P_4) must be selected that is used for the parametrization of Equation (4). Since all Δt have a very high R^2_{adj} in Figure A5, the RMSE of the fitting is used as the second criterion for the selection. In Figure A6, the RMSE of the individual fit variants is shown as a complement to the R^2_{adj} in Figure A5. Table 4 summarizes the minimal RMSE for each SOC and cell format together with the corresponding pulse current type (P_x) and Δt for the temperature estimation with Equation (4) in Section 4.2, the settings (P_x and Δt) for the minimal RMSE from Table 4 as well as all other settings within an error margin of 0.05 K in respect to the minimum error were used. This measure intends to minimize the influence of noise and increase the accuracy of the temperature estimation during the external temperature change, which is discussed in the next section.

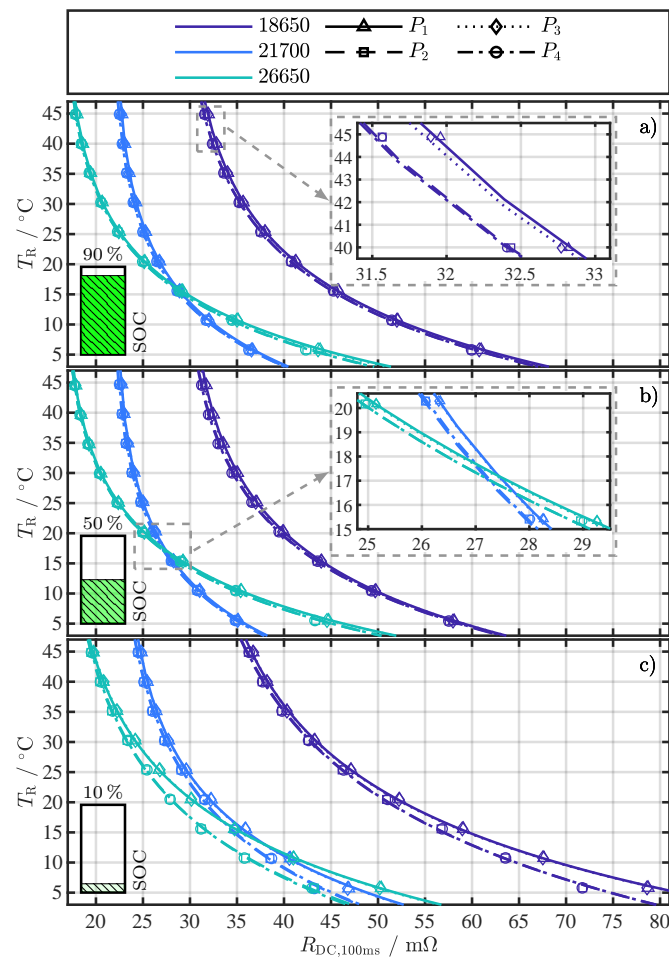


Figure 2. Exemplary fitting results of Equation (4) for $\Delta t = 100$ ms for different cell formats and current changes P_1 to P_4 (see pulse pattern in Figure 1b) at the investigated SOC levels (a) 90%, (b) 50%, and (c) 10%. The marker type represents the averaged value from the repeated pulse pattern (360 values) at each temperature point. The close-ups in (a,b) visualize the minimal difference between current changes $P_{1/3}$ and $P_{2/4}$.

4.2. Transient Temperature R_{DC} Characterization

The results for the temperature estimation with Equation (4) and the setting according to Table 4 are presented in Figure 3. The figure only showcases the results for a SOC of 50%. The originally calculated values ($T_{R,org}$) in Figure 3a–c all tend to increased noise for increased temperatures, whereby the level of noise differs from cell to cell. By considering the corresponding estimation functions in Figure 3d–f, it is apparent that the different slopes of the estimation functions are responsible for the different noise levels. Schmidt et al. [11] also noticed this for their EIS-based temperature estimation method. The exemplary input deviation of ± 0.2 m Ω for the nominal value of 10 $^\circ$ C causes a deviation in temperature below 0.3 K. In contrast, the same input deviation at 40 $^\circ$ C causes a variation between 1.1 K (Figure 3d) and 2.7 K (Figure 3e). However, the filtered values ($T_{R,fltr}$) emphasize that the noise can be significantly reduced by applying a moving average filter.

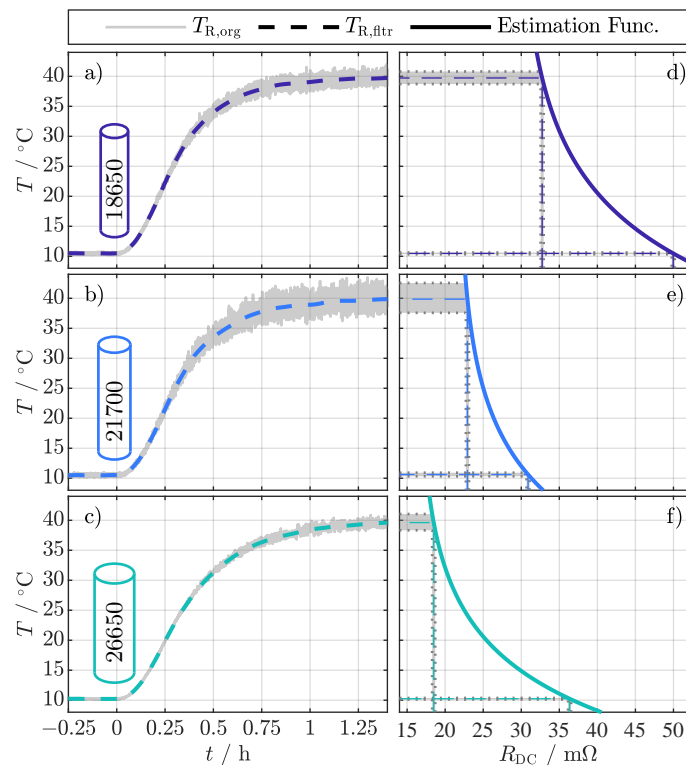


Figure 3. Exemplary temperature estimation results for the investigated cell formats 18650 (a), 21700 (b), and 26650 (c) at a SOC of 50% evaluated with Equation (4) and the setting according to Table 4. $T_{R,org}$ shows the originally calculated values and $T_{R,fltr}$ shows the values filtered with a moving average filter. The different and increased noise can be related to the individual slopes of the estimation functions in (d–f).

Figure 4 relates the sensor temperature data to the filtered T_R . The moment when the setpoint for the climatic chamber temperature (T_{set}) changes from 10 °C to 40 °C was set to zero on the x -axis. The variation of the ambient temperature (T_{amb}) for the different cell formats at the different SOC is negligibly small. However, there is a small difference between cells, probably caused by the positioning of the cells within the climatic chamber. The ambient temperature rises from 10 °C with a constant heating rate of about 100 K h⁻¹ to 35 °C in about 0.25 h and converges to the final temperature of 40 °C in about 1.25 h. Since the mean absolute deviation over all cell surface related temperatures (T_p , T_c , T_n) during each experiment is less than 0.073 K, only the average over the three cell surface temperature sensors (T_{surf}) is depicted in Figure 4. The resistance-related temperature T_R always lags behind the average surface temperature T_{surf} for each cell format and SOC, whereby the difference increases with increasing cell size. This already shows that T_R , like the temperatures of the existing EIS-based methods in Table 1, is related to the internal cell temperature and depends on the cell dimensions. For a detailed analysis, the difference between the surface temperature and the R_{DC} is considered and discussed in comparison to the 2D thermal model in the following section.

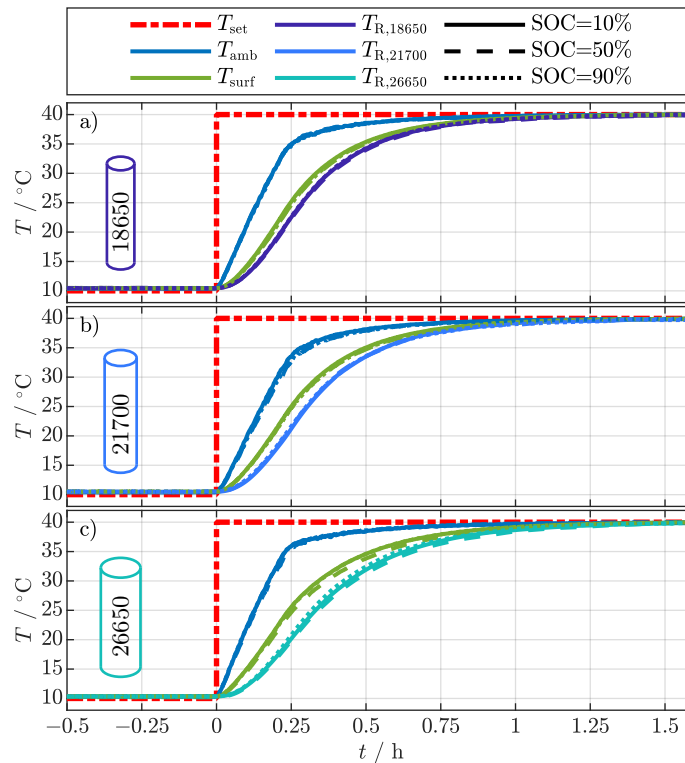


Figure 4. Temperature development during the external temperature change from 10 °C to 40 °C for the different cell formats 18650 (a), 21700 (b), and 26650 (c) at the investigated SOC of 10%, 50%, and 90%.

4.3. Internal Temperature: Model versus T_R

With the help of the 2D thermal model from Section 3, the internal temperature of the cells, especially the jelly roll, can be broken down in more detail and T_R can be assigned to a corresponding internal temperature. For this purpose, six simulations were run evaluating the core (T_{core}), the center (T_{ctr}), and the average (T_{avg}) temperature of the jelly roll. The spatial location of the temperatures is shown in Figure 5j, with the temperature simulated at half of the cell height and at the core of the jelly roll (T_{core}), the temperature simulated at half of the cell height and at the center of the jelly roll (T_{ctr}), and the simulated average jelly roll temperature (T_{avg}). The averaged surface temperature (T_{surf}) was used as the temperature boundary condition on the entire surface of the cells, also shown in Figure 5j. The evaluation of the temperature difference between T_{surf} and the jelly roll temperatures (T_{core} , T_{ctr} , T_{avg}) resulted in the corresponding temperature differences (ΔT_{core} , ΔT_{ctr} , ΔT_{avg}) for the 18650 and 21700 cell at the three SOC points shown in Figure 5a–f. Additionally, the corresponding differences ($\Delta T_{R,18650}$, $\Delta T_{R,21700}$) between T_{surf} and T_R are depicted. For the 26650 cell, only the differences ($\Delta T_{R,26650}$) between T_{surf} and T_R are depicted in Figure 5g–i, since the model parameters for this cell type were not investigated by Steinhardt et al. [31].

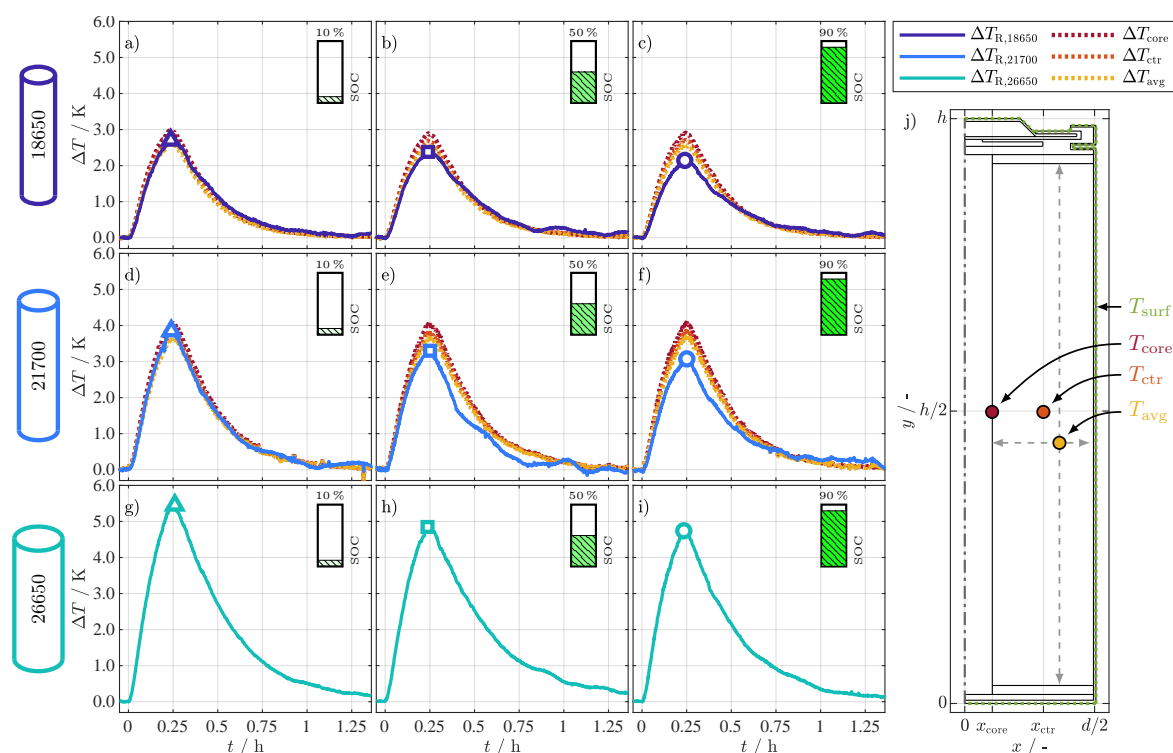


Figure 5. Temperature differences $\Delta T_{R,18650}$ (a–c), $\Delta T_{R,21700}$ (d–f), and $\Delta T_{R,26650}$ (g–i) between the averaged surface temperature (T_{surf}) and the temperature indicated by the R_{DC} (T_{R}) at each SOC point and for each cell format. Additional temperature differences ΔT_{core} , ΔT_{ctr} , and ΔT_{avg} in (a–f) for the three simulated temperature locations of the jelly roll in (j) according to the 2D thermal model simulation results for the 18650 and 21700 format. The differences are again related to the averaged surface temperature. T_{core} and T_{ctr} are simulated at half of the cell height ($h/2$) and at the core (x_{ctr}), respectively at the center (x_{ctr}) of the jelly roll. T_{avg} represents the average simulated jelly roll temperature.

Comparing the differences ΔT_{R} in Figure 5 over the cell format, it is remarkable that they increase with the cell size and decrease with the SOC. For the 18650 format, in Figure 5a–c the maximal difference for T_{R} , marked with symbols, ranges between 2.70 K and 2.14 K. For the 21700 format in Figure 5d–f, the range lies between 3.85 K and 3.07 K; for the 26650 format in Figure 5g–i, between 5.45 K and 4.74 K. There are deviations between simulation- and resistance-related temperature differences for the individual formats depending on the SOC. For a SOC of 10% in Figure 5a,d, the resistance-related differences $\Delta T_{R,18650}$ and $\Delta T_{R,21700}$ are in good accordance with the simulated differences and range between the average and the center temperature, which is in accordance with [20–22] from Table 1. This result seems realistic for two reasons: First, T_{R} maps the temperature dependence of the aggregated processes of the cell (see (E.1) to (E.3)), which corresponds to the concept that T_{R} also maps the aggregated/average temperature of the jelly roll. Second, assuming that the relationship between resistance and temperature (see Figure 2) is almost linear for the temperature differences considered ($\Delta T_{\text{R}} \leq 5.45$ K), the area-related average temperature (T_{avg}) also corresponds to the area-related average value of the resistance. With increasing SOC in Figure 5b,c,e,f $\Delta T_{R,18650}$ and $\Delta T_{R,21700}$ keep decreasing, whereas the simulated temperatures show minor differences between SOCs, although the simulation parameters are adapted to the SOC. For the 18650 format, the maximum simulated difference for T_{core} decreases only by 0.07 K from 2.98 K at 10% SOC to 2.91 K at 90% SOC, which

is in accordance with the increasing through-plane thermal conductivity for this cell [31]. The difference $\Delta T_{R,18650}$, in contrast, decreases by 0.56 K. The simulation results for the maximum difference of T_{core} for the 21700 format stay within 0.03 K, whereas $\Delta T_{R,21700}$ decreases by 0.78 K. The deviations between simulated and R_{DC} -based temperature differences are obvious, but stay below 1.04 K and are closest to T_{avg} . The deviations arise from two possible reasons:

- (R.1) Although the simulation parameters are for the same pristine cell type, they were not determined for exactly the same cell and thus might slightly differ between the cells used in [31] to parameterize the 2D thermal model and the ones used in this study. Also, the SOC points in the study by Steinhardt et al. [31] do not exactly match the SOC points investigated in this study. Since the thermal conductivity of a LIB is dependent on the SOC [47], the parameter deviation in thermal conductivity might partly cause the deviation between the simulation and ΔT_R .
- (R.2) The 2D thermal model does not consider thermal conductivity changes related to mechanical changes. The jelly roll expands when the cell is charged [48] and the contact area and pressure between the layers in the jelly roll and between the jelly roll and the metal casing of the cell increases. Several studies [49,50] showed that increased compression reduces the thermal contact resistance, leading to improved thermal conductivity and therefore reducing the difference between surface and core temperature.

While no specific reason in the previous list can be pinpointed as the decisive one, in sum they explain the deviations between simulated temperature differences and ΔT_R .

4.4. Internal Temperature: Cell Geometry & State of Charge

All cells reach the maximum difference after approximately 0.25 h at the end of the constant heating phase (see Figure 4). The peaks are highlighted with different markers in Figure 5, representing the different SOC, and are used to discuss the dependence on cell geometry and SOC in Figure 6. The dependence of the maximum difference (ΔT_{max}) on the cell diameter is depicted in Figure 6a and on the SOC in Figure 6b.

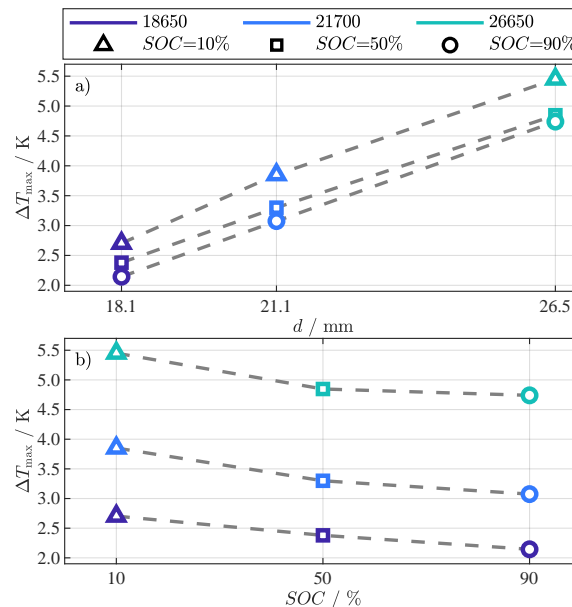


Figure 6. Relation between the maximum of the R_{DC} -based temperature difference (ΔT_{max}) from Figure 5 and cell diameter d (a), respectively SOC (b).

The correlation with the cells' diameter, surface, and volume was investigated using the values for height h and diameter d from Table 2 and the general equations for a cylindrical body. All three geometrical values show a high linear correlation to ΔT_{\max} at any SOC, indicated by a Pearson correlation coefficient of at least 0.99. In Figure 6a, the relation between ΔT_{\max} and the cell diameters is depicted, which had the highest correlation. As expected, the difference ΔT_{\max} increases with rising cell diameter.

The maximum difference steadily decreases with increasing SOC, as depicted in Figure 6b. As already discussed, this is in contrast to the simulation results in Figure 5a–f, but can be explained with model parameter uncertainties (R.1) and missing mechanical dependencies of the model on pressure and thermal contact resistance (R.2).

5. Summary & Conclusions

Knowing the internal temperature of LIBs is essential for performance, aging, and safety aspects. In the literature various studies exist, which determine different internal cell temperatures with EIS-based methods (see Table 1). In contrast to the existing literature methods, we proposed a time-domain approach based on the pulse resistance R_{DC} in our recent work [27]; however, we did not focus on the cell's internal location of the temperature determined with the R_{DC} . Therefore, we investigated the relation of the R_{DC} -based temperature T_R and the surface temperature of three different cylindrical LIBs listed in Table 2 and compared the results to a validated 2D thermal model for the 18650 and 21700 format. First, the temperature estimation function (see Equation (4)) was deduced and parameterized under isothermal conditions for the three SOCs: 10%, 50%, and 90%. Subsequently, the estimation functions were used to determine T_R during an external temperature change from 10 °C to 40 °C. The different slopes of the estimation functions resulted in different temperature noise levels, especially at elevated temperatures above 30 °C with up to 2.7 K. The noise was reduced with a moving average filter, which resulted in the necessary measurement accuracy (see Figure 3). Compared to the averaged surface temperature, T_R was found to represent an internal temperature of the cells, whereby the difference to the averaged surface temperature increased with cell dimensions (see Figure 4). In order to establish a more precise relationship between T_R and the internal cell temperature, the surface temperature difference ΔT_R was compared with the corresponding simulation results of the 2D thermal model (see Figure 5). The simulation results for the average/center temperature of the jelly roll and ΔT_R match for a SOC of 10%. For increased SOCs the simulation results show minor changes, whereas ΔT_R steadily decreases, but is still within 1.04 K to the simulation results and closest to T_{avg} . The difference between simulation and ΔT_R could be traced back to two possible reasons: model parameter uncertainties (R.1) and missing mechanical dependencies of the model on pressure and thermal contact resistance (R.2). Correlating the cell diameter to the temperature difference ΔT_R showed an almost perfect linear relation with a Pearson correlation coefficient of above 0.99 (see Figure 6a). This result shows that the use of resistance-based temperature estimation is more relevant for larger cell formats, as the difference between surface and internal temperature increases and the method determines the average jelly roll temperature. The development of the temperature difference over the SOC showed a decreasing trend (see Figure 6b). This is probably a consequence of the jelly roll expansion, causing a reduced thermal contact resistance between the jelly roll and metal casing and increasing the thermal conductivity.

In conclusion, the following key results of the study can be identified:

1. The R_{DC} can be utilized to determine the internal cell temperature for different cell chemistries and cylindrical cell formats.
2. The comparison with the 2D thermal model shows that T_R most likely represents the average jelly roll temperature (T_{avg}). Thus, T_R offers an advantage over conventional temperature sensors, which only determine the surface temperature at one point of the cell.

3. Consequently, methods as in our previous works [27,28], which are based on the R_{DC} , can contribute to improving the performance, lifetime, and safety of LIBs by detecting internal temperature discrepancies before conventional temperature sensors.
4. An important point regarding the applicability is the temperature range, for which R_{DC} -based methods are applicable. As shown in Figure 3, the accuracy of the method strongly depends on the slope of the estimation function (Equation (4)), which steadily increases with rising temperatures. For this reason, correspondingly precise measurement hardware for the current and voltage monitoring of the BMS is a prerequisite to avoid large temperature estimation errors in the elevated temperature range.

Based on the results of this study, new questions arise that are worth investigating. For example, a detailed study on the relationship between jelly roll expansion and T_R would be interesting, especially the question if T_R follows the nonlinear course of the diameter change of cylindrical LIBs over the SOC, such as measured by [48]. The present study only considered homogeneous surface temperature changes. For safety reasons, an investigation into “hot spots”, induced by locally heating the cells, would also be of interest.

Author Contributions: Conceptualization, S.L.; methodology, S.L.; software, S.L. and M.S.; validation, S.L. and M.S.; formal analysis, S.L. and M.S.; investigation, S.L.; data curation, S.L.; writing—original draft preparation, S.L. and M.S.; writing—review and editing, S.L., M.S. and A.J.; visualization, S.L.; supervision, A.J.; project administration, S.L.; funding acquisition, A.J. All authors have read and agreed to the published version of the manuscript.

Funding: This research was funded by the German Federal Ministry of Education and Research (BMBF) via the research project OSLiB (grant number: 03X90330A). The project was overseen by Project Management Juelich (Ptj).

Data Availability Statement: Not applicable.

Conflicts of Interest: The funders had no role in the design of the study; in the collection, analyses, or interpretation of data; in the writing of the manuscript, or in the decision to publish the results.

Abbreviations

The following abbreviations are used in this manuscript:

BMS	battery management system
CC	constant current
CMU	cell measurement unit
CTS	cell test system
CV	constant voltage
DVA	differential voltage analysis
EIS	electrochemical impedance spectroscopy
FEM	finite element model
LIB	lithium-ion battery
LMO	LiMn ₂ O ₄
NMC	nickel manganese cobalt oxide
NTC	negative temperature coefficient
OCV	open-circuit voltage
R^2	R-Square
R^2_{adj}	adjusted R-Square
R_{DC}	direct current resistance
RMSE	root mean square error
SEI	solid electrolyte interface
SNR	signal-to-noise ratio
SOC	state of charge
SOH	state of health
SSE	sum of square error

SST	total sum of squares
T_{amb}	ambient temperature
T_{avg}	simulated average jelly roll temperature
T_c	temperature at the center of the cell
T_{core}	temperature simulated at half of the cell height and at the core of the jelly roll
T_{ctr}	temperature simulated at half of the cell height and at the center of the jelly roll
ΔT_{ext}	external change in temperature
T_n	temperature at the negative terminal
T_p	temperature at the positive terminal
T_R	temperature indicated by the R_{DC}
$\Delta T_{R,18650}$	temperature difference between T_{surf} and the T_R for the 18650 cell
$\Delta T_{R,21700}$	temperature difference between T_{surf} and the T_R for the 21700 cell
$\Delta T_{R,26650}$	temperature difference between T_{surf} and the T_R for the 26650 cell
T_{surf}	averaged surface temperature

Appendix A. Differential Voltage Analysis

Figure A1 shows the DVA of the three investigated cells and the corresponding markers for silicon (Si_x), graphite (Gr_x), and NMC. The DVAs were evaluated from OCVs gained from a discharge with 0.033 C between 4.2 V to 2.5 V with Q_0 being the discharge capacity. Since the 18650 and 21700 cell have the same chemistry, the markers for silicon, graphite, and NMC in Figure A1a,b are almost identical in SOC and magnitude. The DVA of the 26650 cell in Figure A1c lacks the silicon peaks and only shows the typical graphite peaks, which speaks for a pure graphite anode with no silicon content. The LMO cathode could not be verified by the DVA, but is reported by [34,35].

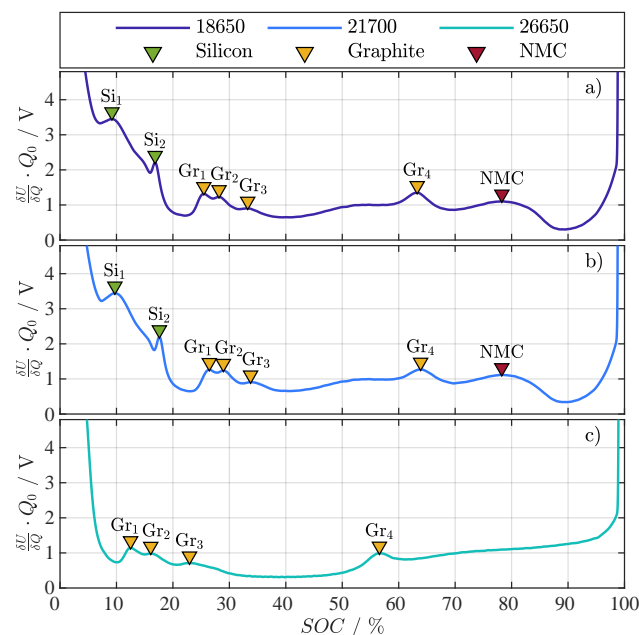


Figure A1. Differential voltage analysis with representative peak markers for silicon (Si_x), graphite (Gr_x), and NMC for the three investigated cell formats: 18650 with NMC | Si/Gr (a), 21700 with NMC | Si/Gr (b), and 26650 with LMO | Gr (c).

Appendix B. Function Parameters

The three fitting parameter E_A , R_0 , and R_1 for Equation (4) in the range of 1 ms to 149 ms are depicted in Figure A2, Figure A3, and Figure A4, respectively. Each figure shows the parameters for the three investigated cell formats and the four different pulse current types (P_1 to P_4), with a subplot for the corresponding SOCs 90%, 50%, and 10%.

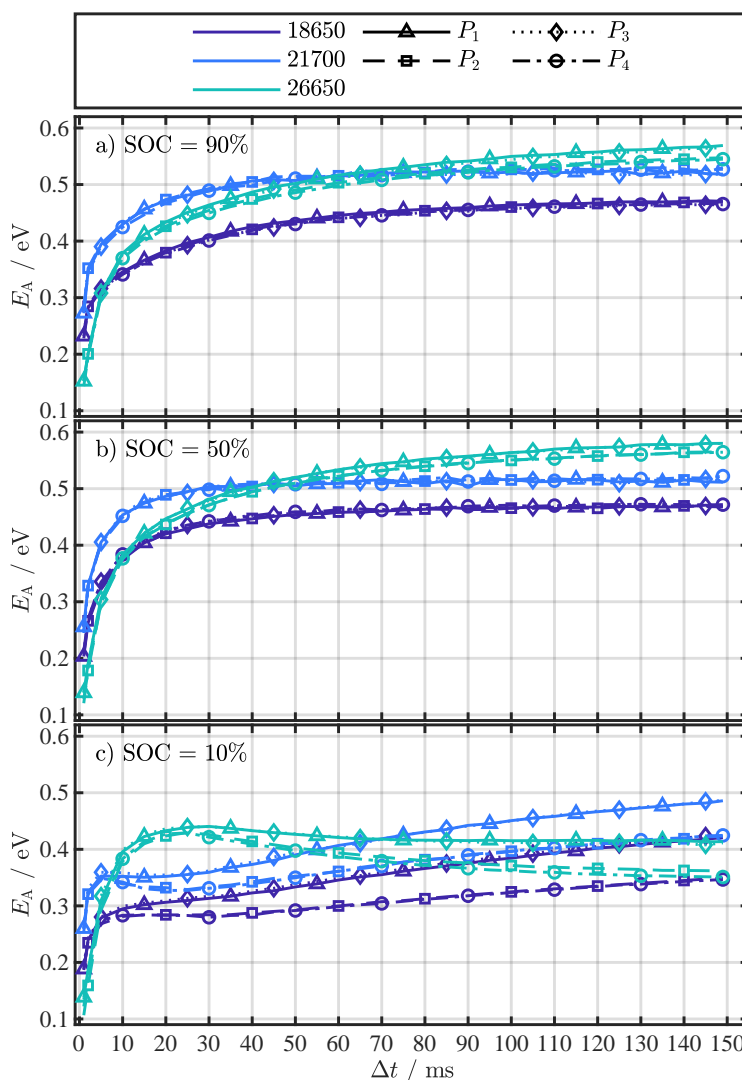


Figure A2. Fitting results for Equation (4) for the parameter E_A , each investigated cell format, and the four different pulse current types (P_1 to P_4) at the SOCs 90% (a), 50% (b), and 10% (c).

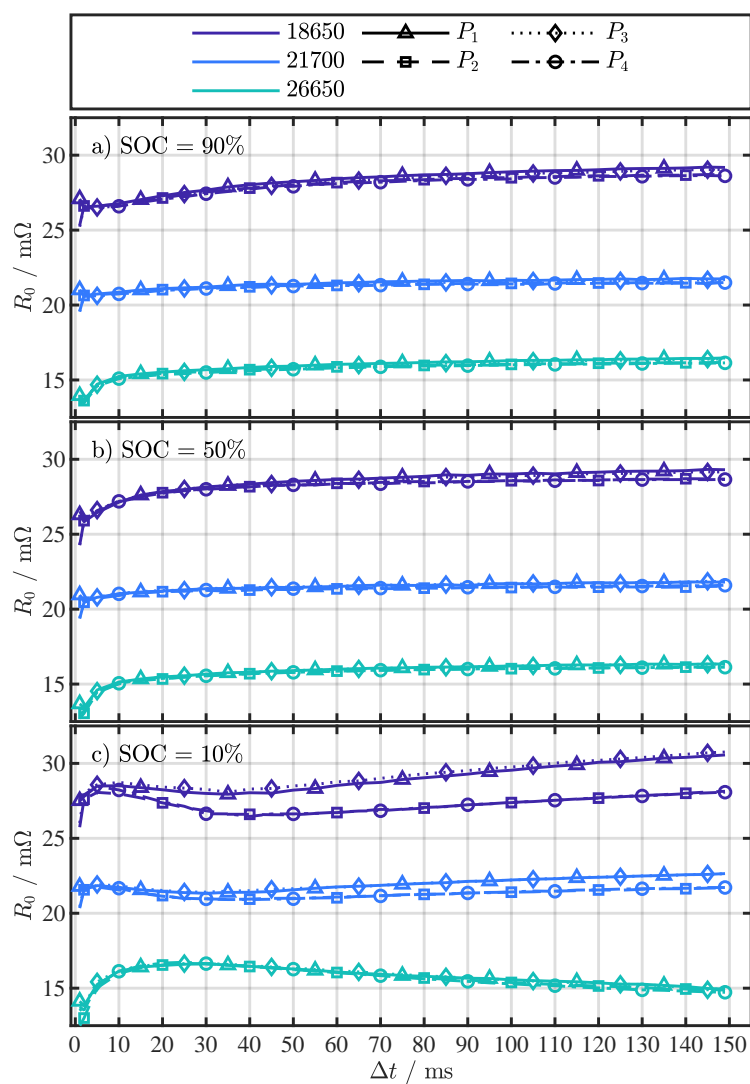


Figure A3. Fitting results for Equation (4) for the parameter R_0 , each investigated cell format, and the four different pulse current types (P_1 to P_4) at the SOCs 90% (a), 50% (b), and 10% (c).

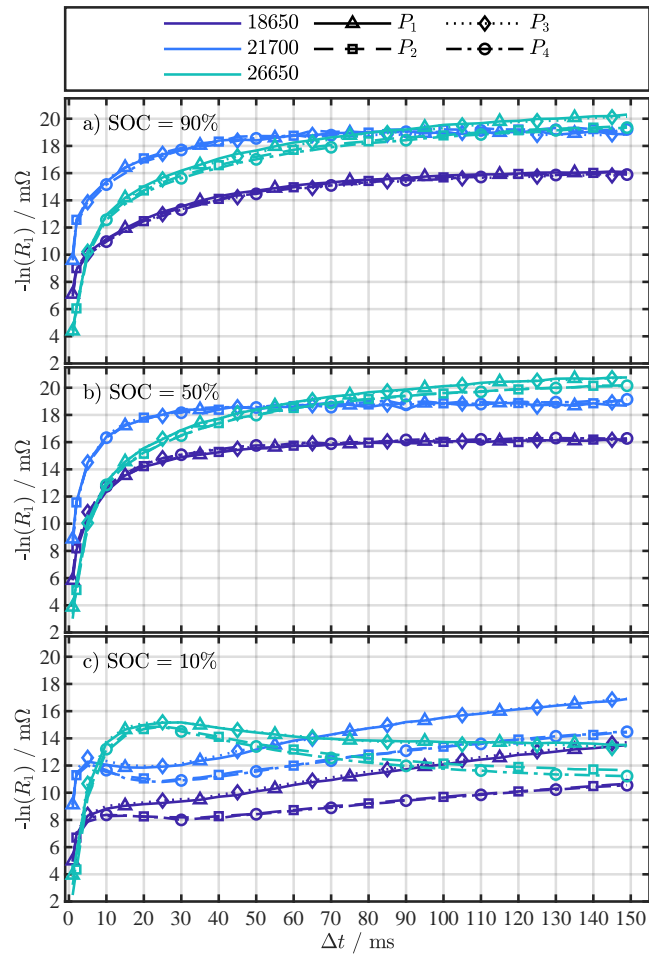


Figure A4. Fitting results for Equation (4) for the parameter R_1 , each investigated cell format, and the four different pulse current types (P_1 to P_4) at the SOC's 90% (a), 50% (b), and 10% (c).

Appendix C. Fitting Quality & Error

This section briefly introduces the calculation of the R_{adj}^2 as a statistical measure of the goodness of a curve fitting result and the RMSE as measure of the fitting error. The results were generated using *MATLAB*'s curve fitting toolbox. The R_{adj}^2 can be calculated from Equations (A1)–(A4), where:

- the sum of square error (SSE) in Equation (A1) describes the total deviation of the response values of the fit \hat{y}_i from the measured response values y_i ,

$$SSE = \sum_{i=1}^n (y_i - \hat{y}_i)^2 \quad (A1)$$

- the total sum of squares (SST) in Equation (A2) describes the total deviation of the mean \bar{y} from the measured response values y_i ,

$$SST = \sum_{i=1}^n (y_i - \bar{y})^2 \quad (A2)$$

- the general R^2 in Equation (A3) determines how successful the fit is in explaining the variation of the data,

$$R^2 = 1 - \frac{SSE}{SST} \tag{A3}$$

- and the adjusted R-Square statistic in Equation (A4) considers the number of fitted model variables m in addition to the number of response values n .

$$R_{adj}^2 = 1 - (1 - R^2) \cdot \frac{n - 1}{n - m} = 1 - \frac{SSE}{SST} \cdot \frac{n - 1}{n - m} \tag{A4}$$

A more detailed description on the calculation of R_{adj}^2 can be found in [45]. Figure A5 shows the R_{adj}^2 for Δt in the range of 1 ms to 149 ms for the investigated cell formats and the four different pulse current types (P_1 to P_4), with each subplot showing one of the investigated SOC of 10%, 50%, and 90%. The R_{adj}^2 values close to 1 indicate an almost optimal fitting quality for the parameters of Equation (4).

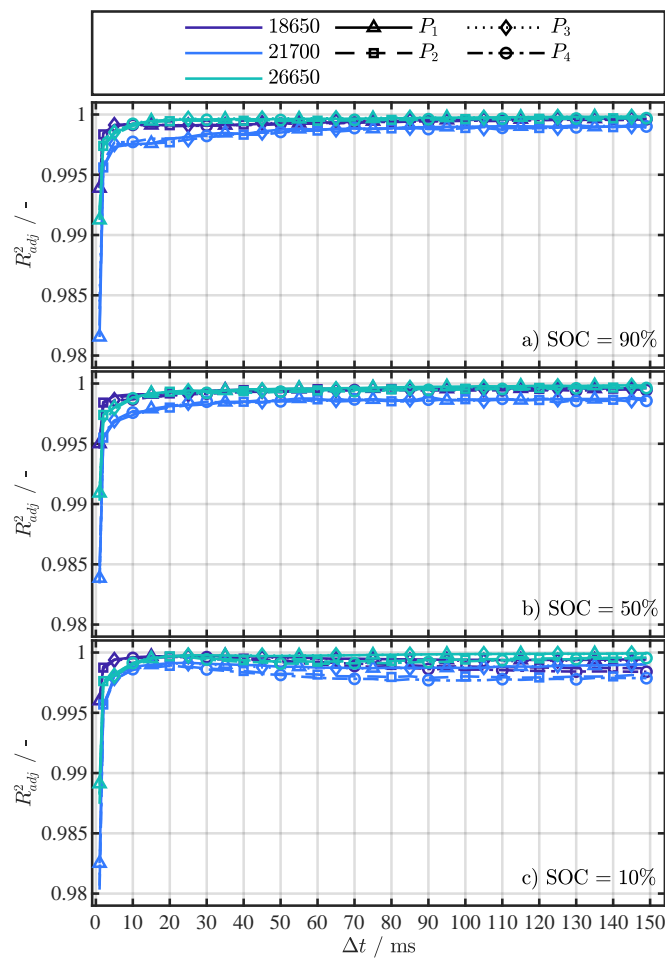


Figure A5. R_{adj}^2 results for fitting Equation (4) for each investigated cell format and the four different pulse current types (P_1 to P_4) at the SOC of 90% (a), 50% (b), and 10% (c).

The RMSE is calculated using Equation (A1) according to Equation (A5):

$$RMSE = \sqrt{\frac{SSE}{n - m}} \quad (A5)$$

The RMSE in Figure A6a,b steadily decreases with increasing Δt leveling below 0.5 K, whereby the error for P_1 and P_3 is minimally smaller than for P_2 and P_4 . This is partially true for a SOC of 10% in Figure A6c as well. In contrast to Figure A6a,b, the RMSE increases again for Δt greater than 25 ms except for the parametrization with P_1 and P_3 for the 26650 cell. Again, the error for P_1 and P_3 is in general smaller than for P_2 and P_4 .

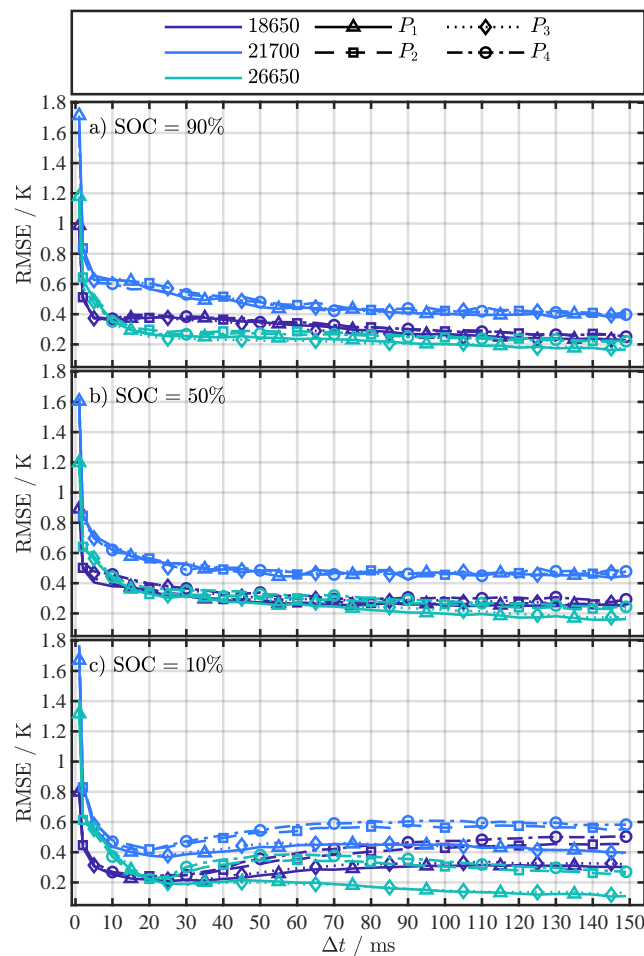


Figure A6. RMSE results for fitting Equation (4) for each investigated cell format and the four different pulse current types (P_1 to P_4) at the SOC 90% (a), 50% (b), and 10% (c).

References

1. Ma, S.; Jiang, M.; Tao, P.; Song, C.; Wu, J.; Wang, J.; Deng, T.; Shang, W. Temperature effect and thermal impact in lithium-ion batteries: A review. *Prog. Nat. Sci. Mater. Int.* **2018**, *28*, 653–666. [CrossRef]
2. Morello, R.; Di Rienzo, R.; Roncella, R.; Saletti, R.; Schwarz, R.; Lorentz, V.; Hoedemaekers, E.; Rosca, B.; Baronti, F. Advances in Li-Ion Battery Management for Electric Vehicles. In Proceedings of the IECON 2018-44th Annual Conference of the IEEE Industrial Electronics Society, Washington, DC, USA, 21–23 October 2018; IEEE: Piscataway, NJ, USA, 2018; pp. 4949–4955. [CrossRef]

3. Alipour, M.; Ziebert, C.; Conte, F.V.; Kizilel, R. A Review on Temperature-Dependent Electrochemical Properties, Aging, and Performance of Lithium-Ion Cells. *Batteries* **2020**, *6*, 35. [\[CrossRef\]](#)
4. Rajmakers, L.; Danilov, D.L.; Eichel, R.A.; Notten, P. A review on various temperature-indication methods for Li-ion batteries. *Appl. Energy* **2019**, *240*, 918–945. [\[CrossRef\]](#)
5. Beelen, H.; Mundaragi Shivakumar, K.; Rajmakers, L.; Donkers, M.; Bergveld, H.J. Towards impedance-based temperature estimation for Li-ion battery packs. *Int. J. Energy Res.* **2020**, *44*, 2889–2908. [\[CrossRef\]](#)
6. Richardson, R.R.; Zhao, S.; Howey, D.A. On-board monitoring of 2-D spatially-resolved temperatures in cylindrical lithium-ion batteries: Part II. State estimation via impedance-based temperature sensing. *J. Power Sources* **2016**, *327*, 726–735. [\[CrossRef\]](#)
7. Liu, X.; Ai, W.; Naylor Marlow, M.; Patel, Y.; Wu, B. The effect of cell-to-cell variations and thermal gradients on the performance and degradation of lithium-ion battery packs. *Appl. Energy* **2019**, *248*, 489–499. [\[CrossRef\]](#)
8. Srinivasan, R. Monitoring dynamic thermal behavior of the carbon anode in a lithium-ion cell using a four-probe technique. *J. Power Sources* **2012**, *198*, 351–358. [\[CrossRef\]](#)
9. Carkhuff, B.G.; Demirev, P.A.; Srinivasan, R. Impedance-Based Battery Management System for Safety Monitoring of Lithium-Ion Batteries. *IEEE Trans. Ind. Electron.* **2018**, *65*, 6497–6504. [\[CrossRef\]](#)
10. Srinivasan, R.; Carkhuff, B.G.; Butler, M.H.; Baisden, A.C. Instantaneous measurement of the internal temperature in lithium-ion rechargeable cells. *Electrochim. Acta* **2011**, *56*, 6198–6204. [\[CrossRef\]](#)
11. Schmidt, J.P.; Arnold, S.; Loges, A.; Werner, D.; Wetzel, T.; Ivers-Tiffée, E. Measurement of the internal cell temperature via impedance: Evaluation and application of a new method. *J. Power Sources* **2013**, *243*, 110–117. [\[CrossRef\]](#)
12. Rajmakers, L.; Danilov, D.L.; van Lammeren, J.; Lammers, M.; Notten, P. Sensorless battery temperature measurements based on electrochemical impedance spectroscopy. *J. Power Sources* **2014**, *247*, 539–544. [\[CrossRef\]](#)
13. Beelen, H.; Rajmakers, L.; Donkers, M.; Notten, P.; Bergveld, H.J. An Improved Impedance-Based Temperature Estimation Method for Li-ion. *IFAC-PapersOnLine* **2015**, *48*, 383–388. [\[CrossRef\]](#)
14. Spinner, N.S.; Love, C.T.; Rose-Pehrsson, S.L.; Tuttle, S.G. Expanding the Operational Limits of the Single-Point Impedance Diagnostic for Internal Temperature Monitoring of Lithium-ion Batteries. *Electrochim. Acta* **2015**, *174*, 488–493. [\[CrossRef\]](#)
15. Sun, J.; Wei, G.; Pei, L.; Lu, R.; Song, K.; Wu, C.; Zhu, C. Online Internal Temperature Estimation for Lithium-Ion Batteries Based on Kalman Filter. *Energies* **2015**, *8*, 4400–4415. [\[CrossRef\]](#)
16. Zhu, J.G.; Sun, Z.C.; Wei, X.Z.; Dai, H.F. A new lithium-ion battery internal temperature on-line estimate method based on electrochemical impedance spectroscopy measurement. *J. Power Sources* **2015**, *274*, 990–1004. [\[CrossRef\]](#)
17. Zhu, J.; Sun, Z.; Wei, X.; Dai, H. Battery Internal Temperature Estimation for LiFePO₄ Battery Based on Impedance Phase Shift under Operating Conditions. *Energies* **2017**, *10*, 60. [\[CrossRef\]](#)
18. Srinivasan, R.; Demirev, P.A.; Carkhuff, B.G. Rapid monitoring of impedance phase shifts in lithium-ion batteries for hazard prevention. *J. Power Sources* **2018**, *405*, 30–36. [\[CrossRef\]](#)
19. Wang, L.; Lu, D.; Song, M.; Zhao, X.; Li, G. Instantaneous estimation of internal temperature in lithium-ion battery by impedance measurement. *Int. J. Energy Res.* **2020**, *44*, 3082–3097. [\[CrossRef\]](#)
20. Rajmakers, L.H.J.; Danilov, D.L.; van Lammeren, J.P.M.; Lammers, T.J.G.; Bergveld, H.J.; Notten, P.H.L. Non-Zero Intercept Frequency: An Accurate Method to Determine the Integral Temperature of Li-Ion Batteries. *IEEE Trans. Ind. Electron.* **2016**, *63*, 3168–3178. [\[CrossRef\]](#)
21. Haussmann, P.; Melbert, J. Internal Cell Temperature Measurement and Thermal Modeling of Lithium Ion Cells for Automotive Applications by Means of Electrochemical Impedance Spectroscopy. *SAE Int. J. Altern. Powertrains* **2017**, *6*, 261–270. [\[CrossRef\]](#)
22. Wang, X.; Wei, X.; Chen, Q.; Zhu, J.; Dai, H. Lithium-ion battery temperature on-line estimation based on fast impedance calculation. *J. Energy Storage* **2019**, *26*, 100952. [\[CrossRef\]](#)
23. Richardson, R.R.; Ireland, P.T.; Howey, D.A. Battery internal temperature estimation by combined impedance and surface temperature measurement. *J. Power Sources* **2014**, *265*, 254–261. [\[CrossRef\]](#)
24. Richardson, R.R.; Howey, D.A. Sensorless Battery Internal Temperature Estimation Using a Kalman Filter With Impedance Measurement. *IEEE Trans. Sustain. Energy* **2015**, *6*, 1190–1199. [\[CrossRef\]](#)
25. Xie, Y.; Li, W.; Hu, X.; Lin, X.; Zhang, Y.; Dan, D.; Feng, F.; Liu, B.; Li, K. An Enhanced Online Temperature Estimation for Lithium-Ion Batteries. *IEEE Trans. Transp. Electrification* **2020**, *6*, 375–390. [\[CrossRef\]](#)
26. Forgez, C.; Vinh Do, D.; Friedrich, G.; Morcrette, M.; Delacourt, C. Thermal modeling of a cylindrical LiFePO₄/graphite lithium-ion battery. *J. Power Sources* **2010**, *195*, 2961–2968. doi: 10.1016/j.jpowsour.2009.10.105. [\[CrossRef\]](#)
27. Ludwig, S.; Zilberman, I.; Horsche, M.F.; Wohlers, T.; Jossen, A. Pulse resistance based online temperature estimation for lithium-ion cells. *J. Power Sources* **2021**, *490*, 229523. [\[CrossRef\]](#)
28. Ludwig, S.; Zilberman, I.; Oberbauer, A.; Rogge, M.; Fischer, M.; Rehm, M.; Jossen, A. Adaptive method for sensorless temperature estimation over the lifetime of lithium-ion batteries. *J. Power Sources* **2022**, *521*, 230864. [\[CrossRef\]](#)
29. Tranter, T.G.; Timms, R.; Shearing, P.R.; Brett, D.J.L. Communication—Prediction of Thermal Issues for Larger Format 4680 Cylindrical Cells and Their Mitigation with Enhanced Current Collection. *J. Electrochem. Soc.* **2020**, *167*, 160544. [\[CrossRef\]](#)
30. Tomaszewska, A.; Chu, Z.; Feng, X.; O’Kane, S.; Liu, X.; Chen, J.; Ji, C.; Endler, E.; Li, R.; Liu, L.; et al. Lithium-ion battery fast charging: A review. *eTransportation* **2019**, *1*, 100011. [\[CrossRef\]](#)
31. Steinhardt, M.; Gillich, E.I.; Rheinfeld, A.; Kraft, L.; Spielbauer, M.; Bohlen, O.; Jossen, A. Low-effort determination of heat capacity and thermal conductivity for cylindrical 18650 and 21700 lithium-ion cells. *J. Energy Storage* **2021**, *42*, 103065. [\[CrossRef\]](#)

32. Shenzhen Fest Technology Co., Ltd. Efest IMR 26650 5000mAh 40A Flat Top Battery. Available online: <https://www.efestpower.com/index.php?ac=article&at=read&did=448>. (accessed on 18 January 2022).
33. Popp, H.; Zhang, N.; Jahn, M.; Arrinda, M.; Ritz, S.; Faber, M.; Sauer, D.U.; Azais, P.; Cendoya, I. Ante-mortem analysis, electrical, thermal, and ageing testing of state-of-the-art cylindrical lithium-ion cells. *e & i Elektrotechnik und Informationstechnik* **2020**, *137*, 169–176. [[CrossRef](#)]
34. Wei, Y.; Agelin-Chaab, M. Experimental investigation of a novel hybrid cooling method for lithium-ion batteries. *Appl. Therm. Eng.* **2018**, *136*, 375–387. [[CrossRef](#)]
35. Wei, Y.; Agelin-Chaab, M. Development and experimental analysis of a hybrid cooling concept for electric vehicle battery packs. *J. Energy Storage* **2019**, *25*, 100906. [[CrossRef](#)]
36. Gantenbein, S.; Weiss, M.; Ivers-Tiffée, E. Impedance based time-domain modeling of lithium-ion batteries: Part I. *J. Power Sources* **2018**, *379*, 317–327. [[CrossRef](#)]
37. Bernardi, D. A General Energy Balance for Battery Systems. *J. Electrochem. Soc.* **1985**, *132*, 5. doi: 10.1149/1.2113792. [[CrossRef](#)]
38. Illig, J.; Ender, M.; Chrobak, T.; Schmidt, J.P.; Klotz, D.; Ivers-Tiffée, E. Separation of Charge Transfer and Contact Resistance in LiFePO₄-Cathodes by Impedance Modeling. *J. Electrochem. Soc.* **2012**, *159*, A952–A960. [[CrossRef](#)]
39. Zhou, X.; Huang, J.; Pan, Z.; Ouyang, M. Impedance characterization of lithium-ion batteries aging under high-temperature cycling: Importance of electrolyte-phase diffusion. *J. Power Sources* **2019**, *426*, 216–222. [[CrossRef](#)]
40. Barai, A.; Uddin, K.; Widanage, W.D.; McGordon, A.; Jennings, P. A study of the influence of measurement timescale on internal resistance characterisation methodologies for lithium-ion cells. *Sci. Rep.* **2018**, *8*, 21. [[CrossRef](#)]
41. Song, J.Y.; Wang, Y.Y.; Wan, C.C. Conductivity Study of Porous Plasticized Polymer Electrolytes Based on Poly(vinylidene fluoride) A Comparison with Polypropylene Separators. *J. Electrochem. Soc.* **2000**, *147*, 3219. [[CrossRef](#)]
42. Suresh, P.; Shukla, A.K.; Munichandraiah, N. Temperature dependence studies of a.c. impedance of lithium-ion cells. *J. Appl. Electrochem.* **2002**, *32*, 267–273. [[CrossRef](#)]
43. Muto, S.; Tatsumi, K.; Kojima, Y.; Oka, H.; Kondo, H.; Horibuchi, K.; Ukyo, Y. Effect of Mg-doping on the degradation of LiNiO₂-based cathode materials by combined spectroscopic methods. *J. Power Sources* **2012**, *205*, 449–455. [[CrossRef](#)]
44. Schranzhofer, H.; Bugajski, J.; Santner, H.J.; Korepp, C.; Möller, K.C.; Besenhard, J.O.; Winter, M.; Sitte, W. Electrochemical impedance spectroscopy study of the SEI formation on graphite and metal electrodes. *J. Power Sources* **2006**, *153*, 391–395. [[CrossRef](#)]
45. Raju, N.S.; Bilgic, R.; Edwards, J.E.; Fleer, P.F. Methodology Review: Estimation of Population Validity and Cross-Validity, and the Use of Equal Weights in Prediction. *Appl. Psychol. Meas.* **1997**, *21*, 291–305. [[CrossRef](#)]
46. Fuller, T.F. Relaxation Phenomena in Lithium-Ion-Insertion Cells. *J. Electrochem. Soc.* **1994**, *141*, 982. [[CrossRef](#)]
47. Maleki, H.; Hallaj, S.A.; Selman, J.R.; Dinwiddie, R.B.; Wang, H. Thermal Properties of Lithium-Ion Battery and Components. *J. Electrochem. Soc.* **1999**, *146*, 947–954. [[CrossRef](#)]
48. Willenberg, L.; Dechent, P.; Fuchs, G.; Teuber, M.; Eckert, M.; Graff, M.; Kürten, N.; Sauer, D.U.; Figgemeier, E. The Development of Jelly Roll Deformation in 18650 Lithium-Ion Batteries at Low State of Charge. *J. Electrochem. Soc.* **2020**, *167*, 120502. [[CrossRef](#)]
49. Maleki, H.; Selman, J.; Dinwiddie, R.; Wang, H. High thermal conductivity negative electrode material for lithium-ion batteries. *J. Power Sources* **2001**, *94*, 26–35. [[CrossRef](#)]
50. Richter, F.; Kjelstrup, S.; Vie, P.J.; Burheim, O.S. Thermal conductivity and internal temperature profiles of Li-ion secondary batteries. *J. Power Sources* **2017**, *359*, 592–600. [[CrossRef](#)]

3.2 Relation between Average Cell Temperature, Temperature Gradients and Pulse Resistance

In Section 3.1, T_R closely matches the average jelly roll temperature. It was assumed that this is the case for relatively small internal temperature gradients ($\Delta T_R \leq 5.45 \text{ K}$) and that therefore the cell resistance and the derived temperature T_R correspond to the average temperature of the electrode area [238]. This relation has already been investigated in a few studies in the literature and is discussed in more detail in the following with respect to Section 3.1.

Troxler et al. [243] investigated a pouch cell with different internal temperature gradients, applied externally with Peltier elements perpendicular to the electrode stack. The average cell temperature T_{avg} remained constant at 15°C and the temperature gradient was increased from the isothermal state in 5 K steps up to a temperature spread of 40 K between -5°C and 35°C . Compared to the isothermal state, the EIS measurements of the cell exhibited progressively lower impedance, in terms of the charge transfer resistance, with imposed temperature gradients. The authors explained this behavior based on the assumption that the cell is a parallel connection of n internal single cells, like the stacked electrodes in Fig. 2.4b suggest, over which the temperature gradient extends linearly. The total resistance of the parallel connection R_p was then calculated with Eq. (3.3).

$$R_p = \left[\sum_{i=1}^n \frac{1}{R(T_i)} \right]^{-1} \quad (3.3)$$

Thus, the overall impedance behavior of the cell is dominated by the part that has the smallest resistance and is therefore the hottest.

Schmidt et al. [45] conducted a comparable study also investigating a pouch cell, which is study #3 in Tables 2.4 to 2.6. In this study, both the average cell temperature T_{avg} and the temperature gradients were varied, with temperature gradients ranging from 4 K at $T_{\text{avg}} = 28^\circ\text{C}$ to 20 K at $T_{\text{avg}} = 20^\circ\text{C}$. In contrast to [243], the impedance values measured under temperature gradients in [45] did not clearly tend to the higher temperature impedance values, but rather corresponded to the impedance behavior of T_{avg} under isothermal conditions. However, Schmidt et al. [45] did not consider the charge transfer resistance as in [243], but the characteristics of the real part of the impedance at 10.3 kHz, which they related to the impedance behavior of the electrolyte. In addition to a linear progression of the internal temperature gradient as in [243], the authors in [45] considered a constant internal progression and a progression that follows a third degree polynomial. The three progressions were based on different assumptions on the thermal conductivity properties within the cell. Using the same assumption for R_p as in [243], they calculated a corresponding parallel resistance with Eq. (3.3) for the three different internal temperature progressions. The calculated resistance values for R_p differed only slightly with a maximum deviation below 1%, whereby the assumption of a constant temperature progression matched the measurement results most accurately. They further argued that no hotspot within the cell can be detected with their method, due to the small differences to T_{avg} .

Richardson et al. [47] considered the internal temperature distribution of a 26650 cylindrical cell using EIS measurements and a 1D thermal model, which is study #5 in Tables 2.4 to 2.6. They continuously refined their approach in [229] (#8) and [231] (#14). In accordance with [243] and [45], they developed a model to reflect the influence of the temperature distribution in the cell on the impedance. Since the authors used cylindrical cells, as in this work, rather than pouch cells with individual electrode

stacks as in [243] and [45], they could not express the impedance using Eq. (3.3). Instead, they used a radially symmetric representation of the measured admittance Y , the inverse of the impedance, as a function of the temperature progression $T(r)$ over the radius r as in Eq. (3.4).

$$Y = 2\pi h \int_{r_i}^{r_o} r \cdot y(T(r)) dr \quad (3.4)$$

The part of the cell contributing to Y in Eq. (3.4) has an outermost radius r_o and height h , as shown in Fig. 3.2a. The production-related empty space in the core of the cell is taken into account with the lower integration limit r_i . The function y describes the volume-related admittance as a function of the temperature progression $T(r)$ in the cell and was modeled by a second degree polynomial. The polynomial was determined using the real part of the admittance at 215 Hz from EIS measurements at isothermal temperature conditions and normalized using the volume $V = (r_o^2 - r_i^2)\pi h$. In the Nyquist plot in [47], this frequency falls within the range of the processes of SEI and charge transfer, as shown in Fig. 2.7b. Using this approach, they were able to show that their method can be used to deduce the temperature distribution of the cell at internal temperature gradients from the admittance measured at isothermal temperature. For this purpose, they compared the internal temperature distribution determined from the admittance with the values of temperature sensors attached to the cell core ($\approx r_i$) and surface ($\approx r_o$). In their study, they investigated temperature gradients of at most 10 K at an average temperature T_{avg} of about 35 °C. They also pointed out in [229] that the temperature determined from the measured admittance can be seen as the volume average temperature. However, with the restriction that this is only valid for small temperature gradients. For larger temperature gradients, the measured impedance does not necessarily correspond to T_{avg} , since the relationship between temperature and impedance is non-linear [229].

The conclusion from all three studies [45; 47; 243] is that the temperature determined from the impedance does not necessarily correspond to the average temperature of the cell in the presence of temperature gradients. However, the exact relationship depends on the impedance feature, the temperature estimation method, and the temperature gradient as the following summary shows:

- In [243], measurements of the charge transfer resistance were considered at temperature gradients up to 40 K and the impedance was dominated by the hottest part of the cell.
- In [45], the impedance behavior of the electrolyte is considered using the real part at 10.3 kHz at temperature gradients up to 20 K. The study concluded that the temperature determined from the impedance most closely corresponds to the mean cell temperature.
- In [47], the real part of the admittance at 215 Hz in the SEI and charge transfer domain at a maximum internal temperature gradient of 10 K was considered. Here, as in [45], the measured impedance corresponds most closely to the average cell temperature and was additionally used to determine the temperature distribution in the cell, which was confirmed by measurement.

The result of [238] in Section 3.1 shows, in agreement with [47] and [45], that the resistance in the time domain is closest to the average cell temperature. In [238], relatively small temperature gradients with a maximum of 5.45 K occur compared to 40 K in [243], 20 K in [45], and 10 K in [47] and therefore the deviations from the average cell temperature are small as well. This is consistent to the expectation that for small temperature gradients, the influence of the non-linear relationship between temperature and impedance is small as well and therefore T_{avg} and the impedance related temperature match [229]. To confirm this, Eq. (3.4) is applied to the results obtained in [238] from Section 3.1. The function y for the volume-related admittance from [47] is adapted respectively to the estimation function Eq. (3.1),

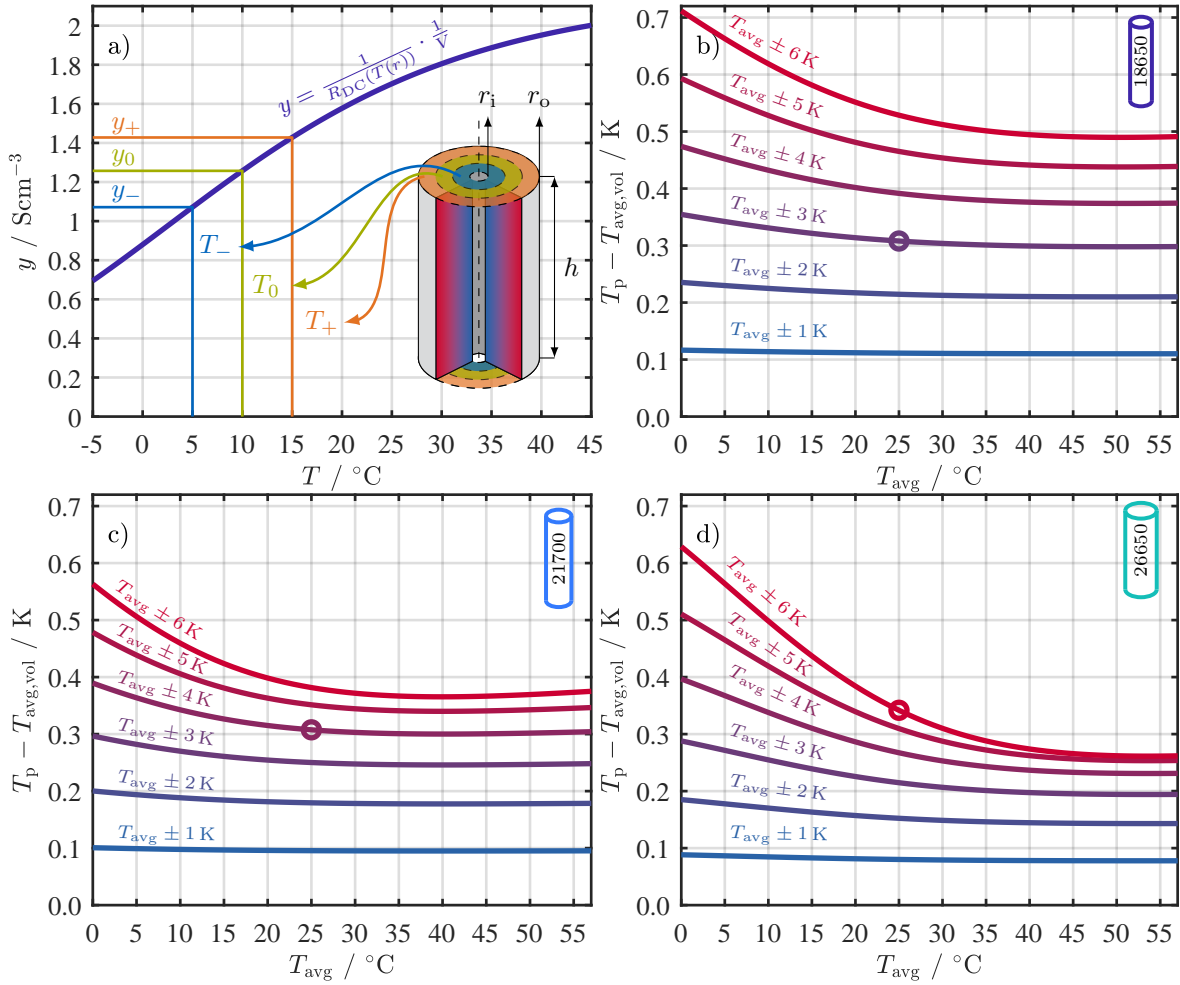


Figure 3.2: Results of the investigation on the relation of internal temperature gradients and the temperature determined by the resistance regarding the publication [238]. a) Example for the volume-related conductance of the 18650 cell at $SOC = 50\%$, the pulse type P_1 and $\Delta t = 100$ ms. Difference between the temperature T_p , determined with the volume-related conductance, and the volume average cell temperature $T_{avg,vol}$ for temperature gradients from ± 1 K to ± 6 K for b) the 18650, c) the 21700, and d) the 26650 cell. The circles mark the worst case scenario for the temperature gradients determined in [238].

resulting in a volume-related conductance in Eq. (3.5).

$$y(T(r)) = \frac{1}{R_{DC}(T(r))} \cdot \frac{1}{V} \quad (3.5)$$

The course of y is shown in Fig. 3.2a using the 18650 cell at 50% SOC , for $\Delta t = 100$ ms and the pulse type P_1 as example. Since it was shown in [45] that the progression of the temperature gradient has little influence on the impedance value, a linear temperature progression from r_i to r_o is assumed, which can be described with Eq. (3.6):

$$T(r) = \frac{T_o - T_i}{r_o - r_i}(r - r_i) + T_i \quad \forall r \in [r_i, r_o], \quad (3.6)$$

where T_o is the temperature at the outside of the jelly roll at the radius r_o and T_i is the temperature

at the inside of the jelly roll at the radius r_i . In combination with the linear temperature progression from Eq. (3.6), the volume average temperature of the cell is obtained according to Eq. (3.7):

$$\begin{aligned}
 T_{\text{avg,vol}} &= \frac{2\pi h}{V} \int_{r_i}^{r_o} r \cdot T(r) dr = \\
 &= \frac{1}{r_o^2 - r_i^2} \int_{r_i}^{r_o} r \cdot \left(\frac{T_o - T_i}{r_o - r_i} (r - r_i) + T_i \right) dr = \dots \\
 &= \frac{2}{3} \cdot \frac{(T_o - T_i) (r_o^3 - r_i^3)}{(r_o - r_i) (r_o^2 - r_i^2)} + T_i - \frac{T_o - T_i}{r_o - r_i} \cdot r_i
 \end{aligned} \tag{3.7}$$

As in [238], a gradient in the cell is investigated which arises during external heating. To denote the linear gradient from Eq. (3.6), its average value according to Eq. (3.8) and its spread to $T_{i/o}$ are used in the following.

$$T_{\text{avg}} = \frac{T_o + T_i}{2} \tag{3.8}$$

Figures 3.2b to 3.2d show the deviations between T_p and $T_{\text{avg,vol}}$ for all three cells from Table 3.1 with respect to T_{avg} from 0°C to 50°C and an internal temperature spread from ± 1 K to ± 6 K around T_{avg} . T_p is calculated using Eq. (3.4), Eq. (3.5), and Eq. (3.2). For this purpose, the cell is quantized into radially symmetric domains, each spanning a temperature range of 0.1 K. For each domain, the volume-related conductance is calculated with Eq. (3.5) and integrated with Eq. (3.4). With the inverse $R_p = \frac{1}{G_p}$ taken from the integration result, the temperature T_p can finally be calculated with Eq. (3.2). The procedure is indicated as a simplified example using the three quantization ranges T_- , T_0 , and T_+ in Fig. 3.2a. The temperature T_p in Figs. 3.2b to 3.2d is larger for each cell than the volume average temperature $T_{\text{avg,vol}}$ and thus tends to represent the warmer part of the cell. The deviation between T_p and $T_{\text{avg,vol}}$ decreases slightly with increasing T_{avg} , which can be attributed to the flattening of y in Fig. 3.2a with increasing temperature. In absolute terms, the deviation from $T_{\text{avg,vol}}$ also increases with increasing gradients. In the investigation in Section 3.1, the maximum deviation between the measured cell surface temperature and the temperature T_R determined from the resistance arises at a surface temperature of about 25°C. The difference ranges between approximately 3 K for the 18650 cell, 4 K for the 21700 cell, and 6 K for the 26650 cell. As a worst case approximation these differences can be used as the spread around the average temperature T_{avg} in Figs. 3.2b to 3.2d. With this assumption, the deviation between T_p and $T_{\text{avg,vol}}$ is still less than 0.4 K. The corresponding points are marked with a circle in Figs. 3.2b to 3.2d. In Fig. 5 in [238] showing the comparison with the thermal model, this limit is never exceeded, but rather T_R tends to remain below $T_{\text{avg,vol}}$. At this point it must be mentioned that the thermal model cannot be seen as an absolute reference, as already discussed in [238].

4 Sensorless Online Pulse Resistance Temperature Estimation - Method Development

Chapter 4 extends the R_{DC} approach for temperature estimation from Chapter 3 and focuses on the topic of the applicability of the R_{DC} as a means of sensorless temperature estimation in a BMS during regular operation of a battery system. The scope of Chapter 4 is once more highlighted in Fig. 4.1 as content guidance. The thematic priorities were to scale the method from cell to module, focus on temperature gradients in the module, extend the pulse analysis from predefined pulses to actual load profiles, and to implement and validate a temperature estimation method.

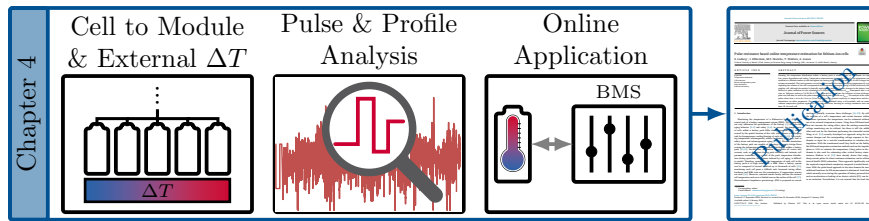


Figure 4.1: Scope of Chapter 4.

The results of the study were published in the research article *Pulse resistance based online temperature estimation for lithium-ion cells* [244]. The study is divided into two parts. The first part aims to determine the dependencies of the R_{DC} on various influencing parameters and to develop a method for determining the temperature of individual cells using the R_{DC} . The same 18650 cell type as in Table 3.1 was investigated. The objective of the first part was to design a methodology that is easy to integrate into a BMS and is as independent as possible from all influencing parameters apart from temperature. The procedure used to achieve the goal of the first part is illustrated in the flow chart in Fig. 4.2. In addition to the dependence on temperature and SOC, the influence of the following parameters on the R_{DC} as shown in Fig. 4.2a were investigated on cell level: pulse direction, pulse amplitude, pulse shape, and pulse on/off. To describe the resistance behavior for pulses that change from an idle state ($I = 0$) to a state under load ($I \neq 0$), the term “pulse on” was used and for the opposite situation “pulse off”. The pulse shape was varied by changing the pulse rise/fall time ($t_{r/f}$). For all parameters, the R_{DC} was calculated according to Eq. (2.30), also depicted in Fig. 4.2b, and analyzed for different periods (Δt) reaching from 1 ms to 10s after the current change. The initial analysis showed that the R_{DC} in the investigated calculation periods is always SOC dependent. Based on these results, a SOC dependent reference is needed to estimate the temperature. This R_{DC} reference consists of an 8th degree polynomial that is dependent on the SOC and is individually parametrized for each temperature considered in the study, as shown in Fig. 4.2c. The polynomial reference was parametrized systematically with different R_{DC} parametrization sets over the considered calculation periods, whereby one set consists of R_{DC} s filtered according to one or more influencing parameters. An exponential temperature estimation function similar to study #16 [233] and study #20 [54] in Table 2.4 was used to estimate the temperature. The estimation function based on the modified Arrhenius law,

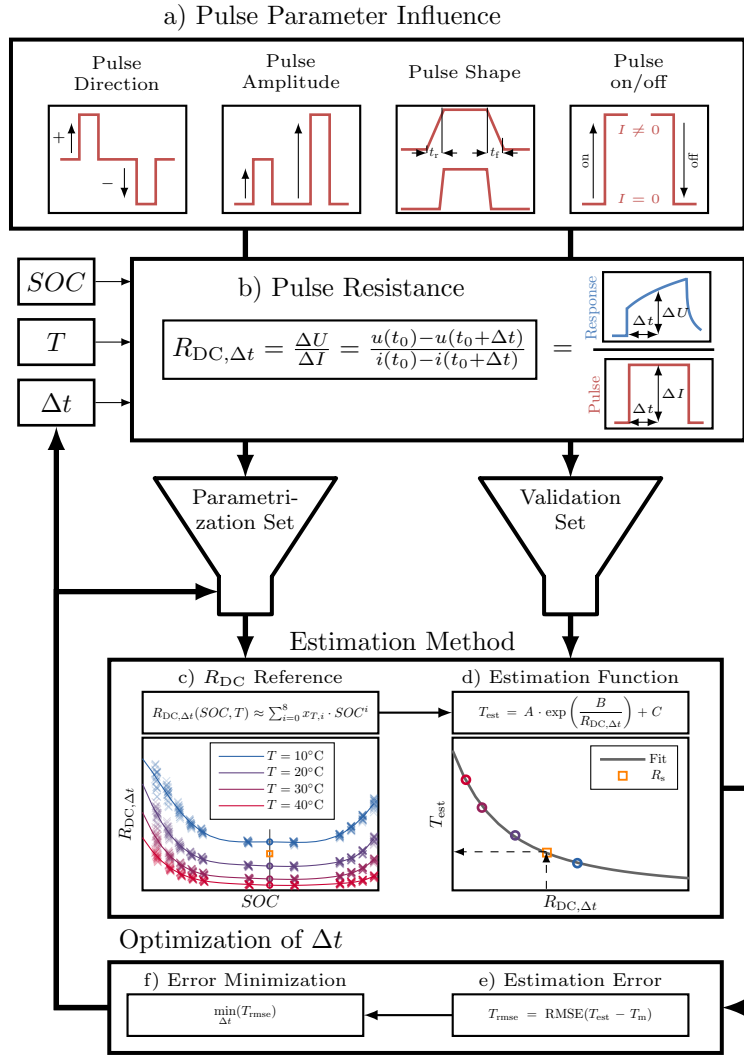


Figure 4.2: Flowchart showing the development process for the temperature estimation method in [244]. From top to bottom: a) investigated pulse parameters; b) R_{DC} resistance calculation and other influence factors; followed by filters for method parametrization and validation; estimation method with examples for c) R_{DC} reference and d) estimation function; and finally the optimization of Δt with e) the calculation of the estimation error and f) the minimization of the estimation error. Adapted from [245].

as in Eq. (3.2) from Chapter 3, was not applied, since mathematical problems could cause issues in a BMS at elevated temperatures. On the one hand there is the danger that at the calculated R_{DC} becomes equal to R_0 and thus the difference in Eq. (3.2) results in zero and falls into the definition gap of the logarithm. On the other hand, the case $R_1 = R_{DC} - R_0$ could occur, which would lead to a division by zero in Eq. (3.2).

The temperature estimation is illustrated using the example value R_s in Fig. 4.2d and the following three steps. In the first step, the SOC at which R_s was calculated serves as input for the polynomial reference in Fig. 4.2c. In the second step, the resulting R_{DC} values from the reference are used to fit the temperature estimation function in Fig. 4.2d. In the third step, R_s is inserted in the temperature estimation function to get the estimated temperature (T_{est}).

Finally, part one of the study culminated in the optimization of the temperature estimation over the

calculation period (Δt). For this purpose, the estimation error, in form of the **RMSE** as shown in Fig. 4.2e, was calculated according to Eq. (2.39) for different R_{DC} validation sets. The R_{DC} validation sets included the original parametrization set and other R_{DC} sets different to the original parametrization set with unknown parameters such as an unknown current amplitude. Finally, the error for each validation set was minimized using the equation in Fig. 4.2f. It became evident that for an accurate temperature estimation, a large congruence between parametrization and validation set is essential. The optimum of the calculation period (Δt) can be found in a plateau from approximately 10 ms to several 100 ms, where the **RMSE** has its minimum and the pulse parameter influence is negligibly small. To avoid an increased influence of the **pulse rise/fall time** ($t_{r/f}$), the calculation period Δt has to be larger than $t_{r/f}$.

The second part of the study focuses on the transferability of the first part to the module level and the application of the developed method to realistic driving profiles. For this purpose, a module of six serially connected 18650 cells of the same type as used in the first part of the study was set up. These cells were not exactly the same cells as in the first part of the study to evaluate cell-to-cell transferability of the method. In order to generate a temperature difference between the cells of the module, the cells were embedded in copper blocks, which were connected with a copper rail. A constant external temperature gradient ΔT of 5 K between 25 °C and 30 °C was enforced on the module with the help of two Peltier elements at the ends of the copper rail. This setup simulated a possible temperature inhomogeneity that could occur in a battery pack. The method was finally validated by discharging the module with a concatenated series of different driving profiles. Due to the swapped cells and the continuous current change of the driving profiles compared to the single pulses in the first part of the study, two adjustments were necessary to realize the method at module level:

1. The intrinsic cell differences were compensated by an offset correction of the R_{DC} reference.
2. Before calculating a R_{DC} value, each current change in the driving profile passed through a multi-stage filter in order to exclude pulses that deviate too much from the pulses investigated in the first part of the study.

With all adjustments in place, the validation of the developed method with the driving profiles resulted in a **RMSE** of 0.59 K to 0.93 K and 0.96 K to 1.11 K respectively, depending on the settings of the multi-stage filter. Compared to the validation results for the state of the art methods from Table 2.6, the **RMSEs** are in the range of the average **RMSE** of 0.858 K and are thus competitive with the existing methods in the literature.

Authors Contribution

Max F. Horsche initially developed the idea for using the R_{DC} , calculated from load changes, for general state estimation of **LIBs**. Sebastian Ludwig took up this idea and transferred it to develop the methodology for temperature estimation, with the support of Ilya Zilberman. The study was designed and executed by Sebastian Ludwig with the help of Tim Wohlers, who was involved in the preliminary tests. The manuscript was written by Sebastian Ludwig. Andreas Jossen supervised the work. All authors discussed the data and commented on the results.

Pulse resistance based online temperature estimation for lithium-ion cells

Ludwig S., Zilberman I., Horsche M.F., Wohlers T., Jossen A.

Journal of Power Sources 490, 229523, 2020

Permanent web link:

<https://doi.org/10.1016/j.jpowsour.2021.229523>



This article is available under the Creative Commons CC-BY-NC-ND license (<https://creativecommons.org/licenses/by-nc-nd/4.0/>) and permits non-commercial use of the work as published, without adaptation or alteration provided the work is fully attributed.



Contents lists available at ScienceDirect

Journal of Power Sources

journal homepage: www.elsevier.com/locate/jpowsour

Pulse resistance based online temperature estimation for lithium-ion cells

S. Ludwig*, I. Zilberman, M.F. Horsche, T. Wohlers, A. Jossen

Technical University of Munich (TUM), Institute for Electrical Energy Storage Technology (EES), Arcisstrasse 21, 80333 Munich, Germany

ARTICLE INFO

Keywords:

Temperature estimation
Cell resistance
Battery management system
State estimation
Lithium-ion battery

ABSTRACT

Knowing the temperature distribution within a battery pack is vital, because of the impact on capacity loss, power degradation and safety. Temperature measurements are usually realized with temperature sensors attached to a limited number of cells throughout the battery pack, leaving the majority of cells in larger battery systems unattended. This work presents a novel sensorless method for determining the temperature of a cell by exploiting the relation of the cell's overpotential and temperature exemplary using a 18650 nickel-rich/silicon-graphite cell, although the method is basically applicable to any cell. Current changes in the battery load are utilized as pulse excitation for the calculation of a direct-current resistance $R_{DC,\Delta t}$ determined after a certain time Δt . Reference pulses at 10/20/30/40 °C are recorded to investigate the influence of state-of-charge and pulse rise/fall-time, as well as the pulse-current amplitude and direction on $R_{DC,\Delta t}$. The analysis of the reference pulses shows that a Δt in the 10 ms to 100 ms regime has the greatest sensitivity to temperature and the least dependence on other parameters. The method is finally validated using a 6S1p-module with an externally constant temperature gradient applied to the serial connection, showing an average estimation error smaller than 1 K for each cell.

1. Introduction

Monitoring the temperature of a lithium-ion battery (LIB) is a crucial task of a battery management system (BMS). The temperature not only influences the performance of the battery [1], but also the aging behavior [2–4] and safety [5,6]. In general, the temperatures of cells within a battery pack differ during operation [7,8], simply caused by the spatial location of the cells, which poses a challenging task for homogeneous cooling/heating of each cell [9,10]. The resulting temperature inhomogeneity within the battery pack may lead to safety issues and inhomogeneous aging [11,12]. Thermal simulations of the battery pack are capable of detecting systematic design flaws causing the inhomogeneous temperature distribution within a battery pack [13,14]. Nevertheless, simulations cannot take all events into account, such as deviations during pack assembly and intrinsic cell parameter variations. Also a shift of the pack temperature distribution during operation, for instance induced by cell aging, is difficult to model. Therefore, monitoring the temperature of each cell in the battery pack is of high interest for a BMS. Since a battery system can be composed of several hundred up to thousands of cells [15], monitoring each cell poses a difficult task. Increased wiring effort, hardware and BMS costs are the consequence, if temperature sensors are used [16]. Moreover, external sensors barely indicate the internal cell temperature and cover a limited area on the surface of the cell [17]. Electrochemical impedance spectroscopy (EIS) is proposed in several

studies to partially overcome these challenges [16–23]. By utilizing the relation of a cell's temperature and certain features within the impedance spectrum, the temperature can be estimated without the use of an external temperature sensor. Using these EIS-based methods does not increase the wiring effort, since the existing connections for voltage monitoring can be utilized, but there is still the additional effort and cost for the hardware performing the sinusoidal excitation. Wang et al. [24] recently developed an approach using the instant current changes and the corresponding voltage response in the time domain as input for a wavelet transformation to calculate the cell impedance. With the transformed result they build on the findings of the EIS-based temperature estimation methods and use the impedance's phase at 10 Hz to estimate the temperature. Using pulses in the time domain is also used for estimating other critical battery states. For instance, Mathew et al. [25] have already shown that using only sharp current pulses for direct resistance estimation can be utilized for state-of-health (SOH) estimation. Their approach significantly reduces the required computational complexity compared to model-based solutions. With the pulse-based approach in the time domain the need for additional hardware for EIS measurements is eliminated. Load changes, which naturally occur during the operation of battery powered devices, such as acceleration or braking of an electric vehicle (EV), can be used as an excitation. Nevertheless, it is not ensured that the load changes

* Corresponding author.

E-mail address: sebastian.ludwig@tum.de (S. Ludwig).<https://doi.org/10.1016/j.jpowsour.2021.229523>

Received 17 September 2020; Received in revised form 24 November 2020; Accepted 13 January 2021

Available online 1 February 2021

0378-7753/© 2021 The Authors.

Published by Elsevier B.V. This is an open access article under the CC BY-NC-ND license

<http://creativecommons.org/licenses/by-nc-nd/4.0/>

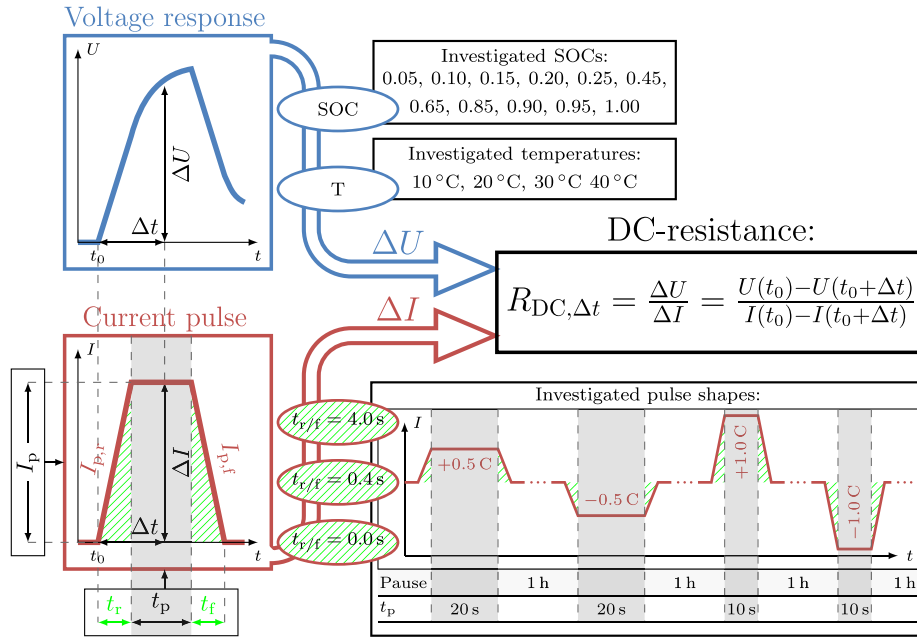


Fig. 1. Investigated SOC, temperatures and pulse parameters.

in an application are perfectly pulse shaped. Therefore, this study has the goals to (i) find the criteria the pulses have to meet to be suitable for temperature estimation and (ii) develop a sensorless temperature estimation method in the time domain. The method only requires the generally monitored parameters, current and voltage, to calculate a direct current (DC) resistance $R_{DC,\Delta t} = \frac{\Delta U}{\Delta I}$ for a certain resistance-calculation-period Δt after a current change (pulse). The focus lies on a simple time domain based approach without the need for additional excitation hardware or a complex transformation from the time domain to the frequency domain, which is online applicable in a BMS.

The work is structured as follows. In the first step, different load changes, including rectangular and non-rectangular pulses, are experimentally evaluated at different temperatures and state-of-charge (SOCs). The relation of the resistance $R_{DC,\Delta t}$ and temperature is analyzed in terms of resistance-calculation-period Δt , the pulse parameters and the SOC. In the next step, the results of the analysis are incorporated in the parametrization of a temperature estimation function $T_{est} = f(R_{DC,\Delta t})$ and the search for the optimal resistance-calculation-period. Finally, the online applicability of the method is validated with a representative battery module of six serial connected cells.

2. Experimental

This chapter describes the investigated cell and the conducted experiments for the pulse parameter analysis and the method validation.

2.1. Investigated cell

The developed method aims at applications with changing load currents, such as EVs. The trend for EVs points to batteries with higher energy density and capacity. Nickel-rich lithium-ion cells are a recent chemistry to fulfill this demand, although they show a poor interfacial stability [26]. Silicon as an anode material or as an additive to a conventional graphite anode is also a recent development [27,28]. For this reason, a commercial nickel-rich NMC/SiC high-energy 18650 lithium-ion cell (INR18650-MJ1) from LG Chem with a nominal capacity of 3.5 Ah is the objective of the study. For a detailed chemistry description of this cell the authors refer to [12,29-31].

Table 1

Parameter overview with expectation (μ) and standard deviation (σ) of the cells used for the pulse parameter analysis at 25 °C. The capacity C_{act} was measured according to the manufacturer's standard CC discharge procedure with $I_{CC} = -0.2C$ from 4.2 V to 2.5 V followed by a CV stage with a cut-off current of $I_{CV} > -50$ mA. The resistance was determined at 50% SOC with a discharge current pulse of 1.0C. According to Sturm et al. [29] the composition of the active material of the cathode amounts to 82% nickel, 6.3% manganese and 11.7% cobalt. The proportion of silicon in the anode amounts to 3.5 wt%.

Parameter	Cell			μ	σ
	C_1	C_2	C_3		
C_{act} / Ah	3.389	3.421	3.407	3.406	0.016
$R_{DC,10s} / \text{m}\Omega$	45.3	44.2	45.0	44.7	0.569

2.2. Pulse experiment

The three selected cells for the pulse parameter analysis are listed in Table 1. Besides the temperature, several pulse parameters influence the voltage response, and thereby the resistive behavior of a cell. To investigate the influence of the pulse parameters and the temperature, an experiment with different pulses was conducted. Fig. 1 depicts the investigated influence factors on the DC-resistance $R_{DC,\Delta t}$. The influence of SOC and temperature on the voltage response was investigated by performing current pulses at eleven SOC steps and for four temperatures. To cover a large variety of possible load changes in an application, the shape of the current pulses was altered according to the pattern in Fig. 1. The pattern varied the pulse amplitude I_p , current direction and pulse duration t_p , and was performed at each SOC and temperature point. To investigate the influence of (non)-rectangular pulses, the pulse pattern was repeated for three different rise/fall-times $t_{r/f}$. The rise/fall-time refers to the individual pulse edges. To distinguish DC-resistances calculated on the rising edge and the falling edge of the pulse, the corresponding pulses are named $I_{p,r}$ for rising and $I_{p,f}$ for falling edges.

The details of the test sequence for the pulse parameter experiment are documented in Table 2. The sequence started with a 3 h pause to

Table 2

Test procedure for generating pulses with different parameters. Steps #1–3 were measured with a BaSyTec CTS. Steps #4–18 were measured with a BioLogic VMP3 with 5 A Booster. Temperatures were set with a Binder KT 115 climatic chamber with a maximal temperature fluctuation of ± 0.1 K.

#	Step	Parameter	Termination
for $T_{\text{exp}} = 10/20/30/40^\circ\text{C}$			
1	Pause	$T = 25^\circ\text{C}$	$t > 3$ h
2	Charge (CC)	$I = +0.5$ C	$U > 4.2$ V
3	Charge (CV)	$U = 4.2$ V	$I < +50$ mA
4	Pause	$T = T_{\text{exp}}$	$t > 3$ h
for $\text{SOC}_{\text{exp}} = 0.95/0.90/0.85/0.65/0.45/0.25/0.20/0.15/0.10/0.05$			
for $t_{\text{r/f}}^a = 0.0/0.4/4.0$ s			
5	Charge pulse	$I_p = +0.5$ C, $t_{\text{r/f}}$	$t_p > 20$ s
6	Pause		$t > 1$ h
7	Discharge pulse	$I_p = -0.5$ C, $t_{\text{r/f}}$	$t_p > 20$ s
8	Pause		$t > 1$ h
9	Charge pulse	$I_p = +1.0$ C, $t_{\text{r/f}}$	$t_p > 10$ s
10	Pause		$t > 1$ h
11	Discharge pulse	$I_p = -1.0$ C, $t_{\text{r/f}}$	$t_p > 10$ s
12	Pause		$t > 1$ h
end			
13	Discharge (CC)	$I = -0.2$ C	$\text{SOC} = \text{SOC}_{\text{exp}}$
14	Pause		$\frac{dU}{dt} < 5$ mV h ⁻¹
end			
15	Discharge (CC)	$I = -0.2$ C	$U < 2.5$ V
16	Discharge (CV)	$U = 2.5$ V	$I > -50$ mA
end			

^aAlthough the test device's minimal rise/fall-time for current changes is 40 μ s, the "instant" current changes are denoted with $t_{\text{r/f}} = 0.0$ s.

acclimatize the cells to the reference temperature of 25 °C. The cell was then fully charged by a constant-current (CC) charge according to the manufacturer's specifications followed by a constant-voltage (CV) phase. A period of 3 h of acclimatization at the corresponding experiment temperature T_{exp} is followed by a sequence of four pulses charging/discharging the cells according to Step #5 to #12. The selected pulse duration avoided larger SOC or temperature changes and the absolute charge-throughput of the pulses was equal. The pause of 1 h in between the pulses resulted in a voltage drift of less than ± 2 mV h⁻¹ before the subsequent pulse, which is sufficient enough to assume that the relaxation processes are almost completed and the pulses start from an equilibrated state. The sequence of four pulses from Step #5 to #12 was repeated for three different pulse rise/fall-times $t_{\text{r/f}} = 0.0$ s, 0.4 s and 4.0 s. Subsequently, the SOC was adjusted according to Step #13. Since the voltage relaxation after Step #13 differs with temperature and SOC and may affect the result of the pulses [32,33], the following pause in Step #14 ended after the cell voltage change per hour was less than 5 mV h⁻¹. The pause was followed by the pulse pattern for the next SOC. Since the charge transfer resistance and diffusion resistance increases at the periphery of the SOC range [34,35], finer SOC steps were used towards the limits.

2.3. Validation experiment

To validate the temperature estimation method, a 6s1p-module of the same cell type was used. However, the cells of the module were not the same as the ones for the pulse parameter analysis. There were two reasons for this: (i) only three cells were used in the pulse parameter analysis and six were needed for the validation experiment; (ii) by using six different cells for the validation experiment the transferability of the method within the same cell type is demonstrated. The initial parameters of the six module cells (C_4 to C_9) are listed in Table 3. The module setup is shown in Fig. 2a and ensured different temperatures for each cell in the module but minimized a possible temperature gradient within the cylindrical cells [36]. Thereby, the comparison of the estimated temperature and the external reference temperature sensor

Table 3

Parameter overview with expectation (μ) and standard deviation (σ) of the cells used for the validation experiment at 25 °C. The cells were the same as in [12]. The capacity C_{act} was measured according to the manufacturer's standard CC discharge procedure with $I_{\text{CC}} = -0.2$ C from 4.2 V to 2.5 V followed by a CV stage with a cut-off current of $I_{\text{CV}} > -50$ mA. The resistance was measured at 50 % SOC with a discharge current of 1.0 C.

Parameter	Cell						μ	σ
	C_4	C_5	C_6	C_7	C_8	C_9		
C_{act}/Ah	3.461	3.469	3.461	3.47	3.462	3.463	3.464	0.004
$R_{\text{DC},10\text{s}}/\text{m}\Omega$	42.3	42.7	42.3	43.0	42.4	42.0	42.45	0.3507

was not distorted by cell internal temperature deviations. To achieve this, the cells of the module were wrapped in high thermal conductivity foil and enclosed in copper blocks to ensure thermal contact via heat conduction. The copper blocks with the embedded cell were screwed to a common copper rail with a Peltier element at each end of the rail. To ensure a minimal thermal transfer resistance between the copper rail and block, the contact area was lubricated with thermal grease. By setting the Peltier elements to different temperatures, a temperature gradient ΔT developed over the module. For more information about the module setup and cells, the authors refer to [12].

The validation scenario applied the current-profiles of 14 concatenated drive cycles of the 149 drive cycles presented by Campestrini et al. [37] to the 6s1p-module. With the variety of drive cycles, the method was tested for all kinds of EV application scenarios. Fig. 2b shows the resulting module current for the 14 drive cycles. While applying the drive cycles, a temperature gradient of $\Delta T = 5^\circ\text{C}$ from 25 °C to 30 °C was enforced on the module. Fig. 2c shows the sensor-offset corrected cell temperatures during the drive cycles. The offset calibration for all temperature sensors was performed at 25 °C. All six cells kept an almost constant temperature during the drive cycles with a maximal average deviation of ± 0.086 K from the mean cell temperature.

3. Results and discussion

The first part of this chapter discusses the influence of temperature, SOC and the pulse parameters on the $R_{\text{DC},\Delta t}$ by analyzing the results from the pulse experiment of Section 2.2. Subsequently, a temperature estimation method is proposed and benchmarked against the experimental pulse data. Lastly, the results of the estimation method are presented and validated with the module and driving profiles depicted in Fig. 2.

3.1. Parameter influence

The goal of this section is to narrow down the resistance-calculation-period Δt , in which the estimation method is the most resilient against any parameter variation.

Fig. 3 is utilized to interpret all investigated parameters (temperature, SOC and pulse shape) from the pulse experiment in Section 2.2. Each row of Fig. 3 depicts the influence on $R_{\text{DC},\Delta t}$ for a specific pulse parameter and Δt over the SOC for all four experimental temperatures. The three investigated cells from Table 1 feature an almost equal curve shape, only differing in an resistance offset between the curves of the individual cells. For this reason, the curves depicted in Section 2.2 represent the average $R_{\text{DC},\Delta t}$ of the three cells from Table 1 for a specific pulse parameter and Δt . The averaged DC-resistance values are scaled, allowing an easier comparison between the different time scales.

3.1.1. Temperature and SOC influence

This section focuses on the general temperature and SOC sensitivity of Fig. 3. The temperature has a major influence on the properties and processes of a lithium-ion cell. Be it the ionic/electronic conductivity of a cell's materials [38–40] or the electrochemical processes within the

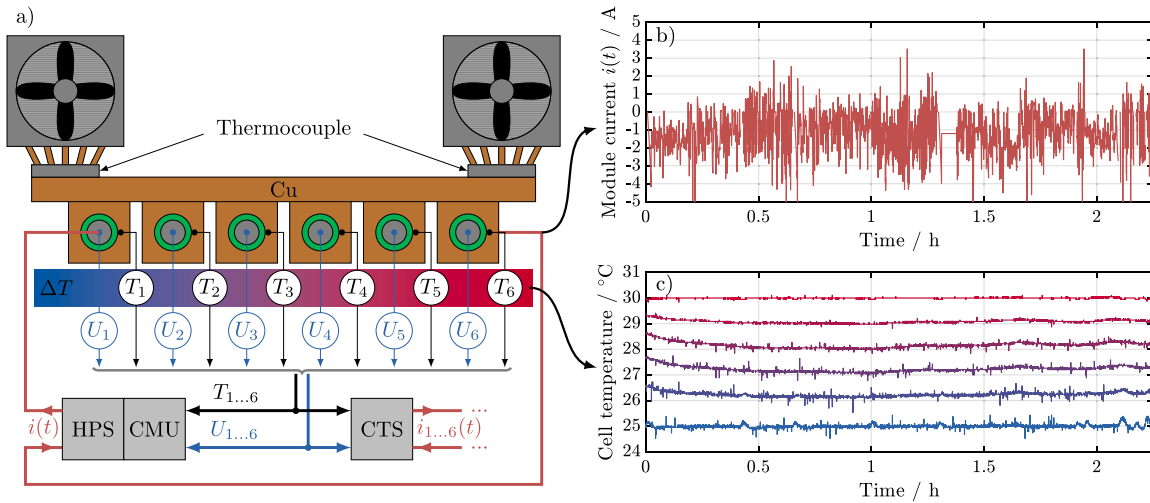


Fig. 2. Overview of the test setup for the 6s1p-module used for method validation (a) [12]. On the module level, a High-Power-System (HPS) was used to drive the module current $i(t)$. The temperature as well as the cell voltage was monitored with a Cell-Measurement-Unit (CMU). For cell level cycling and monitoring, each cell was connected to a Cell-Testing-System (CTS). To control the temperature gradient and measure the cell temperatures, PT100 temperature sensors were used. The temperature sensors for the cells were integrated in the copper blocks and mounted on the surface of each cell. Six clipboards connected the positive and negative tabs of each cell with gold contact pins in a 4-wire connection to a configuration plug, allowing measurements on the cell level as well as module level. BaSyTec measurement equipment accuracy as follows: HPS: precision of 0.05%; CMU voltage measurement: resolution of 0.2 mV and accuracy of 2.5 mV; CMU temperature measurement: precision of 1 °C and resolution of <0.1 °C; CTS: accuracy of ± 0.3 mV and ± 0.5 μ A in the smallest range for the voltage and current measurement. Applied module current $i(t)$ scaled to the limits of the cell (maximal charge current of 3.5 A) and the HPS (maximal current 5 A) (b), and corresponding cell temperatures T_1 to T_6 (c).

cell [41,42], all are affected by temperature and ultimately affect the $R_{DC,\Delta t}$. Depending on the resistance-calculation-period Δt , the voltage response ΔU is influenced by different processes, represented by three resistance-calculation-periods in Fig. 3a to Fig. 3f. The resistance-calculation-periods in Fig. 3a to Fig. 3f were selected according to the time scales for dynamic processes in lithium-ion batteries according to [42–44].

In Fig. 3a and Fig. 3d the resistance-calculation-period is set to 1 ms representing the shortest time scale, still allowing a reasonable sampling rate for a BMS. In this time domain, the major contribution to the DC-resistance comes from the ohmic losses of the cell [42,43]. The temperature behavior of the ohmic part is caused by the limited electronic conductivity of the current collectors, the electrodes, the electrolyte ionic conductivity and the conduction properties of their interfaces [45,46]. Except for the current collectors, all other materials show an increasing conductivity with increasing temperature. However, taking the overall high electronic conductivity of the current collectors into account, the contribution to the potential drop ΔU and the electronic conductivity change over temperature is negligibly small [42,47]. The temperature behavior of the anode's materials of the investigated cell, graphite [48,49] and silicon [50], has a minor effect on the $R_{DC,\Delta t}$, because both materials show a minor conductivity increase with increasing temperature compared to the other materials. The cathode of the investigated cell is made of nickel-rich NMC, which has a relatively low ionic/electronic conductivity with high Arrhenius-like temperature dependence [39,40]. Therefore, the cathode is most likely one of the main contributors to the temperature behavior of the cell's ohmic resistance. The other main contributor to the ohmic resistance with major dependence on temperature is the electrolyte, also with an Arrhenius-like behavior [38,42,51,52]. Since $\Delta t = 1$ ms does not only include the instant voltage response related to the sole ohmic losses of a cell, the solid electrolyte interface (SEI) and the charge transfer reaction also contribute to the $R_{DC, 1 \text{ ms}}$. Both, the SEI and the charge transfer reaction, are temperature dependent and increase in impedance with decreasing temperatures [17,21,35,41,42,52–54]. Besides the temperature influence, the dependence on SOC is apparent, especially at the periphery of the SOC range.

By increasing Δt to 10 ms in Fig. 3b and Fig. 3e, the contribution of the charge transfer reaction at both electrodes increases and its SOC dependence becomes even more apparent. In general, the charge transfer resistance can be described with an Arrhenius-like exponential dependency on temperature [42,52,55]. As a result, the distance between the curves of the different temperatures in Fig. 3b and Fig. 3e is more distinct compared to Fig. 3a and Fig. 3c, and the sensitivity of the DC-resistance for temperature changes is increased.

Fig. 3c and Fig. 3f depict the DC-resistance for $\Delta t = 1000$ ms. In this time domain the charge transfer reactions are completely included in the impedance with a partial contribution of the diffusion-driven processes. At the SOC extremes and lower temperatures, the charge transfer reaction has a dominant contribution to the resistance of the cell. Here, the electrodes are almost fully lithiated/delithiated and the intercalation/deintercalation is aggravated. Additionally, the increased resistance at lower temperatures is related to the slower diffusion of the lithium-ions within the electrodes [1,23,56,57].

Looking at the temperature and SOC behavior of the DC-resistance in all three representative time domains of Fig. 3a to Fig. 3f, the following two facts can be concluded:

1. The temperature behavior of the DC-resistance shows a non-linear behavior. It is assumed to be mainly influenced by the Arrhenius-like dependence of the relevant processes and materials in all investigated time domains.
2. The DC-resistance is SOC-dependent in all investigated time domains.

Compared to the other two time domains, a spread for the different pulse shape parameters, especially in the lower SOC region below 20%, stands out for $\Delta t = 1000$ ms in Fig. 3c and Fig. 3f. A detailed investigation on this resistance spread and on the general pulse parameter influence in the different time domains is done in the next section.

3.1.2. Pulse shape influence

As depicted in Fig. 1, the current pulse shape was altered by changing several pulse parameters in the pulse experiment of Section 2.2

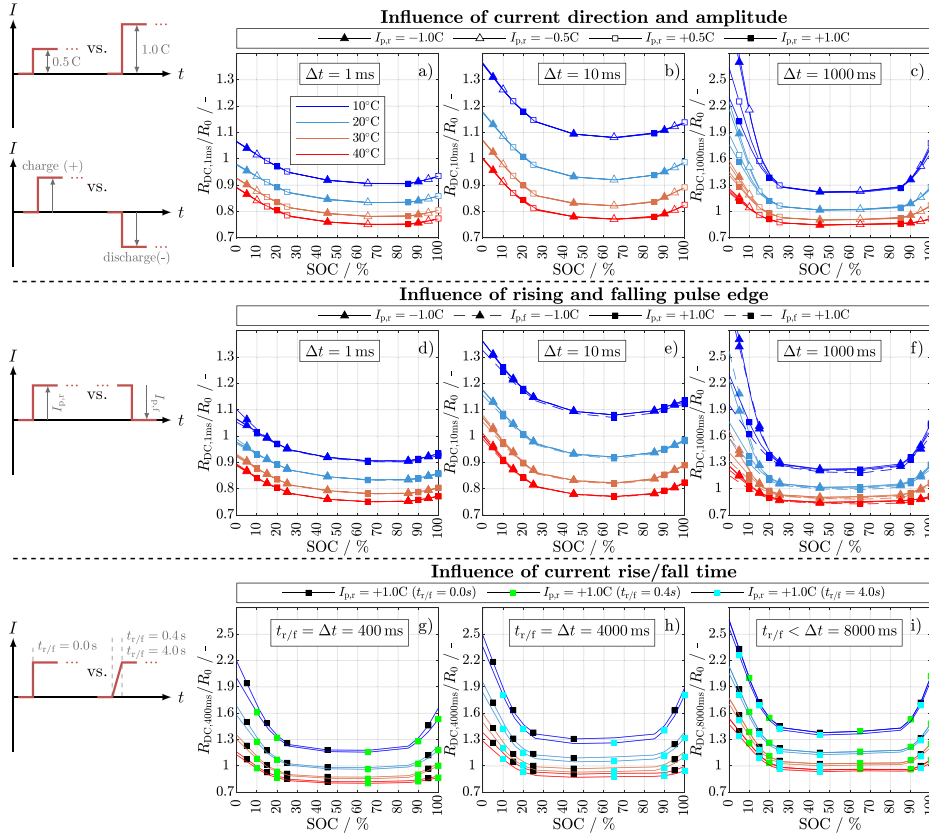


Fig. 3. Influence of the pulse parameters current amplitude/direction (a–c), excitation/idle pulses (d–f) and pulse rise/fall-time (g–i) on $R_{DC,\Delta t}$ for different Δt . $\Delta t = 1$ ms for (a,d), $\Delta t = 10$ ms for (b,e), $\Delta t = 1000$ ms for (c,f), $\Delta t = t_{r/f} = 400$ ms for (g), $\Delta t = t_{r/f} = 4000$ ms for (h) and $\Delta t = 8000$ ms for (i). All values are scaled to $R_0 = 40$ m Ω , which is the maximal cell impedance at 1 kHz, 23 °C and 100% SOC according to the manufacturer’s specifications. For the sake of clarity not all SOC markers for each curve are depicted.

to investigate the influence on the DC-resistance and to find the least parameter dependent time domain for Δt .

The first regarded parameters are the pulse current direction and the pulse amplitude. The first row, Fig. 3a to Fig. 3c, depicts the influence of the pulse current direction and the pulse amplitude at different Δt . Only rising pulses $I_{p,r}$ are included. There is no noteworthy difference between the $R_{DC,\Delta t}$ evident for short Δt (1 ms and 10 ms) in Fig. 3a and Fig. 3b. For longer Δt , such as in Fig. 3c, the resistance values increase, especially in the SOC regime below 20% and temperatures of 20 °C and less. A possible explanation, also reported by [34] and [42], is the increased charge transfer and diffusion polarization. Besides the resistance increase, two additional effects are visible in Fig. 3c that can be explained with the Butler–Volmer equation [58,59]. The first one is the non-linearity of the voltage–current relation. With increasing current density the corresponding slope of activation overpotential decreases, which causes a smaller resistance for the pulses with a current of $\pm 1.0C$ compared to $\pm 0.5C$. The second effect is the current direction dependency of the resistance values. The cathode approaches its lithiated state and the anode its delithiated state for the SOC regime below 20%. In this case, the intercalation in the cathode active material, respectively the deintercalation out of the anode active material (discharge pulse), gets less favorable, while the reversed process (charge pulse) gets more favorable. Since the reaction rates of the electrochemical process decrease with temperature, the effect increases for lower temperatures. [42,60,61]

As a result, the resistance values of different temperatures start to overlap with increasing Δt , which makes the $R_{DC,\Delta t}$ in this time

domain impractical for temperature estimation. The same effect with inverted pulse direction evolves for the SOC regime over 90%. Since the electrodes are not fully utilized because of the limited stability of the electrolyte above 4.2 V [62] and the increased potential for lithium plating at a higher SOC during charging, the resistance increase and spread is less distinct. In terms of temperature estimation for the investigated cell, this means that the resistance-calculation-period Δt must be limited to values below 1 s to avoid an ambiguous resistance–temperature relation and a distinction of pulses with respect to current direction and amplitude.

The effects of rising ($I_{p,r}$) and falling ($I_{p,f}$) pulses for charging and discharging currents with 1.0C are depicted in the second row of Fig. 3. There is a minimal difference in $R_{DC,\Delta t}$ for the short Δt (1 ms and 10 ms) in Fig. 3d and Fig. 3e for the majority of the SOC range. The deviations merely increase at 10 °C and a SOC below 10%. Since the pulses are too short, the influence of the open-circuit-voltage (OCV) is not relevant for the difference. However, in the case where $R_{DC,\Delta t}$ is calculated from $I_{p,r}$ pulses (solid lines), the system starts from an equilibrated state with no concentration gradient in the cell, since no current was applied for 1 h. In the case of $R_{DC,\Delta t}$ calculated from $I_{p,f}$ pulses (dashed lines), the current is flowing prior to the pulses and the electrode surface of the cell is already polarized [63]. When the pulse is turned off, the system returns to the equilibrium state and the concentration gradient, which was built up before, is reduced. This difference in Li-ion concentration between the $I_{p,r}$ and $I_{p,f}$ pulses results in a small overpotential difference and might be cause for the

difference in $R_{DC,\Delta t}$ [60]. The effect increases with increasing Δt in Fig. 3f, again particularly at 10 °C and a SOC below 20 %. With respect to temperature estimation, this again means that as long as Δt is small enough, excitation and idle pulses have a negligibly small influence on the resulting $R_{DC,\Delta t}$, such as in the case for pulse current direction and amplitude.

The last investigated factor is the pulse shape altered by changing the rise and fall time $t_{r/f}$ of the pulses, as depicted in Fig. 3g to Fig. 3i. This is achieved by comparing the rectangular pulses with the pulses having a larger rise/fall-time at the moment when $t_{r/f} = \Delta t$. For the sake of clarity only rising pulses with 1.0C are compared. The markers for the pulses are the same as before, only the difference in the rise/fall-time is indicated by the color of the markers. In Fig. 3g the DC-resistances for $t_{r/f} = \Delta t = 400$ ms are compared. The pulses with instantaneous current rise (black markers) show a slight increased resistance compared to the ones with $t_{r/f} = 400$ ms (green markers), especially in the peripheral SOC regions and at lower temperatures. This is probably caused by the difference in charge-throughput for the different pulses. In general, the charge-throughput of the pulses can be calculated by integrating the current pulses:

$$Q = \int I(t) dt \quad (1)$$

For rectangular pulses ($t_{r/f} = 0.0$ s) the integral can be simplified to

$$Q_R = I \cdot \Delta t \quad (2)$$

For pulses with $t_{r/f} > 0.0$ s the integral can either be simplified to

$$Q_T = \frac{1}{2} I \cdot \Delta t \text{ for } \Delta t \leq t_{r/f} \quad (3)$$

or to

$$Q_T = \frac{1}{2} I \cdot t_{r/f} + I \cdot (\Delta t - t_{r/f}) \text{ for } \Delta t > t_{r/f}.$$

Comparing the different pulses in Fig. 3g, where $\Delta t = t_{r/f} = 400$ ms, the charge-throughput of the rectangular pulses is twice as large as the one of the pulses with $t_{r/f} = 400$ ms. Therefore, the polarization and ultimately the resistance is larger as well. Fig. 3h shows the same effect for the pulses with $t_{r/f} = 4.0$ s (cyan markers) at $\Delta t = t_{r/f} = 4.0$ s. The relative ratio in charge-throughput in Fig. 3h is still twice as much as the one for the pulses with $t_{r/f} = 400$ ms in Fig. 3g. However, since $t_{r/f} = 4.0$ s in Fig. 3h is ten times longer than $t_{r/f} = 400$ ms in Fig. 3g, the absolute difference in charge-throughput is larger, and the resistance difference is more apparent in Fig. 3h. When Δt is increased above $t_{r/f}$ the relative difference in charge-throughput diminishes and the difference of the DC-resistances as well. This is illustrated by increasing Δt to 8000 ms in Fig. 3i. Here, the relative charge-throughput for the pulses with $t_{r/f} = 0.0$ s compared to the pulses with $t_{r/f} = 400$ ms amounts to $\frac{Q_T}{Q_R} = \frac{7.8}{8}$ and compared to the pulses with $t_{r/f} = 4.0$ s to $\frac{Q_T}{Q_R} = \frac{6}{8}$. For this reason, the curves for $t_{r/f} = 0.0$ s and 0.4 s already overlap and the distance to the curve for $t_{r/f} = 4.0$ s is reduced. In the context of temperature estimation this suggests that as long as Δt is longer than the rise/fall-time, the pulse shape has a minor influence on the resulting $R_{DC,\Delta t}$.

After analyzing temperature, SOC and shape influence on the DC-resistance in this and the previous section, the following conclusions can be drawn for the estimation method:

- The temperature estimation method has to fit the non-linear temperature behavior of the cell.
- Δt must be short enough ($\Delta t < 1$ s) to avoid a pulse edge, direction and amplitude distinction.
- Δt must be larger than $t_{r/f}$ of the pulses occurring in the application to minimize the influence of the rise/fall-time.
- Besides temperature, only the SOC remains as an influence factor. All other factors, the current direction, the current amplitude and the rise/fall-time, have a negligible influence.

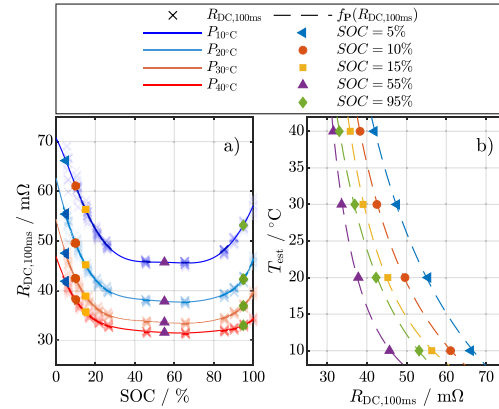


Fig. 4. Temperature estimation function example. Calculated $R_{DC,100ms}$ and polynomial fits $P_T(SOC)$ for all experimental cells (a). Temperature estimation function fit for marked example SOC points $SOC = 5/10/15/55/95\%$ (b).

As a result, this leaves the corridor $t_{r/f} < \Delta t < 1$ s for the resistance-calculation-period Δt , in which acceptable sampling rates for a BMS are possible and a large variety of pulses can be used for a robust temperature estimation method without any differentiation of the pulse shape. Nonetheless, the questions still remain: what kind of estimation function should be used and which resistance-calculation-period and which pulse parameter combination is optimal for the parametrization.

3.2. Temperature estimation function

This section describes the proposed temperature estimation function (TEF) and the way it is parameterized. Since only four temperature and eleven SOC points were investigated, the goal is to find a continuous functional description of the DC-resistance for any SOC and temperature. Looking at the volume of tested pulse parameters and their possible combinations, a simplified way to represent a subset of pulse parameters S_i , used for the parametrization of the TEF, is needed. In this regard a specific subset S_i contains all $R_{DC,\Delta t}$, which can be calculated from all pulses meeting the selection criteria. The different subsets of $R_{DC,\Delta t}$ are then approximated by a SOC-dependent polynomial $P_T(SOC)$ of 8th degree described by Eq. (4) for a certain Δt and for a specific experimental temperature $T \in [10^\circ\text{C}, 20^\circ\text{C}, 30^\circ\text{C}, 40^\circ\text{C}]$.

$$P_T(SOC) = \sum_{i=0}^8 x_i \cdot SOC^i \approx R_{DC,\Delta t}(SOC, T) \quad (4)$$

Fig. 4a serves as an example representing the polynomials for $R_{DC,100ms}$ fitted to a subset of pulses S_i . In this case, S_i includes rising and falling pulses with ± 0.5 C and ± 1.0 C for $t_{r/f} = 0.0$ s of all cells from Table 1. An overview of all tested subsets can be found in Fig. 5. In the example in Fig. 4a, all calculated DC-resistances from the subset are marked with 'x' in the temperature related color. The resulting polynomial fit for each temperature is represented by a solid line. To retrieve the temperature from the four polynomial representations, the resistance values at the specific SOC are evaluated for each temperature. These four points are represented by the vector $\mathbf{P}(SOC)$ in Eq. (5):

$$\mathbf{P}(SOC) = \begin{pmatrix} P_{10^\circ\text{C}}(SOC) \\ P_{20^\circ\text{C}}(SOC) \\ P_{30^\circ\text{C}}(SOC) \\ P_{40^\circ\text{C}}(SOC) \end{pmatrix} \quad (5)$$

The markers, except for 'x' in Fig. 4a and Fig. 4b, depict the resistance-temperature relation for the vector $\mathbf{P}(SOC)$ for exemplary SOC points.

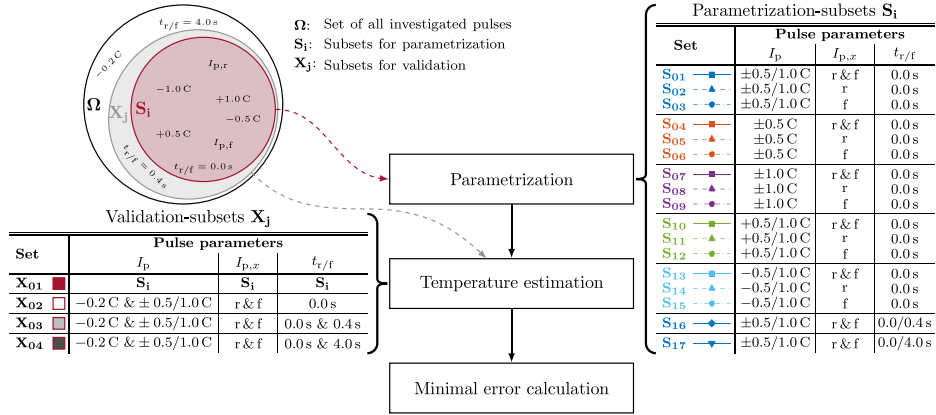


Fig. 5. Flowchart depicting the steps for finding error minimum for different combination of parametrization- and validation-subsets. Next to the parametrization- and validation-subsets names, their marking/color scheme is depicted to explicitly distinguish them.

Since $P(SOC)$ only represent the temperature related to four resistance values, an approximation function is needed for the resistance values outside and in between these points. To describe the non-linear behavior between DC-resistance and temperature, an exponential function was selected. The estimation function f_p in Eq. (6) maps the resistance-temperature behavior for each vector $P(SOC)$ at a specific SOC point.

$$T_{est} = f_p(R_{DC,\Delta t}) = A \cdot e^{\frac{B}{R_{DC,\Delta t}}} + C \quad (6)$$

The temperature T_{est} is the temperature estimated with f_p and the function variables A , B and C are SOC-dependent parameters fitted to each vector $P(SOC)$. The dashed lines in Fig. 4b represent f_p for the exemplary SOC points from Fig. 4a. The corresponding course of the function variables is depicted in Fig. S2.

3.3. Parametrization- and validation-subsets

After determining the TEF, the next step is to find suitable subsets of pulses for the parametrization of f_p and the corresponding Δt for temperature estimation. To achieve this, the flowchart in Fig. 5 is used. The circles on the left hand side of Fig. 5 represent different subsets of pulses containing specific parameters, where Ω is the set containing all pulses. In the following, two different type of subsets of Ω will be distinguished. The first type are parametrization-subsets S_i , used to parameterize f_p . The second type are validation-subsets X_j , used to determine the accuracy and optimal Δt of the parametrization-subsets. This is done in the three steps depicted in the center of Fig. 5. In the first step, different subsets S_i taken from all pulses are used to parameterize the polynomial representation according to Eq. (4). The 17 validation-subsets used in this work are depicted in the table on the right of Fig. 5, including the pulse parameters contained in the subsets. The polynomials $P_T(SOC)$ are generated for each of the 17 subsets for Δt reaching from 1 ms to 10 s. In the second step, the TEF of Eq. (6) is used to estimate the temperature for the pulses of the four validation-subsets X_j in the table on the left of Fig. 5. Each validation-subset tests a specific property, which will be described in the discussion of Figs. 6 and 7. In the third step, the suitability for temperature estimation of the parametrization-subsets S_i is determined for each validation-subset X_j . As a measure for the suitability, the root mean square error (RMSE) is calculated according to Eq. (7).

$$RMSE_{S_i}(X_j) = \sqrt{\frac{1}{|X_j|} \sum_{x \in X_j} (T_{est,x} - T_{m,x})^2} \quad (7)$$

$T_{est,x}$ is the temperature estimated with f_p for each resistance value calculated from the pulses in the validation-subset X_j and $T_{m,x}$ is the measured temperature during the experiment. Finally, the minimal RMSE according to Eq. (8) is utilized to find the most suitable resistance-calculation-period Δt in each subset S_i for each X_j .

$$RMSE_{S_i}(X_j)_{min} = \min_{\Delta t \in [10^{-3}, 10, 10\text{ s}]} RMSE_{S_i}(X_j) \quad (8)$$

3.4. Optimal parametrization-subset and resistance-calculation-period

The results of the error calculation for the different parametrization- and validation-subsets are discussed in this section. Fig. 6 depicts the results for the validation with X_{01} (left column), where parametrization- and validation-subset are equal, and X_{02} (right column), where all pulses with $t_{r/f} = 0.0\text{ s}$ are included. The figure investigates the influence of the pulse parameters on the TEF, when only pulses with a rise/fall-time $t_{r/f} = 0.0\text{ s}$ are considered. Fig. 6a and Fig. 6b exemplary depict the course of the RMSE over the resistance-calculation-period for the corresponding validation-subsets. For short Δt all subsets indicate an increased error, followed by an error decline and leading to a more or less distinct error plateau with increasing Δt . By increasing Δt further, the error shows a steeper increase leading to a linear course with a constant slope.

In Fig. 6a the validation-subset X_{01} is equal to the individual parametrization-subsets S_i . This represents an application case, where all load changes are known prior to the parametrization of the TEF. For the sake of clarity, not all 15 parametrization-subsets are depicted. For X_{02} in Fig. 6b all pulses with a rise/fall-time $t_{r/f} = 0.0\text{ s}$ and additionally pulses with -0.2 C , unknown to the parametrization-subsets, are included. Since the parametrization-subsets stay the same, they only partly include the pulses of the validation-subset. This represents an application case, where not all of the load changes are known prior to the parametrization of the TEF. The general shape of the error course is not influenced compared to Fig. 6a, but all curves show an increased error course and error minima. Again, only exemplary curves are depicted for the sake of clarity.

In the pulse shape analysis in Section 3.1.2, it is assumed that the optimal resistance-calculation-period is located in between the boundaries of $t_{r/f} < \Delta t < 1\text{ s}$. This assumption is confirmed considering Fig. 6c and Fig. 6d. For X_{01} in Fig. 6c, where the validation- and parametrization-subset are equal, the majority of the error minima are located in between 13 ms to 95 ms. The only exceptions are the error minima for S_{11} and S_{12} at 800 ms and 830 ms, respectively. The minimal RMSE for the subsets are within 0.95 K and 1.18 K. Part of this error

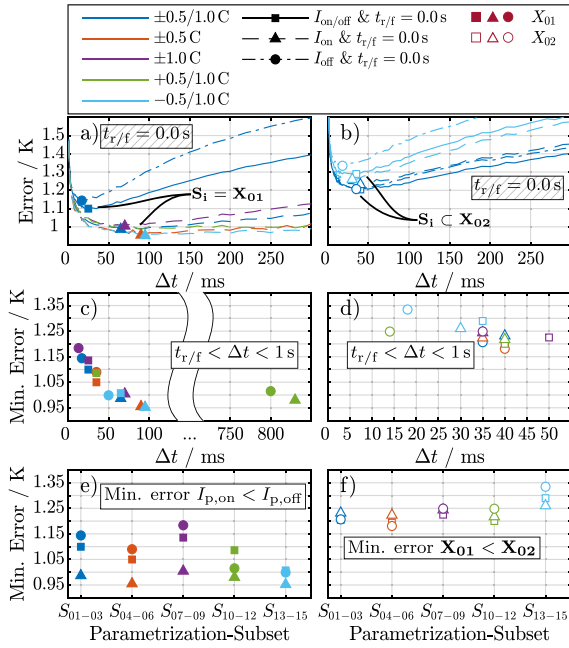


Fig. 6. Error behavior of the different parametrization-subsets validated with X_{01} , where the validation- and parametrization-subset are equal, and X_{02} , including all pulses with $t_{r/f} = 0.0$ s. Exemplary error course over Δt for X_{01} (a) and X_{02} (b). Resistance-calculation-period of error minima of the parametrization-subsets validated with X_{01} (c) and X_{02} (d). Comparison of the minimal error of the different parametrization-subsets for X_{01} (e) and X_{02} (f). The markers represent the minimum error of the parametrization-subsets. Table S1 in the supplementary gives a detailed overview with the RMSE minima and the related resistance-calculation-periods for all parametrization- and validation-subsets.

is related to the generation of the TEF. Since the TEF is generated from the average values of the three cells in Table 1, the TEF is not perfectly adjusted to a specific cell and the error minima is partly caused by the resistance variation between the cells. To improve the estimation method, a procedure, which adjusts the TEF to specific cells, is introduced later in Section 3.5. For validation-subset X_{02} in Fig. 6d, the range for the optimal resistance-calculation-period is even smaller. The minimal RMSE for the subsets are within 1.18 K and 1.33 K and below 50 ms.

Fig. 6e and Fig. 6f are utilized to judge if a specific combination of pulse parameters is beneficial for the parametrization. For validation-subset X_{01} in Fig. 6e, the parametrization-subsets including only pulses with rising edges $I_{p,r}$, have smaller minimal errors compared to those including the same pulses with falling edges $I_{p,f}$. This might be caused by the fact that rising pulses start from an idle state and no concentration gradients are present in the cell. Whereas falling pulses start from a previously polarized cell. The reduced error for parametrization-subsets with rising pulses is no longer present for validation-subset X_{02} in Fig. 6f. Here, no specific parametrization seems to be advantageous and the error minima are higher compared to X_{01} .

Fig. 7 investigates the influence of the rise/fall-time, utilizing the validation-subsets X_{03} and X_{04} . As in Fig. 6, each column of Fig. 7 represents the results for one validation-subset. Additionally to the 15 parametrization-subsets as seen in Fig. 6, the subsets S_{16} and S_{17} are added to the parametrization-subsets in Fig. 7, containing pulses with the same rise/fall-time as the corresponding validation-subsets X_{03} and X_{04} .

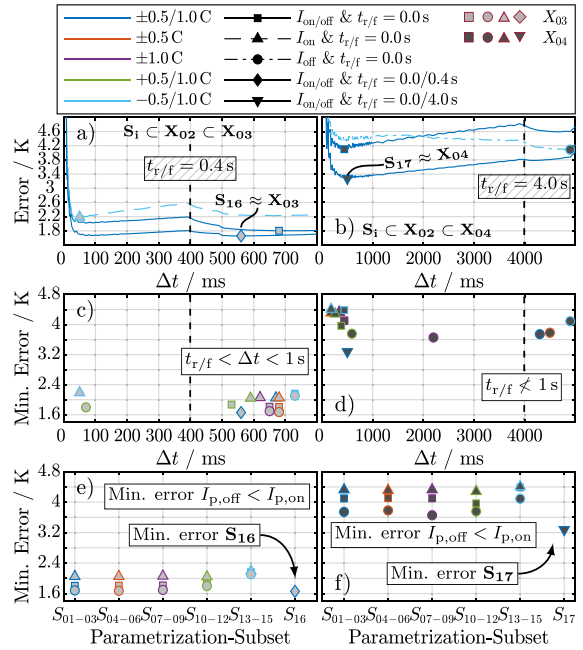


Fig. 7. Error behavior of the different parametrization-subsets validated with X_{03} , including the same pulses as X_{02} and all pulses with $t_{r/f} = 0.4$ s, and X_{04} , including the same pulses as X_{02} and all pulses with $t_{r/f} = 4.0$ s. Exemplary error course over Δt for X_{03} (a) and X_{04} (b). Resistance-calculation-period of error minima of the parametrization-subsets validated with X_{03} (c) and X_{04} (d). Comparison of the minimal error of the different parametrization-subsets for X_{03} (e) and X_{04} (f). Table S1 in the supplementary gives a detailed overview with the RMSE minima and the related resistance-calculation-periods for all parametrization- and validation-subsets.

Fig. 7a and Fig. 7b exemplarily depict the course of the RMSE over Δt . By adding the pulses with $t_{r/f} = 0.4$ s and 4.0 s to the validation-subsets, a second error decline evolves after Δt passes $t_{r/f}$. Since the amount of pulses differing from the parametrization-subsets increases, the general RMSE increases as well, especially for validation-subset X_{04} in Fig. 7b, which includes the pulses with $t_{r/f} = 4.0$ s. Nevertheless, the parametrization-subsets S_{16} and S_{17} , including the pulses with the corresponding rise/fall-time of the validation-subsets, show the lowest error course.

The minimal RMSE of the parametrization-subsets and the corresponding resistance-calculation-periods for X_{03} and X_{04} are depicted in Fig. 7c and Fig. 7d. The assumption for the minimal error corridor $t_{r/f} < \Delta t < 1$ s holds for the majority of the parametrization-subsets in Fig. 7c. However, the two subsets S_{12} and S_{14} violate the assumption. The reason can be seen in Fig. 7a, by observing the error course for S_{14} (dashed line). The error increase after the first error plateau is steeper than for the other parametrization-subsets and therefore the second error decline after Δt passes $t_{r/f} = 0.4$ s does not fall below the first one. This results in an error minimum, which occurs at $\Delta t < t_{r/f}$. For all other parametrization-subsets in Fig. 7c, the resistance-calculation-period with the minimal RMSE lies between 530 ms and 730 ms. For the RMSE minima in Fig. 7d the assumption cannot be fulfilled, since $t_{r/f} = 4.0$ s $>$ 1 s. Therefore, there are error minima above 4.0 s, below 1 s and even in between, with the majority of the error minima below 1 s.

Fig. 7e and Fig. 7f are utilized to judge if a specific combination of pulse parameters is beneficial for the parametrization. In contrast to validation-subset X_{01} in Fig. 6e, the parametrization-subsets including falling pulses $I_{p,f}$ have a smaller minimal error compared to those

including the same pulses with rising pulses $I_{p,r}$, for validation-subset X_{03} in Fig. 7e. As already noted in Fig. 7a, parametrization-subset S_{16} , including the pulses with $t_{r/f} = 0.4$ s, has the smallest minimal RMSE (1.66 K) for X_{03} . Except for the generally higher minimal RMSE, the statements of Fig. 7e are transferable to Fig. 7f. Here, parametrization-subset S_{17} , including the pulses with $t_{r/f} = 4.0$ s, has the smallest minimal RMSE (3.28 K) for X_{04} . Bringing all findings together, the optimal subsets have to fulfill the following requirements:

- The closer the parametrization pulses are to the actual pulses occurring in the application, the smaller the estimation error.
- If only rectangular pulses occur in the application, the optimal resistance-calculation-period can be found below 1 s.
- If pulses with $t_{r/f} > 0.0$ s occur in the application, the optimal resistance-calculation-period Δt for the TEF is longer than $t_{r/f}$. However, pulses with long $t_{r/f}$ should be excluded from the temperature estimation, because of the increasing error caused by the DC-resistance dependence on pulse shape for increasing Δt (Section 3.1).

3.5. Validation experiment

To validate the results of the last two sections for conditions close to an application, the TEF was tested with the experimental setup shown in Fig. 2. The pulses in the current-profile (Fig. 2b) for the validation are more extensive than the ones used for the subsets to generate the TEFs. In addition to unknown pulse amplitudes, the current-profile also contains pulses, not starting from and not returning to an idle state. Besides, the current-profile rarely includes resting periods, which are relatively short compared to the resting period of 1 h before each reference pulse. Even if a linear polarization behavior for the relevant time domain ($\Delta t < 1$ s) and current range is assumed, the current-profile is only partly utilizable for temperature estimation. To take extensive and irregular pulses of a current-profile into account and to incorporate the findings from the last section, the pulse filter with three conditions in Fig. 8a is introduced. The first condition excludes pulses with long $t_{r/f}$, causing increased errors such as for $t_{r/f} = 0.4$ s and small current changes by accepting only pulses which have an absolute current change rate $|\Delta I_{r/f}|$ within $t_{r/f}$ larger than a minimal change rate ΔI_{min} . In the validation experiment, two minimal change rates are evaluated: $\Delta I_{min} = 0.2$ C to achieve conditions similar to X_{02} and $\Delta I_{min} = 0.1$ C to have a validation scenario with pulses differing even more from the parametrization-subset than in X_{02} . The second condition ensures that there is no current direction change during $t_{r/f}$. After $t_{r/f}$ the pulse should hold a stable current value till Δt is reached. To ensure this, the third condition limits the current fluctuation to stay within the tolerance ΔI_{tol} . For the validation experiment, ΔI_{tol} was set to 10 mA to avoid the influence of the HPS current sampling precision. If all three conditions are fulfilled, the pulse is used to calculate a $R_{DC,\Delta t}$. To determine the other filter parameters, as well as Δt and S_i for the validation experiment, the sampling rate of the test system, the module current, and its current changes had to be considered. The maximal sampling rate of 200 Sample/s was applied to the test equipment. Nevertheless, the first valid data point, after a current change, is sampled after 100 ms, if current-profiles are a part of the test sequence. For this reason Δt had to be longer than 100 ms and the limit for $t_{r/f}$ was set to 100 ms. Assuming the current changes are known for the application, the selection of a suitable subset S_i can be accomplished by analyzing the current change distribution. The module current contained charge and discharge pulses with the majority of current changes in the regime of 0.4 C and less (Fig. S1). The closest error behavior for these kind of pulses is represented by validation-subset X_{02} and parametrization-subset S_{04} , which shows the best congruence in pulse parameters with the module current-profile. According to Fig. 6c, the optimal resistance-calculation-period for S_{04} and X_{02} is $\Delta t = 40$ ms. Nevertheless, Δt is set to 120 ms to fulfill the

Table 4

Settings for the algorithm used for the method validation in Fig. 8a and the estimation error results for each cell in the validation module for the corresponding setting.

Parameter	Value						
$S_i/-$	S_{04}						
$\Delta t/ms$	120						
$t_{r/f}/ms$	100						
$\Delta I_{min}/C$	0.1/0.2						
$\Delta I_{tol}/mA$	10						
Cell	C_4	C_5	C_6	C_7	C_8	C_9	
$R_{DC,offset}^a/m\Omega$	2.31	2.18	2.41	1.83	2.51	2.74	
$RMSE_{S_{04}}(0.1C)^b/K$	1.11	0.96	1.08	0.96	1.01	0.97	
$RMSE_{S_{04}}(0.2C)^b/K$	0.93	0.65	0.90	0.59	0.67	0.77	

^aCalculated at 25 °C, SOC = 50 % and $\Delta t = 120$ ms.

^b $RMSE_{S_i}(\Delta I_{min})$ calculated according to Eq. (4).

condition $t_{r/f} < \Delta t < 1$ s. The RMSE of 1.26 K for S_{04} at this resistance-calculation-period is still relatively close to the minimal RMSE of 1.18 K for S_{06} .

In general, the resistance of cells slightly differ, even if they are from the same production batch and are treated equally. This is also the case for the cells used in the pulse experiment (Table 1) and the validation experiment (Table 3). Since the function variables of the TEF in Eq. (6) are fitted to the average of the pulse experiment cells, a correction is needed to make the TEF applicable to the validation experiment cells. Since the shape of the DC-resistance curves of the cells used in the pulse experiment only differed by an offset, the correction is achieved by adding an individual offsets $R_{DC,offset}$ to each cell of the validation experiment before applying the TEF. The offset is determined with the pulses used to calculate the $R_{DC,10s}$ in Table 3 at SOC = 50 % and 25 °C, though evaluated for $\Delta t = 120$ ms instead of 10 s. At this temperature and SOC the influence of any pulse parameter is minimal, which makes the offset correction more robust. The difference between the $R_{DC,120ms}$ of each experimental cell and the resistance calculated by the inverse function of f_p for SOC = 50 % and 25 °C results in the offset $R_{DC,offset}$. An overview of all settings for the pulse filter, the offset values and the results of the validation experiment for each cell is listed in Table 4. The offset values $R_{DC,offset}$ reaching from 1.83 m Ω to 2.74 m Ω seem to be quite high in relation to the DC-resistance of the cells in Table 3. However, according to the $R_{DC,10s}$ distribution for the same cell measured by Zilberman et al. [31], the cells used in the 6s1p-module are from the lower end of the DC-resistance range of the investigated cell and the cells used for the pulse experiment are from the upper end, leading to this relatively high offset values.

After the offset correction, the final step is applied to the $R_{DC,120ms}$ in Fig. 8a. If several $R_{DC,120ms}$ are calculated within a window $t_w = 10$ s, the values are averaged and only one temperature estimation is performed. This reduces the influence of outliers and decreases the estimation error. The only missing variable for the TEF is the SOC of each cell. To determine the SOC, the coulomb counting method is applied [64–67]. The initial state-of-charge SOC_0 was determined by utilizing the relation between the SOC and the OCV. The coulombic efficiency for charging/discharging the cell was assumed to be one. The values for the actual capacity C_{act} of each cell were taken from Table 3.

Fig. 8b shows the measured cell temperature T_m of cell C_9 in the module and serves as example to visualize the estimated temperatures for two different pulse current change limits ΔI_{min} . Since more pulses were valid for the temperature estimation with $\Delta I_{min} = 0.1$ C, the temperature is continuously estimated during the load profile. Whereas the temperature estimation for $\Delta I_{min} = 0.2$ C shows gaps of up to 10 min between two estimation points. The estimation error $RMSE_{S_{04}}(\Delta I_{min})$ for $\Delta I_{min} = 0.1$ C is higher for each cell than for 0.2 C (Table 4). An increased estimation error is visible for $\Delta I_{min} = 0.1$ C, especially at the 2 h mark in Fig. 8b. At this point, the current-profile of Fig. 2b shows only small current changes close to the current change limit. However, the error of each cell is smaller than the minimal RMSE for any S_i

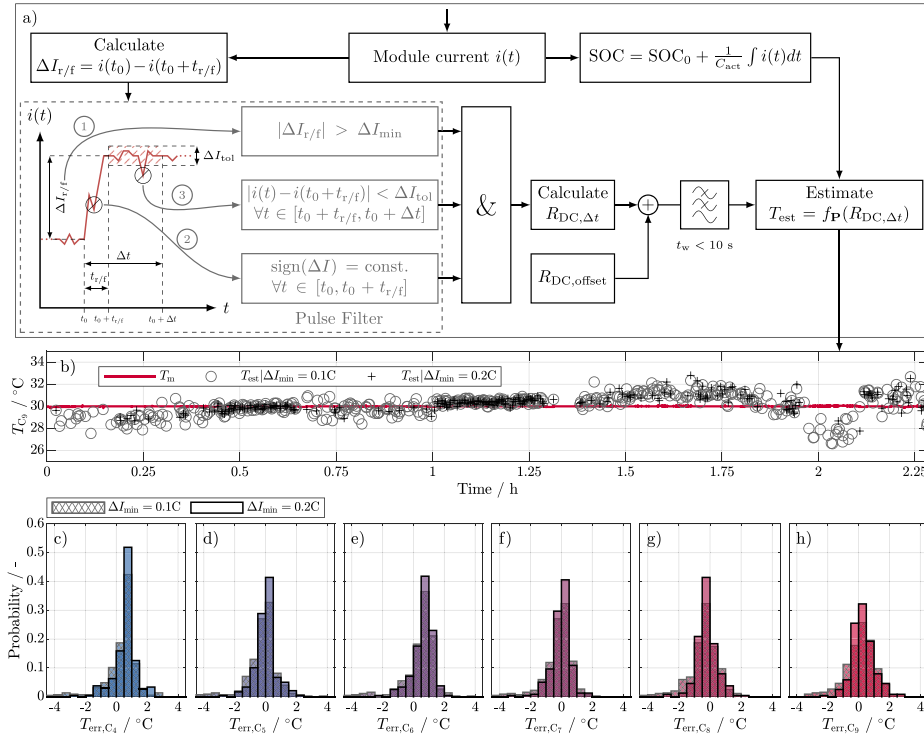


Fig. 8. Algorithm for the method validation with pulse filter (a). Exemplary temperature estimation results for cell C_9 with two different pulse filter settings and corresponding measured cell temperature (b). Error probability for each module cell for the two different pulse filter settings (c-h).

validated with X_{02} . The RMSE for $\Delta I_{min} = 0.1C$ are between 0.96 K and 1.11 K. For $\Delta I_{min} = 0.2C$ the RMSE ranges between 0.59 K and 0.93 K. The detailed estimation error probability for each cell in the module is depicted in Fig. 8c to Fig. 8h, showing that the majority of the estimation errors are within ± 1 K for any cell.

Although the method was validated with unknown cells, it was only validated for newly acquired cells. Since aging influences the impedance and capacity of a cell [4,30,68], the estimation method needs to be adapted over the application lifetime, in particular for increasing non-linear battery behavior towards the end of life. A possible approach to solve this issue is already part of the module validation. By updating the offset correction $R_{DC,offset}$ of each cell, aging induced impedance changes could be compensated. To get the offset values, the battery has to be in an idle state without any temperature or SOC discrepancy, such as a parking EV after being charged and balanced. In this case only one temperature sensor for the whole battery pack is needed, serving as a reference. Before the application is used again, an intentional pulse, for example triggered by the battery charger, can be utilized to calculate the new offset correction. A randomized pulse, such as caused by turning on the EV, can be considered to calculate the new offset correction as well. Nevertheless, further investigations are necessary to validate this approach, since it assumes a resistance increase, which is uniform over the whole SOC range. Along with the compensation of the DC-resistance, an accurate SOC estimation over lifetime is significant for the estimation method. To achieve this, a more sophisticated SOC estimator [69,70] than the coulomb counter used for the validation is required, especially tracing the capacity fade with an accurate SOH estimator.

Another issue occurs for systems with parallel connected cells. If the current distribution is known and is not affected by the connection itself, the temperature estimation method of this work can be applied

without limitations. In this case, it is possible to calculate the individual DC-resistances of each cell in the parallel connection and estimate the temperature with the TEF. However, further experiments are needed to investigate and validate this assumption. If the current distribution is unknown, which is usually the case, the estimation method cannot determine the temperature of each cell.

4. Conclusion

In this work, an online temperature estimation method based on DC-resistance $R_{DC,\Delta t}$ is proposed. Unlike previous studies, the method does neither rely on a transformation of the pulses to the frequency domain nor on additional equipment for excitation. The method entirely relies on the current and voltage signals in the time domain generated by the application, even considering deviations from the ideal edges of a pulse. To investigate the temperature behavior and the underlying processes in the time domain, the pulse based DC-resistance values $R_{DC,\Delta t}$ were regarded for a variety of pulse shapes and Δt . Based on the results, an estimation method was proposed and benchmarked for various combinations of pulse subsets and Δt from 1 ms to 10 s. The results showed that there is not the one optimal combination of pulses and Δt for the proposed estimation method. The following facts have to be considered to find the optimal combination:

- As long as Δt is short enough, avoiding a major influence of DC-resistance spread at low SOC and temperatures, the different pulse parameters (pulse amplitude, pulse direction and rising/falling pulse) have a negligible influence on the estimation result, making the estimation method independent of the pulse shape. However, the dependence on SOC still remains. If Δt is too short, the estimation error increases. In the remaining intermediate

time domain from approximately 10 ms to several 100 ms, the estimation error has its minimum and shows only a slight error increase. For the investigated cell, the minimal RMSE amounts to 0.95 K for $\Delta t = 95$ ms.

- If the current change of the pulse does not happen instantaneously, but rises/falls till reaching a steady value, the estimation method is also applicable as long as Δt is longer than the rise/fall-time $t_{r/f}$ of the pulse. Nevertheless, for an acceptable estimation error, $t_{r/f}$ and Δt are limited. For the investigated cell, the shortest verified rise/fall-time $t_{r/f}$ for a non-rectangular excitation pulse is 0.4 s with a minimal RMSE of 1.66 K for $\Delta t = 560$ ms.
- The validation on the module level showed that the method can be applied to serial connected cells. By filtering the pulses occurring in the continuous current-profile and adjusting the calculated DC-resistance with a simple offset $R_{DC,offset}$ to the cells of the module, the RMSE of each cell was reduced to less than 1 K (Table 4).

Although the method was investigated and validated under several conditions, there are still open questions for future studies. As mentioned at the end of the discussion, the influence of aging on the estimation method and application of the estimation method to parallel connected cells are the most urgent ones. In addition, the validity for other cell chemistries and the behavior for other thermal boundary conditions, like a changing temperature gradient during cycling, are of interest.

CRedit authorship contribution statement

S. Ludwig: Conceptualization, Methodology, Software, Project administration, Writing - original draft, Visualization, Data curation, Investigation, Writing - review & editing. **I. Zilberman:** Conceptualization, Writing - review & editing. **M.F. Horsche:** Conceptualization, Writing - review & editing. **T. Wohlers:** Software, Investigation. **A. Jossen:** Writing - review & editing, Supervision.

Declaration of competing interest

The authors declare that they have no known competing financial interests or personal relationships that could have appeared to influence the work reported in this paper.

Acknowledgment

This work has received funding from the European Union's Horizon 2020 research and innovation programme under the grant 'Electric Vehicle Enhanced Range, Lifetime And Safety Through INGenious battery management' [EVERLASTING-713771].

Appendix A. Supplementary data

Supplementary material related to this article can be found online at <https://doi.org/10.1016/j.jpowsour.2021.229523>.

References

- [1] S. Ma, M. Jiang, P. Tao, C. Song, J. Wu, J. Wang, T. Deng, W. Shang, Temperature effect and thermal impact in lithium-ion batteries: A review, *Prog. Nat. Sci.: Mater. Int.* 28 (6) (2018) 653–666, <http://dx.doi.org/10.1016/j.pnsc.2018.11.002>.
- [2] T. Waldmann, M. Wilka, M. Kasper, M. Fleischhammer, M. Wohlfahrt-Mehrens, Temperature dependent ageing mechanisms in Lithium-ion batteries - A Post-Mortem study, *J. Power Sources* 262 (2014) 129–135, <http://dx.doi.org/10.1016/j.jpowsour.2014.03.112>.
- [3] M. Naumann, M. Schimpe, P. Keil, H.C. Hesse, A. Jossen, Analysis and modeling of calendar aging of a commercial LiFePO₄/graphite cell, *J. Energy Storage* 17 (2018) 153–169, <http://dx.doi.org/10.1016/j.est.2018.01.019>.
- [4] S.F. Schuster, M.J. Brand, C. Campestrini, M. Gleissenberger, A. Jossen, Correlation between capacity and impedance of lithium-ion cells during calendar and cycle life, *J. Power Sources* 305 (2016) 191–199, <http://dx.doi.org/10.1016/j.jpowsour.2015.11.096>.
- [5] M. Fleischhammer, T. Waldmann, G. Bisle, B.-I. Hogg, M. Wohlfahrt-Mehrens, Interaction of cyclic ageing at high-rate and low temperatures and safety in lithium-ion batteries, *J. Power Sources* 274 (2015) 432–439, <http://dx.doi.org/10.1016/j.jpowsour.2014.08.135>.
- [6] A. Friesen, F. Horsthemke, X. Mönninghoff, G. Brunklaus, R. Krafft, M. Börner, T. Risthaus, M. Winter, F.M. Schappacher, Impact of cycling at low temperatures on the safety behavior of 18650-type lithium ion cells: Combined study of mechanical and thermal abuse testing accompanied by post-mortem analysis, *J. Power Sources* 334 (2016) 1–11, <http://dx.doi.org/10.1016/j.jpowsour.2016.09.120>.
- [7] X.M. Xu, R. He, Research on the heat dissipation performance of battery pack based on forced air cooling, *J. Power Sources* 240 (2013) 33–41, <http://dx.doi.org/10.1016/j.jpowsour.2013.03.004>.
- [8] B. Wu, V. Yufit, M. Marinescu, G.J. Offer, R.F. Martinez-Botas, N.P. Brandon, Coupled thermal-electrochemical modelling of uneven heat generation in lithium-ion battery packs, *J. Power Sources* 243 (2013) 544–554, <http://dx.doi.org/10.1016/j.jpowsour.2013.05.164>.
- [9] C. Zhao, W. Cao, T. Dong, F. Jiang, Thermal behavior study of discharging/charging cylindrical lithium-ion battery module cooled by channeled liquid flow, *Int. J. Heat Mass Transfer* 120 (2018) 751–762, <http://dx.doi.org/10.1016/j.jihheatmasstransfer.2017.12.083>.
- [10] A. Tang, J. Li, L. Lou, C. Shan, X. Yuan, Optimization design and numerical study on water cooling structure for power lithium battery pack, *Appl. Therm. Eng.* 159 (2019) 113760, <http://dx.doi.org/10.1016/j.applthermaleng.2019.113760>.
- [11] X. Liu, W. Ai, M. Naylor Marlow, Y. Patel, B. Wu, The effect of cell-to-cell variations and thermal gradients on the performance and degradation of lithium-ion battery packs, *Appl. Energy* 248 (2019) 489–499, <http://dx.doi.org/10.1016/j.apenergy.2019.04.108>.
- [12] I. Zilberman, S. Ludwig, M. Schiller, A. Jossen, Online aging determination in lithium-ion battery module with forced temperature gradient, *J. Energy Storage* 28 (2020) 101170, <http://dx.doi.org/10.1016/j.est.2019.101170>.
- [13] L. Wang, D. Lu, M. Song, X. Zhao, G. Li, Instantaneous estimation of internal temperature in lithium-ion battery by impedance measurement, *Int. J. Energy Res.* 18 (2) (2020) 207, <http://dx.doi.org/10.1002/er.5144>.
- [14] C. Ji, B. Wang, S. Wang, S. Pan, Du Wang, P. Qi, K. Zhang, Optimization on uniformity of lithium-ion cylindrical battery module by different arrangement strategy, *Appl. Therm. Eng.* 157 (2019) 113683, <http://dx.doi.org/10.1016/j.applthermaleng.2019.04.093>.
- [15] A. Fill, S. Koch, K.P. Birke, Algorithm for the detection of a single cell contact loss within parallel-connected cells based on continuous resistance ratio estimation, *J. Energy Storage* 27 (2020) 101049, <http://dx.doi.org/10.1016/j.est.2019.101049>.
- [16] R. Koch, A. Jossen, Temperature measurement of large format pouch cells with impedance spectroscopy, in: EVS28 International Electric Vehicle Symposium and Exhibition, 2015.
- [17] J.P. Schmidt, S. Arnold, A. Loges, D. Werner, T. Wetzal, E. Ivers-Tiffée, Measurement of the internal cell temperature via impedance: Evaluation and application of a new method, *J. Power Sources* 243 (2013) 110–117, <http://dx.doi.org/10.1016/j.jpowsour.2013.06.013>.
- [18] L. Rajmakers, D.L. Danilov, J. van Lammeren, M. Lammers, P. Notten, Sensorless battery temperature measurements based on electrochemical impedance spectroscopy, *J. Power Sources* 247 (2014) 539–544, <http://dx.doi.org/10.1016/j.jpowsour.2013.09.005>.
- [19] L.H.J. Rajmakers, D.L. Danilov, J.P.M. van Lammeren, T.J.G. Lammers, H.J. Bergveld, P.H.L. Notten, Non-zero intercept frequency: An accurate method to determine the integral temperature of li-ion batteries, *IEEE Trans. Ind. Electron.* 63 (5) (2016) 3168–3178, <http://dx.doi.org/10.1109/TIE.2016.2516961>.
- [20] R.R. Richardson, P.T. Ireland, D.A. Howey, Battery internal temperature estimation by combined impedance and surface temperature measurement, *J. Power Sources* 265 (2014) 254–261, <http://dx.doi.org/10.1016/j.jpowsour.2014.04.129>.
- [21] R. Srinivasan, B.G. Carkhuff, M.H. Butler, A.C. Baisden, Instantaneous measurement of the internal temperature in lithium-ion rechargeable cells, *Electrochim. Acta* 56 (17) (2011) 6198–6204, <http://dx.doi.org/10.1016/j.electacta.2011.03.136>.
- [22] R. Srinivasan, Monitoring dynamic thermal behavior of the carbon anode in a lithium-ion cell using a four-probe technique, *J. Power Sources* 198 (2012) 351–358, <http://dx.doi.org/10.1016/j.jpowsour.2011.09.077>.
- [23] G. Zhu, K. Wen, W. Lv, X. Zhou, Y. Liang, F. Yang, Z. Chen, M. Zou, J. Li, Y. Zhang, W. He, Materials insights into low-temperature performances of lithium-ion batteries, *J. Power Sources* 300 (2015) 29–40, <http://dx.doi.org/10.1016/j.jpowsour.2015.09.056>.
- [24] X. Wang, X. Wei, Q. Chen, J. Zhu, H. Dai, Lithium-ion battery temperature online estimation based on fast impedance calculation, *J. Energy Storage* 26 (2019) 100952, <http://dx.doi.org/10.1016/j.est.2019.100952>.
- [25] M. Mathew, S. Janhunen, M. Rashid, F. Long, M. Fowler, Comparative analysis of lithium-ion battery resistance estimation techniques for battery management systems, *Energies* 11 (6) (2018) 1490, <http://dx.doi.org/10.3390/en11061490>.

- [26] X. Zhang, Q. Wu, X. Guan, F. Cao, C. Li, J. Xu, Lithium dendrite-free and fast-charging for high voltage nickel-rich lithium metal batteries enabled by bifunctional sulfone-containing electrolyte additives, *J. Power Sources* 452 (2020) 227833, <http://dx.doi.org/10.1016/j.jpowsour.2020.227833>.
- [27] S. Casino, P. Niehoff, M. Börner, M. Winter, Protective coatings on silicon particles and their effect on energy density and specific energy in lithium ion battery cells: A model study, *J. Energy Storage* 29 (2020) 101376, <http://dx.doi.org/10.1016/j.est.2020.101376>.
- [28] K.H. Kim, J. Shon, H. Jeong, H. Park, S.-J. Lim, J.S. Heo, Improving the cyclability of silicon anodes for lithium-ion batteries using a simple pre-lithiation method, *J. Power Sources* 459 (2020) 228066, <http://dx.doi.org/10.1016/j.jpowsour.2020.228066>.
- [29] J. Sturm, A. Rheinfeld, I. Zilberman, F.B. Spingler, S. Kosch, F. Frie, A. Jossen, Modeling and simulation of inhomogeneities in a 18650 nickel-rich, silicon-graphite lithium-ion cell during fast charging, *J. Power Sources* 412 (2019) 204–223, <http://dx.doi.org/10.1016/j.jpowsour.2018.11.043>.
- [30] I. Zilberman, J. Sturm, A. Jossen, Reversible self-discharge and calendar aging of 18650 nickel-rich, silicon-graphite lithium-ion cells, *J. Power Sources* 425 (2019) 217–226, <http://dx.doi.org/10.1016/j.jpowsour.2019.03.109>.
- [31] I. Zilberman, S. Ludwig, A. Jossen, Cell-to-cell variation of calendar aging and reversible self-discharge in 18650 nickel-rich, silicon-graphite lithium-ion cells, *J. Energy Storage* 26 (2019) 100900, <http://dx.doi.org/10.1016/j.est.2019.100900>.
- [32] F.M. Kindermann, A. Noel, S.V. Erhard, A. Jossen, Long-term equalization effects in Li-ion batteries due to local state of charge inhomogeneities and their impact on impedance measurements, *Electrochim. Acta* 185 (2015) 107–116, <http://dx.doi.org/10.1016/j.electacta.2015.10.108>.
- [33] A. Barai, G.H. Chouchelamane, Y. Guo, A. McGordon, P. Jennings, A study on the impact of lithium-ion cell relaxation on electrochemical impedance spectroscopy, *J. Power Sources* 280 (2015) 74–80, <http://dx.doi.org/10.1016/j.jpowsour.2015.01.097>.
- [34] Q.-A. Huang, Y. Shen, Y. Huang, L. Zhang, J. Zhang, Impedance characteristics and diagnoses of automotive lithium-ion batteries at 7.5% to 93.0% state of charge, *Electrochim. Acta* 219 (2016) 751–765, <http://dx.doi.org/10.1016/j.electacta.2016.09.154>.
- [35] M. Schönleber, C. Uhlmann, P. Braun, A. Weber, E. Ivers-Tiffée, A consistent derivation of the impedance of a lithium-ion battery electrode and its dependency on the state-of-charge, *Electrochim. Acta* 243 (2017) 250–259, <http://dx.doi.org/10.1016/j.electacta.2017.05.009>.
- [36] P.J. Osswald, S.V. Erhard, J. Wilhelm, H.E. Hoster, A. Jossen, Simulation and measurement of local potentials of modified commercial cylindrical cells, *J. Electrochem. Soc.* 162 (10) (2015) A2099–A2105, <http://dx.doi.org/10.1149/2.0561510jes>.
- [37] C. Campestrini, M.F. Horsche, I. Zilberman, T. Heil, T. Zimmermann, A. Jossen, Validation and benchmark methods for battery management system functionalities: State of charge estimation algorithms, *J. Energy Storage* 7 (2016) 38–51, <http://dx.doi.org/10.1016/j.est.2016.05.007>.
- [38] M. Schmidt, U. Heider, A. Kuehner, R. Oesten, M. Jungnitz, N. Ignat'ev, P. Sartori, Lithium fluoroalkylphosphates: A new class of conducting salts for electrolytes for high energy lithium-ion batteries, *J. Power Sources* 97–98 (2001) 557–560, [http://dx.doi.org/10.1016/S0378-7753\(01\)00640-1](http://dx.doi.org/10.1016/S0378-7753(01)00640-1).
- [39] R. Amin, Y.-M. Chiang, Characterization of electronic and ionic transport in $\text{Li}_{1-x}\text{Ni}_{0.33}\text{Mn}_{0.33}\text{Co}_{0.33}\text{O}_2$ (nmc₃₃₃) and $\text{Li}_{1-x}\text{Ni}_{0.50}\text{Mn}_{0.20}\text{Co}_{0.30}\text{O}_2$ (nmc₂₃₂) as a function of Li content, *J. Electrochem. Soc.* 163 (8) (2016) A1512–A1517, <http://dx.doi.org/10.1149/2.0131608jes>.
- [40] S. Wang, M. Yan, Y. Li, C. Vinado, J. Yang, Separating electronic and ionic conductivity in mix-conducting layered lithium transition-metal oxides, *J. Power Sources* 393 (2018) 75–82, <http://dx.doi.org/10.1016/j.jpowsour.2018.05.005>.
- [41] S.S. Zhang, K. Xu, T.R. Jow, The low temperature performance of Li-ion batteries, *J. Power Sources* 115 (1) (2003) 137–140, [http://dx.doi.org/10.1016/S0378-7753\(02\)00618-3](http://dx.doi.org/10.1016/S0378-7753(02)00618-3).
- [42] S. Gantenbein, M. Weiss, E. Ivers-Tiffée, Impedance based time-domain modeling of lithium-ion batteries: Part I, *J. Power Sources* 379 (2018) 317–327, <http://dx.doi.org/10.1016/j.jpowsour.2018.01.043>.
- [43] A. Jossen, Fundamentals of battery dynamics, *J. Power Sources* 154 (2) (2006) 530–538, <http://dx.doi.org/10.1016/j.jpowsour.2005.10.041>.
- [44] U. Kreuer, F. Röder, E. Harinath, R.D. Braatz, B. Bedürftig, R. Findeisen, Review—Dynamic models of li-ion batteries for diagnosis and operation: A review and perspective, *J. Electrochem. Soc.* 165 (16) (2018) A3656–A3673, <http://dx.doi.org/10.1149/2.1061814jes>.
- [45] M. Park, X. Zhang, M. Chung, G.B. Less, A.M. Sastry, A review of conduction phenomena in Li-ion batteries, *J. Power Sources* 195 (24) (2010) 7904–7929, <http://dx.doi.org/10.1016/j.jpowsour.2010.06.060>.
- [46] A. Nyman, T.G. Zavalis, R. Elger, M. Behm, G. Lindbergh, Analysis of the polarization in a li-ion battery cell by numerical simulations, *J. Electrochem. Soc.* 157 (11) (2010) A1236, <http://dx.doi.org/10.1149/1.3486161>.
- [47] J. Illig, M. Ender, T. Chrobak, J.P. Schmidt, D. Klotz, E. Ivers-Tiffée, Separation of charge transfer and contact resistance in lifepo 4 -cathodes by impedance modeling, *J. Electrochem. Soc.* 159 (7) (2012) A952–A960, <http://dx.doi.org/10.1149/2.030207jes>.
- [48] R.W. Powell, The thermal and electrical conductivity of carbon and graphite to high temperatures, *Proc. Phys. Soc.* (1939).
- [49] R.A. Bueerschaper, Thermal and electrical conductivity of graphite and carbon at low temperatures, *J. Appl. Phys.* 15 (5) (1944) 452–454, <http://dx.doi.org/10.1063/1.1707454>.
- [50] R.C. Chittick, J.H. Alexander, H.F. Sterling, The preparation and properties of amorphous silicon, *J. Electrochem. Soc.* 116 (1) (1969) 77, <http://dx.doi.org/10.1149/1.2411779>.
- [51] G. Moumouzias, G. Ritzoulis, D. Siapakas, D. Terzidis, Comparative study of LiBF₄, LiAsF₆, LiPF₆, and LiClO₄ as electrolytes in propylene carbonate–diethyl carbonate solutions for Li/LiMn₂O₄ cells, *J. Power Sources* 122 (1) (2003) 57–66, [http://dx.doi.org/10.1016/S0378-7753\(03\)00348-3](http://dx.doi.org/10.1016/S0378-7753(03)00348-3).
- [52] W. Waag, S. Käbitz, D.U. Sauer, Experimental investigation of the lithium-ion battery impedance characteristic at various conditions and aging states and its influence on the application, *Appl. Energy* 102 (2013) 885–897, <http://dx.doi.org/10.1016/j.apenergy.2012.09.030>.
- [53] A. Senyshyn, M.J. Mühlbauer, O. Dolotko, H. Ehrenberg, Low-temperature performance of Li-ion batteries: The behavior of lithiated graphite, *J. Power Sources* 282 (2015) 235–240, <http://dx.doi.org/10.1016/j.jpowsour.2015.02.008>.
- [54] S.J. An, J. Li, C. Daniel, D. Mohanty, S. Nagpure, D.L. Wood, The state of understanding of the lithium-ion-battery graphite solid electrolyte interphase (SEI) and its relationship to formation cycling, *Carbon* 105 (2016) 52–76, <http://dx.doi.org/10.1016/j.carbon.2016.04.008>.
- [55] Q. Zhang, Q. Guo, R.E. White, A new kinetic equation for intercalation electrodes, *J. Electrochem. Soc.* 153 (2) (2006) A301, <http://dx.doi.org/10.1149/1.2142287>.
- [56] C.-K. Huang, J.S. Sakamoto, J. Wolfenstine, S. Surampudi, The limits of low-temperature performance of li-ion cells, *J. Electrochem. Soc.* 147 (8) (2000) 2893, <http://dx.doi.org/10.1149/1.1393622>.
- [57] C.-M. Wu, C.-C. Chang, M. Avdeev, P.-I. Pan, W.-H. Li, In operando detection of lithium diffusion behaviors at low temperature in 18650 Li-ion battery anode, *Physica B* 551 (2018) 305–308, <http://dx.doi.org/10.1016/j.physb.2018.02.032>.
- [58] M. Doyle, Modeling of galvanostatic charge and discharge of the lithium/polymer/insertion cell, *J. Electrochem. Soc.* 140 (6) (1993) 1526, <http://dx.doi.org/10.1149/1.2221597>.
- [59] T.F. Fuller, Simulation and optimization of the dual lithium ion insertion cell, *J. Electrochem. Soc.* 141 (1) (1994) 1, <http://dx.doi.org/10.1149/1.2054684>.
- [60] A. Barai, K. Uddin, W.D. Widanage, A. McGordon, P. Jennings, A study of the influence of measurement timescale on internal resistance characterisation methodologies for lithium-ion cells, *Sci. Rep.* 8 (1) (2018) 21, <http://dx.doi.org/10.1038/s41598-017-18424-5>.
- [61] A. Latz, J. Zausch, Thermodynamic derivation of a Butler–Volmer model for intercalation in Li-ion batteries, *Electrochim. Acta* 110 (2013) 358–362, <http://dx.doi.org/10.1016/j.electacta.2013.06.043>.
- [62] K. Xu, Toward reliable values of electrochemical stability limits for electrolytes, *J. Electrochem. Soc.* 146 (11) (1999) 4172, <http://dx.doi.org/10.1149/1.1392609>.
- [63] T.F. Fuller, Relaxation phenomena in lithium-ion-insertion cells, *J. Electrochem. Soc.* 141 (4) (1994) 982, <http://dx.doi.org/10.1149/1.2054868>.
- [64] K.S. Ng, C.-S. Moo, Y.-P. Chen, Y.-C. Hsieh, Enhanced coulomb counting method for estimating state-of-charge and state-of-health of lithium-ion batteries, *Appl. Energy* 86 (9) (2009) 1506–1511, <http://dx.doi.org/10.1016/j.apenergy.2008.11.021>.
- [65] M. Becherif, M.C. Péra, D. Hissel, S. Jemei, Enhancement of the Coulomb counter estimator by the on-board vehicle determination of battery initial state of charge, *IFAC Proc. Vol.* 45 (21) (2012) 621–626, <http://dx.doi.org/10.3182/20120902-4-FR-2032.00109>.
- [66] M.A. Awadallah, B. Venkatesh, Accuracy improvement of SOC estimation in lithium-ion batteries, *J. Energy Storage* 6 (2016) 95–104, <http://dx.doi.org/10.1016/j.est.2016.03.003>.
- [67] Y. Zou, X. Hu, H. Ma, S.E. Li, Combined state of charge and state of health estimation over lithium-ion battery cell cycle lifespan for electric vehicles, *J. Power Sources* 273 (2015) 793–803, <http://dx.doi.org/10.1016/j.jpowsour.2014.09.146>.
- [68] J. Schmitt, A. Maheshwari, M. Heck, S. Lux, M. Vetter, Impedance change and capacity fade of lithium nickel manganese cobalt oxide-based batteries during calendar aging, *J. Power Sources* 353 (2017) 183–194, <http://dx.doi.org/10.1016/j.jpowsour.2017.03.090>.
- [69] M.A. Hannan, M. Lipu, A. Hussain, A. Mohamed, A review of lithium-ion battery state of charge estimation and management system in electric vehicle applications: Challenges and recommendations, *Renew. Sustain. Energy Rev.* 78 (2017) 834–854, <http://dx.doi.org/10.1016/j.rser.2017.05.001>.
- [70] L. Tao, J. Ma, Y. Cheng, A. Noktehdan, J. Chong, C. Lu, A review of stochastic battery models and health management, *Renew. Sustain. Energy Rev.* 80 (2017) 716–732, <http://dx.doi.org/10.1016/j.rser.2017.05.127>.

Supplementary

Table S1: Investigated subsets \mathbf{S}_i of pulses for generating the temperature estimation function and their minimal estimation error with the corresponding Δt .

Set	Pulse Parameters			Δt / ms $\text{RMSE}_{\mathbf{S}_i}(X_j)_{\min}$ / K							
	I_p	$I_{p,x}$	$t_{r/f}$	X_{01}		X_{02}		X_{03}		X_{04}	
\mathbf{S}_{01}	$\pm 0.5/1.0\text{ C}$	r/f	0.0 s	25	1.10	40	1.20	680	1.80	440	4.10
\mathbf{S}_{02}		r		65	0.99	40	1.23	670	2.05	340	4.32
\mathbf{S}_{03}		f		17	1.14	35	1.21	680	1.68	4300	3.74
\mathbf{S}_{04}	$\pm 0.5\text{ C}$	r/f	0.0 s	35	1.05	40	1.19	680	1.81	440	4.11
\mathbf{S}_{05}		r		90	0.95	35	1.22	680	2.05	180	4.31
\mathbf{S}_{06}		f		35	1.09	40	1.18	680	1.67	4500	3.78
\mathbf{S}_{07}	$\pm 1.0\text{ C}$	r/f	0.0 s	25	1.14	50	1.23	650	1.81	440	4.10
\mathbf{S}_{08}		r		70	1.00	35	1.24	620	2.06	340	4.32
\mathbf{S}_{09}		f		13	1.18	35	1.25	650	1.70	2200	3.66
\mathbf{S}_{10}	$+0.5/1.0\text{ C}$	r/f	0.0 s	35	1.09	40	1.20	530	1.87	380	3.97
\mathbf{S}_{11}		r		830	0.98	40	1.22	590	2.04	260	4.28
\mathbf{S}_{12}		f		800	1.02	14	1.25	70	1.80	590	3.76
\mathbf{S}_{13}	$-0.5/1.0\text{ C}$	r/f	0.0 s	65	1.01	35	1.29	730	2.16	440	4.38
\mathbf{S}_{14}		r		95	0.95	30	1.26	50	2.19	180	4.41
\mathbf{S}_{15}		f		50	1.00	18	1.33	730	2.11	4900	4.09
\mathbf{S}_{16}	$\pm 0.5/1.0\text{ C}$	r/f	0.0/0.4 s	580	1.65	7	1.31	560	1.66	380	3.58
\mathbf{S}_{17}	$\pm 0.5/1.0\text{ C}$	r/f	0.0/4.0 s	590	3.36	8	1.53	80	1.72	500	3.28

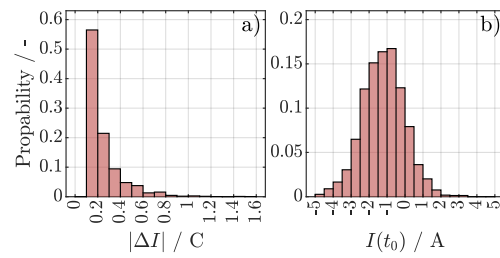


Figure S1: Distribution of the absolute current change $|\Delta I|$ for the module current $i(t)$ of Fig. 2b with a change greater than 0.1 C after 100 ms (a) and the distribution of the corresponding current at the beginning $I(t_0)$ of the detected current changes (b).

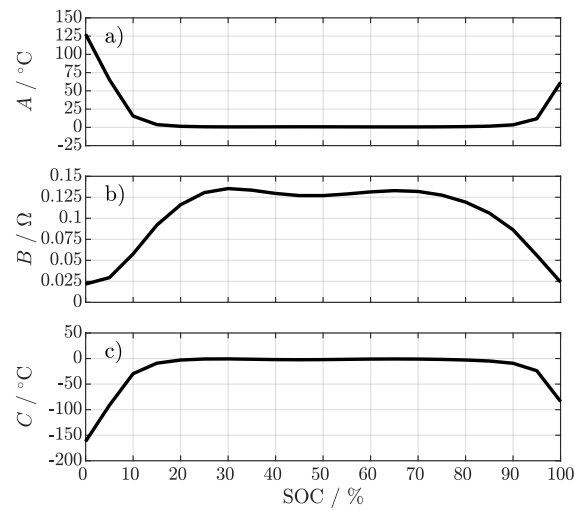


Figure S2: Exemplary parameters A (a), B (b) and C (c) for the temperature estimation function f_P (Eq. (6)). The temperature estimation function was parameterized for $R_{DC,100\text{ ms}}$.

5 Effects of Temperature Inhomogeneities on Battery Modules under Cyclic Aging

The fundamentals in Section 2.3 outlined the various effects of temperature on lifetime, performance, and safety, and thus the need to monitor the temperature in a battery-powered system. The effects in Section 2.3 are primarily related to single cells only and ignore effects that occur in interconnected systems. In addition, aging changes the impedance and capacity of the cells, which directly affects the estimation method in Chapter 4. For this reason, this chapter addresses the aging of LIBs, specifically the effects of aging on the module from Chapter 4 under inhomogeneous temperature boundary conditions, whereas the next chapter focuses on the effects on the temperature estimation method from Chapter 4. As before, the scope of Chapter 5 is once more illustrated in Fig. 5.1.

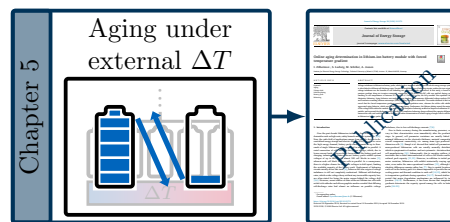


Figure 5.1: Scope of Chapter 5.

In order to investigate the effects of aging on the module under temperature inhomogeneities, the module was continuously cycled until the first cell in the module reached a SOH of approximately 80%. The aging procedure and its results are summarized in the publication *Online aging determination in lithium-ion battery module with forced temperature gradient* [246]. The cyclic aging followed the pattern shown in Fig. 5.2a and is briefly presented in the following. Before starting the aging experiment the cells were initially characterized using a checkup to determine their capacity, OCV, and R_{DC} at 25 °C. After the initial checkup, the cells were fully charged and the external temperature gradient ΔT of 5 K between 25 °C and 30 °C was restored and maintained during the following pattern:

- one cycle with a **constant-current (CC)** discharge/charge,
- followed by a dynamic cycle, which consisted of a discharge with different randomized driving cycles and a **CC** charge,
- and finally three consecutive cycles with **CC** discharge/charge.

This pattern was repeated until twenty cycles (counting **CC** and dynamic cycles) were reached. The dynamic cycles are used later in Chapter 6 to investigate the effect of aging on the temperature estimation method. After a relaxation step and restoring the module temperature to 25 °C, the module was dissipatively balanced to the cell with the lowest cell voltage U_{bal} and another checkup was performed for the individual cells. To negate the effects of the checkup on the module, the individual cell voltages were restored to U_{bal} before restarting the aging pattern.

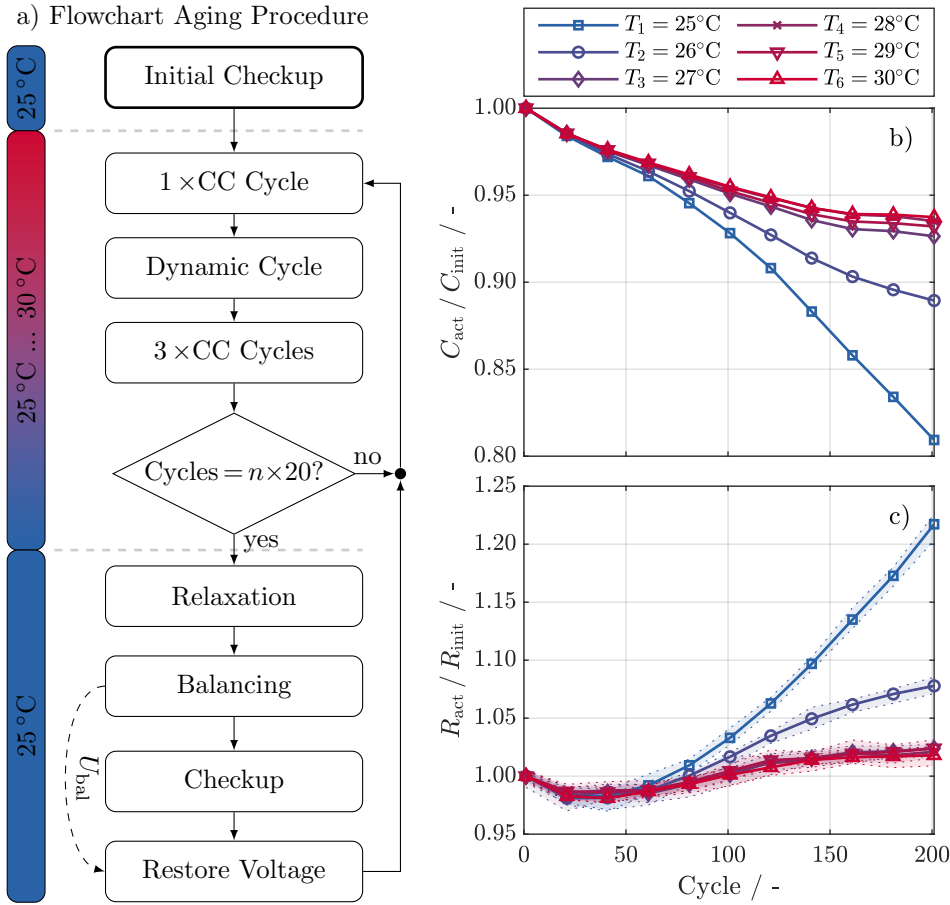


Figure 5.2: a) Flowchart of aging procedure with boundary temperature conditions and evaluation of the checkups showing b) the capacity and c) resistance in relation to the initial checkup. The resistance is the average value for $\Delta t = 120$ ms with the shaded areas as indication for the maximal spread of the different pulses used in the checkup. See Table 2 in [245] for details. Adapted from [245].

The evaluation of the checkups resulted in the capacity fade and resistance change shown in Fig. 5.2b and Fig. 5.2c. Analyzing the checkup data with [differential voltage analysis \(DVA\)](#) and a post-mortem examination of the cells yielded the following additional findings:

- The degradation of the colder cells was linked to lithium plating, possibly due to deeper cycling and the associated increased mechanical stress on the anode.
- The plating reaction was responsible for the majority of the voltage drift between the cells, which in sum amounted to more than 75 mV.
- The voltage drift limited the module's accessible energy. However, the dissipative balancing improved the module utilization.

The results are consistent with Section 2.3 and the effects of low temperature and high current loads on the anode presented in Fig. 2.6, which lead to lithium plating [123; 124] and site loss of particles [18; 180–182] and consequently reduce the capacity and increase the resistance of a cell. By interconnecting the cells in a module, this effect was enhanced for the limiting cell at 25 °C, whereas the voltage window during cycling was limited for the warmer cells above 26 °C, resulting in less aging for these cells. The relatively small gradient of 5 K at moderate temperatures has a critical effect on the system

behavior, emphasizing the importance of temperature monitoring for each cell in a battery powered system. Finally, the study showed that the capacity loss correlates with the cumulative load, which is dissipated during the balancing step in the flowchart of Fig. 5.2a, and hence the SOH of the cells can be determined using this information.

Authors Contribution

Design and execution of the experiment were performed by Ilya Zilberman. Sebastian Ludwig supported the design and execution of the cycling procedure and performed post-mortem analysis. Martin Schiller was involved in the preliminary tests. Andreas Jossen supervised this work, the manuscript was written by Ilya Zilberman and was edited by all authors.

Online aging determination in lithium-ion battery module with forced temperature gradient

Zilberman I., Ludwig S., Schiller M., Jossen A.

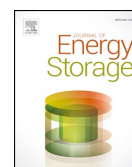
Journal of Energy Storage 28, 101170, 2020

Permanent web link:

<https://doi.org/10.1016/j.est.2019.101170>



Subscription article, reproduced by permission of Elsevier. Authors of this Elsevier article retain the right to include it in a thesis or dissertation, provided it is not published commercially. Permission is not required, but please ensure that you reference the journal as the original source. For more information on this and on other retained rights, please visit: <https://www.elsevier.com/about/our-business/policies/copyright#Author-rights>



Online aging determination in lithium-ion battery module with forced temperature gradient



I. Zilberman*, S. Ludwig, M. Schiller, A. Jossen

Institute for Electrical Energy Storage Technology, Technical University of Munich (TUM), Arcisstr. 21, Munich 80333, Germany

ARTICLE INFO

Keywords:

Aging
Voltage drift
Lithium plating
Battery pack
Balancing

ABSTRACT

Voltage imbalance in lithium-ion battery packs, which leads to impaired utilization of the whole energy-storage system, is often linked to different self-discharge rates. Despite the established use of balancing circuits, neither the true origin of voltage imbalance nor the benefits of cell balancing are as yet completely understood. In this study, a forced temperature gradient along six in-series connected, commercial 18650 nickel-rich/SiC cells was applied during cycles resulting in cell temperatures of between 25 °C and 30 °C. Every 20 cycles, the 6s1p module was equalized using dissipative balancing. Aging behavior was analyzed using checkup measurements, differential voltage analysis (DVA) and conclusive scanning electron microscope (SEM) imaging of negative electrodes. The results obtained in this work reveal that the forced temperature gradient caused different degradation rates, whereas the colder cells exhibited aggravated aging behavior, which was linked to lithium plating. Furthermore, the lithium plating caused the majority of the voltage drift within the module. The application of dissipative balancing enabled an improved utilization of the module, and increased the discharge energy. Finally, the cumulative balancing charge reflected the capacity differences between the cells, and could therefore be used for the online determination of relative aging of single cells or cell blocks in lithium-ion battery packs.

1. Introduction

Over the past decade lithium-ion technology has overcome several downsides such as high costs, safety hazards and short system life [1,2]. Now, the wide field of applications ranges from mobile devices to decentralized energy storage and electric vehicles (EVs). In order to cover the high energy demand, battery packs usually consist of up to thousands of single lithium-ion cells connected in series and in parallel. A serial connection of cells increases the system voltage, which, due to lower current loads, reduces ohmic losses within the battery pack and charging infrastructure. State-of-the-art battery packs exhibit system voltages of up to 800V with almost 200 cell blocks in series [3], whereas each cell block contains cells in parallel. As a consequence, there is a higher chance for cell block voltages to drift apart, limiting the available capacity of the battery pack. Deployment of balancing circuits usually solves this issue [4], however the true origin of voltage imbalance is still not completely understood. Different self-discharge rates, which evoke voltage decay without any irreversible capacity loss, are often stated for being the major reason behind the voltage drift [5,6]. However, recent studies of state-of-the-art lithium-ion cells with nickel-rich cathodes and silicon-graphite anodes revealed that differing self-discharge rates had almost no influence on possible voltage

imbalance, due to low self-discharge currents [7,8].

Due to finite accuracy during the manufacturing processes, cells vary in their characteristics even immediately after the production stage. In general, cell parameter variations are usually linked to minimal differences in the electrode thickness, material composition, overall component connectivity, etc. among same type produced lithium-ion cells [9]. Rumpf et al. showed that initial cell parameters of mass-produced lithium-ion cells are usually normally distributed, which is symptomatic of random - and not systematic - deviation during cell manufacturing [10]. Subsequently, due to negative outliers, it is inevitable that a serial interconnection of cells or cell blocks results in reduced pack capacity [11,12]. However, in addition to initial parameter variation, lithium-ion cells exhibit intrinsically varying aging rates, even under the same operational conditions [13], although the absolute differences remain rather low [7]. Due to spatial location of each cell in the battery pack it is almost impossible to provide the same cooling power and thermal condition to each cell [14,15], which leads to temperature gradients during operation [16,17]. Several studies reported that major degradation mechanisms are influenced by temperature [18,19]. Furthermore, it has been shown that temperature gradients deteriorate the capacity spread among the cells in battery packs [20–22].

* Corresponding author.

E-mail address: ilya.zilberman@tum.de (I. Zilberman).

<https://doi.org/10.1016/j.est.2019.101170>

Received 30 September 2019; Received in revised form 19 November 2019; Accepted 18 December 2019
2352-152X/ © 2020 Elsevier Ltd. All rights reserved.

A forced temperature gradient was applied by Klein et al. in order to investigate the influence of non-uniform temperature conditions on current distributions among cells in parallel [23]. In that investigation, all cells were placed in an enclosing aluminum casing, while Peltier elements on each side of the aluminum block controlled the non-uniform temperature distribution. Using two lithium-ion cells in series, one of which was placed in a climate chamber at 55 °C and another at 25 °C, Chiu et al. showed that temperature gradients have a negative impact on pack performance and can induce safety issues, if cell voltage supervision is neglected [24]. However, no detailed information on voltage imbalance was presented. Cordoba et al. demonstrated via simulation that the lifetime of a battery pack depends on the topology, thermal properties, cell balancing and intrinsic cell parameter variations, whereas the latter were not significant for the aging progression of the pack [25]. Unfortunately, voltage-drift progression was not also presented. Wang et al. compared the aging behaviors of four different battery pack typologies, including serial connection with uniform temperature distribution among all cells [26]. The presented empirical study revealed a higher degradation rate of battery packs compared to single cell aging. More details on possible roots of such behavior were provided by Zheng et al. [27]. Reduced capacity of a battery pack consisting of two cells at 30 °C and 45 °C connected in series was linked to voltage imbalance, which was induced by different rates of loss of lithium inventory. However, no cell balancing during the cycling was applied. A comprehensive aging study of two 8s14p modules with dissipative balancing and naturally emerged temperature gradients was carried out by Campestrini et al. [28]. Results revealed no considerable deviations between single cell and battery pack aging. Owing to the fact that dissipative balancing was active during the entire time and not only during the idle phases, no statement regarding balancing charges and voltage imbalance could be made, since the influence of impedances was more dominant than the influence of different capacities.

To date, there has been no study investigating module aging with forced temperature gradients for in-series connections, while evaluating the root of the voltage imbalance and balancing effort. The goal of this work is to investigate whether balancing charges can be used for the online determination of cell aging. In order to isolate the influence of serial connection, no cells in parallel were considered.

This paper is organized as follows. First, the investigated cells, experimental setup and all test sequences are described. After that, the aging progressions of each cell are evaluated and the roots of the aging are discussed using differential voltage analysis (DVA) and scanning electron microscope (SEM) imaging. Subsequently, the aging progression of the module is presented with corresponding energy, voltage drift and balancing charge progressions. Finally, the results are concluded.

2. Experimental

2.1. Cell and experimental setup

The object of this study was a commercial NMC(nickel-rich)/SiC 18650 high energy lithium-ion cell INR18650-MJ1 from LGChem with a nominal capacity of 3.5 Ah and a specific energy of 259.6 Wh kg⁻¹. According to the cell manufacturer, the recommended operation window is between 4.2 V and 2.5 V. Sturm et al. performed an analysis of active materials and measured half-cell open circuit voltage (OCV) curves for both electrodes of the same MJ1 cell [29]. Electrode balancing revealed an oversized cathode (~ 9.4%) and an almost complete use of the anode (> 99%) [29]. Such extreme utilization of the anode facilitated the high energy density of the cell. The amount of silicon in graphite was measured via inductively coupled plasma-optical emission spectroscopy (ICP-OES) and amounted to ~ 3.5 wt % [29]. The ratio of nickel, manganese and cobalt in the active material of the cathode, determined via ICP-OES, amounted to 82%-6.3%-11.7% respectively, indicating the dominance of nickel in the cathode.

For this experiment, six pristine cells were selected with constant current (CC) discharge capacities at 25 °C of between 3.461 Ah and

Table 1

Overview of parameters of six cells used in the experiment, including the capacity of the cell and the internal resistance.

Parameter	1	2	3	4	5	6	μ	σ
C / Ah	3.461	3.469	3.461	3.47	3.462	3.463	3.464	0.004
$R_{\text{DC10s}} / \text{m}\Omega$	42.3	42.7	42.3	43.0	42.4	42.0	42.45	0.3507

3.47 Ah. The R_{DC10s} value, which is a DC resistance, calculated after a 10 s discharge pulse with 1 C at 50% SOC, ranged from 42.0 m Ω to 43.0 m Ω . Details of each cell, including mean and standard deviation values, are summarized in Table 1.

Fig. 1a shows the test setup for 6s1p module aging with a forced temperature gradient. Each cell was encapsulated in a copper block, in order to allow a thermal contact via heat conduction. The cylinder wall within the cell block was covered with the high thermal conductivity foil Softtherm 86/600 with a thermal resistance of 0.2 K W⁻¹ and a foil thickness of 0.5 mm. Additionally, an increase in cell pressure due to the mechanical expansion of the cell during lithiation was prevented thanks to the low Young modulus of the foil material, which amounted to 77 N cm⁻². PT100 temperature sensors were integrated into copper blocks and were mounted onto the surface of each cell. The sensors were logged with the Cell Measurement Unit (CMU) from Basytec during the experiment. All temperature sensors in the experimental set up underwent offset correction at 25 °C. Each cell block was screwed to a copper flat rail, whereby the contact areas were lubricated with a heat paste, in order to minimize the thermal transfer resistance. Two Peltier elements MCTE1-19913L-S from Multicomp with attached heat sinks were mounted onto each side of the flat bar. Each Peltier element was separately controlled via a custom-made H-bridge circuit allowing a maximum output power of 200 W. For the temperature control, two additional temperature sensors were used, which were placed in small drill holes beneath the Peltier elements. Fig. 1b shows temperature settling with a temperature gradient $\Delta T = 5 \text{ K}$ at 25 °C without any current load. All temperatures became and remained constant after approx. 20 min, although the temperatures were not completely equidistantly distributed. Such discrepancy was due to the fact that the copper set-up was not thermally isolated, which implied a loss heat flow proportional to the temperature difference between the cell block and the environment. All cells, including cell blocks, were placed into an assembly with six clipboards, which connected the positive and negative tabs of the cells with gold contact pins in a 4-wire connection. During cycling, each cell voltage was logged with a CMU. Resolution of the CMU voltage measurement amounted to 0.2 mV with an accuracy of 2.5 mV. The clipboard wiring allowed the connection of all six cells in series. The cycling of the 6s1p module was accomplished with a High Power System (HPS) from Basytec with a maximum current of 5 A and maximum voltage of 60 V. Checkup measurements were performed on the cell level with the Cell Testing System (CTS) from Basytec with a precision of +/- 0.3 mV and +/- 0.5 μA in the smallest range for the voltage and current measurement respectively. For checkup sequences, the wiring of the clipboard assembly was changed to single-cell configuration. Fig. 1c shows cell temperature progression during module cycling with 1 C discharge, 10 min pause and subsequent 1 C charge, while applying a temperature gradient $\Delta T = 5 \text{ K}$ between 25 °C and 30 °C. All cells managed to maintain a quasi-isothermal condition with a maximum deviation of +/- 0.4 °C, which was sufficient for the experiment.

After the aging experiment, SEM images of the anode of a pristine cell, of the cell, which aged at 25 °C and of the cell, which aged at 30 °C were taken. All cells were discharged at 0.5 C–2.5 V using CCCV protocol with the termination current amounting to 50 mA. Afterwards, all cells were opened in a glovebox under argon atmosphere and several samples from each negative electrode were punched out. Finally, SEM images were taken using a JEOL JCM-6000 in high vacuum mode, with an acceleration voltage of 15 kV and a high filament and probe current.

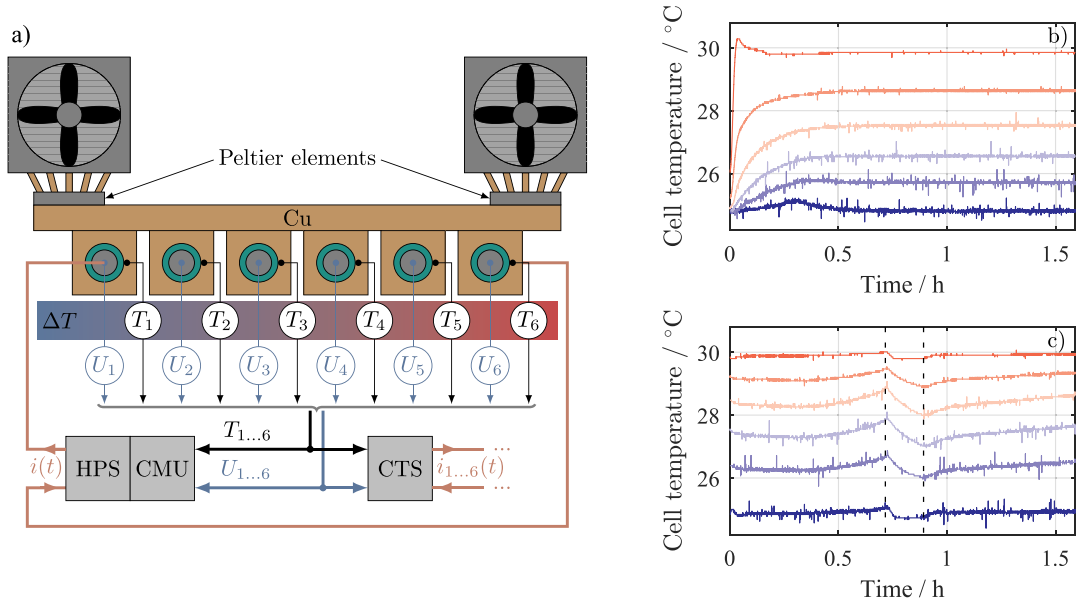


Fig. 1. (a) Overview of the test setup for 6s1p module aging with forced temperature gradient, (b) cell surface temperature while applying a temperature gradient $\Delta T = 5$ K without current load, (c) cell surface temperature during 1 C discharge, 10 min pause and subsequent 1 C charge, while applying a temperature gradient $\Delta T = 5$ K.

2.2. Test sequence

In the following, the checkup routine and overall test sequence are described. Each checkup measurement included a slow constant current (CC) discharge at 0.033 C for the purpose of differential voltage analyses (DVA) and subsequent R_{DC10s} determination at 50% SOC. DVA is an established method in order to analyze degradation mechanisms as loss of lithium inventory (LLI) and loss of active materials (LAM) and was successfully applied in the past [8,30,31]. At the same time, the CC discharge capacity was used for the evaluation of the degradation behavior and the determination of the absolute irreversible capacity loss. In order to guarantee a fixed starting point for a discharge, each cell was charged to 4.2 V via the constant current constant voltage protocol (CCCV). A detailed description of the checkup sequence is given in the Table 2. During the checkup measurements, all cells exhibited 25 °C and were rested at this temperature for at least 2h before the start of the measurement.

Fig. 2 gives an overview of all test sequences during the experiment. After the initial checkup measurement, the module was equalized by charging each cell at 25 °C to 4.2 V using the CCCV protocol, with a termination current of 0.001 C. Subsequently a temperature gradient $\Delta T = 5$ K at 25 °C was applied with a thermal equalization time of 2h, in order to establish a homogeneous temperature distribution of between 25 °C and 30 °C. The cycling routine included four CC cycles with 1 C, and charge and discharge termination at the cell level at 4.2 V and 2.5 V

Table 2
Checkup sequence consists cycles for cell capacity determination (steps 3-4) and determination of internal impedance R_{DC10s} (steps 5-7).

Step	Parameters	Termination
1. Charge CCCV	$I = 0.5$ C, $U = 4.2$ V	$I < 0.001$ C
2. Pause		$t > 30$ min
3. Discharge CC	$I = -0.033$ C	$U < 2.5$ V
4. Pause		$t > 30$ min
5. Charge CC	$I = 0.5$ C	SOC > 50%
6. Pause		$t > 10$ min
7. Discharge CC	$I = -1$ C	$t > 10$ s

respectively. For further investigations, which are not discussed in this work, a concatenation of randomly chosen load profiles from the database presented in [32] was applied with the same discharge termination criteria. A dynamic cycle was deemed to be a single CC cycle, despite the higher charge throughput. Subsequently, the module was CC charged to 4.2 V. Combined with CC cycles, the whole sequence was repeated four times, resulting in 20 consecutive cycles. After each cycling sequence, the temperature distribution was set back to 25 °C. All cells rested for at least 12 h after the last 1 C charge, so that most overpotentials were decayed [33]. Subsequently, clipboard wiring was changed to single cell configuration and each cell was connected to the CTS. Dissipative balancing was performed by discharging each cell to the lowest cell voltage U_{bal} (see Fig. 2) within the module using a CCCV protocol, with the termination current of 0.001 C. After that, the aforementioned checkup sequence from Table 2 took place, with conclusive 0.33 C, 0.66 C, 1 C charge and discharge pulses at 50% SOC, whereas a 1 C discharge pulse was used for R_{DC10s} determination. At the end, each cell was charged to the latest U_{bal} using a CCCV protocol, with a termination current of 0.001 C. This approach reduced the possible influence of checkup measurement on the voltage drift within the module. During the experiment, 200 cycles and 11 checkup measurements were conducted.

3. Results and discussion

3.1. Cell level

In the following, the evaluation of checkup measurements during the experiment is presented and discussed. Fig. 3a depicts the progression of relative capacity for each cell over 200 cycles. The colors in Fig. 3 represent the position of each cell along the temperature gradient, whereby blue represents the coldest cell at 25 °C, and red represents the hottest cell at 30 °C. The results reveal that the forced temperature gradient facilitated different aging rates within in-series connection. During the first 40 cycles, all cells exhibited similar aging rates. Afterwards, the cell at 25 °C started to show an aggravated aging behavior, which continued till the end of the experiment, when it reached almost 80% of the initial capacity. The cell at 26 °C also exhibited an aggravated capacity loss, however the aging rate

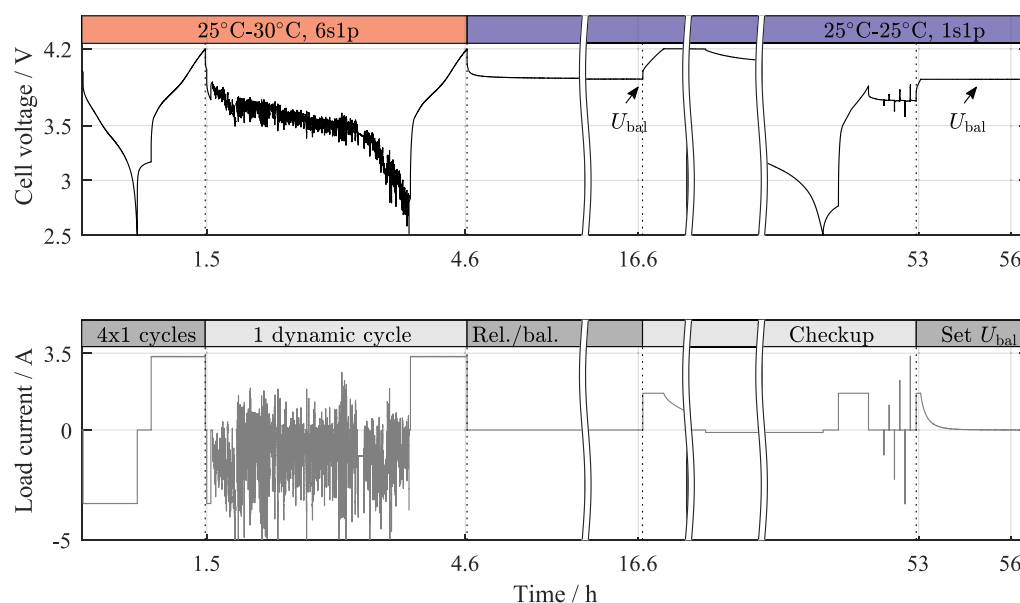


Fig. 2. Overview of all test sequences used in the aging experiment. Figure at the bottom depicts different current loads, whereas the figure at the top depicts the corresponding voltage response.

seemed to decelerate towards the end of the experiment, when it finally reached approx. 90% of the initial capacity. Cells above 26 °C all showed similar aging behavior, reaching approx. 94% of their initial capacities after 200 cycles. The progression of the impedance increase is depicted in Fig. 3b. The cell at 25 °C showed the highest increase, resulting in approx. 130% of the initial impedance at the end of the experiment. Similar to capacity progression, the cell at 26 °C also showed an additional impedance increase, whereas cells above 26 °C exhibited the least impedance increase. Furthermore, Fig. 3c presents the correlation between the relative capacity loss and impedance increase, which is similar for all cells in the module. It stands to reason that impedance could be used for the online determination of aging inhomogeneities within the scope of the presented 6s1p MJ1 module aging. However, not all lithium-ion cells exhibit such a consistent correlation between capacity loss and impedance increase [34], which makes this method not generally applicable.

The aforementioned aging behavior might be linked to the fact, that the charge throughput of a serial connection of cells is usually determined by the cell, which reaches the end of charge and discharge voltages first. It results in maximum depth of discharge (DOD) for the limiting cell and decreasing DOD for other cells during the course of aging. Furthermore, temperature dependency on degradation behavior during cycling and in particular improved capacity retention at elevated temperatures, were already reported in literature [35–37]. Such behavior was linked to irreversible capacity loss due to lithium plating

at lower temperatures.

In general, power fade and deteriorating energy storage ability are often linked to side reactions and the loss of active materials (LAM) on both electrodes [30,38]. LAM is usually attributed to the particle cracking and loss of electrical contact [30]. In that way, a part of the electrode's active mass is no longer available for the intercalation and deintercalation of lithium, which can be observed in the compression of the half-cell potential [39]. Anodic side reactions, such as the growth and repair of the solid electrolyte interface (SEI), result in LLI, which leads to a delithiation of the negative electrode and an associated shift of the anode half-cell potential, resulting in capacity decrease [40]. Several studies have shown that both degradation mechanisms might occur simultaneously in cells with a pure graphite anode [41] and with a silicon-graphite blend anode [42,43]. Furthermore, LAM at low SOC's was deemed to be responsible for degradation of the silicon-graphite electrode due to high mechanical stress during lithiation [44,45].

Cathodic side reactions, such as electrolyte oxidation and transition-metal dissolution, provoke a reinsertion of lithium into the positive electrode, which can be observed in form of a potential decrease without any capacity loss [46,47], and might even lead to an increase in cell capacity [31]. Similarly to anodic side reactions, cathodic side reactions also result in an associated shift of the cathode half-cell potential. However, side reactions, such as transition metal dissolution, might also lead to LAM. It has been shown that increased NMC cathode

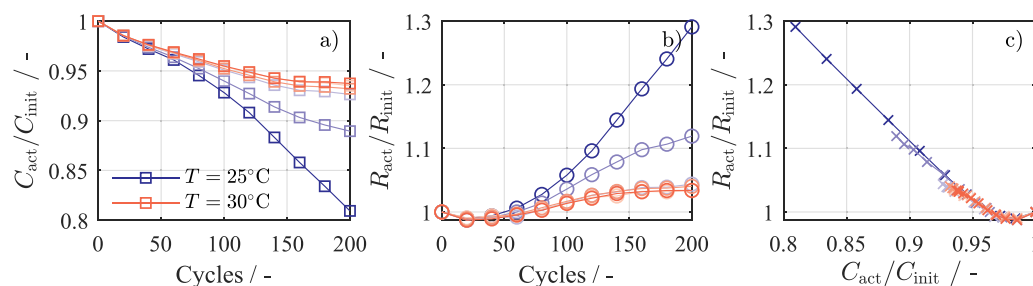


Fig. 3. (a) Relative capacity loss of each cell, (b) relative impedance increase of each cell, (c) correlation between capacity loss and impedance increase.

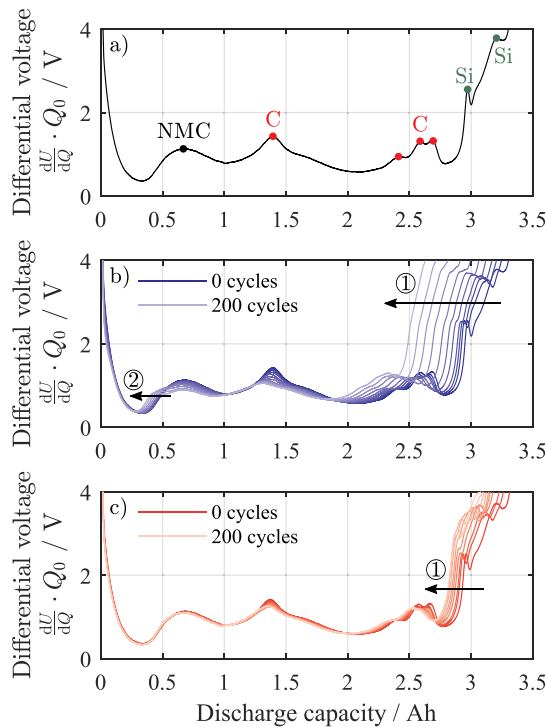


Fig. 4. (a) Measured differential voltage of the full cell for a 0.033 C discharge with assigned characteristic material markers, (b) differential voltage progression of the cell cycled at 25 °C, (c) differential voltage progression of the cell cycled at 30 °C.

potential accelerated the degradation of active materials [48,49], especially in the case of nickel rich cathodes [50].

Due to the shift and compression of half-cell potentials, the described degradation mechanisms can be observed via differential voltage analysis (DVA), which has been already successfully applied in the past [51]. Fig. 4a depicts the differential voltage in the discharge direction of the MJ1 cell, with accordingly distinctive material markers. Graphite electrodes usually exhibit a steep ascent of the potential towards delithiation [52]. Silicon-graphite composite electrodes, on the other hand, exhibit a smoother increase [53]. A smooth increase of this type results in two distinctive peaks in the differential voltage of the negative electrode and can be also observed in the full-cell characteristic between 2.9 Ah and 3.4 Ah in Fig. 4a. The distance between those two peaks is attributed to the storage capability of silicon. The peak at ca. 1.4 Ah indicates the phase transition between LiC_{12} and LiC_6 [54]. Further phase transition peaks of graphite are located between 2.4 Ah and 2.7 Ah. Finally, the nickel-rich cathode is represented only with one peak at ca. 0.7 Ah [29].

Fig. 4b shows the evolution of differential voltages of the cell at 25 °C during cycling, whereby all curves are aligned at the left side. Over the course of aging, the distance between Si distinctive peaks decreased, such that no part of either peak was noticeable, which is a sign for the loss of storage capability of silicon in the anode. However, the overall cell capacity loss was much higher and bore no relation to the loss of silicon, as depicted by ① in Fig. 4b. Furthermore, a shift of the NMC peak was observed ②. Previously, a case study was conducted, which investigated how different degradation mechanisms influence the differential voltage of the full cell through the compression and shifting of the half-cell potentials of the MJ1 cell [8]. The results revealed that the shift in the NMC peak as in ② is a sign of LAM at the negative electrode, which occurred at low SOC. Despite a small shift in

the main graphite peak, no statement regarding the LLI can be made, since the negative electrode suffered from LAM according to DVA. The cell at 30 °C did not exhibit such severe degradation, as shown in the evolution of differential voltages during cycling in Fig. 4c. It can be seen that the presence of silicon faded ① over the course of aging, however, in contrast to the cell at 25 °C, the remainder of the differential voltage characteristics stayed almost the same.

From DVA it can be concluded that both cells suffered from a loss of silicon in the anode during cycle aging, which has been already reported in literature [44,45]. Such behavior was linked to the high volumetric expansion of silicon particles during the lithiation, which facilitated the separation of the electrical contact between particles. The cell at 25 °C suffered additionally from LAM at low SOC, which most likely led to the observed capacity decrease.

Deteriorated aging behavior is often linked to the deposition of metallic lithium, also referred to as lithium plating, which occurs on the negative electrode during charging [55]. Triggered by cell operation at high charge rates and/or low temperatures, lithium plating leads to severe capacity loss due to the formation of passivating surface films and due to the consumption of lithium [56,57]. Lithium plating occurs if the potential at the graphite electrode-electrolyte interface falls below 0V vs. Li/Li^+ . Under certain circumstances a reverse reaction - lithium stripping - can be observed, however this process is not completely reversible [58,59]. The presence of lithium stripping is usually a clear evidence for occurred plating reaction. A stripping reaction is evident in the relaxation voltage, which exhibits a slower relaxation, sometimes even a plateau and is usually lower than normal relaxation voltage [60,61].

Fig. 5a depicts cell voltages and Fig. 5b temperatures during the 140th cycle and the subsequent relaxation phase at 25 °C before the balancing routine. After the cycling, the temperature control automatically switched to 25 °C for each cell and reached its set temperature

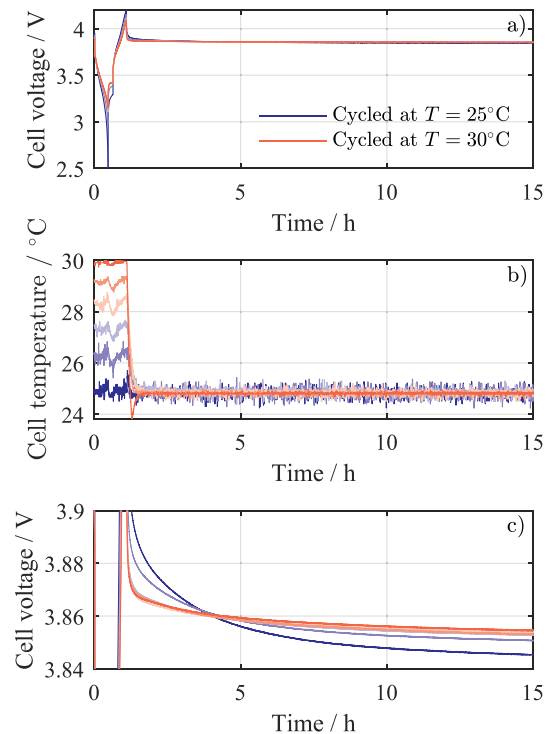


Fig. 5. (a) Cell voltages and (b) temperature during the 140th cycle and subsequent relaxation phase at 25 °C, (c) enlarged view of cell voltages during the relaxation phase.

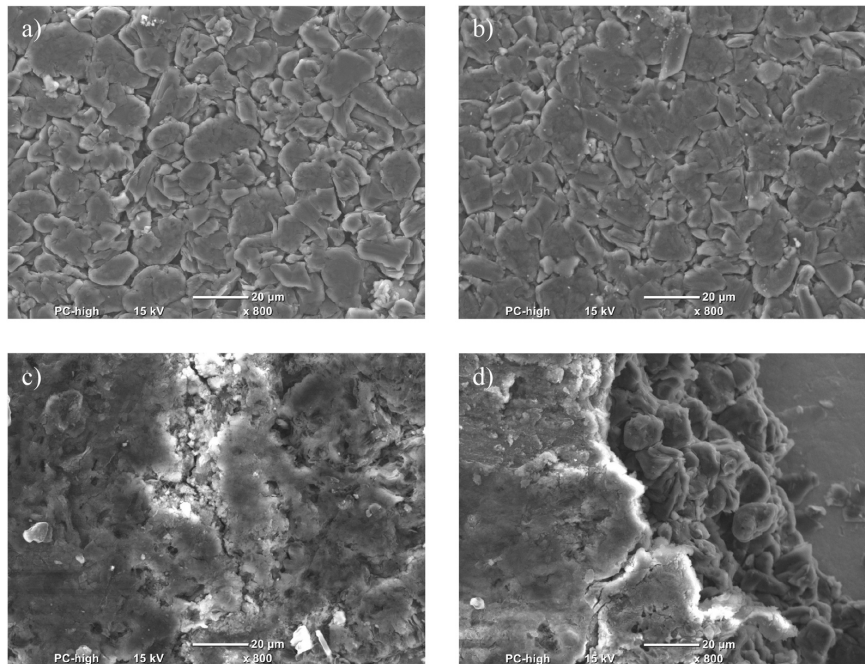


Fig. 6. SEM images of the negative electrode of (a) pristine cell, (b) cell aged at 30 °C, (c) cell aged at 25 °C, (d) cell aged at 25 °C with a provoked crack.

after 20 min, as shown in Fig. 5b. Therefore, during the relaxation process, all cells exhibited 25 °C. Fig 5c depicts an enlarged view of Fig. 5a. It can be seen that cells aged at 25 °C and 26 °C, which also showed deteriorated aging behavior, differed in voltage relaxation. The cell aged at 25 °C in particular exhibited the aforementioned stripping behavior, whereas cells above 26 °C exhibited a normal voltage relaxation behavior. Severe aging behavior of the cell at 25 °C was therefore most likely due to lithium plating. However, since it has been shown that voltage-plateau technique might be misleading due to concentration gradients within the cell [62], a post-mortem analysis was carried out and is described in the following.

In order to verify the presence of lithium plating, SEM images of the negative electrode were taken, whereby a pristine cell, the cell aged at 25 °C and the cell aged at 30 °C were compared. In the case of the inhomogeneous texture of the electrode, the probes were taken from areas which were the majority of the electrodes surface. Fig. 6a shows the anode particles of the pristine cell. The structure of the anode in Fig. 6b, which belongs to the cell aged at 30 °C, is not entirely altered, however, the arrangement of particles seems to be more dense. Such slight electrode

degradation is in accordance with results from the DVA. In contrast, Fig. 6c, which represents the anode of the cell aged at 25 °C, shows severe structural differences. Individual graphite particles are no longer visible due to the inhomogeneous surface film near the separator. A provoked crack of the graphite electrode, which is shown in Fig. 6d, confirms that the observed film is confined to the surface layer, since intact particles are visible beneath it. Combined with results from DVA and voltage relaxation, the observed surface film is most likely a deposition of metallic lithium. Several simulative investigation of lithium plating revealed that such films initially occur near the separator [58,63], which is in accordance with the findings from the evaluation of SEM images.

Despite the use of easily deformed heat foil in the cell holder, the compression of cells can not be completely ruled out. It has been reported, that compression might facilitate lithium plating [64]. However, since all cells from the 6s1p module were placed in cell holders, and a clear temperature dependency regarding the aging behavior was observed, compression was most likely not the major reason for lithium plating.

The evaluation of single cell aging behavior revealed that the forced temperature gradient was able to cause different aging rates within a

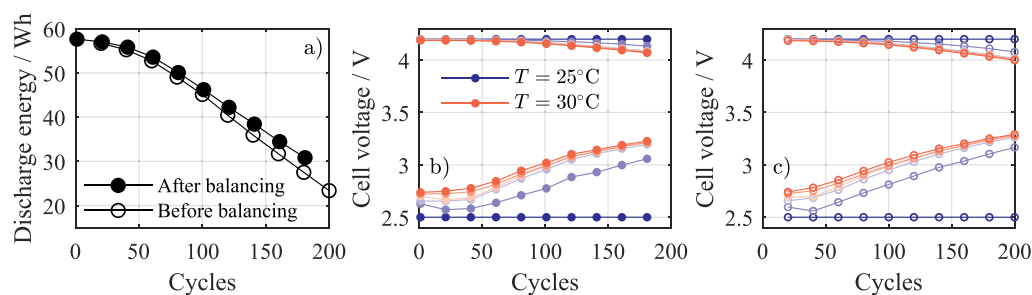


Fig. 7. (a) Progression of the module CC discharge energy before and after balancing, (b) end of charge and discharge voltages of each cell in the first cycle after balancing, (c) end of charge and discharge voltages of each cell in the last cycle before balancing.

6s1p module. During cycle aging, all cells suffered from the loss of storage capability of the silicon. Cells aged at 25 °C and 26 °C additionally experienced lithium plating, which led to severe capacity loss due to the loss of active materials of the anode at low SOC. Furthermore, the limiting cell experienced the highest DOD and therefore the highest mechanical stress, which could increase overpotentials and facilitate lithium plating.

3.2. Module level

In the following, the influence of different cell degradation rates on module aging behavior is described and progressions of module discharge energy, voltage imbalance and balancing charges are presented. Fig. 7a shows the progression of module discharge energy, which was withdrawn in the last cycle before and at the second cycle after the balancing procedure. The second discharge cycle was used for comparison due to the application of the dissipative equalization technique, which deteriorated the discharge energy of the first cycle after balancing. The results reveal that the discharge energy decreased almost by half after 200 cycles, despite the positive influence of cell balancing.

The origin of such behavior lay in the progression of cell voltages, which are shown in Fig. 7b and c. Fig. 7b depicts the end-of-charge and end-of-discharge voltages after - and Fig. 7c before - the balancing routine. From the beginning of the experiment, the cell at 25 °C remained the limiting cell, reaching the end-of-charge and discharge voltages first, whereas the cell at 30 °C exhibited the highest end-of-discharge voltage as early as the first cycle. Such behavior was linked to reduced overpotentials of lithium-ion cells at higher temperatures [65]. The combination of aggravated capacity loss and impedance increase of the cell at 25 °C, and steep slope of the OCV in the low SOC region resulted in an increasing difference between the end-of-charge voltages. Such behavior is not unusual, since the goal of dissipative balancing is to maximize the available energy by equalizing cell voltages at the upper area of the SOC. In that way, cells would exhibit higher voltage during the discharge, resulting in a higher voltage discrepancy towards the end-of-discharge, as confirmed by the presented results.

Despite the application of dissipative balancing, the differences between single end-of-charge voltages also increased during the module aging. Due to the lack of a CV phase after CC charging and the high impedance of the

limiting cell, the relaxation voltage was several hundred mV lower than the end-of-charge voltage at 4.2 V. Equalization at the relaxation voltage and increasing capacity difference consequently led to a voltage drift at the end of charge. Such balancing strategy would not be applicable for industrial applications, since the module was not optimally utilized, however, it demonstrated that dissipative balancing was able to improve overall energy content. The influence of balancing can be also seen in Fig. 7b, in which the end-of-charge voltages are slightly higher than in Fig. 7c, which allowed a longer discharge, resulting in increased energy.

The dissipated balancing charges for each cell after every 20 cycles are shown in Fig. 8a. The limiting cell at 25 °C exhibited the lowest voltage before the balancing routine. Therefore its balancing charge remained zero over the course of the experiment. Even after the first 20 cycles, the balancing charge started to increase, whereas the cell at 30 °C remained the cell with the highest balancing effort. Since the differences between single balancing charges were not clearly separable, the cumulative balancing charge was additionally evaluated, which is shown in Fig. 8b. The progressions of cumulative balancing charges reveal a finer resolution of the temperature dependency, whereas the higher temperature during cycling resulted in a higher cumulative balancing charge. Fig. 8c depicts differences between the capacity of the limiting and the remaining cells during the experiment. A correlation plot between the cumulative balancing charge and capacity differences, shown in Fig. 8f, reveals a strong correlation (Pearson = 0.995) between the two parameters. It can be therefore deduced that within the scope of the presented experiment, a cumulative balancing charge might be used for online aging determination, or at least for the recognition of lithium plating.

Fig. 8d depicts voltage differences between the limiting and the remaining cells immediately before the balancing procedure, and after 12 h of voltage relaxation at 25 °C. The voltage differences increased during the aging, despite the application of dissipative balancing every 20 cycles. At the end of the experiment, the voltage difference between the limiting and remaining cells amounted to almost 20 mV. Assuming that changes in OCV during aging are negligible and that all cells exhibit almost the same self-discharge rates, an equal charge and discharge of the in-series connection of cells would not lead to any voltage drift, since all cell blocks would exhibit the same charge throughput. Even altering capacities and impedances would not cause a voltage drift, as long as the charge throughput were the

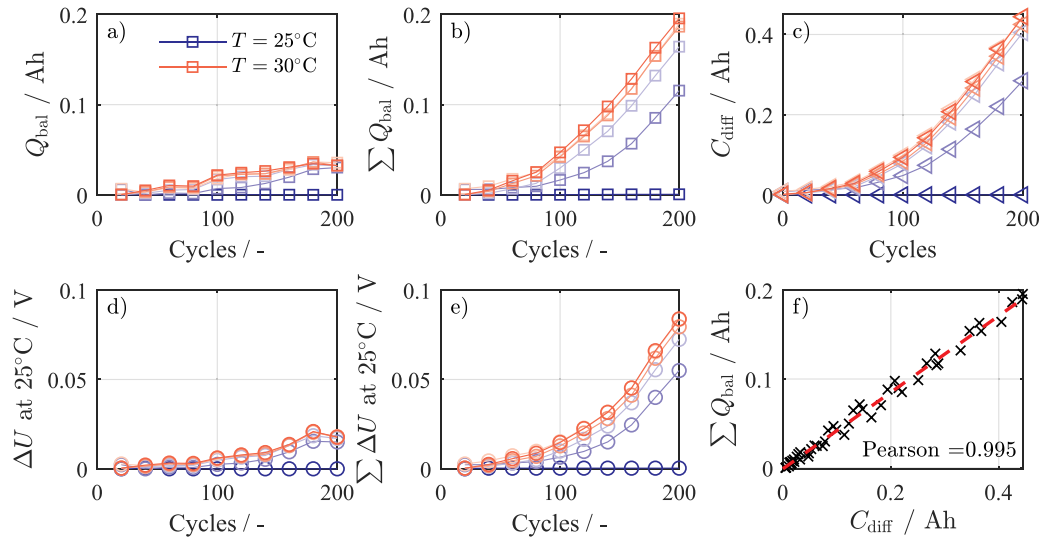


Fig. 8. (a) Progression of balancing charge of each cell, (b) cumulative balancing charge of each cell, (c) capacity differences between the limiting and remaining cells, (d) progression of voltage differences between cells with the lowest and remaining voltages at the end of the relaxation phase, (e) cumulative voltage differences between cells with the lowest and remaining voltages at the end of the relaxation phase, (f) correlation between cumulative balancing charge and capacity differences with the corresponding Pearson coefficient.

same for all cell blocks. In contrast to that, in the case of lithium plating, the charge would not only participate in the main intercalation reaction but also in parasitic plating reaction, resulting in the formation of passivating surface films. In that way, cells, which experienced lithium plating would exhibit lower charge throughput, resulting in lower SOC. Therefore, in combination with the asymmetric characteristic of the reversed stripping reaction [60], the observed high voltage drift within the 6s1p module is most likely linked to lithium plating.

The cumulative voltage differences, as shown in Fig. 8e reveal similar dependency in comparison to cumulative balancing charges. However, this outcome is due to the linear relationship between the OCV and SOC, where the evaluation of relaxation voltages took place. If the OCV characteristic exhibited a high curvature or, in general, a non-linear behavior, the cumulative voltage differences would be misleading.

Despite the fact that the complete potential of the 6s1p module was not utilized during cycling, dissipative balancing accomplished to increase the energy of the module. Voltage drift was most likely brought about by the lithium-plating reaction of colder cells and cumulative balancing charge was able to reflect differences in the capacity and aging behavior of single cells.

4. Summary and conclusion

In this work, cycle aging behavior of a 6s1p battery module with dissipative balancing and forced temperature distribution was investigated. The temperature gradient amounted to 5 K, ranging from 25 °C to 30 °C during cycling. After every 20 cycles the temperature of all cells was set to 25 °C, after which the balancing routine and checkup measurements were conducted. Degradation mechanisms were analyzed using differential voltages over the course of the experiment. Additionally, SEM images of negative electrodes were taken as a part of post-mortem analysis. The main findings are summarized below:

1. Temperature gradient during cycling led to differing aging rates, whereas the colder cells showed aggravated aging behavior. DVA revealed that all cells suffered from the loss of storage capabilities of silicon. However, the severe degradation of colder cells was linked to lithium plating, possibly due to deeper cycling and therefore the increased mechanical stress of the negative electrode.
2. Plating reaction caused the majority of the voltage drift within the in-series configuration of cells, limiting the module's available energy. The application of dissipative balancing allowed an improved utilization of the module.
3. The cumulative balancing charge showed a strong correlation with capacity differences between the limiting and remaining cells.

The results of this experimental study suggest, that the evaluation of the cumulative balancing charge might be used for the online detection of lithium plating in MJ1 battery packs. However, there are some limitations to this approach. The equalization must take place in an idle state, in order to ensure that the terminal voltage is not disturbed by high load currents. Additionally, a homogeneous temperature distribution must be provided during the balancing procedure. Furthermore, a sufficient voltage measurement accuracy, low tolerance balancing resistors and stable clock source for numerical current integration have to be considered in the BMS design. Therefore, further validation must be performed in order to ensure the applicability of the presented balancing strategy with different lithium-ion chemistries, battery pack configurations and different thermal gradients. Future work will address how different aging mechanisms affect the OCV and the terminal voltage, and subsequently the state of inhomogeneity of the battery pack.

CRedit authorship contribution statement

I. Zilberman: Conceptualization, Methodology, Software, Validation, Visualization, Investigation, Writing - original draft, Writing

- review & editing, S. Ludwig: Writing - review & editing, Methodology, Investigation, M. Schiller: Validation, A. Jossen: Resources, Writing - review & editing.

Declaration of Competing Interest

The authors declare that they have no known competing financial interests or personal relationships that could have appeared to influence the work reported in this paper.

Acknowledgements

This work has received funding from the European Union's Horizon 2020 research and innovation program under the grant "Electric Vehicle Enhanced Range, Lifetime And Safety Through INGenious battery management" (EVERLASTING 713771). The presented data of this work is available under [<http://doi.org/10.4121/uuid:f4575140-b2cf-4aa2-a6d5-e48d60dc0f8f>]

The authors would like to thank Korbinian Schmidt for supporting with the design and assembly of the experimental setup.

References

- [1] B. Scrosati, J. Garche, Lithium batteries: Status, prospects and future, *J. Power Sources* 195 (9) (2010) 2419–2430, <https://doi.org/10.1016/j.jpowsour.2009.11.048>.
- [2] G.E. Blomgren, The development and future of lithium ion batteries, *J. Electrochem. Soc.* 164 (1) (2017) A5019–A5025, <https://doi.org/10.1149/2.0251701jes>.
- [3] V. Reber, Neue Möglichkeiten Durch Laden mit 800 Volt, 2016 (accessed March 15, 2019), URL: [https://www.porscheengineering.com/filestore/download/peg/de/pemagazin-01-2016-artikel-e-power-%E2%80%93-Neue-M%3C%B6gmbh-01-2016.pdf](https://www.porscheengineering.com/filestore/download/peg/de/pemagazin-01-2016-artikel-e-power/default/047e5361-3dfb-11e6-8697-0019999cd470/e-power-%E2%80%93-Neue-M%3C%B6gmbh-01-2016.pdf).
- [4] M.M. Hoque, M.A. Hannan, A. Mohamed, A. Ayob, Battery charge equalization controller in electric vehicle applications: a review, *Renew. Sustain. Energy Rev.* 75 (2017) 1363–1385, <https://doi.org/10.1016/j.rser.2016.11.126>.
- [5] L. Zhou, Y. Zheng, M. Ouyang, L. Lu, A study on parameter variation effects on battery packs for electric vehicles, *J. Power Sources* 364 (2017) 242–252, <https://doi.org/10.1016/j.jpowsour.2017.08.033>.
- [6] L. Lu, X. Han, J. Li, J. Hua, M. Ouyang, A review on the key issues for lithium-ion battery management in electric vehicles, *J. Power Sources* 226 (2013) 272–288, <https://doi.org/10.1016/j.jpowsour.2012.10.060>.
- [7] I. Zilberman, S. Ludwig, A. Jossen, Cell-to-cell variation of calendar aging and reversible self-discharge in 18650 nickel-rich, silicon-graphite lithium-ion cells, *J. Energy Storage* 26 (2019) 100900, <https://doi.org/10.1016/j.est.2019.100900>.
- [8] I. Zilberman, J. Sturm, A. Jossen, Reversible self-discharge and calendar aging of 18650 nickel-rich, silicon-graphite lithium-ion cells, *J. Power Sources* 425 (2019) 217–226, <https://doi.org/10.1016/j.jpowsour.2019.03.109>.
- [9] J. Schnell, C. Nentwich, F. Endres, A. Kollenda, F. Distel, T. Knoche, G. Reinhart, Data mining in lithium-ion battery cell production, *J. Power Sources* 413 (2019) 360–366, <https://doi.org/10.1016/j.jpowsour.2018.12.062>.
- [10] K. Rumpf, M. Naumann, A. Jossen, Experimental investigation of parametric cell-to-cell variation and correlation based on 1100 commercial lithium-ion cells, *J. Energy Storage* 14 (2017) 224–243, <https://doi.org/10.1016/j.est.2017.09.010>.
- [11] B. Kenney, K. Darcovich, D.D. MacNeil, L.J. Davidson, Modelling the impact of variations in electrode manufacturing on lithium-ion battery modules, *J. Power Sources* 213 (2012) 391–401, <https://doi.org/10.1016/j.jpowsour.2012.03.065>.
- [12] D. Shin, M. Poncino, E. Macii, Naehyuck Chang, A statistical model-based cell-to-cell variability management of li-ion battery pack, *IEEE Trans. Computer-Aided Des. Integr. Circuits Syst.* 34 (2) (2015) 252–265, <https://doi.org/10.1109/TCAD.2014.2384506>.
- [13] T. Baumhöfer, M. Brühl, S. Rothgang, D.U. Sauer, Production caused variation in capacity aging trend and correlation to initial cell performance, *J. Power Sources* 247 (2014) 332–338, <https://doi.org/10.1016/j.jpowsour.2013.08.108>.
- [14] A. Tang, J. Li, L. Lou, C. Shan, X. Yuan, Optimization design and numerical study on water cooling structure for power lithium battery pack, *Appl. Thermal Eng.* 159 (2019) 113760, <https://doi.org/10.1016/j.applthermaleng.2019.113760>.
- [15] C. Zhao, W. Cao, T. Dong, F. Jiang, Thermal behavior study of discharging/charging cylindrical lithium-ion battery module cooled by channelled liquid flow, *Int. J. Heat Mass Transf.* 120 (2018) 751–762, <https://doi.org/10.1016/j.jheatmasstransfer.2017.12.083>.
- [16] B. Wu, Y. Yuft, M. Marinescu, G.J. Offer, R.F. Martinez-Botas, N.P. Brandon, Coupled thermal-electrochemical modelling of uneven heat generation in lithium-ion battery packs, *J. Power Sources* 243 (2013) 544–554, <https://doi.org/10.1016/j.jpowsour.2013.05.164>.
- [17] X.M. Xu, R. He, Research on the heat dissipation performance of battery pack based on forced air cooling, *J. Power Sources* 240 (2013) 33–41, <https://doi.org/10.1016/j.jpowsour.2013.03.004>.
- [18] M. Ecker, N. Nieto, S. Käbitz, J. Schmalstieg, H. Blanke, A. Warnecke, D.U. Sauer, Calendar and cycle life study of li(nimnco)o2-based 18650 lithium-ion batteries, *J. Power Sources* 248 (2014) 839–851, <https://doi.org/10.1016/j.jpowsour.2013.09.143>.

- [19] M. Naumann, M. Schimpe, P. Keil, H.C. Hesse, A. Jossen, Analysis and modeling of calendar aging of a commercial lifePo4/graphite cell, *J. Energy Storage* 17 (2018) 153–169, <https://doi.org/10.1016/j.est.2018.01.019>.
- [20] M. Baumann, L. Wildfeuer, S. Rohr, M. Lienkamp, Parameter variations within li-ion battery packs – theoretical investigations and experimental quantification, *J. Energy Storage* 18 (2018) 295–307, <https://doi.org/10.1016/j.est.2018.04.031>.
- [21] S.F. Schuster, M.J. Brand, P. Berg, M. Gleissenberger, A. Jossen, Lithium-ion cell-to-cell variation during battery electric vehicle operation, *J. Power Sources* 297 (2015) 242–251, <https://doi.org/10.1016/j.jpowsour.2015.08.001>.
- [22] S. Paul, C. Diegelmann, H. Kabza, W. Tillmetz, Analysis of ageing inhomogeneities in lithium-ion battery systems, *J. Power Sources* 239 (2013) 642–650, <https://doi.org/10.1016/j.jpowsour.2013.01.068>.
- [23] M.P. Klein, J.W. Park, Current distribution measurements in parallel-connected lithium-ion cylindrical cells under non-uniform temperature conditions, *J. Electrochem. Soc.* 164 (9) (2017) A1893–A1906, <https://doi.org/10.1149/2.0011709jes>.
- [24] K.-C. Chiu, C.-H. Lin, S.-F. Yeh, Y.-H. Lin, C.-S. Huang, K.-C. Chen, Cycle life analysis of series connected lithium-ion batteries with temperature difference, *J. Power Sources* 263 (2014) 75–84, <https://doi.org/10.1016/j.jpowsour.2014.04.034>.
- [25] A. Cordoba-Arenas, S. Onori, G. Rizzoni, A control-oriented lithium-ion battery pack model for plug-in hybrid electric vehicle cycle-life studies and system design with consideration of health management, *J. Power Sources* 279 (2015) 791–808, <https://doi.org/10.1016/j.jpowsour.2014.12.048>.
- [26] X. Wang, Z. Wang, L. Wang, Z. Wang, H. Guo, Dependency analysis and degradation process-dependent modeling of lithium-ion battery packs, *J. Power Sources* 414 (2019) 318–326, <https://doi.org/10.1016/j.jpowsour.2019.01.021>.
- [27] Y. Zheng, M. Ouyang, L. Lu, J. Li, Understanding aging mechanisms in lithium-ion battery packs: From cell capacity loss to pack capacity evolution, *J. Power Sources* 278 (2015) 287–295, <https://doi.org/10.1016/j.jpowsour.2014.12.105>.
- [28] C. Campestrini, P. Keil, S.F. Schuster, A. Jossen, Ageing of lithium-ion battery modules with dissipative balancing compared with single-cell ageing, *J. Energy Storage* 6 (2016) 142–152, <https://doi.org/10.1016/j.est.2016.03.004>.
- [29] J. Sturm, A. Rheinfeld, I. Zilberman, F.B. Spingler, S. Kosch, F. Frie, A. Jossen, Modeling and simulation of inhomogeneities in a 18650 nickel-rich, silicon-graphite lithium-ion cell during fast charging, *J. Power Sources* 412 (2019) 204–223, <https://doi.org/10.1016/j.jpowsour.2018.11.043>.
- [30] C.R. Birkl, M.R. Roberts, E. McTurk, P.G. Bruce, D.A. Howey, Degradation diagnostics for lithium ion cells, *J. Power Sources* 341 (2017) 373–386, <https://doi.org/10.1016/j.jpowsour.2016.12.011>.
- [31] P. Keil, A. Jossen, Calendar aging of nca lithium-ion batteries investigated by differential voltage analysis and coulomb tracking, *J. Electrochem. Soc.* 164 (1) (2017) A6066–A6074, <https://doi.org/10.1149/2.0091701jes>.
- [32] C. Campestrini, M.F. Horsche, I. Zilberman, T. Heil, T. Zimmermann, A. Jossen, Validation and benchmark methods for battery management system functionalities: State of charge estimation algorithms, *J. Energy Storage* 7 (2016) 38–51, <https://doi.org/10.1016/j.est.2016.05.007>.
- [33] F.M. Kindermann, A. Noel, S.V. Erhard, A. Jossen, Long-term equalization effects in li-ion batteries due to local state of charge inhomogeneities and their impact on impedance measurements, *Electrochimica Acta* 185 (2015) 107–116, <https://doi.org/10.1016/j.electacta.2015.10.108>.
- [34] N. Omar, M.A. Monem, Y. Firouz, J. Salminen, J. Smekens, O. Hegazy, H. Gaulous, G. Mulder, P. van den Bossche, T. Coosemans, J. van Mierlo, Lithium iron phosphate based battery – assessment of the aging parameters and development of cycle life model, *Appl. Energy* 113 (2014) 1575–1585, <https://doi.org/10.1016/j.apenergy.2013.09.003>.
- [35] M. Ecker, P. Shafiq Sabet, D.U. Sauer, Influence of operational condition on lithium plating for commercial lithium-ion batteries – electrochemical experiments and post-mortem-analysis, *Appl. Energy* 206 (2017) 934–946, <https://doi.org/10.1016/j.apenergy.2017.08.034>.
- [36] S.F. Schuster, T. Bach, E. Fleder, J. Müller, M. Brand, G. Sextl, A. Jossen, Nonlinear aging characteristics of lithium-ion cells under different operational conditions, *J. Energy Storage* 1 (2015) 44–53, <https://doi.org/10.1016/j.est.2015.05.003>.
- [37] T. Waldmann, M. Wilka, M. Kasper, M. Fleischhammer, M. Wohlfahrt-Mehrens, Temperature dependent ageing mechanisms in lithium-ion batteries – a post-mortem study, *J. Power Sources* 262 (2014) 129–135, <https://doi.org/10.1016/j.jpowsour.2014.03.112>.
- [38] J. Vetter, P. Novák, M.R. Wagner, C. Veit, K.-C. Möller, J.O. Besenhard, M. Winter, M. Wohlfahrt-Mehrens, C. Vogler, A. Hammouche, Ageing mechanisms in lithium-ion batteries, *J. Power Sources* 147 (1–2) (2005) 269–281, <https://doi.org/10.1016/j.jpowsour.2005.01.006>.
- [39] K. Kleiner, P. Jakes, S. Scharnner, V. Liebau, H. Ehrenberg, Changes of the balancing between anode and cathode due to fatigue in commercial lithium-ion cells, *J. Power Sources* 317 (2016) 25–34, <https://doi.org/10.1016/j.jpowsour.2016.03.049>.
- [40] I. Bloom, A.N. Jansen, D.P. Abraham, J. Knuth, S.A. Jones, V.S. Battaglia, G.L. Henriksen, Differential voltage analyses of high-power, lithium-ion cells, *J. Power Sources* 139 (1–2) (2005) 295–303, <https://doi.org/10.1016/j.jpowsour.2004.07.021>.
- [41] X. Han, M. Ouyang, L. Lu, J. Li, Y. Zheng, Z. Li, A comparative study of commercial lithium ion battery cycle life in electrical vehicle: Aging mechanism identification, *J. Power Sources* 251 (2014) 38–54, <https://doi.org/10.1016/j.jpowsour.2013.11.029>.
- [42] M. Wetjen, D. Pritzl, R. Jung, S. Solchenbach, R. Ghadimi, H.A. Gasteiger, Differentiating the degradation phenomena in silicon-graphite electrodes for lithium-ion batteries, *J. Electrochem. Soc.* 164 (12) (2017) A2840–A2852, <https://doi.org/10.1149/2.1921712jes>.
- [43] M. Klett, J.A. Gilbert, S.E. Trask, B.J. Polzin, A.N. Jansen, D.W. Dees, D.P. Abraham, Electrode behavior re-visited: Monitoring potential windows, capacity loss, and impedance changes in li 1.03 (ni 0.5 co 0.2 mn 0.3) 0.97 o 2 /silicon-graphite full cells, *J. Electrochem. Soc.* 163 (6) (2016) A875–A887, <https://doi.org/10.1149/2.0271606jes>.
- [44] M. Wetjen, S. Solchenbach, D. Pritzl, J. Hou, V. Tileli, H.A. Gasteiger, Morphological changes of silicon nanoparticles and the influence of cutoff potentials in silicon-graphite electrodes, *J. Electrochem. Soc.* 165 (7) (2018) A1503–A1514, <https://doi.org/10.1149/2.1261807jes>.
- [45] S. Müller, P. Pietsch, B.-E. Brandt, P. Baade, V. de Andrade, F. de Carlo, V. Wood, Quantification and modeling of mechanical degradation in lithium-ion batteries based on nanoscale imaging, *Nature Commun.* 9 (1) (2018) 2340, <https://doi.org/10.1038/s41467-018-04477-1>.
- [46] N.N. Sinha, A.J. Smith, J.C. Burns, G. Jain, K.W. Eberman, E. Scott, J.P. Gardner, J.R. Dahn, The use of elevated temperature storage experiments to learn about parasitic reactions in wound licoo2 graphite cells, *J. Electrochem. Soc.* 158 (11) (2011) A1194, <https://doi.org/10.1149/2.007111jes>.
- [47] J. Xu, R.D. Deshpande, J. Pan, Y.-T. Cheng, V.S. Battaglia, Electrode side reactions, capacity loss and mechanical degradation in lithium-ion batteries, *J. Electrochem. Soc.* 162 (10) (2015) A2026–A2035, <https://doi.org/10.1149/2.0291510jes>.
- [48] I. Buchberger, S. Seidlmayer, A. Pokharel, M. Piana, J. Hattendorff, P. Kudejova, R. Gilles, H.A. Gasteiger, Aging analysis of graphite/lini 1/3 mn 1/3 co 1/3 o 2 cells using xrd, pga, and ac impedance, *J. Electrochem. Soc.* 162 (14) (2015) A2737–A2746, <https://doi.org/10.1149/2.0721514jes>.
- [49] L.M. Thompson, W. Stone, A. Eldesoky, N.K. Smith, C.R.M. McFarlane, J.S. Kim, M.B. Johnson, R. Petibon, J.R. Dahn, Quantifying changes to the electrolyte and negative electrode in aged nmc532/graphite lithium-ion cells, *J. Electrochem. Soc.* 165 (11) (2018) A2732–A2740, <https://doi.org/10.1149/2.0721811jes>.
- [50] J. Li, L.E. Downie, L. Ma, W. Qiu, J.R. Dahn, Study of the failure mechanisms of lini 0.8 mn 0.1 co 0.1 o 2 cathode material for lithium ion batteries, *J. Electrochem. Soc.* 162 (7) (2015) A1401–A1408, <https://doi.org/10.1149/2.1011507jes>.
- [51] K. Honkura, T. Horiba, Study of the deterioration mechanism of licoo2/graphite cells in charge/discharge cycles using the discharge curve analysis, *J. Power Sources* 264 (2014) 140–146, <https://doi.org/10.1016/j.jpowsour.2014.04.036>.
- [52] P. Keil, S.F. Schuster, J. Wilhelm, J. Travi, A. Hauser, R.C. Karl, A. Jossen, Calendar aging of lithium-ion batteries, *J. Electrochem. Soc.* 163 (9) (2016) A1872–A1880, <https://doi.org/10.1149/2.0411609jes>.
- [53] V.G. Khomenko, V.Z. Barsukov, J.E. Doninger, I.V. Barsukov, Lithium-ion batteries based on carbon-silicon-graphite composite anodes, *J. Power Sources* 165 (2) (2007) 598–608, <https://doi.org/10.1016/j.jpowsour.2006.10.059>.
- [54] T. Ohzuku, I. Yasunobi, S. Keijiro, Formation of lithium-graphite intercalation compounds in nonaqueous electrolytes and their application as a negative electrode for a lithium ion (shuttlecock) cell, *J. Electrochem. Soc.* 140 (9) (1993) 2490–2498, <https://doi.org/10.1149/1.2220849jes>.
- [55] T. Waldmann, B.-I. Hogg, M. Wohlfahrt-Mehrens, Li plating as unwanted side reaction in commercial li-ion cells – a review, *J. Power Sources* 384 (2018) 107–124, <https://doi.org/10.1016/j.jpowsour.2018.02.063>.
- [56] M. Ouyang, Z. Chu, L. Lu, J. Li, X. Han, X. Feng, G. Liu, Low temperature aging mechanism identification and lithium deposition in a large format lithium iron phosphate battery for different charge profiles, *J. Power Sources* 286 (2015) 309–320, <https://doi.org/10.1016/j.jpowsour.2015.03.178>.
- [57] M. Petzl, M. Kasper, M.A. Danzer, Lithium plating in a commercial lithium-ion battery – a low-temperature aging study, *J. Power Sources* 275 (2015) 799–807, <https://doi.org/10.1016/j.jpowsour.2014.11.065>.
- [58] C. von Lüdgers, J. Keil, M. Webersberger, A. Jossen, Modeling of lithium plating and lithium stripping in lithium-ion batteries, *J. Power Sources* 414 (2019) 41–47, <https://doi.org/10.1016/j.jpowsour.2018.12.084>.
- [59] D. Ren, K. Smith, D. Guo, X. Han, X. Feng, L. Lu, M. Ouyang, J. Li, Investigation of lithium plating-stripping process in li-ion batteries at low temperature using an electrochemical model, *J. Electrochem. Soc.* 165 (10) (2018) A2167–A2178, <https://doi.org/10.1149/2.0661810jes>.
- [60] C. von Lüdgers, V. Zinth, S.V. Erhard, P.J. Osswald, M. Hofmann, R. Gilles, A. Jossen, Lithium plating in lithium-ion batteries investigated by voltage relaxation and in situ neutron diffraction, *J. Power Sources* 342 (2017) 17–23, <https://doi.org/10.1016/j.jpowsour.2016.12.032>.
- [61] S. Schindler, M. Bauer, M. Petzl, M.A. Danzer, Voltage relaxation and impedance spectroscopy as in-operando methods for the detection of lithium plating on graphite anodes in commercial lithium-ion cells, *J. Power Sources* 304 (2016) 170–180, <https://doi.org/10.1016/j.jpowsour.2015.11.044>.
- [62] I.D. Campbell, M. Marzook, M. Marinescu, G.J. Offer, How observable is lithium plating? Differential voltage analysis to identify and quantify lithium plating following fast charging of cold lithium-ion batteries, *J. Electrochem. Soc.* 166 (4) (2019) A725–A739, <https://doi.org/10.1149/2.0821904jes>.
- [63] P. Arora, Mathematical modeling of the lithium deposition overcharge reaction in lithium-ion batteries using carbon-based negative electrodes, *J. Electrochem. Soc.* 146 (10) (1999) 3543, <https://doi.org/10.1149/1.1392512>.
- [64] T.C. Bach, S.F. Schuster, E. Fleder, J. Müller, M.J. Brand, H. Lorrmann, A. Jossen, G. Sextl, Nonlinear aging of cylindrical lithium-ion cells linked to heterogeneous compression, *J. Energy Storage* 5 (2016) 212–223, <https://doi.org/10.1016/j.est.2016.01.003>.
- [65] W. Waag, S. Käbitz, D.U. Sauer, Experimental investigation of the lithium-ion battery impedance characteristic at various conditions and aging states and its influence on the application, *Appl. Energy* 102 (2013) 885–897, <https://doi.org/10.1016/j.apenergy.2012.09.030>.

6 Sensorless Online Pulse Resistance Temperature Estimation - Aging Compensation

The scope of Chapter 6, as depicted once again in Fig. 6.1, is the continuous determination of temperature over aging. However, the influence of aging on impedance based temperature estimation methods

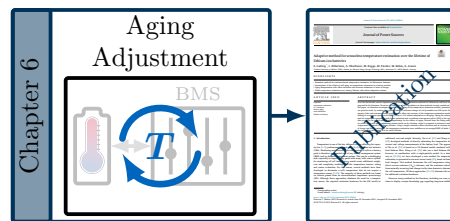


Figure 6.1: Scope of Chapter 6.

is hardly investigated in the literature, as Table 2.5 showed. Only a few studies (#4, #11, #16, and #22) consider and investigate the influence of aging. Others studies (#7, #12, #13, #15, and #20) exclude aging effects and refer to the results of the studies, which investigated aging. And still others exclude effects of aging on their method (#1 and #14) or neglect the topic aging entirely (#2, #3, #5, #7, #9, #17, #18, #19, #23, and #25). As the results of Chapter 5 show, the capacity and resistance of a LIB can change significantly over aging. A majority of the existing studies in Table 2.5 do not investigate the effect of aging on their methods and only study #16 proposes an adaptation methodology. The method developed in Chapter 4 is dependent on both parameters, capacity and resistance, since it is based on an exact SOC determination and a static reference for the relation between resistance and temperature. This raised the questions of whether the method from Chapter 4 can be used without further ado over the lifetime of a LIB, or whether adjustments to aging are necessary. And if they are necessary, how they can be implemented.

The following publication, entitled *Adaptive method for sensorless temperature estimation over the lifetime of lithium-ion batteries* [245], sets out to answer these questions. Initially, the publication focuses on the effects of aging on the temperature estimation method presented in Chapter 4 and its performance without any adjustment. The results show that without any adjustment to aging the method performs poorly and the RMSE of the cell aged at 25 °C rises to 15.0 K, followed by the cell at 26 °C with a RMSE of approximately 7.5 K. The other four cells with temperatures of 27 K and above end at a RMSE of roughly 2.9 K. As a consequence of the rapidly increasing RMSE, an adjustment scheme was developed, which relies on the adjustment of the R_{DC} reference of the temperature estimation method. For this purpose the R_{DC} reference was interpolated and refitted to the corresponding cell temperatures between 25 °C and 30 °C. After that, the R_{DC} reference was adjusted to fit the R_{DC} values gained from the dynamic cycles applied to the module during the aging procedure, as shown in the flowchart in Fig. 5.2a. The adjustment was achieved solely by scaling and shifting the initial R_{DC} reference according to Eq. (6.1) using a nonlinear least-squares solver (NLS)

in MATLAB.

$$R_{\text{DC,fit}}(Q_{\text{dis}}) \approx \sum_{i=0}^8 x_{T,i} \cdot \underbrace{\left(\frac{Q_{\text{dis}}}{C_{\text{act}}} + S\tilde{O}C_0 \right)^i}_{C \text{ fade}} + \underbrace{\tilde{R}_{\text{DC,offset}}}_{R_{\text{DC}} \text{ increase}} \quad (6.1)$$

The initial reference for each temperature T was represented by a 8th degree polynomial with the coefficients $x_{T,i}$. The initial variable of the reference polynomial, the **SOC**, was expanded to $\frac{Q_{\text{dis}}}{C_{\text{act}}} + S\tilde{O}C_0$, which allowed to adjust the polynomial along the x-axis by scaling the charge throughput Q_{dis} to the actual capacity C_{act} of the cycle and shifting the **SOC** starting point of the dynamic cycle to $S\tilde{O}C_0$. Shifting the reference along the y-axis was realized by adding the offset term $\tilde{R}_{\text{DC,offset}}$. The comparison with the values needed for the adjustment in Eq. (6.1) and the checkup results, as shown in Fig. 5.2b and Fig. 5.2c, revealed a strong correlation between the capacity fade and $S\tilde{O}C_0$ as well as the resistance change and $\tilde{R}_{\text{DC,offset}}$. Ultimately, that means that the method can be adapted to aging as long as the **SOC** determination over aging is correct and a resistance offset value can be calculated regularly at a defined temperature. In the publication [238] from Chapter 5, a method for determination of the **SOH** using the accumulated balancing loads is presented and additionally there exist various methods in the literature [247–252] for a correct **SOC** determination over the course of aging. The resistance offset $\tilde{R}_{\text{DC,offset}}$ could be determined during regular maintenance or idle periods of the battery system. During the idle periods, the battery system must be in a thermal equilibrium state and the actual temperature for the system must be determined via a conventional temperature sensor. By applying a pulse excitation on the battery for a short period of time, for example by intentionally turning on the load of the system, the new offset value can be calculated.

Finally, the accuracy of the developed aging adjustment method was evaluated and compared to the initial result without adjustment. By using the adjustment method with the values of the **NLS**, the initial **RMSE** of the cell aged at 25 °C was reduced from a maximum of close to 15 K to a maximum of 2 K. On average over all cycles, the error of the individual cells was between 0.80 K and 1.02 K. By using the adjustment method with the values gained from the checkups, the **RMSE** was also reduced and reached a maximum value of 4 K. On average over all cycles, the error of the individual cells was between 0.88 K and 1.51 K. Comparing the accuracy of the temperature estimation with the **RMSE** values from Table 2.6, the aging adjusted method is still better than study #9 with the highest error of 4.94 K and is close to the average **RMSE** of 0.858 K for the cells with lowest error.

Authors Contribution

The experimental data was collected in the context of the publication from Chapter 5 and the contributions of the authors are accordingly as mentioned in Chapter 5. Furthermore, Sebastian Ludwig evaluated the data, developed the method presented in the study, and wrote the manuscript. Preliminary results and the initial manuscript were discussed with Andreas Oberbauer, Marcel Rogge, Macro Fischer and Mathias Rehm. Andreas Jossen supervised this work, all authors edited and reviewed the manuscript.

Adaptive method for sensorless temperature estimation over the lifetime of lithium-ion batteries

Ludwig S., Zilberman I., Oberbauer A., Rogge M., Fischer M., Rehm M., Jossen A.

Journal of Power Sources 521, 230864, 2022

Permanent web link:

<https://doi.org/10.1016/j.jpowsour.2021.230864>



Subscription article, reproduced by permission of Elsevier. Authors of this Elsevier article retain the right to include it in a thesis or dissertation, provided it is not published commercially. Permission is not required, but please ensure that you reference the journal as the original source. For more information on this and on other retained rights, please visit: <https://www.elsevier.com/about/our-business/policies/copyright#Author-rights>



Contents lists available at ScienceDirect

Journal of Power Sources

journal homepage: www.elsevier.com/locate/jpowsour

Adaptive method for sensorless temperature estimation over the lifetime of lithium-ion batteries

S. Ludwig*, I. Zilberman, A. Oberbauer, M. Rogge, M. Fischer, M. Rehm, A. Jossen

Technical University of Munich (TUM), Institute for Electrical Energy Storage Technology (EES), Arcisstrasse 21, 80333 Munich, Germany

HIGHLIGHTS

- Sensorless method for resistance-based temperature estimation for lithium-ion batteries.
- Investigation of the effects of cell aging on temperature estimation in a battery module.
- Aging compensation with offset correction and accurate estimation of state of charge.
- Stable temperature estimation over battery lifetime with online adaptation scheme.

ARTICLE INFO

Keywords:

temperature estimation
d.c. resistance
battery aging
state estimation
lithium-ion battery

ABSTRACT

Over the last decade, several impedance-based temperature estimation methods for lithium-ion cells have been proposed in the literature. However, the influence of cell degradation on these methods is rarely considered. In this paper, we therefore investigate the influence of aging on the temperature estimation method, presented in our previous work, by tracking the capacity fade and resistance change of a 6s1p module over 200 cycles. Both capacity fade and resistance change were found to affect the accuracy of the temperature estimation method, leading to a root mean square error (RMSE) of up to 15 K without adaptation to cell aging. Fitting the reference used for temperature estimation with linear operations and a nonlinear least-squares solver (NLS) to the aging data proved to be a valid method of compensating for the effects of aging. Derived from the fitting results, an online applicable aging adjustment scheme based on the checkup values is proposed to maintain a stable temperature estimation over battery lifetime. Using a simple resistance offset correction and an accurate state of charge and health estimation, the temperature estimation error stabilizes at an average RMSE of below 2 K for each cell in the module over its entire lifetime.

1. Introduction

Temperature is one of the key influence factors affecting the capacity loss [1–3], performance [4] and safety [5,6] of lithium-ion batteries (LIBs). Monitoring and controlling the temperature of cells in a battery pack is therefore an essential task of any battery management system (BMS) and/or thermal management system. This can be a challenging task, especially in larger battery packs with many cells, since a system for monitoring all cell temperatures would create additional weight, cost and complexity resulting from the temperature sensors, wiring and sensor evaluation. For this reason, several methods have been developed to determine a cell's temperature that do not require a temperature sensor [7–23]. The majority of these methods are based on criteria gained from an electrochemical impedance spectroscopy (EIS). Although these approaches eliminate the need for a temperature sensor, the required excitation hardware for the EIS results in

additional cost and weight. Recently, Xie et al. [21] and Wang et al. [22] developed methods of directly estimating the temperature from current and voltage measurements of the battery load. The approach of Xie et al. [21] is based on a 1D thermal model combined with a dual Kalman filter. Wang et al. [22] also use a dual Kalman filter, however, in combination with a single-particle model. In a similar way to [21,22], we have developed a new method for temperature estimation, as presented in our most recent work [23], based on battery load changes. This method determines the cell temperature using a direct current resistance (R_{DC}) reference, and the resistance calculate from naturally occurring load changes in the time domain to determine the cell temperature. All three approaches [21–23] eliminate the need for additional excitation hardware.

However, many methods in the literature, including our own, continue to display a major knowledge gap regarding long-term stability.

* Corresponding author.

E-mail address: sebastian.ludwig@tum.de (S. Ludwig).

<https://doi.org/10.1016/j.jpowsour.2021.230864>

Received 7 October 2021; Received in revised form 22 November 2021; Accepted 29 November 2021
0378-7753/© 2021 Elsevier B.V. All rights reserved.

To our knowledge, the effects of aging on impedance-based temperature estimation methods have so far only been investigated by Rajmakers et al. [10] and Zhu et al. [14]. For Rajmakers et al. [10], the intercept frequency f_0 , which is the frequency at the zero crossing of the imaginary part of the EIS, is the key parameter for estimating temperature. To investigate the influence of aging on their estimation method, an 7.5 Ah NCA cell was cycled to a remaining capacity of about 75%. The results indicated, that the functional relation between f_0 and temperature is not affected by the capacity loss. The authors thus concluded that their method is state of health (SOH) independent. Zhu et al. [14] identified a frequency range, within which the phase shift and the impedance magnitude of the EIS can be used to estimate the temperature. The effects of aging on their method were investigated by subjecting a cell to more than 400 cycles to a remaining capacity of 75%. The aging procedure increased the impedance, though the phase shift characteristic remained largely unaffected. The authors concluded that their method requires updating in line with the SOH, for instance during regular vehicle maintenance. Srinivasan et al. [7] developed a method of estimating the temperature that relies solely on the phase shift in the frequency range of 40 Hz to 100 Hz. They attribute the temperature dependence of their method to the ionic conduction of the solid-electrolyte-interphase (SEI) between the anode and the electrolyte. By arguing that the degradation of LIBs mostly affects the cathode and that the anode remains virtually unchanged under normal use conditions of the cell, investigations on the effects of aging on their temperature estimation method have been excluded. A few authors [16, 18,19] at least consider the topic of aging before excluding any further investigations on the effects of aging on their method by arguing that their method is based on an EIS feature, which is independent of aging according to Rajmakers et al. [10] and/or Zhu et al. [14]. However, the majority of publications [8,9,11,13,15,17,20–23] do not consider or mention the effects of aging on their temperature estimation method at all. Furthermore, to our knowledge, there are currently no studies into the effects of aging on temperature estimation methods under dynamic load profiles, which would be more application-oriented than the constant current (CC) cyclic aging employed in [10,14].

For this reason, this publication aims to investigate the effects of aging on our temperature estimation under dynamic load profiles based on the R_{DC} described in our previous work [23] and to present an adjustment method for the R_{DC} reference to counter the effects and maintain a stable temperature estimation over the lifetime of the battery. To preserve the online suitability of our method, the adjustment is based solely on figures that are commonly available in a BMS or can be derived from generally monitored values, such as cell current and voltage. The adjustment method uses these values to scale and shift the R_{DC} reference so as to automatically compensate for the effects of capacity loss and the resistance change of the cells during aging.

The remainder of this publication is structured as follows. Section 2 introduces the experimental investigation, including the examined cells, the experimental setup and the aging procedure. The temperature estimation method from our previous work [23] is briefly outlined at the end of Section 2. Section 3 presents the results of the aging procedure. Subsequently, the adjustment scheme and the results of the temperature estimation using the adjustment scheme are presented and discussed. Section 4 summarizes the results and presents the key conclusions of the study.

2. Experiment

The examined cells and the experimental setup used in this aging study, are the same as those in [24]. The previous study [24] investigated the cyclic aging behavior of a 6s1p module under an enforced temperature gradient and concludes that the capacity loss correlates with the balancing effort of the cells in the module. Two categories of load cycles were used to age the module. The first category comprises standard CC discharge/charge cycles, while the second category

Table 1

Initial capacities C_{init} and resistances $R_{DC,10s}$ along with the expectation (μ) and standard deviation (σ) of the module cells at 25 °C [24]. The capacity was measured in accordance with the manufacturer's standard a discharge procedure with $I_{CC} = -670$ mA (-0.2 C) from 4.2 V to 2.5 V, followed by a constant voltage (CV) stage with a cut-off current of $I_{CV} > -50$ mA. The resistance was measured at 50% SOC with a discharge current of 1.0 C.

Parameter	Cell						μ	σ
	C_1	C_2	C_3	C_4	C_5	C_6		
C_{init}/Ah	3.461	3.469	3.461	3.470	3.462	3.463	3.464	0.004
$R_{DC,10s}/m\Omega$	42.3	42.7	42.3	43.0	42.4	42.0	42.45	0.3507

consists of dynamic electric vehicles driving cycles derived from [25], which were intended for the validation of the temperature estimation method presented in our previous work [23] as well as for the investigation of the method's performance during aging presented in this publication. In the following, we present a comprehensive description of the cells, the experimental setup used and the aging experiment conducted in [24].

2.1. Cells

The aging study was conducted on six INR18650MJ1 nickel-rich NMC/SiC cylindrical cells made by LG-Chem, with a minimum nominal capacity of 3.35 Ah. The active cathode material is composed of 82% nickel, 6.3% manganese, and 11.7% cobalt [26]. The proportion of silicon in the anode amounts to 3.5 wt% [26]. The initial cell parameters are presented in Table 1.

2.2. Setup

Fig. 1a shows the setup for the aging experiment with an imposed temperature gradient. Each of the six cells from Table 1 was encased in a high thermal conductivity foil and embedded in a copper block. The copper blocks were screwed onto a copper crossbar. To minimize the thermal transfer resistance between the blocks and the crossbar, the contact areas were lubricated with a heat paste. Two Peltier elements were placed at the ends of the crossbar to generate a constant temperature gradient ΔT along the crossbar, thus creating a temperature gradient over the cells. PT100 temperature sensors were integrated into the copper crossbar and blocks to control the temperature gradient and monitor the cell temperatures. Each cell was connected separately using a clipboard with gold contact pins in a 4-wire configuration. The clipboards can either be configured to a 6s1p module or be used for individual cell investigations. In module configuration, a high power system (HPS) made by BaSyTec was used to cycle the cells, while a cell measurement unit (CMU), also from BaSyTec, monitored the individual cell voltages ($U_1 \dots U_6$) and temperatures ($T_1 \dots T_6$). A cell test system (CTS), also made by BaSyTec, was used for individual cell investigations, such as checkups. For a detailed description of the measurement equipment, the authors refer to [23,24].

2.3. Aging procedure

Fig. 1b shows the flowchart of the aging procedure. After an initial checkup, the module was repeatedly cycled twenty times, following the pattern of an initial CC cycle, a dynamic cycle, and three additional CC cycles. Each time twenty cycles were reached, the aging procedure was interrupted for the purpose of cell balancing and performing checkups. In total, the procedure shown in the flowchart in Fig. 1b was repeated until the first cell reached a SOH close to 80%, a common end of life criterion for LIBs. This corresponded to 10 iterations represented by the flowchart or a total of 200 cycles (CC and dynamic cycles) and 11 checkups, including the initial checkup. The details of each step are explained in the following sections.

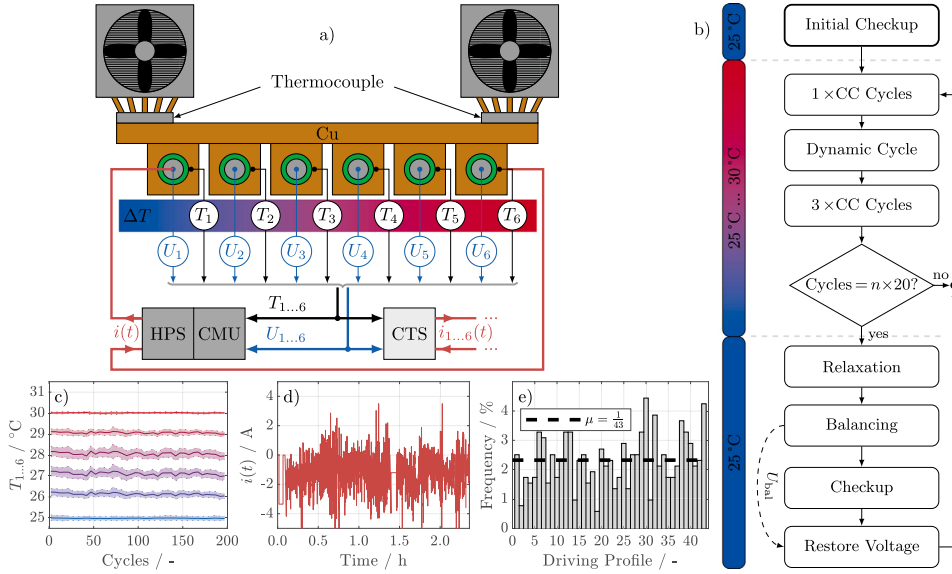


Fig. 1. Experimental setup and aging procedure: (a) Experimental setup including Peltier elements for temperature gradient control, a module test device (HPS), cell voltage and temperature monitoring (CMU) in module configuration, and single cell cycling and monitoring (CTS). (b) Flowchart of the aging experiment with cell temperatures on the left. [24] (c) Average temperature (solid line) and two times standard deviation (transparent area) of each cell for dynamic cycles during the aging procedure. (d) Example dynamic cycle used for temperature estimation. (e) Distribution of the 43 randomly selected driving profiles for discharging the module in the dynamic cycles.

Cell Configuration & Temperature. The bars on the left of the flowchart in Fig. 1b, represent the cell temperatures during the aging experiment. The cells are in single cell configuration during checkups, relaxation, balancing, and restoring the voltage after checkups. During these phases, the cells are always at the reference temperature of 25 °C. During the actual cyclic aging phase, the cells are connected to a 6s1p module and a temperature gradient is imposed on them. The temperature gradient was set to $\Delta T = 5$ K between 25 °C and 30 °C during cyclic aging to represent a possible temperature inhomogeneity in a battery module [27,28]. Fig. 1c shows the average cell temperatures for the dynamic cycles of the 200 cycles in the aging experiment, whereby the transparent areas enclose the temperature variations within two standard deviations. It is evident from Fig. 1c that all cells maintained a quasi-isothermal condition during the dynamic cycles, with a maximum deviation of ± 0.4 °C [24].

(Initial) Checkup. A checkup was performed at the beginning and after every 20th iteration. The checkup included a CC discharge with a low current of 0.033C for the purpose of differential voltage analysis (DVA) and to obtain the discharge capacity of the cell for the study in [24]. Discharge and charge pulses at 50% SOC were used subsequently to track the R_{DC} at 50% SOC. Table 2 summarizes the test sequence for the checkups. After the initial checkup, the cells were CCCV charged to 4.2 V with 0.001 C as the termination current of the CV phase. This ensured that the aging experiment commenced with fully charged cells and with no initial charge imbalances other than the intrinsic ones shown in Table 1. All other checkups in the experiment were followed by a “Restore Voltage” step, which is explained below.

CC Cycle. Cyclic aging mainly comprised CC cycles with a 1C discharge followed by a 1C charge. Discharging and charging of the module was terminated when the first cell reached the respective voltage limits of 2.5 V or 4.2 V. Between each charge and discharge, the module rested for 10 min. Four out of five cycles were CC cycles, interrupted only by dynamic cycles.

Table 2

Checkup sequence for tracing the cell capacities (steps 1–3) and resistance R_{DC} (steps 7–10).

Step	Parameters	Termination	
1.	Charge CCCV	$I_{CC} = 0.5$ C, $U = 4.2$ V	$I_{CV} \leq 0.001$ C
2.	Pause		$t \geq 30$ min
3.	Discharge CC	$I_{CC} = -0.033$ C	$U \leq 2.5$ V
4.	Pause		$t \geq 30$ min
5.	Charge CC	$I_{CC} = 0.5$ C	$SOC \geq 50\%$
6.	Pause		$t \geq 30$ min
Repeat for $I_{pulse} = \frac{1}{3} / \frac{2}{3} / 1$ C			
7.	Discharge CC	$-I_{pulse}$	$t \geq 10$ s
8.	Pause		$t \geq 10$ min
9.	Charge CC	I_{pulse}	$t \geq 10$ s
10.	Pause		$t \geq 10$ min

Dynamic Cycle. Fig. 1d shows an exemplary dynamic cycle, which was used to evaluate the estimation method during cycling. Before the dynamic cycle began, the module was discharged by 5% of the nominal cell capacity to avoid overcharging during the subsequent driving profiles. From the database in [25], 43 driving profiles were selected for the dynamic cycles in the aging study. The duration of the driving profiles was between 126 s and 3143 s, with a charge throughput between -0.0194 Ah and -0.9208 Ah. To avoid repetitive patterns in the dynamic cycles, the 43 driving profiles were selected at random. In each dynamic cycle, the randomly selected driving profiles were concatenated until the first cell in the module reached its cutoff voltage of 2.5 V or 15 driving profiles were executed. The randomized number, which determined the driving profile, was generated using a floating CMU channel. Fig. 1e shows the frequency of the 43 driving profiles during the full aging experiment. Each driving profile was selected at least three times, although some were selected more often and others less than the expected value of $\mu = \frac{1}{43}$. After the discharge with the driving profiles, the module was charged with 1 C.

Relaxation & Balancing. Each completion of a total of 20 CC and dynamic cycles, the cyclic aging procedure was interrupted for a balancing step, followed by a checkup. Prior to balancing, the cells rested for at least 12 h to allow most overpotentials to decay [29]. After the relaxation step, balancing was performed by discharging each cell to the lowest cell voltage U_{bal} in the module. Balancing was realized using a CCCV protocol, with $I_{\text{CC}} = -0.033\text{C}$ and the termination current $I_{\text{CV}} \geq -0.001\text{C}$.

Restore Voltage. After the relaxation and balancing step, a checkup was performed as in Table 2. Although checkup measurements are necessary to evaluate the aging behavior of the module, they also interfere with it by changing the voltage of the cells, since the checkup ends at a SOC of 50% for each cell. Depending on the capacity fade, this would result in different voltages both among the cells and compared with the previous balancing step. The ‘‘Restore Voltage’’ step was therefore introduced to minimize the possible influence of the checkup measurement on the aging behavior of the module. Each cell was charged to the most recent U_{bal} from the balancing step using a CCCV protocol, with $I_{\text{CC}} = 0.5\text{C}$ and the termination current $I_{\text{CV}} \leq 0.001\text{C}$. This final step completed one loop of the flowchart, and the next loop then commenced with the CC cycle step.

2.4. Temperature estimation method

The dynamic cycles in the aging procedure were introduced to evaluate the temperature estimation method in our previous work [23] and investigate the long-term stability of the method in this work. To gain a better understanding of the temperature estimation method, the principle is outlined briefly in this section using Fig. 2.

In our previous work we investigated the influence of various pulse parameters on the R_{DC} for different temperatures. The parameters are pulse direction, amplitude, rise and fall time, pulse exaction (on), and pulse relaxation (off). The cell type investigated in the present aging study is the same as in the previous characterization study, albeit using different cells to those listed in Table 1. The aim of the characterization study was to determine a reference to estimate the cell temperature based on $R_{\text{DC},\Delta t}$ that is independent from as many pulse parameters as possible and thus applicable to a wide variety of load changes in any application. The resistance calculation time Δt determines the timing of the R_{DC} calculation after the current change at t_0 and served as a tuning parameter. Besides temperature and pulse parameters, the influence of the SOC was considered. The temperature estimation method itself was developed as follows.

The first step was to calculate the $R_{\text{DC},\Delta t}$ for all investigated pulse parameters, SOC, temperatures and Δt from 1 ms to 10 s. In the second step, a parametrization filter was employed to select a subset of the R_{DC} , which were subsequently used to fit the SOC dependent 8th degree reference polynomial in Eq. (1) for each of the investigated temperatures T .

$$R_{\text{DC},\Delta t}(\text{SOC}, T) \approx \sum_{i=0}^8 x_{T,i} \cdot \text{SOC}^i \quad (1)$$

Fig. 2a shows an example of the filtered R_{DC} , marked by ‘x’, and the corresponding R_{DC} reference polynomials for $\Delta t = 120\text{ms}$ and temperatures T of 10 °C, 20 °C, 30 °C and 40 °C. To estimate the temperature T_{est} from the reference polynomials, the estimation function in Eq. (2) was introduced with the SOC dependent parameters A , B , and C .

$$T_{\text{est}} = A \cdot \exp\left(\frac{B}{R_{\text{DC},\Delta t}}\right) + C \quad (2)$$

The estimation process is illustrated by an example R_{DC} point R_s , marked by a red square in Figs. 2a and 2b. By inserting the SOC of R_s into the R_{DC} reference polynomials (Eq. (1)), four additional R_{DC} values with known temperatures are obtained. In Figs. 2a and 2b, the four points are marked by circles. The four points are then used to fit the

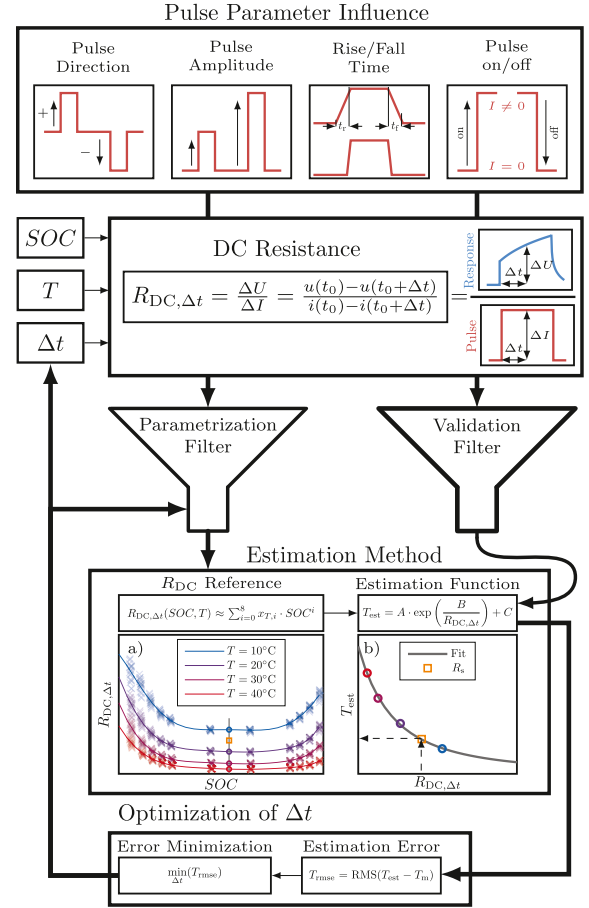


Fig. 2. Development and working principle of the temperature estimation method in [23]. From top to bottom: investigated pulse parameters; R_{DC} resistance calculation and other influence factors; filters for method parametrization and validation; estimation method with examples for (a) R_{DC} reference and (b) estimation function; optimization of Δt . (For interpretation of the references to color in this figure legend, the reader is referred to the web version of this article.)

estimation function of Eq. (2). Finally R_s is inserted into the estimation function to estimate the temperature T_{est} .

In the third step, the performance of each R_{DC} reference generated by the parametrization filter and Δt was evaluated and the method optimized. For this purpose, both known and unknown R_{DC} values from a second validation filter, were passed to the estimation function to estimate the temperature. The robustness and performance of each R_{DC} reference were rated by calculating T_{rmse} , the root mean square error (RMSE), using Eq. (3).

$$T_{\text{rmse}} = \sqrt{\frac{1}{|\mathbf{X}|} \sum_{x \in \mathbf{X}} (T_{\text{est},x} - T_{m,x})^2} \quad (3)$$

$|\mathbf{X}|$ is the cardinality of all elements x (R_{DC}) defined by the validation filter and Δt . $T_{\text{est},x}$ and $T_{m,x}$ are the estimated and measured temperatures of each x .

Finally, the optimal Δt for temperature estimation was determined by minimizing RMSE for the different parametrization and validation

filters according to Eq. (4).

$$\min_{\Delta t}(T_{\text{rmse}}) \quad (4)$$

The pulse parameter influence results showed that good accordance of the parametrization and validation filters is essential for accurate temperature estimation results. The optimal resistance calculation time Δt can be found in a plateau from approximately 10 ms to several 100 ms, where T_{rmse} has its minimum and the pulse parameter influence is negligibly small. To avoid an increased influence of the pulse rise/fall time $t_{r/f}$, Δt has to be larger than $t_{r/f}$.

After the pulse parameter analysis, the method was validated with the module from Fig. 1a. The module was discharged with a dynamic cycle as in Fig. 1d. Based on the results of the pulse parameter influence analysis, the resistance calculation time Δt was set to 120 ms. Since pulse-shaped current changes are not given in real-world applications, additional filters were applied to avoid the following scenarios:

- If the absolute current change is too small, the signal-to-noise ratio (SNR) also becomes too small, which may result in outliers in the resistance calculation. Therefore, the absolute current change $|\Delta I|$ in Eq. (5) must exceed a minimum current change ΔI_{min} to ensure a reasonable SNR.

$$|\Delta I| > \Delta I_{\text{min}} \quad (5)$$

The selection of the minimum current change ΔI_{min} is not only limited by the current changes in the load of the application, but also by the measurement accuracy and resolution of the BMS measuring equipment.

- If the rise/fall time $t_{r/f}$ for the current change is too long and the part of the pulse with a constant current is too short with respect to Δt , the resulting resistance will not be suitable for temperature estimation. Therefore, $t_{r/f}$ was limited to $t_{r/f,\text{max}}$ according to Eq. (6).

$$t_{r/f} < t_{r/f,\text{max}} < \Delta t \quad (6)$$

- Pulses with currents that change between the start of the pulse at t_0 and the maximum rise/fall time $t_{r/f,\text{max}}$ were not investigated and therefore excluded (Eq. (7)).

$$\text{sign}\left(\frac{\partial i(t)}{\partial t}\right) = \text{sign}\left(\frac{\partial u(t)}{\partial t}\right) = \text{const.} \quad \forall t \in [t_0, t_{r/f,\text{max}}] \quad (7)$$

This also excludes pulses where the current change ΔI and ΔU are inconsistent. In general, it should be noted that ΔI_{min} and $t_{r/f,\text{max}}$ must be selected in such a way that any measurement noise in current $i(t)$ and voltage $u(t)$ does not affect the filter criterion in Eq. (7). In addition to ΔI_{min} and $t_{r/f,\text{max}}$, high sampling rates could cause unintentional filtering of pulses. In the case of small ΔI_{min} and/or large $t_{r/f,\text{max}}$ combined with a high sampling rate, current $\frac{\partial i(t)}{\partial t}$ and voltage $\frac{\partial u(t)}{\partial t}$ changes can be affected by the measurement noise and might therefore be inconsistent, which discards a pulse from the temperature estimation.

- So far, the investigated pulses remained at a constant current level after the rise/fall time. To avoid the influence of varying currents after $t_{r/f}$ until Δt is reached, the current fluctuation must remain within a certain limit ΔI_{tol} (Eq. (8)).

$$|i(t) - \Delta I| < \Delta I_{\text{tol}} \quad \forall t \in [t_{r/f,\text{max}}, \Delta t] \quad (8)$$

Table 3 presents the parametrization filter settings and the values needed for Eqs. (5) to (8), which were used in our previous work [23] and apply to this work too. The final parameter τ_w in Table 3, describes the range of the averaging window, which was used to additionally reduce the influence of outliers and decreases the estimation error. If several R_{DC} were calculated within the window τ_w , the values were averaged and only one temperature estimation performed. Since the SOC is needed to retrieve the R_{DC} values from the reference, a simple SOC

Table 3

Parameter settings for the validation of the temperature estimation method presented in [23].

Parameter	Value
Parametrization filter	$\pm 0.5^\circ\text{C}$ & $t_{r/f} = 0.0\text{ s}^*$
Δt	120 ms
$t_{r/f,\text{max}}$	100 ms
ΔI_{min}	670 mA (0.2 C)
ΔI_{tol}	10 mA
τ_w	10 s

*Although the test device has a minimum rise/fall time of 40 μs for current changes, the “instant” current changes are denoted by $t_{r/f} = 0.0\text{ s}$.

estimation was implemented using the Coulomb counting method [30–33]. The individual cell SOC is tracked using Eq. (9) with the specific cell capacity C_{act} and the initial state of charge SOC_0 at t_0 :

$$\text{SOC} = \text{SOC}_0 + \frac{1}{C_{\text{act}}} \int_{t_0}^t i(\tau) d\tau \quad (9)$$

Before the validation of the method with the module, a final adjustment to the R_{DC} reference was necessary. As mentioned above, the module cells in Table 1 differ from those used for the pulse parameter analysis in our previous work [23]. To compensate for the intrinsic offset between the cells [34], an individual $R_{\text{DC,offset}}$ was calculated with Eq. (10).

$$R_{\text{DC,offset}} = R_{\text{act}} - R_{\text{DC,ref}} \quad (10)$$

R_{act} was calculated from the initial checkup pulse of the module cells at 50% SOC and 25 °C, and $R_{\text{DC,ref}}$ is the corresponding value from the inverted estimation function (Eq. (2)) at the same SOC and temperature. By subtracting $R_{\text{DC,offset}}$ from the R_{DC} , which is calculated from a pulse of the dynamic cycle, the R_{DC} reference is applicable to the module cells, although the R_{DC} reference was initially parameterized with different cells. The resulting temperature RMSE for the validation of the module ranged between 0.59 K to 0.93 K. The initial idea from our previous work of adjusting the calculated R_{DC} to the R_{DC} reference for unknown cells is developed further in this work to compensate for the effects of aging and will be presented and discussed in the next section.

3. Results & discussion

The first part of this section briefly presents and discusses the aging behavior of the module in terms of capacity and R_{DC} development of the checkups. The initial temperature estimation method is then applied to the dynamic cycles to motivate the need for an adjustment over its lifetime. Next, the R_{DC} values of the dynamic cycles are presented and an aging adjustment scheme will be derived from the dynamic cycles and the checkup results. Finally, the results of the adjustment scheme are presented and discussed.

3.1. Module aging behavior

Fig. 3a shows the progression of the relative capacity for each cell over the 200 cycles. The colors in Fig. 3 represent the position along the temperature gradient ΔT in the module, as introduced in Fig. 1. Up until cycle 40, all cells display a similar aging course. After this point, the capacity fade of the cells at 25 °C and 26 °C increases compared to the other cells. The cell at 25 °C in particular displays an increased aging rate, reaching a SOH of almost 80% after 200 cycles. The capacity loss of the cell at 26 °C still is increased, ending at a SOH of approximately 90%. The cells at 27 °C and above show the lowest capacity loss and reach a SOH of around 94%. [24]

The relative resistance increase for $\Delta t = 120\text{ ms}$, which is the relevant Δt for the estimation method, is illustrated in Fig. 3b. The solid

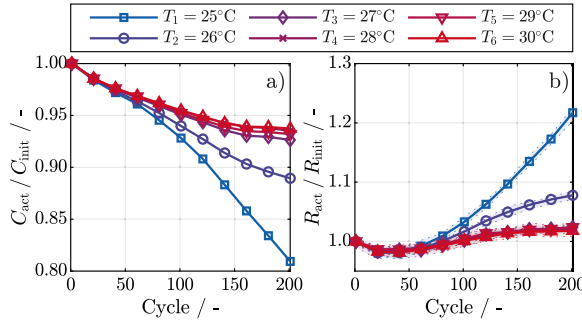


Fig. 3. Checkup results. (a) Relative capacity loss of each cell and (b) relative resistance increase of each cell in relation to the first checkup. The resistance was calculated at $\Delta t = 120$ ms after the current change of the pulses (steps 7–10 in Table 2) and averaged over all pulses. The shaded areas represent the maximum deviation from the averaged values. [24].

lines represent the averaged value for all R_{DC} calculated from the pulses of steps 7–10 in Table 2, whereas the shaded areas cover the maximum spread of all R_{DC} . Overall the maximal deviation from the average R_{DC} does not exceed 0.047%, which means that the R_{DC} for the checkup conditions remains independent of the pulse parameters, which we investigated in our previous work [23] (see Fig. 2). The resistance increase develops in a similar manner to the capacity fade. However, before the resistance increases after about 60 cycles, the resistance of all cells initially decreases to a minimum of almost 98%. Similar behavior was reported for the same cell by [35] and for other cells by [3,36,37]. After the 60 cycle mark, the resistance starts to increase again. The cell at 25°C shows the highest increase, resulting in approximately 120% of the initial resistance after 200 cycles, while that of the cell at 26°C rises to 108%. The cells above 26°C show only a minor increase in resistance, reaching approximately 102% by the end of the experiment.

The cause of the aging behavior shown in Fig. 3 was discussed in detail in [24] and is only briefly summarized here. The main reason for the different aging rates is the temperature gradient between the cells, whereby the colder cells showed increased capacity fade and resistance increase. A DVA performed on the open circuit voltages (OCVs) of the checkup (step 3 in Table 2) revealed that all cells suffered from a loss of storage capability of silicon. However, this alone does not explain the severe degradation of the colder cells. Evidence of lithium stripping in the relaxation behavior after charging [24,38,39] and scanning electron microscope (SEM) images of the anode strongly suggests that lithium plating is probably the main reason for the aggravated aging of the colder cells. [24]

3.2. Temperature estimation without aging adjustment

The R_{DC} reference for temperature estimation is directly affected by capacity fade and the increase in cell resistance, since it is SOC dependent and the offset correction of Eq. (10) is only performed once and therefore does not compensate for the changes depicted in Fig. 3. However, it is not clear yet what the effects on estimation accuracy of the method are. We therefore investigated the performance of our estimation method for all dynamic cycles in the aging experiment applying the settings from Section 2.4 and Table 3. The performance was rated in terms of the RMSE using Eq. (3). Fig. 4 shows the error for each cell over the course of aging. The estimation error increases initially, though never passing a RMSE of 1.8 K. Up until cycle 67, the error even decreases to its initial level of about 0.8 K. This is in accordance with the aging behavior shown in Fig. 3, where the cells show a relatively low capacity fade and resistance change. In

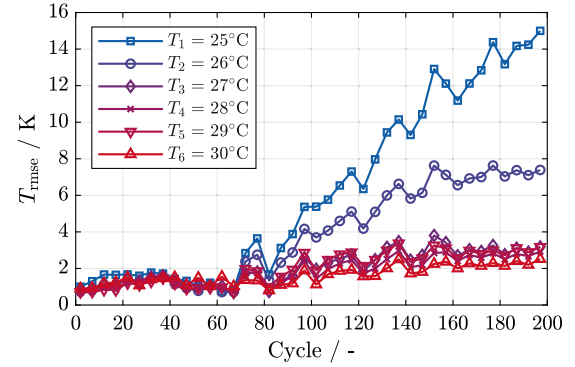


Fig. 4. Temperature RMSE using Eq. (3) for each cell according to the temperature estimation method without adjustment to capacity fade and increased resistance over the module's lifetime.

conclusion, the estimation method seems to be robust against minor deviations in capacity and resistance. After cycle 67, the estimation error starts to increase again in accordance with the aging course of the respective cells in Fig. 3. The cell at 25°C shows the largest error increase, ending at a RMSE of 15.0 K, followed by the cell at 26°C with a RMSE of approximately 7.5 K. The cells at 27°C and above end at a RMSE of roughly 2.9 K.

Although this is a substantially lower degree of error than with the cells at 25°C and 26°C, the estimation method becomes more and more impractical as capacity fades and resistance increases. It is thus necessary to adjust the estimation method to compensate for the effects of capacity loss and resistance increase over the module's lifetime.

3.3. Aging behavior for dynamic cycles

Before we introduce the adjustment scheme for the temperature estimation method, we present and discuss the general results of R_{DC} development in the dynamic cycles, illustrated in Fig. 5. For the sake of clarity, only the results of the cells at 25°C and 30°C are shown, representing the two extreme cases with the highest and lowest degradation effects. Fig. 5a shows the maximum and minimum cell voltages for all dynamic cycles. With the exception of cycle 52, all dynamic cycles ended at the discharge cut-off voltage of 2.5 V or slightly below it, with the coldest cell being the limiting cell in the module. Only in cycle 52 was the discharge load of the randomly chosen driving profiles insufficient to fully discharge the module, which meant that no cell reached the cut-off voltage. Due to the increase in resistance and the resulting higher overpotential, the maximum voltage U_{max} at the start of the dynamic cycles decreases as the aging experiment progresses. The voltage window of the cell at 30°C decreases over the cycles, due to the increased capacity fade of the cell at 25°C compared to the one at 30°C. The amount of capacity discharged during one cycle for the limiting cell at 25°C decreases as aging progresses, as shown in Fig. 3. The cell at 30°C experiences the same amount of discharged capacity, as the module is connected in series. However, the lower capacity fade of the cell at 30°C means that the SOC change is smaller, while the voltage U_{min} at the end of the cycle is higher.

Figs. 5b and 5c show the R_{DC} calculated during example dynamic cycles before filtering with t_w using Eqs. (5) to (8). The results are plotted against the discharged capacity Q_{dis} to visualize the effects of capacity fade and the resulting reduction of the voltage window in Fig. 5a. The example R_{DC} cycles for the limiting cell at 25°C in Fig. 5b always show an increasing resistance branch towards the end of the cycle, which is typical of the investigated cell at low SOC [23]. Since the capacity of the cell decreases with increasing cycles, the resistance

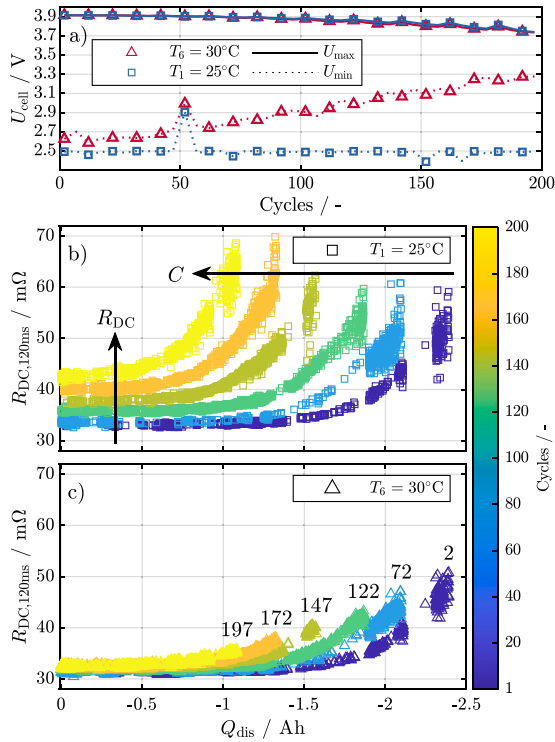


Fig. 5. Example behavior during the dynamic cycles of the cell at 25°C and 30°C. (a) Maximum and minimum cell voltages. Unfiltered (according to Table 3) R_{DC} over the discharged capacity Q_{dis} for example dynamic cycles for the cell at (b) 25°C and (c) 30°C, whereby the values next to the individual curves represent the exact cycle number.

increase starts at less discharged capacity Q_{dis} as the aging experiment progresses. In contrast, the cell at 30°C in Fig. 5c reaches the increasing resistance branch less and less as the cycle count progresses, which is in accordance with the smaller voltage window for this cell in Fig. 5a and the higher capacity in Fig. 3a. Apart from the effects of capacity fade on the R_{DC} , the resistance increase from Fig. 3b is visible for both cells in Figs. 5b and 5c. Since the resistance increase in Fig. 3b for the cell at 25°C is about 20% but only about 2% for the cells at 30°C, the shift towards higher R_{DC} values is more obvious for the cell at 25°C than for the cell at 30°C.

It can be concluded from the results of Figs. 3 and 5 that both capacity fade and the resistance change have to be considered for the aging adjustment of the estimation method. The question is whether an accurate SOC estimation, considering the SOH, is enough to compensate for the capacity fade or whether additional measures are necessary to ensure the reliable adjustment of the estimation method. It is also necessary to clarify whether the resistance increase is independent of the SOC or if it differs over the course of aging in different SOC regions, as reported by Waag et al. [40]. The next section introduces a solution method that addresses the resistance change and capacity fade. First, the R_{DC} reference is independently adjusted to the dynamic cycles of Fig. 5 with linear operations and fitted to the course of aging using a nonlinear least-squares solver (NLS). In the second step, the correlation of the linear adjustment parameters from the NLS and the checkup values from Fig. 3 is investigated to establish a way for an online adjustment scheme to compensate for the effects of aging on temperature estimation.

3.4. Aging adjustment scheme

Fig. 6a visualizes the temperature estimation concept from our previous work [23] in black and the extension for the aging adjustment scheme based on the checkup results from Fig. 3 in blue. Since it cannot be assumed that the checkup results represent either an optimal or even a valid solution for the aging adjustment scheme, an independent adjustment was performed in advance based on linear fitting and detached from the checkup values; this is visualized in red. The fitting parameters $\bar{R}_{\text{DC}, \text{offset}}$ and $\bar{S}\bar{O}C_0$ are explained below in Section 3.4.2.

The overall estimation procedure in Fig. 6a, which is described in Section 2.4, is not altered until after filtering with t_w . If a current change ΔI and its corresponding voltage response ΔU pass through the pulse filters in accordance with Eqs. (5) to (8), the R_{DC} for $\Delta t = 120 \text{ms}$ is calculated and averaged in the window t_w . After this point, the initial variation between the cells is compensated for by subtracting $R_{\text{DC}, \text{offset}}$, which is calculated with Eq. (10). The resulting R_{DC} value, together with the R_{DC} reference (Eq. (1)) for the current SOC (Eq. (9)), form the input of the estimation function (Eq. (2)), which delivers the estimated temperature T_{est} .

3.4.1. Assumptions for aging adjustment

In order for the aging adjustment scheme to work solely with linear adjustments to the R_{DC} reference, the following assumptions are made:

- A1. The resistance change is constant over the whole SOC range and can therefore be interpreted as an offset along the R_{DC} reference y-axis. This also means that a single measurement at any SOC is enough to determine the offset.
- A2. The resistance change measured at a given aging state and temperature results in a proportional change in resistance at another temperature. This effect was already verified in the study by Waag et al. [40].
- A3. The capacity fade does not affect the general curve shape of the R_{DC} reference represented by the polynomial in Eq. (1). This ultimately means that the coefficients $x_{T,i}$ in Eq. (1) are not altered over the lifetime of the battery and a correctly calculated SOC should compensate for the capacity fade.
- A4. Aging does not affect the general exponential temperature behavior of the resistance described in Eq. (2). Again, Waag et al. [40] already observed this effect in their study.

Based on these four assumptions, the following aging adjustment scheme was investigated.

3.4.2. Aging adjustment with nonlinear least squares fit

The adjustment shown in red in Fig. 6a is realized with the curve fitting function of MATLAB using a NLS. The adjustment takes advantage of the fact that the temperature of the cells is relatively stable during the dynamic cycles, as shown in Fig. 1c. Assuming each cell remains at its average temperature during all cycles, an individual new reference polynomial can be interpolated for the average temperature using Eqs. (1) and (2), in the following two steps:

1. The resistances for the entire SOC range at the average temperature are interpolated using the inverse of Eq. (2).
2. The interpolated R_{DC} reference values from the previous step are fitted to a new polynomial of Eq. (1) to represent the initial R_{DC} behavior at the average cell temperature during the dynamic cycles.

The effects of aging caused by capacity fade and increased resistance on this new interpolated R_{DC} reference are compensated for each dynamic cycle and cell by extending Eq. (1) to its new form in Eq. (11):

$$R_{\text{DC}, \text{fit}}(Q_{\text{dis}}) \approx \sum_{i=0}^8 x_{T,i} \cdot \underbrace{\left(\frac{Q_{\text{dis}}}{C_{\text{act}}} + \bar{S}\bar{O}C_0 \right)^i}_{C \text{ fade}} + \underbrace{\bar{R}_{\text{DC}, \text{offset}}}_{R_{\text{DC}} \text{ increase}} \quad (11)$$

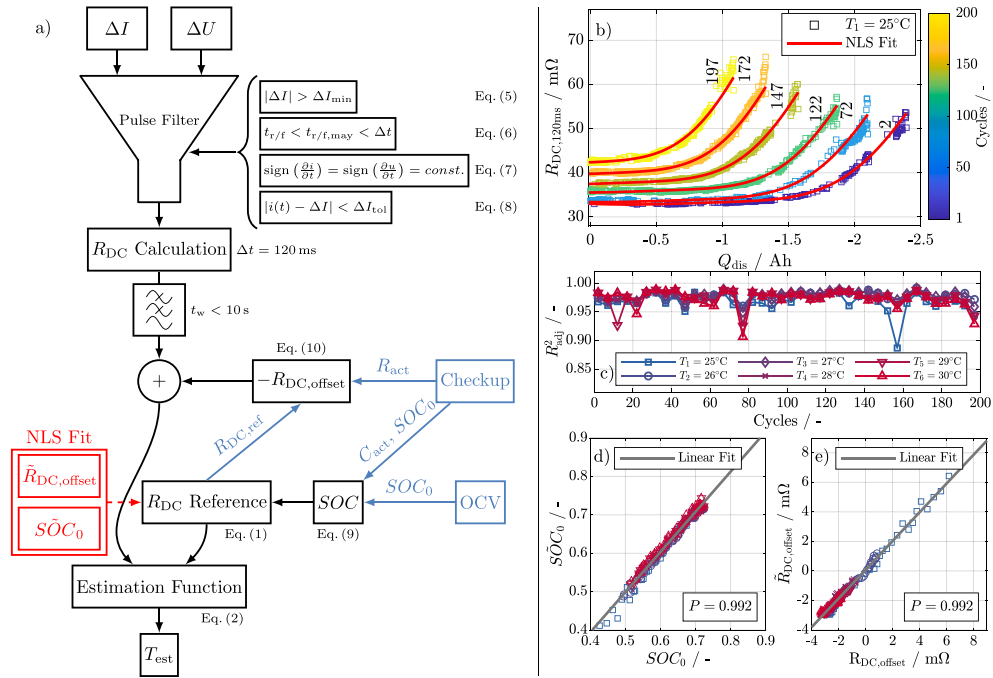


Fig. 6. (a) Concept of the temperature estimation method with aging adjustment extensions. Checkup-based aging adjustment in blue and adjustment based on the independent nonlinear least-squares solver (NLS) fit in red; (b) Filtered R_{DC} values of example dynamic cycles and corresponding NLS fit of the R_{DC} reference; (c) Goodness of fit measured with the adjusted R-Square (R_{adj}^2) for all module cells over all dynamic cycles; Correlation of the NLS fit parameters and the corresponding checkup values for (d) SOC_0 and SOC_0 , and for (e) $\bar{R}_{DC,offset}$ and $R_{DC,offset}$. (For interpretation of the references to color in this figure legend, the reader is referred to the web version of this article.)

The NLS is applied to Eq. (11) with $\bar{S}\bar{O}C_0$ and $\bar{R}_{DC,offset}$ as optimization variables and C_{act} as a given constant. The solver is only constrained by logical boundaries, keeping $\bar{S}\bar{O}C_0$ within a range from 0 to 1 and $\bar{R}_{DC,offset}$ in the ± 50 m Ω region. In the aging adjustable reference $R_{DC,fit}$, the capacity fade is compensated for by scaling the charge throughput Q_{dis} of the dynamic cycles to the actual cell capacity C_{act} and shifting it to the state of charge at the beginning of each dynamic cycle SOC_0 . The actual cell capacity C_{act} is taken from the checkup results in Fig. 3a. If assumption A3 proves to be true, the results of the NLS for $\bar{S}\bar{O}C_0$, should match the initial state of charge SOC_0 from Eq. (9). The resistance increase is compensated for by adding $\bar{R}_{DC,offset}$.

Fig. 6b shows the example curve fitting result and the filtered and averaged R_{DC} for the cell at 25°C. Compared to the same unfiltered R_{DC} from Fig. 5b, the spread of the resistance values is considerably reduced. Also, the adjusted reference $R_{DC,fit}$ is in good accordance with the R_{DC} calculated from the dynamic cycles. This suggests that the assumed linear adjustment requirements in Section 3.4.1 appear to hold. However, in order to render a quantitative statement on the fitting quality, the adjusted R-Square (R_{adj}^2) of the NLS fit was evaluated. The calculation of the R_{adj}^2 , which is a measure of the goodness of the fit, is described in the Appendix. The R_{adj}^2 results for all six cells are shown in Fig. 6c. Aside from a few exceptions, which are most likely caused by the lack of pulses in the dynamic cycles, the R_{adj}^2 is above 0.95, which is close to a perfect fit. This again reinforces the assumptions made in Section 3.4.1. In conclusion, the linear adjustment of the R_{DC} reference is a valid approach to compensate for the aging effects of the investigated module. The next section investigates the correlation between the checkup results and the independently fitted parameters and discusses the implementation of an online aging adjustment scheme based on the checkup values.

3.4.3. Aging adjustment with checkup values

The aim of this section is first of all to derive the corresponding values for the NLS fitting parameters from the checkup values and integrate them in the temperature estimation method, as shown in blue in Fig. 6a. As described in the previous section, scaling the charge throughput Q_{dis} with C_{act} and shifting with $\bar{S}\bar{O}C_0$ in Eq. (11) is equivalent to a SOC estimation. The parameter $\bar{S}\bar{O}C_0$ should therefore correspond to SOC_0 in the SOC estimation based on Coulomb counting in Eq. (9) and C_{act} is obtained from the checkup in any case. Since SOC estimators based on Coulomb counting have a tendency to drift due to measurement inaccuracies [41], the initial state of charge SOC_0 is updated during checkups and additionally with the OCV [30], when the module is at rest prior to the dynamic cycles. Fig. 6d correlates the fitted parameter $\bar{S}\bar{O}C_0$ to the corresponding value SOC_0 from the checkup-based adjustment. The Pearson correlation coefficient [42] is above 0.99, indicating a strong linear correlation between the checkup-based adjustment and the NLS-based adjustment. The fitting parameter $\bar{R}_{DC,offset}$ describes the aging-induced resistance difference between the individual cell resistance and the R_{DC} reference, similar to the initial compensation of the intrinsic difference between the R_{DC} reference and the module cells in Eq. (10). Therefore, the continuous update of $R_{DC,offset}$ with the R_{act} values from the checkups has the same effect. This is evident from the Pearson correlation coefficient [42] in Fig. 6e, which is again above 0.99. The linear fit results for the correlated values in Figs. 6d and 6e in Eq. (12) finally confirm that the checkup and the NLS adjustment are almost equal. In both cases, the coefficient for gain is close to 1 and the coefficient for offset is close to 0, which suggests a one-to-one relation.

$$\text{Linear fit for Fig. 6d: } \bar{S}\bar{O}C_0 = 1.0461 \times SOC_0 - 0.0245 \quad (12)$$

$$\text{Linear fit for Fig. 6e: } \bar{R}_{DC,offset} = 0.9728 \times R_{DC,offset} + 0.0769 \text{ m}\Omega$$

Four conclusions can be drawn from Fig. 6b to Fig. 6e. The first is that adjusting the initial R_{DC} reference with linear operations (Eq. (11))

is a suitable way of compensating for the effects of aging (Figs. 6b and 6c). The second is that the linear adjustment parameters correlate with the checkup values (Figs. 6d and 6e). This leads us to conclusion three: A SOC estimation based on Coulomb counting with OCV reset at resting periods and with SOH adjustment of the cell capacity C_{act} , scales and shifts the calculated R_{DC} to the initial R_{DC} reference. Finally, conclusion four is that only a single pulse at a known SOC and temperature is needed to compensate for the resistance increase. Since the checkup-based adjustment scheme shown in blue in Fig. 6a aims for the usability in a real-world application, the question remains: how can $R_{DC,offset}$, SOC_0 , and C_{act} be retrieved online.

A feasible way of updating all three values is during regular vehicle maintenance process, as suggested by Zhu et al. [14] for their temperature estimation method. However, given that neither the temperature estimation method nor the aging adjustment presented in this work is exclusively intended for LIB powered vehicles or applications, for which maintenance routines are common, other ways of retrieving the checkup values online are discussed in the following. State of charge [43–45] and state of health [46–48] estimation are frequent topics of battery research, and various methods of precisely tracking both states over the lifetime of a LIB can be found in the literature. It should therefore be possible to update SOC_0 and C_{act} online without the need for maintenance. Keeping track of $R_{DC,offset}$ is also possible without the need for a maintenance routine. For example a resting period of the battery powered device can be used to obtain $R_{DC,offset}$. Assuming that the battery is in thermal equilibrium due to the resting period, a single temperature sensor is sufficient to determine the temperature of all cells. By generating a defined pulse, for example with a connected battery charger or by intentionally switching on a load, the resistance of each cell, of which voltage and current are measured, can be calculated for the given temperature. Using the respective R_{DC} reference at the given temperature, the new $R_{DC,offset}$ can be calculated in line with Eq. (10).

3.5. Temperature estimation with aging adjustment

This section compares the temperature estimation results of the two aging adjustment schemes from Sections 3.4.2 and 3.4.3 over all dynamic cycles. Fig. 7a–f show the RMSE of each cell for the NLS-based aging adjustment scheme, while Fig. 7g–l show the RMSE of each cell for the checkup-based aging adjustment scheme. The RMSE for the NLS adjustment in Fig. 7a–f remains at a relatively constant level of about 1 K for all cells. Although the RMSE increases in a few exceptional dynamic cycles, it never goes beyond 1.92 K. The average RMSE (\bar{T}_{rmse}) per cell ranges between 0.8 K and 1.02 K. The checkup-based aging adjustment in Fig. 7g–l shows a comparable result to the NLS aging adjustment. The average RMSE for the cells from 27 °C to 30 °C is slightly higher, though it is smaller for the cell at 26 °C. The cell at 25 °C is the only one with an increasing error trend towards the end of the experiment, reaching a maximum RMSE of 3.78 K. It is also the one cell with the highest capacity fade and resistance increase in Fig. 3. The increased error can be explained by contemplating Fig. 6d. The markers for the cell at 25 °C at the end of the aging experiment are the blue squares for $SOC_0 \leq 0.5$, and they show the highest deviation from the linear correlation to the NLS fit ($S\bar{O}C_0$). On the one hand, this difference does not have any prominent effect on the temperature estimation error in the central SOC region above 25% SOC, where the R_{DC} reference is relative flat. In the SOC regions below 25%, on the other hand, the R_{DC} reference increases and an incorrect SOC estimation leads to an increased temperature estimation error. This ultimately shows that a precise SOC estimation for each cell over the lifetime of the battery is essential for good temperature estimation results. However, if the overall estimation error of Fig. 7g–l is compared to the initial errors shown in Fig. 4, a clear improvement can be seen for all cells. In particular, the maximum RMSE for the cell at 25 °C has been significantly lowered from 15.0 K to 3.78 K.

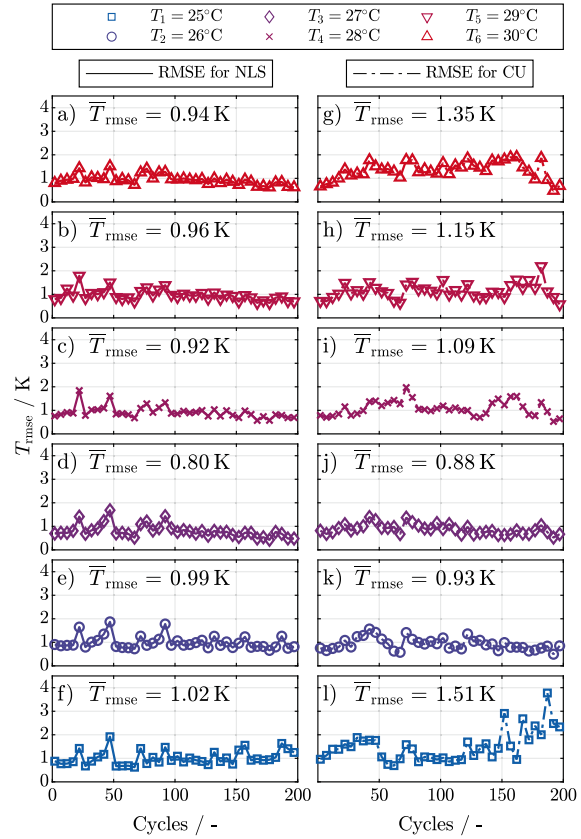


Fig. 7. RMSE and average RMSE (\bar{T}_{rmse}) for all six cells in the investigated module over all dynamic cycles for (a)–(f) the aging adjustment based on the NLS fit and for (g)–(l) the aging adjustment based on the checkup results.

4. Summary & conclusion

This work investigates the effects of LIB aging in a 6s1p module on the R_{DC} reference based temperature estimation method presented in our previous work [23]. The evaluation of the error development in Fig. 4 shows that without adjustments, the RMSE of the estimation method rises to 15 K, which makes the method unsuitable for temperature estimation. Consequently, the feasibility of an adjustment scheme for the R_{DC} reference of the temperature estimation method based on linear operations was investigated. The result of the NLS fit proves, with an adjusted R-Square above 0.95 for almost all cycles, that adjusting the R_{DC} reference by the simple operations of shifting and scaling is a valid approach for the cell under investigation. The strong correlation, demonstrated by a Pearson coefficient larger than 0.99, in conjunction with the almost one-to-one relation in Eq. (12) between the NLS fitting variables and the checkup values confirms that these checkup values, namely the actual capacity C_{act} and the actual resistance R_{act} , and precise SOC tracking (SOC_0), are required for online adjustment of the temperature estimation method. Since SOC and SOH tracking is a common task of a BMS, and since there is a large variety of precise methods in existence [43–48], the cell specific capacity (C_{act}) and state of charge (SOC_0) can be assumed to be available for the aging adjustment. The actual resistance R_{act} at a given SOC and temperature, which is used to calculate the resistance offset against the R_{DC} reference, can also be retrieved online. Examples are defined pulses generated by a

battery charger or the power electronics. Finally, the estimation error with the aging adjustment scheme is evaluated for the NLS fit and the adjustment with the checkup values in Fig. 7. The NLS fit shows the overall better results with an average RMSE between 0.80 K and 1.02 K. Nevertheless, the checkup-based adjustment performed relatively well, with an average RMSE of between 0.88 K and 1.51 K.

Although the adjustment scheme investigated in this work provides a simple way of obtaining a stable temperature estimation over a battery's lifetime, some open questions still remain for further investigations. The main cause of aging in the investigated module is linked to lithium plating and the loss of storage capability of silicon [24]. For this type of aging, the adaptation method provides sufficient compensation. However, it is not clear whether the adaptation method also works for other aging mechanisms. Moreover, a change in cell chemistry might lead to less favorable results with the adaptation method. Further investigations are therefore needed to ensure the broader applicability of the method presented.

CRedit authorship contribution statement

S. Ludwig: Conceptualization, Methodology, Software, Project administration, Writing – original draft, Visualization, Data curation, Investigation, Writing – review & editing. **I. Zilberman:** Conceptualization, Writing - Review & Editing. **A. Oberbauer:** Writing – review & editing. **M. Rogge:** Writing – review & editing. **M. Fischer:** Writing – review & editing. **M. Rehm:** Writing – review & editing. **A. Jossen:** Supervision, Writing - review & editing.

Declaration of competing interest

The authors declare that they have no known competing financial interests or personal relationships that could have appeared to influence the work reported in this paper.

Acknowledgments

This research is funded by the German Federal Ministry of Education and Research (BMBF) via the research project OSLIB (grant number: 03X90330 A). The project is overseen by Project Management Juelich (PtJ).

This work has received funding from the European Union's Horizon 2020 research and innovation programme under the grant 'Electric Vehicle Enhanced Range, Lifetime And Safety Through INGenious battery management' [EVERLASTING-713771].

Appendix. Adjusted R-Square

This section gives a short introduction to the adjusted R-Square (R_{adj}^2) as a statistical measure of the goodness of a curve fitting result, as described in [49,50]. To determine the R_{adj}^2 , the following equations are required.

The sum of square error (SSE) in Eq. (A.1) describes the total deviation of the response values of the fit \hat{y}_i from the measured response values y_i .

$$SSE = \sum_{i=1}^n (y_i - \hat{y}_i)^2 \quad (A.1)$$

The total sum of squares (SST) in Eq. (A.2) describes the total deviation of the mean \bar{y} from the measured response values y_i .

$$SST = \sum_{i=1}^n (y_i - \bar{y})^2 \quad (A.2)$$

The general R-Square (R^2) in Eq. (A.3) determines how successful the fit is in explaining the variation of the data, and is calculated from SSE and SST.

$$R^2 = 1 - \frac{SSE}{SST} \quad (A.3)$$

R^2 ranges between zero and one. The closer R^2 is to 1, the greater is the fraction of variance, which is accounted for by the model. As the number of fitted model variables increases, R^2 will also increase, although the fitting quality may not improve in a practical sense. To avoid such over-fitting, the adjusted R-Square statistic in Eq. (A.4) can be used.

$$R_{adj}^2 = 1 - (1 - R^2) \cdot \frac{n-1}{n-m} = 1 - \frac{SSE}{SST} \cdot \frac{n-1}{n-m} \quad (A.4)$$

The R_{adj}^2 statistic adjusts R^2 based on the residual degrees of freedom, which is defined as the number of response values n minus the number of fitted variables m estimated from the response values. The R_{adj}^2 can take any value less than or equal to one. As with R^2 , values closer to one indicate a better fit quality, whereas negative values indicate that the model contains terms that are not helpful for predicting the response.

References

- [1] T. Waldmann, M. Wilka, M. Kasper, M. Fleischhammer, M. Wohlfahrt-Mehrens, Temperature dependent ageing mechanisms in lithium-ion batteries – A post-mortem study, *J. Power Sources* 262 (2014) 129–135, <http://dx.doi.org/10.1016/j.jpowsour.2014.03.112>.
- [2] S.F. Schuster, M.J. Brand, C. Campestrini, M. Gleissenberger, A. Jossen, Correlation between capacity and impedance of lithium-ion cells during calendar and cycle life, *J. Power Sources* 305 (2016) 191–199, <http://dx.doi.org/10.1016/j.jpowsour.2015.11.096>.
- [3] M. Naumann, M. Schimpe, P. Keil, H.C. Hesse, A. Jossen, Analysis and modeling of calendar aging of a commercial LiFePO₄/graphite cell, *J. Energy Storage* 17 (2018) 153–169, <http://dx.doi.org/10.1016/j.est.2018.01.019>.
- [4] S. Ma, M. Jiang, P. Tao, C. Song, J. Wu, J. Wang, T. Deng, W. Shang, Temperature effect and thermal impact in lithium-ion batteries: A review, *Prog. Nat. Sci.* 28 (2018) 653–666, <http://dx.doi.org/10.1016/j.pnsc.2018.11.002>.
- [5] M. Fleischhammer, T. Waldmann, G. Bisle, B. Hogg, M. Wohlfahrt-Mehrens, Interaction of cyclic ageing at high-rate and low temperatures and safety in lithium-ion batteries, *J. Power Sources* 274 (2015) 432–439, <http://dx.doi.org/10.1016/j.jpowsour.2014.08.135>.
- [6] A. Friesen, F. Horsthemke, X. Mönninghoff, G. Brunklaus, R. Krafft, M. Börner, T. Risthaus, M. Winter, F.M. Schappacher, Impact of cycling at low temperatures on the safety behavior of 18650-type lithium ion cells: Combined study of mechanical and thermal abuse testing accompanied by post-mortem analysis, *J. Power Sources* 334 (2016) 1–11, <http://dx.doi.org/10.1016/j.jpowsour.2016.09.120>.
- [7] R. Srinivasan, B.G. Carkhuff, M.H. Butler, A.C. Baisden, Instantaneous measurement of the internal temperature in lithium-ion rechargeable cells, *Electrochim. Acta* 56 (2011) 6198–6204, <http://dx.doi.org/10.1016/j.electacta.2011.03.136>.
- [8] R. Srinivasan, Monitoring dynamic thermal behavior of the carbon anode in a lithium-ion cell using a four-probe technique, *J. Power Sources* 198 (2012) 351–358, <http://dx.doi.org/10.1016/j.jpowsour.2011.09.077>.
- [9] J.P. Schmidt, S. Arnold, A. Loges, D. Werner, T. Wetzel, E. Ivers-Tiffée, Measurement of the internal cell temperature via impedance: Evaluation and application of a new method, *J. Power Sources* 243 (2013) 110–117, <http://dx.doi.org/10.1016/j.jpowsour.2013.06.013>.
- [10] L. Rajimakers, D. Danilov, J. van Lammeren, M. Lammers, P. Notten, Sensorless battery temperature measurements based on electrochemical impedance spectroscopy, *J. Power Sources* 247 (2014) 539–544, <http://dx.doi.org/10.1016/j.jpowsour.2013.09.005>.
- [11] R.R. Richardson, P.T. Ireland, D.A. Howey, Battery internal temperature estimation by combined impedance and surface temperature measurement, *J. Power Sources* 265 (2014) 254–261, <http://dx.doi.org/10.1016/j.jpowsour.2014.04.129>.
- [12] H. Beelen, L. Rajimakers, M. Donkers, P. Notten, H. Bergveld, An improved impedance-based temperature estimation method for Li-ion, *IFAC-PapersOnLine* 48 (2015) 383–388, <http://dx.doi.org/10.1016/j.ifacol.2015.10.055>.
- [13] R. Koch, A. Jossen, Temperature Measurement of Large Format Pouch Cells with Impedance Spectroscopy, in: *EVS28 International Electric Vehicle Symposium and Exhibition*, 2015.
- [14] J. Zhu, Z. Sun, X. Wei, H. Dai, A new lithium-ion battery internal temperature on-line estimate method based on electrochemical impedance spectroscopy measurement, *J. Power Sources* 274 (2015) 990–1004, <http://dx.doi.org/10.1016/j.jpowsour.2014.10.182>.
- [15] N.S. Spinner, C.T. Love, S.L. Rose-Pehrsson, S.G. Tuttle, Expanding the operational limits of the single-point impedance diagnostic for internal temperature monitoring of lithium-ion batteries, *Electrochim. Acta* 174 (2015) 488–493, <http://dx.doi.org/10.1016/j.electacta.2015.06.003>.
- [16] L.H. Rajimakers, D.L. Danilov, J.P. van Lammeren, T.J. Lammers, H.J. Bergveld, P.H.L. Notten, Non-zero intercept frequency: An accurate method to determine the integral temperature of Li-ion batteries, *IEEE Trans. Ind. Electron.* 63 (2016) 3168–3178, <http://dx.doi.org/10.1109/TIE.2016.2516961>.

- [17] R.R. Richardson, S. Zhao, D.A. Howey, On-board monitoring of 2-D spatially-resolved temperatures in cylindrical lithium-ion batteries: Part II. State estimation via impedance-based temperature sensing, *J. Power Sources* 327 (2016) 726–735, <http://dx.doi.org/10.1016/j.jpowsour.2016.06.104>.
- [18] J. Zhu, Z. Sun, X. Wei, H. Dai, Battery internal temperature estimation for LiFePO₄ battery based on impedance phase shift under operating conditions, *Energies* 10 (2017) 60, <http://dx.doi.org/10.3390/en10010060>.
- [19] X. Wang, X. Wei, Q. Chen, J. Zhu, H. Dai, Lithium-ion battery temperature online estimation based on fast impedance calculation, *J. Energy Storage* 26 (2019) 100952, <http://dx.doi.org/10.1016/j.est.2019.100952>.
- [20] H. Beelen, K. Munderagi Shivakumar, L. Rajmakers, M. Donkers, H.J. Bergveld, Towards impedance-based temperature estimation for Li-ion battery packs, *Int. J. Energy Res.* 44 (2020) 2889–2908, <http://dx.doi.org/10.1002/er.5107>.
- [21] Y. Xie, W. Li, X. Hu, X. Lin, Y. Zhang, D. Dan, F. Feng, B. Liu, K. Li, An enhanced online temperature estimation for lithium-ion batteries, *IEEE Trans. Transp. Electr.* 6 (2020) 375–390, <http://dx.doi.org/10.1109/TTE.2020.2980153>.
- [22] P. Wang, L. Yang, H. Wang, D. Tartakovsky, S. Onori, Temperature estimation from current and voltage measurements in lithium-ion battery systems, *J. Energy Storage* 34 (2021) 102133, <http://dx.doi.org/10.1016/j.est.2020.102133>.
- [23] S. Ludwig, I. Zilberman, M. Horsche, T. Wohlers, A. Jossen, Pulse resistance based online temperature estimation for lithium-ion cells, *J. Power Sources* 490 (2021) 229523, <http://dx.doi.org/10.1016/j.jpowsour.2021.229523>.
- [24] I. Zilberman, S. Ludwig, M. Schiller, A. Jossen, Online aging determination in lithium-ion battery module with forced temperature gradient, *J. Energy Storage* 28 (2020) 101170, <http://dx.doi.org/10.1016/j.est.2019.101170>.
- [25] C. Campestrini, M.F. Horsche, I. Zilberman, T. Heil, T. Zimmermann, A. Jossen, Validation and benchmark methods for battery management system functionalities: State of charge estimation algorithms, *J. Energy Storage* 7 (2016) 38–51, <http://dx.doi.org/10.1016/j.est.2016.05.007>.
- [26] J. Sturm, A. Rheinfeld, I. Zilberman, F. Spingler, S. Kosch, F. Frie, A. Jossen, Modeling and simulation of inhomogeneities in a 18650 nickel-rich, silicon-graphite lithium-ion cell during fast charging, *J. Power Sources* 412 (2019) 204–223, <http://dx.doi.org/10.1016/j.jpowsour.2018.11.043>.
- [27] B. Wu, V. Yufit, M. Marinescu, G.J. Offer, R.F. Martinez-Botas, N.P. Brandon, Coupled thermal-electrochemical modelling of uneven heat generation in lithium-ion battery packs, *J. Power Sources* 243 (2013) 544–554, <http://dx.doi.org/10.1016/j.jpowsour.2013.05.164>.
- [28] X. Xu, R. He, Research on the heat dissipation performance of battery pack based on forced air cooling, *J. Power Sources* 240 (2013) 33–41, <http://dx.doi.org/10.1016/j.jpowsour.2013.03.004>.
- [29] F.M. Kindermann, A. Noel, S.V. Erhard, A. Jossen, Long-term equalization effects in Li-ion batteries due to local state of charge inhomogeneities and their impact on impedance measurements, *Electrochim. Acta* 185 (2015) 107–116, <http://dx.doi.org/10.1016/j.electacta.2015.10.108>.
- [30] K.S. Ng, C. Moo, Y. Chen, Y. Hsieh, Enhanced coulomb counting method for estimating state-of-charge and state-of-health of lithium-ion batteries, *Appl. Energy* 86 (2009) 1506–1511, <http://dx.doi.org/10.1016/j.apenergy.2008.11.021>.
- [31] M. Becherif, M. Péra, D. Hissel, S. Jemei, Enhancement of the coulomb counter estimator by the on-board vehicle determination of battery initial state of charge, *IFAC Proc. Vol.* 45 (2012) 621–626, <http://dx.doi.org/10.3182/20120902-4-FR-2032.00109>.
- [32] Y. Zou, X. Hu, H. Ma, S.E. Li, Combined state of charge and state of health estimation over lithium-ion battery cell cycle lifespan for electric vehicles, *J. Power Sources* 273 (2015) 793–803, <http://dx.doi.org/10.1016/j.jpowsour.2014.09.146>.
- [33] M.A. Awadallah, B. Venkatesh, Accuracy improvement of SOC estimation in lithium-ion batteries, *J. Energy Storage* 6 (2016) 95–104, <http://dx.doi.org/10.1016/j.est.2016.03.003>.
- [34] I. Zilberman, S. Ludwig, A. Jossen, Cell-to-cell variation of calendar aging and reversible self-discharge in 18650 nickel-rich, silicon-graphite lithium-ion cells, *J. Energy Storage* 26 (2019) 100900, <http://dx.doi.org/10.1016/j.est.2019.100900>.
- [35] M. Schindler, J. Sturm, S. Ludwig, A. Durdel, A. Jossen, Comprehensive analysis of the aging behavior of nickel-rich, silicon-graphite lithium-ion cells subject to varying temperature and charging profiles, *J. Electrochem. Soc.* 168 (2021) 060522, <http://dx.doi.org/10.1149/1945-7111/ac03f6>.
- [36] M. Lewerenz, J. Münnix, J. Schmalstieg, S. Käbitz, M. Knips, D.U. Sauer, Systematic aging of commercial LiFePO₄ | Graphite cylindrical cells including a theory explaining rise of capacity during aging, *J. Power Sources* 345 (2017) 254–263, <http://dx.doi.org/10.1016/j.jpowsour.2017.01.133>.
- [37] L. Wildfeuer, N. Wassiliadis, C. Reiter, M. Baumann, M. Lienkamp, Experimental characterization of Li-ion battery resistance at the cell, module and pack level, in: 2019 Fourteenth International Conference on Ecological Vehicles and Renewable Energies, EVER, IEEE, 2019, pp. 1–12, <http://dx.doi.org/10.1109/EVER.2019.8813578>.
- [38] C. von Lüders, V. Zinth, S.V. Erhard, P.J. Osswald, M. Hofmann, R. Gilles, A. Jossen, Lithium plating in lithium-ion batteries investigated by voltage relaxation and in situ neutron diffraction, *J. Power Sources* 342 (2017) 17–23, <http://dx.doi.org/10.1016/j.jpowsour.2016.12.032>.
- [39] S. Schindler, M. Bauer, M. Petzl, M.A. Danzer, Voltage relaxation and impedance spectroscopy as in-operando methods for the detection of lithium plating on graphitic anodes in commercial lithium-ion cells, *J. Power Sources* 304 (2016) 170–180, <http://dx.doi.org/10.1016/j.jpowsour.2015.11.044>.
- [40] W. Waag, S. Käbitz, D.U. Sauer, Experimental investigation of the lithium-ion battery impedance characteristic at various conditions and aging states and its influence on the application, *Appl. Energy* 102 (2013) 885–897, <http://dx.doi.org/10.1016/j.apenergy.2012.09.030>.
- [41] E. Meissner, G. Richter, Battery monitoring and electrical energy management, *J. Power Sources* 116 (2003) 79–98, [http://dx.doi.org/10.1016/S0378-7753\(02\)00713-9](http://dx.doi.org/10.1016/S0378-7753(02)00713-9).
- [42] R. Fisher, Statistical methods for research workers, in: S. Kotz, N.L. Johnson (Eds.), *Breakthroughs in Statistics*, in: Springer Series in Statistics, Springer New York, New York, NY, 1992, pp. 66–70, http://dx.doi.org/10.1007/978-1-4612-4380-9_6.
- [43] M. Hannan, M. Lipu, A. Hussain, A. Mohamed, A review of lithium-ion battery state of charge estimation and management system in electric vehicle applications: Challenges and recommendations, *Renew. Sustain. Energy Rev.* 78 (2017) 834–854, <http://dx.doi.org/10.1016/j.rser.2017.05.001>.
- [44] M. Hossain Lipu, M. Hannan, A. Hussain, A. Ayob, M.H. Saad, T.F. Karim, D.N. How, Data-driven state of charge estimation of lithium-ion batteries: Algorithms, implementation factors, limitations and future trends, *J. Clean. Prod.* 277 (2020) 124110, <http://dx.doi.org/10.1016/j.jclepro.2020.124110>.
- [45] B. Yang, J. Wang, P. Cao, T. Zhu, H. Shu, J. Chen, J. Zhang, J. Zhu, Classification, summarization and perspectives on state-of-charge estimation of lithium-ion batteries used in electric vehicles: A critical comprehensive survey, *J. Energy Storage* 39 (2021) 102572, <http://dx.doi.org/10.1016/j.est.2021.102572>.
- [46] M.H. Lipu, M. Hannan, A. Hussain, M.M. Hoque, P.J. Ker, M. Saad, A. Ayob, A review of state of health and remaining useful life estimation methods for lithium-ion battery in electric vehicles: Challenges and recommendations, *J. Clean. Prod.* 205 (2018) 115–133, <http://dx.doi.org/10.1016/j.jclepro.2018.09.065>.
- [47] H. Tian, P. Qin, K. Li, Z. Zhao, A review of the state of health for lithium-ion batteries: Research status and suggestions, *J. Clean. Prod.* 261 (2020) 120813, <http://dx.doi.org/10.1016/j.jclepro.2020.120813>.
- [48] S. Yang, C. Zhang, J. Jiang, W. Zhang, L. Zhang, Y. Wang, Review on state-of-health of lithium-ion batteries: Characterizations, estimations and applications, *J. Clean. Prod.* 314 (2021) 128015, <http://dx.doi.org/10.1016/j.jclepro.2021.128015>.
- [49] N.S. Raju, R. Bilgic, J.E. Edwards, P.F. Flerer, Methodology review: Estimation of population validity and cross-validity, and the use of equal weights in prediction, *Appl. Psychol. Meas.* 21 (1997) 291–305, <http://dx.doi.org/10.1177/01466216970214001>.
- [50] The MathWorks, Inc., *Curve fitting Toolbox™ user's guide: R2021a*, 2021.

7 Conclusion and Outlook

The global demand for energy storage for a green future in the mobility sector is steadily increasing and so is the market for LIBs. The market for EVs in particular is characterized by tough demands on energy storage. Long ranges, short charging times, reliable power and safety over a wide operating range are some of the challenges faced by EV manufacturers. In this context, the temperature of LIBs often plays a crucial role as it has a decisive impact on lifetime, performance, and safety, and is therefore a key element from system design until the end of a LIB's life cycle. For this reason, monitoring and potentially controlling the temperature is an important function of a BMS. For systems with a very large number of cells, as it is the case with some EV manufacturers, individual cell temperature monitoring by means of temperature sensors is often omitted due to higher cost, weight, and complexity. And even when the temperature is measured with a temperature sensor, it provides only a limited temperature image of the surface of the LIB. This carries the risk that unfavorable or harmful (internal) temperatures of individual cells are not detected at all or are detected too late. The consequences range from faster aging, which can lead to reduced performance and range, to serious dangers for the vehicle and driver due to a thermal runaway. For this reason, there are many approaches to derive the temperature from other battery values to get a full picture of the temperature in the battery storage system. One of these approaches is based on the impedance of LIBs, as this can also be used to obtain an internal temperature information. Many methods in the literature are based on EIS measurements, but this method is accompanied by a complex measurement system and evaluation.

In this work, the idea of determining the temperature from the impedance of a LIB is adopted. However, the impedance is considered in the time domain and load changes of the application itself are used as excitation for the impedance calculation and thus for the temperature determination. This has the advantage of not having to integrate an additional measuring system and complex evaluations as with the EIS approach, but rather relying on the existing current and voltage monitoring of the BMS. This approach gave rise to the research questions Q1 to Q4, which are investigated in this thesis using three commercial cylindrical cell types listed in Table 3.1 with different chemistry and format.

The first study in Chapter 3 addresses the question which temperature the resistance in the time domain (R_{DC}) represents. For this purpose, the relationship between measured surface temperature, modeled internal cell temperature and R_{DC} in relation to chemistry, SOC and format was investigated. In isothermal conditions, an Arrhenius-like relationship of R_{DC} and temperature was found as in equation Eq. (2.37), which has already been reported in various methods listed in Table 2.4. In the case of an inhomogeneous cell temperature generated by a rapid change in ambient temperature, the Arrhenius-like relationship demonstrated that the temperature T_R determined from the R_{DC} corresponds to an internal cell temperature, which is in agreement with the statements from the literature in Table 2.4. The SOC and cell format affect the difference between the measured surface temperature and T_R , with the difference clearly increasing with increasing cell format from about 2.5 K (18650) to about 5 K (26650) and decreasing by about 0.5 K with increasing SOC. By comparing the temperature behavior with a 2D thermal model of the cells, it was shown that T_R is most closely related to the average jelly roll temperature. This relationship was then further investigated using a spatially and temperature

resolved impedance analysis in Section 3.2. A worst case analysis showed that at the investigated temperature gradients in the study, with a maximum of 5.45 K for the 26650 cell, this relationship still holds and the deviation between volume average cell temperature $T_{\text{avg,vol}}$ and temperature T_p derived from volume-related conductance is less than 0.4 K. In the case of external heating T_p tends to be larger than $T_{\text{avg,vol}}$ and the difference increases with increasing gradient. Thus, the first research question Q1 regarding the general and spatial relationship of the temperature and the R_{DC} could be answered. It is consequently possible for a BMS to determine an internal cell temperature using the R_{DC} , which is an advantage over conventional temperature sensors.

How this method can be implemented in a BMS was examined in more detail in Chapter 4. This second study focuses on the development of the method using the 18650 cell from Table 3.1 and addresses the research question Q2 of how and under what conditions the temperature of a cell can be determined from a load profile. In a first step, individual cells were tested under different boundary conditions with various pulse patterns to determine their effects on the resistance behavior in the time domain. With the knowledge gained from these tests, a method for temperature estimation was developed and optimized. The objective was to optimize the calculation period of the resistance Δt and the parametrization of the estimation function to ensure that as many load fluctuations as possible are suitable for the temperature estimation and thus to obtain a continuous temperature characteristic during operation. With the resulting method, the temperature in a 6s1p module could be estimated with a RMSE between 0.59 K and 1.11 K. This is approximately in the same range as the average RMSE of 0.858 K of the methods from the literature in Table 2.6. In addition, the module validation showed that the method can be applied to unknown cells of the same type using a resistance offset correction to account for intrinsic cell to cell variations.

In the fundamentals in Section 2.3, the numerous effects of temperature on lifetime, performance, and safety on individual cells were discussed, motivating the need for temperature monitoring. The effects in Section 2.3 focus primarily on single cells and mostly omit effects that occur in interconnected systems. For this reason, Chapter 5 addresses the effects of temperature gradients in the system during cyclic aging. The aging study was performed with the same module as in Chapter 4. Likewise, the research question Q3 was addressed, which deals with the influence of aging on the R_{DC} and thus also the influence on the method from Chapter 4. It was shown that a temperature gradient of 5 K between 25 °C and 30 °C already has a significant effect on aging in terms of capacity and resistance. After just 200 cycles, the capacity of the limiting cell dropped to about 80% and its resistance increased to slightly above 120%. By comparison, the least aged cell lost only about 6% of capacity and its resistance increased by only about 2%. This demonstrated that even a relatively small temperature gradient of 5 K at moderate temperatures can lead to highly inhomogeneous cyclic aging, making accurate temperature monitoring all the more important. In order to counteract the temperature-induced inhomogeneous aging, temperature monitoring must be accompanied by an adapted operating mode that ensures homogeneous temperatures in the battery pack.

The method developed in Chapter 4 is dependent on resistance and capacity, which both can change significantly over aging as shown in Chapter 5 and thus can also affect the accuracy of the method. In addition, the analysis of the literature in Table 2.5 revealed that battery aging is an often neglected aspect of impedance-based temperature estimation methods. Based on these facts, Chapter 6 addresses question Q4, which focuses on the need and implementation of an adjustment to aging for the temperature estimation method from Chapter 4. Since the RMSE reached up to 15 K without adjustment, an adaptation to changing resistance and capacity was necessary. By means of a correlation analysis, it was shown that it is possible to adapt the method to aging by regularly updating the reference

polynomials used for temperature estimation. For this purpose, the reference polynomials are adapted to the aging state of the cells using equation Eq. (6.1) by scaling and shifting. The scaling and shifting values can be acquired by an accurate SOC determination over the SOH and regular resistance updates at isothermal boundary conditions, which both is achievable during the operation of a battery system. With these measures, the RMSE for the cells could be reduced again to an average level between 0.88 K and 1.51 K over the entire module lifetime.

In summary, this work developed a new method for determining the internal cell temperature using the pulse resistance R_{DC} , which does not place any additional hardware requirements on a BMS and determines the temperature from the load fluctuations during operation. Furthermore, it was shown that even small temperature gradients can have a decisive effect on the aging behavior of a battery system and that the method can be adapted to the aging behavior of the cells during operation to ensure a temperature estimation over the lifetime of the battery system.

Nevertheless, not all aspects have been examined in detail in the thesis. For example, the thesis addressed individual cells and a representative module setup. However, only the serial connection of cells was investigated with the module. An open issue remains the investigation of parallel connected cells. The difficulty in this case lies in particular in the fact that in the application the current distribution of the individual cells is unknown and thus only an impedance of the overall parallel connection can be determined. Moreover, measuring the current by means of shunt resistors in the individual parallel branches is an intervention in the system and could undesirably change the actual behavior of the parallel interconnection [253]. Therefore, the issue of how a temperature gradient across a parallel connection affects impedance-based temperature estimation and whether this gradient can also be detected remains open. In the literature, only the studies #1, #17, and #18 in Table 2.5 examined a system of two cells connected in parallel, but without intentionally creating or considering a gradient in the system. Schmidt et al. [45] and Troxler et al. [243], as discussed in Section 3.2, did not consider a system of cells connected in parallel, but they used this point of view to study the effects of an internal temperature gradient on the layers connected in parallel in a pouch cell. They found that the measured impedance, and thus the temperature determined from it, is dependent on the gradient. With small gradients, the determined temperature tends to correspond to the average cell temperature, and with higher gradients, it tends to the hotspot within the cell. Whether this behavior can be transferred to the parallel connection of individual cells still remains an open question.

Another issue that has been discussed only in marginal detail in Section 2.2 is the behavior of LIBs at high temperatures at which the temperature to resistance relation can reverse and thus a clear determination of the temperature by resistance is no longer possible. In this regard, there are only the studies of Spinner et al. [174] and Srinivasan et al. [234]. In [174], the cells were examined at temperatures up to 95 °C. Due to the small change in impedance at temperatures above 68 °C, their estimation method had to be adapted for this temperature range. Nonetheless, high estimation errors of up to 11.4 K occurred. In [234], the cells were heated until reaching a thermal runaway. Using their phase-based method, the authors were able to detect the sharp temperature rise before and during the thermal runaway. Despite these findings, the behavior of the R_{DC} , and thus the temperature estimation method presented in this thesis, at very high temperatures up to the thermal runaway has not yet been resolved and will be the subject of further investigations in the future.

References

- [1] Nishi, Y.: *Lithium ion secondary batteries; past 10 years and the future*. In: *Journal of Power Sources* 100.1-2 (2001), pp. 101–106. DOI: [10.1016/S0378-7753\(01\)00887-4](https://doi.org/10.1016/S0378-7753(01)00887-4) (see p. 1).
- [2] Liu, H., Wei, Z., He, W., and Zhao, J.: *Thermal issues about Li-ion batteries and recent progress in battery thermal management systems: A review*. In: *Energy Conversion and Management* 150 (2017), pp. 304–330. DOI: [10.1016/j.enconman.2017.08.016](https://doi.org/10.1016/j.enconman.2017.08.016) (see pp. 1, 13, 14, 16, 17, 22, 37).
- [3] Blomgren, G. E.: *The Development and Future of Lithium Ion Batteries*. In: *Journal of The Electrochemical Society* 164.1 (2017), A5019–A5025. DOI: [10.1149/2.0251701jes](https://doi.org/10.1149/2.0251701jes) (see pp. 1, 9).
- [4] Hesse, H., Schimpe, M., Kucevic, D., and Jossen, A.: *Lithium-Ion Battery Storage for the Grid—A Review of Stationary Battery Storage System Design Tailored for Applications in Modern Power Grids*. In: *Energies* 10.12 (2017), p. 2107. DOI: [10.3390/en10122107](https://doi.org/10.3390/en10122107) (see pp. 1, 9).
- [5] Placek, M.: *Projected global battery demand from 2020 to 2030, by application: (in gigawatt hours)*. Ed. by Statista. 2021. URL: <https://www.statista.com/statistics/1103218/global-battery-demand-forecast/> (visited on 11/04/2022) (see p. 1).
- [6] Jacobson, M. Z. et al.: *100% Clean and Renewable Wind, Water, and Sunlight All-Sector Energy Roadmaps for 139 Countries of the World*. In: *Joule* 1.1 (2017), pp. 108–121. DOI: [10.1016/j.joule.2017.07.005](https://doi.org/10.1016/j.joule.2017.07.005) (see p. 1).
- [7] Krems, J. F. and KreiBig, I.: *Electromobility: History, Definitions and an Overview of Psychological Research on a Sustainable Mobility System*. In: *International Encyclopedia of Transportation*. Vol. 50. Elsevier, 2021, pp. 182–186. ISBN: 9780081026724 (see p. 1).
- [8] IEA, I. E. A.: *Global EV Outlook 2021: Accelerating ambitions despite the pandemic*. In: (2021). URL: <https://www.iea.org/data-and-statistics/data-tools/global-ev-data-explorer> (visited on 11/04/2022) (see p. 2).
- [9] Wu, H., Alberts, G., Hooper, J., and Walton, B.: *New market. New entrants. New challenges. Battery Electric Vehicles*. 2019. URL: <https://www2.deloitte.com/content/dam/Deloitte/uk/Documents/manufacturing/deloitte-uk-battery-electric-vehicles.pdf> (visited on 10/15/2022) (see p. 1).
- [10] Shahid, S. and Agelin-Chaab, M.: *A review of thermal runaway prevention and mitigation strategies for lithium-ion batteries*. In: *Energy Conversion and Management: X* 1.2017 (2022), p. 100310. DOI: [10.1016/j.ecmx.2022.100310](https://doi.org/10.1016/j.ecmx.2022.100310) (see pp. 1, 2, 13).
- [11] Sieg, J., Bandlow, J., Mitsch, T., Dragicovic, D., Materna, T., Spier, B., Witzhausen, H., Ecker, M., and Sauer, D. U.: *Fast charging of an electric vehicle lithium-ion battery at the limit of the lithium deposition process*. In: *Journal of Power Sources* 427.2 (2019), pp. 260–270. DOI: [10.1016/j.jpowsour.2019.04.047](https://doi.org/10.1016/j.jpowsour.2019.04.047) (see p. 1).

- [12] Yang, X.-G. and Wang, C.-Y.: *Understanding the trilemma of fast charging, energy density and cycle life of lithium-ion batteries*. In: *Journal of Power Sources* 402 (2018), pp. 489–498. DOI: [10.1016/j.jpowsour.2018.09.069](https://doi.org/10.1016/j.jpowsour.2018.09.069) (see p. 1).
- [13] Wenig, J., Sodenkamp, M., and Staake, T.: *Battery versus infrastructure: Tradeoffs between battery capacity and charging infrastructure for plug-in hybrid electric vehicles*. In: *Applied Energy* 255 (2019), p. 113787. DOI: [10.1016/j.apenergy.2019.113787](https://doi.org/10.1016/j.apenergy.2019.113787) (see p. 1).
- [14] Baik, Y., Hensley, R., Hertzke, P., and Knupfer, S.: *Making electric vehicles profitable*. Ed. by McKinsey & Company. 2019. URL: <https://www.mckinsey.com/industries/automotive-and-assembly/our-insights/making-electric-vehicles-profitable> (visited on 10/15/2022) (see p. 1).
- [15] Chen, M., Bai, F., Lin, S., Song, W., Li, Y., and Feng, Z.: *Performance and safety protection of internal short circuit in lithium-ion battery based on a multilayer electro-thermal coupling model*. In: *Applied Thermal Engineering* 146.15 (2019), pp. 775–784. DOI: [10.1016/j.applthermaleng.2018.10.011](https://doi.org/10.1016/j.applthermaleng.2018.10.011) (see p. 2).
- [16] Mao, B., Chen, H., Cui, Z., Wu, T., and Wang, Q.: *Failure mechanism of the lithium ion battery during nail penetration*. In: *International Journal of Heat and Mass Transfer* 122.1 (2018), pp. 1103–1115. DOI: [10.1016/j.ijheatmasstransfer.2018.02.036](https://doi.org/10.1016/j.ijheatmasstransfer.2018.02.036) (see p. 2).
- [17] Finegan, D. P. et al.: *Characterising thermal runaway within lithium-ion cells by inducing and monitoring internal short circuits*. In: *Energy Environ. Sci.* 10.6 (2017), pp. 1377–1388. DOI: [10.1039/C7EE00385D](https://doi.org/10.1039/C7EE00385D) (see p. 2).
- [18] Alipour, M., Ziebert, C., Conte, F. V., and Kizilel, R.: *A Review on Temperature-Dependent Electrochemical Properties, Aging, and Performance of Lithium-Ion Cells*. In: *Batteries* 6.3 (2020), p. 35. DOI: [10.3390/batteries6030035](https://doi.org/10.3390/batteries6030035) (see pp. 2, 10, 13, 17, 18, 20, 23–25, 94).
- [19] Liu, X., Ai, W., Naylor Marlow, M., Patel, Y., and Wu, B.: *The effect of cell-to-cell variations and thermal gradients on the performance and degradation of lithium-ion battery packs*. In: *Applied Energy* 248 (2019), pp. 489–499. DOI: [10.1016/j.apenergy.2019.04.108](https://doi.org/10.1016/j.apenergy.2019.04.108) (see p. 2).
- [20] Leng, F., Tan, C. M., and Pecht, M.: *Effect of Temperature on the Aging rate of Li Ion Battery Operating above Room Temperature*. In: *Scientific reports* 5 (2015), p. 12967. DOI: [10.1038/srep12967](https://doi.org/10.1038/srep12967) (see pp. 2, 25).
- [21] Fu, R., Xiao, M., and Choe, S.-Y.: *Modeling, validation and analysis of mechanical stress generation and dimension changes of a pouch type high power Li-ion battery*. In: *Journal of Power Sources* 224 (2013), pp. 211–224. DOI: [10.1016/j.jpowsour.2012.09.096](https://doi.org/10.1016/j.jpowsour.2012.09.096) (see pp. 2, 25).
- [22] Song, W., Chen, M., Bai, F., Lin, S., Chen, Y., and Feng, Z.: *Non-uniform effect on the thermal/aging performance of Lithium-ion pouch battery*. In: *Applied Thermal Engineering* 128.4 (2018), pp. 1165–1174. DOI: [10.1016/j.applthermaleng.2017.09.090](https://doi.org/10.1016/j.applthermaleng.2017.09.090) (see p. 2).
- [23] Osswald, P. J., Erhard, S. V., Rheinfeld, A., Rieger, B., Hoster, H. E., and Jossen, A.: *Temperature dependency of state of charge inhomogeneities and their equalization in cylindrical lithium-ion cells*. In: *Journal of Power Sources* 329.9 (2016), pp. 546–552. DOI: [10.1016/j.jpowsour.2016.08.120](https://doi.org/10.1016/j.jpowsour.2016.08.120) (see p. 2).
- [24] Zhang, G., Shaffer, C. E., Wang, C.-Y., and Rahn, C. D.: *In-Situ Measurement of Current Distribution in a Li-Ion Cell*. In: *Journal of The Electrochemical Society* 160.4 (2013), A610–A615. DOI: [10.1149/2.046304jes](https://doi.org/10.1149/2.046304jes) (see p. 2).

- [25] Han, X., Ouyang, M., Lu, L., and Li, J.: *A comparative study of commercial lithium ion battery cycle life in electric vehicle: Capacity loss estimation*. In: *Journal of Power Sources* 268.8 (2014), pp. 658–669. DOI: [10.1016/j.jpowsour.2014.06.111](https://doi.org/10.1016/j.jpowsour.2014.06.111) (see p. 2).
- [26] Fleischhammer, M., Waldmann, T., Bisle, G., Hogg, B.-I., and Wohlfahrt-Mehrens, M.: *Interaction of cyclic ageing at high-rate and low temperatures and safety in lithium-ion batteries*. In: *Journal of Power Sources* 274 (2015), pp. 432–439. DOI: [10.1016/j.jpowsour.2014.08.135](https://doi.org/10.1016/j.jpowsour.2014.08.135) (see pp. 2, 25).
- [27] Friesen, A., Horsthemke, F., Mönninghoff, X., Brunklaus, G., Krafft, R., Börner, M., Risthaus, T., Winter, M., and Schappacher, F. M.: *Impact of cycling at low temperatures on the safety behavior of 18650-type lithium ion cells: Combined study of mechanical and thermal abuse testing accompanied by post-mortem analysis*. In: *Journal of Power Sources* 334.1986 (2016), pp. 1–11. DOI: [10.1016/j.jpowsour.2016.09.120](https://doi.org/10.1016/j.jpowsour.2016.09.120) (see p. 2).
- [28] Ma, S., Jiang, M., Tao, P., Song, C., Wu, J., Wang, J., Deng, T., and Shang, W.: *Temperature effect and thermal impact in lithium-ion batteries: A review*. In: *Progress in Natural Science: Materials International* 28.6 (2018), pp. 653–666. DOI: [10.1016/j.pnsc.2018.11.002](https://doi.org/10.1016/j.pnsc.2018.11.002) (see pp. 2, 3).
- [29] Morello, R., Di Rienzo, R., Roncella, R., Saletti, R., Schwarz, R., Lorentz, V., Hoedemaekers, E., Rosca, B., and Baronti, F.: “Advances in Li-Ion Battery Management for Electric Vehicles.” In: *IECON 2018 - 44th Annual Conference of the IEEE Industrial Electronics Society*. IEEE, 21.10.2018 - 23.10.2018, pp. 4949–4955. ISBN: 978-1-5090-6684-1. DOI: [10.1109/IECON.2018.8591185](https://doi.org/10.1109/IECON.2018.8591185) (see pp. 2, 13, 34, 36, 39).
- [30] Waldmann, T., Wilka, M., Kasper, M., Fleischhammer, M., and Wohlfahrt-Mehrens, M.: *Temperature dependent ageing mechanisms in Lithium-ion batteries – A Post-Mortem study*. In: *Journal of Power Sources* 262 (2014), pp. 129–135. DOI: [10.1016/j.jpowsour.2014.03.112](https://doi.org/10.1016/j.jpowsour.2014.03.112) (see pp. 2, 24).
- [31] Schuster, S. F., Brand, M. J., Campestrini, C., Gleissenberger, M., and Jossen, A.: *Correlation between capacity and impedance of lithium-ion cells during calendar and cycle life*. In: *Journal of Power Sources* 305 (2016), pp. 191–199. DOI: [10.1016/j.jpowsour.2015.11.096](https://doi.org/10.1016/j.jpowsour.2015.11.096) (see pp. 2, 26).
- [32] Naumann, M., Schimpe, M., Keil, P., Hesse, H. C., and Jossen, A.: *Analysis and modeling of calendar aging of a commercial LiFePO₄/graphite cell*. In: *Journal of Energy Storage* 17.12 (2018), pp. 153–169. DOI: [10.1016/j.est.2018.01.019](https://doi.org/10.1016/j.est.2018.01.019) (see pp. 2, 9, 10, 25).
- [33] Park, M., Zhang, X., Chung, M., Less, G. B., and Sastry, A. M.: *A review of conduction phenomena in Li-ion batteries*. In: *Journal of Power Sources* 195.24 (2010), pp. 7904–7929. DOI: [10.1016/j.jpowsour.2010.06.060](https://doi.org/10.1016/j.jpowsour.2010.06.060) (see pp. 2, 13–19, 21).
- [34] Xu, X. M. and He, R.: *Research on the heat dissipation performance of battery pack based on forced air cooling*. In: *Journal of Power Sources* 240 (2013), pp. 33–41. DOI: [10.1016/j.jpowsour.2013.03.004](https://doi.org/10.1016/j.jpowsour.2013.03.004) (see p. 2).
- [35] Wu, B., Yufit, V., Marinescu, M., Offer, G. J., Martinez-Botas, R. F., and Brandon, N. P.: *Coupled thermal–electrochemical modelling of uneven heat generation in lithium-ion battery packs*. In: *Journal of Power Sources* 243 (2013), pp. 544–554. DOI: [10.1016/j.jpowsour.2013.05.164](https://doi.org/10.1016/j.jpowsour.2013.05.164) (see p. 2).

- [36] Zhao, C., Cao, W., Dong, T., and Jiang, F.: *Thermal behavior study of discharging/charging cylindrical lithium-ion battery module cooled by channeled liquid flow*. In: *International Journal of Heat and Mass Transfer* 120 (2018), pp. 751–762. DOI: [10.1016/j.ijheatmasstransfer.2017.12.083](https://doi.org/10.1016/j.ijheatmasstransfer.2017.12.083) (see p. 2).
- [37] Tang, A., Li, J., Lou, L., Shan, C., and Yuan, X.: *Optimization design and numerical study on water cooling structure for power lithium battery pack*. In: *Applied Thermal Engineering* 159 (2019), p. 113760. DOI: [10.1016/j.applthermaleng.2019.113760](https://doi.org/10.1016/j.applthermaleng.2019.113760) (see p. 2).
- [38] Wang, S., Rafiz, K., Liu, J., Jin, Y., and Lin, J. Y. S.: *Effects of lithium dendrites on thermal runaway and gassing of LiFePO₄ batteries*. In: *Sustainable Energy & Fuels* 4.5 (2020), pp. 2342–2351. DOI: [10.1039/DO5E00027B](https://doi.org/10.1039/DO5E00027B) (see pp. 3, 24, 34, 36, 39).
- [39] Ji, C., Wang, B., Wang, S., Pan, S., Du Wang, Qi, P., and Zhang, K.: *Optimization on uniformity of lithium-ion cylindrical battery module by different arrangement strategy*. In: *Applied Thermal Engineering* 157 (2019), p. 113683. DOI: [10.1016/j.applthermaleng.2019.04.093](https://doi.org/10.1016/j.applthermaleng.2019.04.093) (see p. 3).
- [40] Rumpf, K., Naumann, M., and Jossen, A.: *Experimental investigation of parametric cell-to-cell variation and correlation based on 1100 commercial lithium-ion cells*. In: *Journal of Energy Storage* 14.2 (2017), pp. 224–243. DOI: [10.1016/j.est.2017.09.010](https://doi.org/10.1016/j.est.2017.09.010) (see p. 3).
- [41] Ströbel, M., Pross-Brakhage, J., Kopp, M., and Birke, K. P.: *Impedance Based Temperature Estimation of Lithium Ion Cells Using Artificial Neural Networks*. In: *Batteries* 7.4 (2021), p. 85. DOI: [10.3390/batteries7040085](https://doi.org/10.3390/batteries7040085) (see pp. 3, 34, 36, 39).
- [42] Fill, A., Koch, S., and Birke, K. P.: *Algorithm for the detection of a single cell contact loss within parallel-connected cells based on continuous resistance ratio estimation*. In: *Journal of Energy Storage* 27 (2020), p. 101049. DOI: [10.1016/j.est.2019.101049](https://doi.org/10.1016/j.est.2019.101049) (see p. 3).
- [43] Brand, M. J., Hofmann, M. H., Steinhardt, M., Schuster, S. F., and Jossen, A.: *Current distribution within parallel-connected battery cells*. In: *Journal of Power Sources* 334 (2016), pp. 202–212. DOI: [10.1016/j.jpowsour.2016.10.010](https://doi.org/10.1016/j.jpowsour.2016.10.010) (see p. 3).
- [44] Koch, R. and Jossen, A.: *Temperature Measurement of Large Format Pouch Cells with Impedance Spectroscopy*. In: *EVS28 International Electric Vehicle Symposium and Exhibition* (2015) (see pp. 3, 34, 36, 39).
- [45] Schmidt, J. P., Arnold, S., Loges, A., Werner, D., Wetzel, T., and Ivers-Tiffée, E.: *Measurement of the internal cell temperature via impedance: Evaluation and application of a new method*. In: *Journal of Power Sources* 243 (2013), pp. 110–117. DOI: [10.1016/j.jpowsour.2013.06.013](https://doi.org/10.1016/j.jpowsour.2013.06.013) (see pp. 3, 22, 34, 36, 39, 70–72, 123).
- [46] Li, S. et al.: *Optimal cell tab design and cooling strategy for cylindrical lithium-ion batteries*. In: *Journal of Power Sources* 492 (2021), p. 229594. DOI: [10.1016/j.jpowsour.2021.229594](https://doi.org/10.1016/j.jpowsour.2021.229594) (see pp. 3, 25).
- [47] Richardson, R. R., Ireland, P. T., and Howey, D. A.: *Battery internal temperature estimation by combined impedance and surface temperature measurement*. In: *Journal of Power Sources* 265 (2014), pp. 254–261. DOI: [10.1016/j.jpowsour.2014.04.129](https://doi.org/10.1016/j.jpowsour.2014.04.129) (see pp. 3, 34, 36, 39, 70, 71).
- [48] Li, Z., Zhang, J., Wu, B., Huang, J., Nie, Z., Sun, Y., An, F., and Wu, N.: *Examining temporal and spatial variations of internal temperature in large-format laminated battery with embedded thermocouples*. In: *Journal of Power Sources* 241 (2013), pp. 536–553. DOI: [10.1016/j.jpowsour.2013.04.117](https://doi.org/10.1016/j.jpowsour.2013.04.117) (see p. 3).

- [49] Raijmakers, L., Danilov, D. L., van Lammeren, J., Lammers, M., and Notten, P.: *Sensorless battery temperature measurements based on electrochemical impedance spectroscopy*. In: *Journal of Power Sources* 247 (2014), pp. 539–544. DOI: [10.1016/j.jpowsour.2013.09.005](https://doi.org/10.1016/j.jpowsour.2013.09.005) (see pp. 3, 34, 36, 39).
- [50] Raijmakers, L. H. J., Danilov, D. L., van Lammeren, J. P. M., Lammers, T. J. G., Bergveld, H. J., and Notten, P. H. L.: *Non-Zero Intercept Frequency: An Accurate Method to Determine the Integral Temperature of Li-Ion Batteries*. In: *IEEE Transactions on Industrial Electronics* 63.5 (2016), pp. 3168–3178. DOI: [10.1109/TIE.2016.2516961](https://doi.org/10.1109/TIE.2016.2516961) (see pp. 3, 34, 36, 39).
- [51] Srinivasan, R., Carkhuff, B. G., Butler, M. H., Baisden, A. C., and Uy, O. M.: “An external sensor for instantaneous measurement of the internal temperature in lithium-ion rechargeable cells.” In: *Energy Harvesting and Storage: Materials, Devices, and Applications II*. Ed. by N. K. Dhar, P. S. Wijewarnasuriya, and A. K. Dutta. SPIE Proceedings. SPIE, 2011, p. 80350D. DOI: [10.1117/12.884691](https://doi.org/10.1117/12.884691) (see pp. 3, 27, 34, 36, 39).
- [52] Srinivasan, R.: *Monitoring dynamic thermal behavior of the carbon anode in a lithium-ion cell using a four-probe technique*. In: *Journal of Power Sources* 198 (2012), pp. 351–358. DOI: [10.1016/j.jpowsour.2011.09.077](https://doi.org/10.1016/j.jpowsour.2011.09.077) (see pp. 3, 34, 36, 39).
- [53] Zhu, J. G., Sun, Z. C., Wei, X. Z., and Dai, H. F.: *A new lithium-ion battery internal temperature on-line estimate method based on electrochemical impedance spectroscopy measurement*. In: *Journal of Power Sources* 274 (2015), pp. 990–1004. DOI: [10.1016/j.jpowsour.2014.10.182](https://doi.org/10.1016/j.jpowsour.2014.10.182) (see pp. 3, 34, 36, 39).
- [54] Wang, X., Wei, X., Chen, Q., Zhu, J., and Dai, H.: *Lithium-ion battery temperature on-line estimation based on fast impedance calculation*. In: *Journal of Energy Storage* 26 (2019), p. 100952. DOI: [10.1016/j.est.2019.100952](https://doi.org/10.1016/j.est.2019.100952) (see pp. 3, 4, 34, 36, 39, 75).
- [55] Mathew, M., Janhunen, S., Rashid, M., Long, F., and Fowler, M.: *Comparative Analysis of Lithium-Ion Battery Resistance Estimation Techniques for Battery Management Systems*. In: *Energies* 11.6 (2018), p. 1490. DOI: [10.3390/en11061490](https://doi.org/10.3390/en11061490) (see pp. 3, 4).
- [56] Maleki, H. and Howard, J. N.: *Effects of overdischarge on performance and thermal stability of a Li-ion cell*. In: *Journal of Power Sources* 160.2 (2006), pp. 1395–1402. DOI: [10.1016/j.jpowsour.2006.03.043](https://doi.org/10.1016/j.jpowsour.2006.03.043) (see p. 8).
- [57] Guo, R., Lu, L., Ouyang, M., and Feng, X.: *Mechanism of the entire overdischarge process and overdischarge-induced internal short circuit in lithium-ion batteries*. In: *Scientific reports* 6 (2016), p. 30248. DOI: [10.1038/srep30248](https://doi.org/10.1038/srep30248) (see p. 8).
- [58] Braithwaite, J. W., Gonzales, A., Nagasubramanian, G., Lucero, S. J., Peebles, D. E., Ohlhausen, J. A., and Cieslak, W. R.: *Corrosion of Lithium-Ion Battery Current Collectors*. In: *Journal of The Electrochemical Society* 146.2 (1999), pp. 448–456. DOI: [10.1149/1.1391627](https://doi.org/10.1149/1.1391627) (see p. 8).
- [59] Whitehead, A. H. and Schreiber, M.: *Current Collectors for Positive Electrodes of Lithium-Based Batteries*. In: *Journal of Nuclear Materials* 152.11 (2005), A2105. DOI: [10.1149/1.2039587](https://doi.org/10.1149/1.2039587) (see p. 8).
- [60] Chen, J., Liu, J., Qi, Y., Sun, T., and Li, X.: *Unveiling the Roles of Binder in the Mechanical Integrity of Electrodes for Lithium-Ion Batteries*. In: *Journal of The Electrochemical Society* 160.9 (2013), A1502–A1509. DOI: [10.1149/2.088309jes](https://doi.org/10.1149/2.088309jes) (see p. 8).

- [61] Mandal, S., Amarilla, J. M., Ibáñez, J., and Rojo, J. M.: *The Role of Carbon Black in LiMn[₂]O[₄]-Based Composites as Cathodes for Rechargeable Lithium Batteries*. In: *Solid State Ionics* 148.1 (2001), A24. DOI: [10.1149/1.1339026](https://doi.org/10.1149/1.1339026) (see p. 8).
- [62] Mahmud, S., Rahman, M., Kamruzzaman, M., Ali, M. O., Emon, M. S. A., Khatun, H., and Ali, M. R.: *Recent advances in lithium-ion battery materials for improved electrochemical performance: A review*. In: *Results in Engineering* 15.4 (2022), p. 100472. DOI: [10.1016/j.rineng.2022.100472](https://doi.org/10.1016/j.rineng.2022.100472) (see p. 9).
- [63] Korthauer, R.: *Handbuch Lithium-Ionen-Batterien*. Berlin, Heidelberg: Springer Berlin Heidelberg, 2013. ISBN: 978-3-642-30652-5. DOI: [10.1007/978-3-642-30653-2](https://doi.org/10.1007/978-3-642-30653-2) (see p. 9).
- [64] Meister, P., Jia, H., Li, J., Kloepsch, R., Winter, M., and Placke, T.: *Best Practice: Performance and Cost Evaluation of Lithium Ion Battery Active Materials with Special Emphasis on Energy Efficiency*. In: *Chemistry of Materials* 28.20 (2016), pp. 7203–7217. DOI: [10.1021/acs.chemmater.6b02895](https://doi.org/10.1021/acs.chemmater.6b02895) (see p. 9).
- [65] Armand, M. et al.: *Lithium-ion batteries – Current state of the art and anticipated developments*. In: *Journal of Power Sources* 479 (2020), p. 228708. DOI: [10.1016/j.jpowsour.2020.228708](https://doi.org/10.1016/j.jpowsour.2020.228708) (see pp. 9, 10).
- [66] Andre, D., Kim, S.-J., Lamp, P., Lux, S. F., Maglia, F., Paschos, O., and Stiaszny, B.: *Future generations of cathode materials: an automotive industry perspective*. In: *Journal of Materials Chemistry A* 3.13 (2015), pp. 6709–6732. DOI: [10.1039/C5TA00361J](https://doi.org/10.1039/C5TA00361J) (see p. 9).
- [67] Nitta, N., Wu, F., Lee, J. T., and Yushin, G.: *Li-ion battery materials: present and future*. In: *Materials Today* 18.5 (2015), pp. 252–264. DOI: [10.1016/j.mattod.2014.10.040](https://doi.org/10.1016/j.mattod.2014.10.040) (see pp. 9, 10).
- [68] Yoon, C. S., Park, K.-J., Kim, U.-H., Kang, K. H., Ryu, H.-H., and Sun, Y.-K.: *High-Energy Ni-Rich Li[Ni_xCo_yMn_{1-x-y}]O₂ Cathodes via Compositional Partitioning for Next-Generation Electric Vehicles*. In: *Chemistry of Materials* 29.24 (2017), pp. 10436–10445. DOI: [10.1021/acs.chemmater.7b04047](https://doi.org/10.1021/acs.chemmater.7b04047) (see p. 9).
- [69] Wu, F., Maier, J., and Yu, Y.: *Guidelines and trends for next-generation rechargeable lithium and lithium-ion batteries*. In: *Chemical Society reviews* 49.5 (2020), pp. 1569–1614. DOI: [10.1039/C7CS00863E](https://doi.org/10.1039/C7CS00863E) (see pp. 9, 10).
- [70] Manthiram, A.: *A reflection on lithium-ion battery cathode chemistry*. In: *Nature communications* 11.1 (2020), p. 1550. DOI: [10.1038/s41467-020-15355-0](https://doi.org/10.1038/s41467-020-15355-0) (see p. 9).
- [71] Myung, S.-T., Maglia, F., Park, K.-J., Yoon, C. S., Lamp, P., Kim, S.-J., and Sun, Y.-K.: *Nickel-Rich Layered Cathode Materials for Automotive Lithium-Ion Batteries: Achievements and Perspectives*. In: *ACS Energy Letters* 2.1 (2017), pp. 196–223. DOI: [10.1021/acsenergylett.6b00594](https://doi.org/10.1021/acsenergylett.6b00594) (see p. 9).
- [72] Kim, H., Oh, S.-M., Scrosati, B., and Sun, Y.-K.: *High-performance electrode materials for lithium-ion batteries for electric vehicles*. In: *Advances in Battery Technologies for Electric Vehicles*. Vol. 4. Woodhead Publishing Series in Energy. Woodhead Publishing, 2015, pp. 191–241. DOI: [10.1016/B978-1-78242-377-5.00009-1](https://doi.org/10.1016/B978-1-78242-377-5.00009-1) (see p. 9).
- [73] Ding, Y., Cano, Z. P., Yu, A., Lu, J., and Chen, Z.: *Automotive Li-Ion Batteries: Current Status and Future Perspectives*. In: *Electrochemical Energy Reviews* 2.1 (2019), pp. 1–28. DOI: [10.1007/s41918-018-0022-z](https://doi.org/10.1007/s41918-018-0022-z) (see pp. 9, 10, 12).

- [74] Schmuch, R., Wagner, R., Hörpel, G., Placke, T., and Winter, M.: *Performance and cost of materials for lithium-based rechargeable automotive batteries*. In: *Nature Energy* 3.4 (2018), pp. 267–278. DOI: [10.1038/s41560-018-0107-2](https://doi.org/10.1038/s41560-018-0107-2) (see pp. 9, 10, 12).
- [75] Naumann, M., Spingler, F. B., and Jossen, A.: *Analysis and modeling of cycle aging of a commercial LiFePO₄/graphite cell*. In: *Journal of Power Sources* 451.14 (2020), p. 227666. DOI: [10.1016/j.jpowsour.2019.227666](https://doi.org/10.1016/j.jpowsour.2019.227666) (see p. 9).
- [76] Houache, M., Yim, C.-H., Karkar, Z., and Abu-Lebdeh, Y.: *On the Current and Future Outlook of Battery Chemistries for Electric Vehicles—Mini Review*. In: *Batteries* 8.7 (2022), p. 70. DOI: [10.3390/batteries8070070](https://doi.org/10.3390/batteries8070070) (see p. 10).
- [77] Ramasubramanian, B., Sundarrajan, S., Chellappan, V., Reddy, M. V., Ramakrishna, S., and Zaghbi, K.: *Recent Development in Carbon-LiFePO₄ Cathodes for Lithium-Ion Batteries: A Mini Review*. In: *Batteries* 8.10 (2022), p. 133. DOI: [10.3390/batteries8100133](https://doi.org/10.3390/batteries8100133) (see p. 10).
- [78] Winter, M., Besenhard, J. O., Spahr, M. E., and Novák, P.: *Insertion Electrode Materials for Rechargeable Lithium Batteries*. In: *Advanced Materials* 10.10 (1998), pp. 725–763. DOI: [10.1002/\(SICI\)1521-4095\(199807\)10:10%3C725::AID-ADMA725%3E3.0.CO;2-Z](https://doi.org/10.1002/(SICI)1521-4095(199807)10:10%3C725::AID-ADMA725%3E3.0.CO;2-Z) (see pp. 10, 24).
- [79] Asenbauer, J., Eisenmann, T., Kuenzel, M., Kazzazi, A., Chen, Z., and Bresser, D.: *The success story of graphite as a lithium-ion anode material – fundamentals, remaining challenges, and recent developments including silicon (oxide) composites*. In: *Sustainable Energy & Fuels* 4.11 (2020), pp. 5387–5416. DOI: [10.1039/D0SE00175A](https://doi.org/10.1039/D0SE00175A) (see pp. 10, 17, 24).
- [80] Arora, P., White, R. E., and Doyle, M.: *Capacity Fade Mechanisms and Side Reactions in Lithium-Ion Batteries*. In: *Journal of The Electrochemical Society* 145.10 (1998), pp. 3647–3667. DOI: [10.1149/1.1838857](https://doi.org/10.1149/1.1838857) (see pp. 10, 24).
- [81] Jantke, D., Bernhard, R., Hanelt, E., Buhrmester, T., Pfeiffer, J., and Haufe, S.: *Silicon-Dominant Anodes Based on Microscale Silicon Particles under Partial Lithiation with High Capacity and Cycle Stability*. In: *Journal of The Electrochemical Society* 166.16 (2019), A3881–A3885. DOI: [10.1149/2.1311915jes](https://doi.org/10.1149/2.1311915jes) (see p. 10).
- [82] Luo, Z., Fan, D., Liu, X., Mao, H., Yao, C., and Deng, Z.: *High performance silicon carbon composite anode materials for lithium ion batteries*. In: *Journal of Power Sources* 189.1 (2009), pp. 16–21. DOI: [10.1016/j.jpowsour.2008.12.068](https://doi.org/10.1016/j.jpowsour.2008.12.068) (see p. 10).
- [83] Moyassari, E. et al.: *Impact of Silicon Content within Silicon-Graphite Anodes on Performance and Li Concentration Profiles of Li-Ion Cells using Neutron Depth Profiling*. In: *Journal of The Electrochemical Society* 168.2 (2021), p. 020519. DOI: [10.1149/1945-7111/abe1db](https://doi.org/10.1149/1945-7111/abe1db) (see p. 10).
- [84] Popp, H., Zhang, N., Jahn, M., Arrinda, M., Ritz, S., Faber, M., Sauer, D. U., Azais, P., and Cendoya, I.: *Ante-mortem analysis, electrical, thermal, and ageing testing of state-of-the-art cylindrical lithium-ion cells*. In: *e & i Elektrotechnik und Informationstechnik* 137.4-5 (2020), pp. 169–176. DOI: [10.1007/s00502-020-00814-9](https://doi.org/10.1007/s00502-020-00814-9) (see pp. 10, 12, 42).
- [85] Sturm, J., Rheinfeld, A., Zilberman, I., Spingler, F. B., Kosch, S., Frie, F., and Jossen, A.: *Modeling and simulation of inhomogeneities in a 18650 nickel-rich, silicon-graphite lithium-ion cell during fast charging*. In: *Journal of Power Sources* 412 (2019), pp. 204–223. DOI: [10.1016/j.jpowsour.2018.11.043](https://doi.org/10.1016/j.jpowsour.2018.11.043) (see p. 10).
- [86] Lain, Brandon, and Kendrick: *Design Strategies for High Power vs. High Energy Lithium Ion Cells*. In: *Batteries* 5.4 (2019), p. 64. DOI: [10.3390/batteries5040064](https://doi.org/10.3390/batteries5040064) (see p. 10).

- [87] Cheng, X.-B., Zhang, R., Zhao, C.-Z., and Zhang, Q.: *Toward Safe Lithium Metal Anode in Rechargeable Batteries: A Review*. In: *Chemical reviews* 117.15 (2017), pp. 10403–10473. DOI: [10.1021/acs.chemrev.7b00115](https://doi.org/10.1021/acs.chemrev.7b00115) (see p. 10).
- [88] Blomgren, G. E.: *Electrolytes for advanced batteries*. In: *Journal of Power Sources* 81-82 (1999), pp. 112–118. DOI: [10.1016/S0378-7753\(99\)00188-3](https://doi.org/10.1016/S0378-7753(99)00188-3) (see p. 10).
- [89] Haregewoin, A. M., Wotango, A. S., and Hwang, B.-J.: *Electrolyte additives for lithium ion battery electrodes: progress and perspectives*. In: *Energy Environ. Sci.* 9.6 (2016), pp. 1955–1988. DOI: [10.1039/C6EE00123H](https://doi.org/10.1039/C6EE00123H) (see pp. 10, 25).
- [90] Xu, Y.-N., Chung, S.-Y., Bloking, J. T., Chiang, Y.-M., and Ching, W. Y.: *Electronic Structure and Electrical Conductivity of Undoped LiFePO₄*. In: *Journal of The Electrochemical Society* 7.6 (2004), A131. DOI: [10.1149/1.1703470](https://doi.org/10.1149/1.1703470) (see pp. 10, 18).
- [91] Parimalam, B. S. and Lucht, B. L.: *Reduction Reactions of Electrolyte Salts for Lithium Ion Batteries: LiPF₆, LiBF₄, LiDFOB, LiBOB, and LiTFSI*. In: *Journal of The Electrochemical Society* 165.2 (2018), A251–A255. DOI: [10.1149/2.0901802jes](https://doi.org/10.1149/2.0901802jes) (see p. 10).
- [92] Li, Q., Chen, J., Fan, L., Kong, X., and Lu, Y.: *Progress in electrolytes for rechargeable Li-based batteries and beyond*. In: *Green Energy & Environment* 1.1 (2016), pp. 18–42. DOI: [10.1016/j.gee.2016.04.006](https://doi.org/10.1016/j.gee.2016.04.006) (see p. 10).
- [93] Huang, X.: *Separator technologies for lithium-ion batteries*. In: *Journal of Solid State Electrochemistry* 15.4 (2011), pp. 649–662. DOI: [10.1007/s10008-010-1264-9](https://doi.org/10.1007/s10008-010-1264-9) (see p. 11).
- [94] Lee, H., Yanilmaz, M., Toprakci, O., Fu, K., and Zhang, X.: *A review of recent developments in membrane separators for rechargeable lithium-ion batteries*. In: *Energy Environ. Sci.* 7.12 (2014), pp. 3857–3886. DOI: [10.1039/C4EE01432D](https://doi.org/10.1039/C4EE01432D) (see p. 11).
- [95] Choi, J.-A., Kim, S. H., and Kim, D.-W.: *Enhancement of thermal stability and cycling performance in lithium-ion cells through the use of ceramic-coated separators*. In: *Journal of Power Sources* 195.18 (2010), pp. 6192–6196. DOI: [10.1016/j.jpowsour.2009.11.020](https://doi.org/10.1016/j.jpowsour.2009.11.020) (see p. 11).
- [96] Kraft, L., Hoefling, A., Zünd, T., Kunz, A., Steinhardt, M., Tübke, J., and Jossen, A.: *Implications of the Heat Generation of LMR-NCM on the Thermal Behavior of Large-Format Lithium-Ion Batteries*. In: *Journal of The Electrochemical Society* 168.5 (2021), p. 053505. DOI: [10.1149/1945-7111/ac0069](https://doi.org/10.1149/1945-7111/ac0069) (see pp. 11, 12).
- [97] Sturm, J., Frank, A., Rheinfeld, A., Erhard, S. V., and Jossen, A.: *Impact of Electrode and Cell Design on Fast Charging Capabilities of Cylindrical Lithium-Ion Batteries*. In: *Journal of The Electrochemical Society* 167.13 (2020), p. 130505. DOI: [10.1149/1945-7111/abb40c](https://doi.org/10.1149/1945-7111/abb40c) (see pp. 11, 12).
- [98] Rheinfeld, A., Sturm, J., Frank, A., Kosch, S., Erhard, S. V., and Jossen, A.: *Impact of Cell Size and Format on External Short Circuit Behavior of Lithium-Ion Cells at Varying Cooling Conditions: Modeling and Simulation*. In: *Journal of The Electrochemical Society* 167.1 (2020), p. 013511. DOI: [10.1149/2.0112001JES](https://doi.org/10.1149/2.0112001JES) (see p. 11).
- [99] Lee, Y., Son, B., Choi, J., Kim, J. H., Ryou, M.-H., and Lee, Y. M.: *Effect of back-side-coated electrodes on electrochemical performances of lithium-ion batteries*. In: *Journal of Power Sources* 275 (2015), pp. 712–719. DOI: [10.1016/j.jpowsour.2014.11.029](https://doi.org/10.1016/j.jpowsour.2014.11.029) (see p. 11).
- [100] Svens, P., Kjell, M., Tengstedt, C., Flodberg, G., and Lindbergh, G.: *Li-Ion Pouch Cells for Vehicle Applications — Studies of Water Transmission and Packing Materials*. In: *Energies* 6.1 (2013), pp. 400–410. DOI: [10.3390/en6010400](https://doi.org/10.3390/en6010400) (see p. 11).

- [101] Kwade, A., Haselrieder, W., Leithoff, R., Modlinger, A., Dietrich, F., and Droeder, K.: *Current status and challenges for automotive battery production technologies*. In: *Nature Energy* 3.4 (2018), pp. 290–300. DOI: [10.1038/s41560-018-0130-3](https://doi.org/10.1038/s41560-018-0130-3) (see p. 11).
- [102] Schröder, R., Aydemir, M., and Seliger, G.: *Comparatively Assessing different Shapes of Lithium-ion Battery Cells*. In: *Procedia Manufacturing* 8 (2017), pp. 104–111. DOI: [10.1016/j.promfg.2017.02.013](https://doi.org/10.1016/j.promfg.2017.02.013) (see p. 11).
- [103] Reinhart, G. et al.: *Research and Demonstration Center for the Production of Large-Area Lithium-Ion Cells*. In: *Future Trends in Production Engineering*. Ed. by G. Schuh, R. Neugebauer, and E. Uhlmann. Vol. 12. Berlin, Heidelberg: Springer Berlin Heidelberg, 2013, pp. 3–12. ISBN: 978-3-642-24490-2. DOI: [10.1007/978-3-642-24491-9_1](https://doi.org/10.1007/978-3-642-24491-9_1) (see p. 11).
- [104] Lundgren, H., Svens, P., Ekström, H., Tengstedt, C., Lindström, J., Behm, M., and Lindbergh, G.: *Thermal Management of Large-Format Prismatic Lithium-Ion Battery in PHEV Application*. In: *Journal of The Electrochemical Society* 163.2 (2016), A309–A317. DOI: [10.1149/2.09411602jes](https://doi.org/10.1149/2.09411602jes) (see p. 11).
- [105] Bandhauer, T., Garimella, S., and Fuller, T. F.: *Electrochemical-Thermal Modeling to Evaluate Battery Thermal Management Strategies*. In: *Journal of The Electrochemical Society* 162.1 (2015), A125–A136. DOI: [10.1149/2.0571501jes](https://doi.org/10.1149/2.0571501jes) (see p. 11).
- [106] Balakrishnan, P. G., Ramesh, R., and Prem Kumar, T.: *Safety mechanisms in lithium-ion batteries*. In: *Journal of Power Sources* 155.2 (2006), pp. 401–414. DOI: [10.1016/j.jpowsour.2005.12.002](https://doi.org/10.1016/j.jpowsour.2005.12.002) (see p. 12).
- [107] Quinn, J. B., Waldmann, T., Richter, K., Kasper, M., and Wohlfahrt-Mehrens, M.: *Energy Density of Cylindrical Li-Ion Cells: A Comparison of Commercial 18650 to the 21700 Cells*. In: *Journal of The Electrochemical Society* 165.14 (2018), A3284–A3291. DOI: [10.1149/2.0281814jes](https://doi.org/10.1149/2.0281814jes) (see p. 12).
- [108] Placke, T., Kloepsch, R., Dühnen, S., and Winter, M.: *Lithium ion, lithium metal, and alternative rechargeable battery technologies: the odyssey for high energy density*. In: *Journal of Solid State Electrochemistry* 21.7 (2017), pp. 1939–1964. DOI: [10.1007/s10008-017-3610-7](https://doi.org/10.1007/s10008-017-3610-7) (see p. 12).
- [109] Putri, N. H., Rahardian, S., and Budiman, B. A.: *Battery Cells for Electric Vehicles*. In: *International Journal of Sustainable Transportation Technology* 2.2 (2019), pp. 54–57. DOI: [10.31427/IJSTT.2019.2.2.3](https://doi.org/10.31427/IJSTT.2019.2.2.3) (see p. 12).
- [110] Liu, S.: *Competition and Valuation: A Case Study of Tesla Motors*. In: *IOP Conference Series: Earth and Environmental Science* 692.2 (2021), p. 022103. DOI: [10.1088/1755-1315/692/2/022103](https://doi.org/10.1088/1755-1315/692/2/022103) (see p. 12).
- [111] Lu, D.: *Identifying Physical Model Parameter Values for Lithium-Ion Cells*. PhD thesis. Colorado Springs: University of Colorado, 29.04.2022. URL: <https://www.proquest.com/openview/cd3bedcbe06f258ea5f4332db4b20be2/> (see p. 12).
- [112] BMW Group: *Round battery cells for the Neue Klasse*. Ed. by BMW Group. 2022. URL: <https://www.bmwgroup.com/en/news/general/2022/gen6.html> (visited on 10/23/2022) (see p. 12).
- [113] Tranter, T. G., Timms, R., Shearing, P. R., and Brett, D. J. L.: *Communication—Prediction of Thermal Issues for Larger Format 4680 Cylindrical Cells and Their Mitigation with Enhanced Current Collection*. In: *Journal of The Electrochemical Society* 167.16 (2020), p. 160544. DOI: [10.1149/1945-7111/abd44f](https://doi.org/10.1149/1945-7111/abd44f) (see p. 12).

- [114] Wang, P., Yang, L., Wang, H., Tartakovsky, D. M., and Onori, S.: *Temperature estimation from current and voltage measurements in lithium-ion battery systems*. In: *Journal of Energy Storage* 34.9 (2021), p. 102133. DOI: [10.1016/j.est.2020.102133](https://doi.org/10.1016/j.est.2020.102133) (see pp. 12, 25, 27, 29, 31, 33, 34, 36, 39).
- [115] Hausbrand, R., Cherkashinin, G., Ehrenberg, H., Gröting, M., Albe, K., Hess, C., and Jaegermann, W.: *Fundamental degradation mechanisms of layered oxide Li-ion battery cathode materials: Methodology, insights and novel approaches*. In: *Materials Science and Engineering: B* 192.16 (2015), pp. 3–25. DOI: [10.1016/j.mseb.2014.11.014](https://doi.org/10.1016/j.mseb.2014.11.014) (see p. 12).
- [116] Pop, V., Bergveld, H. J., Op het Veld, J. H. G., Regtien, P. P. L., Danilov, D., and Notten, P. H. L.: *Modeling Battery Behavior for Accurate State-of-Charge Indication*. In: *Journal of Power Sources* 153.11 (2006), A2013. DOI: [10.1149/1.2335951](https://doi.org/10.1149/1.2335951) (see p. 12).
- [117] Guyomard, D. and Tarascon, J.-M.: *Rocking-chair or lithium-ion rechargeable lithium batteries*. In: *Advanced Materials* 6.5 (1994), pp. 408–412. DOI: [10.1002/adma.19940060516](https://doi.org/10.1002/adma.19940060516) (see pp. 12, 13).
- [118] Jossen, A.: *Fundamentals of battery dynamics*. In: *Journal of Power Sources* 154.2 (2006), pp. 530–538. DOI: [10.1016/j.jpowsour.2005.10.041](https://doi.org/10.1016/j.jpowsour.2005.10.041) (see pp. 13, 15, 19, 21).
- [119] Illig, J.: *Physically based Impedance Modelling of Lithium-Ion Cells*. 2014 (see pp. 13, 15).
- [120] Gantenbein, S., Weiss, M., and Ivers-Tiffée, E.: *Impedance based time-domain modeling of lithium-ion batteries: Part I*. In: *Journal of Power Sources* 379 (2018), pp. 317–327. DOI: [10.1016/j.jpowsour.2018.01.043](https://doi.org/10.1016/j.jpowsour.2018.01.043) (see pp. 13–15, 18–22, 25, 27, 28, 32).
- [121] Xiong, R. et al.: *Overpotential decomposition enabled decoupling of complex kinetic processes in battery electrodes*. In: *Journal of Power Sources* 553 (2023), p. 232296. DOI: [10.1016/j.jpowsour.2022.232296](https://doi.org/10.1016/j.jpowsour.2022.232296) (see p. 13).
- [122] Väyrynen, A. and Salminen, J.: *Lithium ion battery production*. In: *The Journal of Chemical Thermodynamics* 46.Spring (2012), pp. 80–85. DOI: [10.1016/j.jct.2011.09.005](https://doi.org/10.1016/j.jct.2011.09.005) (see pp. 13, 16, 17, 22, 37).
- [123] Waldmann, T., Hogg, B.-I., and Wohlfahrt-Mehrens, M.: *Li plating as unwanted side reaction in commercial Li-ion cells – A review*. In: *Journal of Power Sources* 384 (2018), pp. 107–124. DOI: [10.1016/j.jpowsour.2018.02.063](https://doi.org/10.1016/j.jpowsour.2018.02.063) (see pp. 13, 24, 94).
- [124] Petzl, M., Kasper, M., and Danzer, M. A.: *Lithium plating in a commercial lithium-ion battery – A low-temperature aging study*. In: *Journal of Power Sources* 275 (2015), pp. 799–807. DOI: [10.1016/j.jpowsour.2014.11.065](https://doi.org/10.1016/j.jpowsour.2014.11.065) (see pp. 13, 24, 94).
- [125] Daniel, C. and Besenhard, J. O.: *Handbook of battery materials*. 2., completely rev. and enl. ed., 1. Reprint. Weinheim: Wiley-VCH-Verl., 2012. ISBN: 978-3-527-32695-2 (see p. 14).
- [126] Gold, V.: *The IUPAC Compendium of Chemical Terminology*. Research Triangle Park, NC: International Union of Pure and Applied Chemistry (IUPAC), 2019. DOI: [10.1351/goldbook](https://doi.org/10.1351/goldbook) (see p. 14).
- [127] Mills, I., ed.: *Quantities, units and symbols in physical chemistry*. 2. ed., reprinted. Oxford: Blackwell Science, 1998. ISBN: 0-632-03583-8 (see p. 14).
- [128] Farmann, A. and Sauer, D. U.: *A study on the dependency of the open-circuit voltage on temperature and actual aging state of lithium-ion batteries*. In: *Journal of Power Sources* 347.9 (2017), pp. 1–13. DOI: [10.1016/j.jpowsour.2017.01.098](https://doi.org/10.1016/j.jpowsour.2017.01.098) (see p. 14).

- [129] Campestrini, C., Kosch, S., and Jossen, A.: *Influence of change in open circuit voltage on the state of charge estimation with an extended Kalman filter*. In: *Journal of Energy Storage* 12.9 (2017), pp. 149–156. DOI: [10.1016/j.est.2017.04.011](https://doi.org/10.1016/j.est.2017.04.011) (see p. 14).
- [130] Illig, J., Ender, M., Chrobak, T., Schmidt, J. P., Klotz, D., and Ivers-Tiffée, E.: *Separation of Charge Transfer and Contact Resistance in LiFePO₄ -Cathodes by Impedance Modeling*. In: *Journal of The Electrochemical Society* 159.7 (2012), A952–A960. DOI: [10.1149/2.030207jes](https://doi.org/10.1149/2.030207jes) (see p. 15).
- [131] Rattanaweeranon, S., Limsuwan, P., Thongpool, V., Piriya Wong, V., and Asanithi, P.: *Influence of Bulk Graphite Density on Electrical Conductivity*. In: *Procedia Engineering* 32 (2012), pp. 1100–1106. DOI: [10.1016/j.proeng.2012.02.061](https://doi.org/10.1016/j.proeng.2012.02.061) (see pp. 15–17).
- [132] Grüneisen, E.: *Die Abhängigkeit des elektrischen Widerstandes reiner Metalle von der Temperatur*. In: *Annalen der Physik* 408.5 (1933), pp. 530–540. DOI: [10.1002/andp.19334080504](https://doi.org/10.1002/andp.19334080504) (see p. 16).
- [133] Matula, R. A.: *Electrical resistivity of copper, gold, palladium, and silver*. In: *Journal of Physical and Chemical Reference Data* 8.4 (1979), pp. 1147–1298. DOI: [10.1063/1.555614](https://doi.org/10.1063/1.555614) (see p. 16).
- [134] Cvijović, D.: *The Bloch-Grüneisen function of arbitrary order and its series representations*. In: *Theoretical and Mathematical Physics* 166.1 (2011), pp. 37–42. DOI: [10.1007/s11232-011-0003-4](https://doi.org/10.1007/s11232-011-0003-4) (see p. 16).
- [135] Desai, P. D., James, H. M., and Ho, C. Y.: *Electrical Resistivity of Aluminum and Manganese*. In: *Journal of Physical and Chemical Reference Data* 13.4 (1984), pp. 1131–1172. DOI: [10.1063/1.555725](https://doi.org/10.1063/1.555725) (see p. 16).
- [136] Partoens, B. and Peeters, F. M.: *From graphene to graphite: Electronic structure around the K point*. In: *Physical Review B* 74.7 (2006). DOI: [10.1103/PhysRevB.74.075404](https://doi.org/10.1103/PhysRevB.74.075404) (see p. 16).
- [137] Wu, M., Xu, B., and Ouyang, C.: *Physics of electron and lithium-ion transport in electrode materials for Li-ion batteries*. In: *Journal of Power Sources* 25.1 (2016), p. 018206. DOI: [10.1088/1674-1056/25/1/018206](https://doi.org/10.1088/1674-1056/25/1/018206) (see pp. 16, 18, 21, 22).
- [138] Tanzi, M. C., Farè, S., and Candiani, G.: *Organization, Structure, and Properties of Materials*. In: *Foundations of Biomaterials Engineering*. Vol. 6. Elsevier, 2019, pp. 3–103. ISBN: 9780081010341. DOI: [10.1016/B978-0-08-101034-1.00001-3](https://doi.org/10.1016/B978-0-08-101034-1.00001-3) (see p. 16).
- [139] Wallace, P. R.: *The Band Theory of Graphite*. In: *Physical Review* 71.9 (1947), pp. 622–634. DOI: [10.1103/PhysRev.71.622](https://doi.org/10.1103/PhysRev.71.622) (see pp. 16, 17).
- [140] Dutta, A. K.: *Electrical Conductivity of Single Crystals of Graphite*. In: *Physical Review* 90.2 (1953), pp. 187–192. DOI: [10.1103/PhysRev.90.187](https://doi.org/10.1103/PhysRev.90.187) (see p. 16).
- [141] Powell, R. W.: *The thermal and electrical conductivity of carbon and graphite to high temperatures*. In: *Proc. Phys. Soc.* (1939), pp. 153–172. DOI: [10.1088/0959-5309/51/1/317](https://doi.org/10.1088/0959-5309/51/1/317) (see pp. 16, 17).
- [142] Buerschaper, R. A.: *Thermal and Electrical Conductivity of Graphite and Carbon at Low Temperatures*. In: *Journal of Applied Physics* 15.5 (1944), pp. 452–454. DOI: [10.1063/1.1707454](https://doi.org/10.1063/1.1707454) (see pp. 16, 17).
- [143] Iwashita, N., Imagawa, H., and Nishiumi, W.: *Variation of temperature dependence of electrical resistivity with crystal structure of artificial graphite products*. In: *Carbon* 61.6 (2013), pp. 602–608. DOI: [10.1016/j.carbon.2013.05.042](https://doi.org/10.1016/j.carbon.2013.05.042) (see pp. 16, 17).

- [144] Billaud, D., McRae, E., and Hérold, A.: *Synthesis and electrical resistivity of lithium-pyrographite intercalation compounds (stages I, II and III)*. In: *Materials Research Bulletin* 14.7 (1979), pp. 857–864. DOI: [10.1016/0025-5408\(79\)90149-1](https://doi.org/10.1016/0025-5408(79)90149-1) (see p. 17).
- [145] Salah, M., Murphy, P., Hall, C., Francis, C., Kerr, R., and Fabretto, M.: *Pure silicon thin-film anodes for lithium-ion batteries: A review*. In: *Journal of Power Sources* 414 (2019), pp. 48–67. DOI: [10.1016/j.jpowsour.2018.12.068](https://doi.org/10.1016/j.jpowsour.2018.12.068) (see pp. 17, 18).
- [146] Butera, R. A. and Waldeck, D. H.: *The Dependence of Resistance on Temperature for Metals, Semiconductors, and Superconductors*. In: *Journal of Chemical Education* 74.9 (1997), p. 1090. DOI: [10.1021/ed074p1090](https://doi.org/10.1021/ed074p1090) (see p. 17).
- [147] Chittick, R. C., Alexander, J. H., and Sterling, H. F.: *The Preparation and Properties of Amorphous Silicon*. In: *Journal of The Electrochemical Society* 116.1 (1969), p. 77. DOI: [10.1149/1.2411779](https://doi.org/10.1149/1.2411779) (see p. 17).
- [148] Pollak, E., Salitra, G., Baranchugov, V., and Aurbach, D.: *In Situ Conductivity, Impedance Spectroscopy, and Ex Situ Raman Spectra of Amorphous Silicon during the Insertion/Extraction of Lithium*. In: *The Journal of Physical Chemistry C* 111.30 (2007), pp. 11437–11444. DOI: [10.1021/jp0729563](https://doi.org/10.1021/jp0729563) (see p. 17).
- [149] Srivastava, J. K., Prasad, M., and Wagner, J. B.: *Electrical Conductivity of Silicon Dioxide Thermally Grown on Silicon*. In: *Journal of The Electrochemical Society* 132.4 (1985), pp. 955–963. DOI: [10.1149/1.2113993](https://doi.org/10.1149/1.2113993) (see p. 17).
- [150] Scholz, R., dos Santos Marques, F., and Riccardi, B.: *Electrical conductivity of silicon carbide composites and fibers*. In: *Journal of Nuclear Materials* 307-311 (2002), pp. 1098–1101. DOI: [10.1016/S0022-3115\(02\)00950-9](https://doi.org/10.1016/S0022-3115(02)00950-9) (see p. 17).
- [151] Levasseur, S., Ménétrier, M., and Delmas, C.: *On the Dual Effect of Mg Doping in LiCoO₂ and Li_{1+δ}CoO₂: Structural, Electronic Properties, and ⁷Li MAS NMR Studies*. In: *Chemistry of Materials* 14.8 (2002), pp. 3584–3590. DOI: [10.1021/cm021107j](https://doi.org/10.1021/cm021107j) (see p. 17).
- [152] Takahashi, Y., Kijima, N., Tokiwa, K., Watanabe, T., and Akimoto, J.: *Single-crystal synthesis, structure refinement and electrical properties of Li_{0.5}CoO₂*. In: *Journal of Physics: Condensed Matter* 19.43 (2007), p. 436202. DOI: [10.1088/0953-8984/19/43/436202](https://doi.org/10.1088/0953-8984/19/43/436202) (see p. 18).
- [153] Marzec, J., Świerczek, K., Przewoźnik, J., Molenda, J., Simon, D., Kelder, E. M., and Schoonman, J.: *Conduction mechanism in operating a LiMn₂O₄ cathode*. In: *Solid State Ionics* 146.3-4 (2002), pp. 225–237. DOI: [10.1016/S0167-2738\(01\)01022-0](https://doi.org/10.1016/S0167-2738(01)01022-0) (see p. 18).
- [154] Chung, S.-Y., Bloking, J. T., and Chiang, Y.-M.: *Electronically conductive phospho-olivines as lithium storage electrodes*. In: *Nature materials* 1.2 (2002), pp. 123–128. DOI: [10.1038/nmat732](https://doi.org/10.1038/nmat732) (see p. 18).
- [155] Wang, S., Yan, M., Li, Y., Vinado, C., and Yang, J.: *Separating electronic and ionic conductivity in mix-conducting layered lithium transition-metal oxides*. In: *Journal of Power Sources* 393 (2018), pp. 75–82. DOI: [10.1016/j.jpowsour.2018.05.005](https://doi.org/10.1016/j.jpowsour.2018.05.005) (see p. 18).
- [156] Amin, R. and Chiang, Y.-M.: *Characterization of Electronic and Ionic Transport in Li_{1-x}Ni_{0.33}Mn_{0.33}Co_{0.33}O₂ (NMC 333) and Li_{1-x}Ni_{0.50}Mn_{0.20}Co_{0.30}O₂ (NMC 523) as a Function of Li Content*. In: *Journal of The Electrochemical Society* 163.8 (2016), A1512–A1517. DOI: [10.1149/2.0131608jes](https://doi.org/10.1149/2.0131608jes) (see p. 18).

- [157] Amin, R., Ravnsbæk, D. B., and Chiang, Y.-M.: *Characterization of Electronic and Ionic Transport in $Li_{1-x}Ni_{0.8}Co_{0.15}Al_{0.05}O_2$ (NCA)*. In: *Journal of The Electrochemical Society* 162.7 (2015), A1163–A1169. DOI: [10.1149/2.0171507jes](https://doi.org/10.1149/2.0171507jes) (see p. 18).
- [158] Heikes, R. R. and Johnston, W. D.: *Mechanism of Conduction in Li-Substituted Transition Metal Oxides*. In: *The Journal of Chemical Physics* 26.3 (1957), pp. 582–587. DOI: [10.1063/1.1743350](https://doi.org/10.1063/1.1743350) (see p. 17).
- [159] Antolini, E.: *LiCoO₂: formation, structure, lithium and oxygen nonstoichiometry, electrochemical behaviour and transport properties*. In: *Solid State Ionics* 170.3-4 (2004), pp. 159–171. DOI: [10.1016/j.ssi.2004.04.003](https://doi.org/10.1016/j.ssi.2004.04.003) (see p. 17).
- [160] Chen, Y.-H., Wang, C.-W., Liu, G., Song, X.-Y., Battaglia, V. S., and Sastry, A. M.: *Selection of Conductive Additives in Li-Ion Battery Cathodes*. In: *Journal of The Electrochemical Society* 154.10 (2007), A978. DOI: [10.1149/1.2767839](https://doi.org/10.1149/1.2767839) (see p. 18).
- [161] Dasgupta, D., Demichelis, F., and Tagliaferro, A.: *Electrical conductivity of amorphous carbon and amorphous hydrogenated carbon*. In: *Philosophical Magazine B* 63.6 (1991), pp. 1255–1266. DOI: [10.1080/13642819108205558](https://doi.org/10.1080/13642819108205558) (see p. 18).
- [162] Orikasa, Y. et al.: *Ionic Conduction in Lithium Ion Battery Composite Electrode Governs Cross-sectional Reaction Distribution*. In: *Scientific reports* 6 (2016), p. 26382. DOI: [10.1038/srep26382](https://doi.org/10.1038/srep26382) (see p. 18).
- [163] Ding, M. S., Xu, K., Zhang, S. S., Amine, K., Henriksen, G. L., and Jow, T. R.: *Change of Conductivity with Salt Content, Solvent Composition, and Temperature for Electrolytes of LiPF₆ in Ethylene Carbonate-Ethyl Methyl Carbonate*. In: *The Journal of Physical Chemistry* 148.10 (2001), A1196. DOI: [10.1149/1.1403730](https://doi.org/10.1149/1.1403730) (see pp. 18, 19).
- [164] Landesfeind, J. and Gasteiger, H. A.: *Temperature and Concentration Dependence of the Ionic Transport Properties of Lithium-Ion Battery Electrolytes*. In: *Journal of The Electrochemical Society* 166.14 (2019), A3079–A3097. DOI: [10.1149/2.0571912jes](https://doi.org/10.1149/2.0571912jes) (see p. 19).
- [165] Cai, H., Tong, X., Chen, K., Shen, Y., Wu, J., Xiang, Y., Wang, Z., and Li, J.: *Electrospun Polyethylene Terephthalate Nonwoven Reinforced Polypropylene Separator: Scalable Synthesis and Its Lithium Ion Battery Performance*. In: *Polymers* 10.6 (2018). DOI: [10.3390/polym10060574](https://doi.org/10.3390/polym10060574) (see p. 19).
- [166] Landinger, T. F., Schwarzberger, G., and Jossen, A.: *High frequency impedance characteristics of cylindrical lithium-ion cells: Physical-based modeling of cell state and cell design dependencies*. In: *Journal of Power Sources* 488.2 (2021), p. 229463. DOI: [10.1016/j.jpowsour.2021.229463](https://doi.org/10.1016/j.jpowsour.2021.229463) (see p. 19).
- [167] Landinger, T. F., Schwarzberger, G., and Jossen, A.: *A Physical-Based High-Frequency Model of Cylindrical Lithium-Ion Batteries for Time Domain Simulation*. In: *IEEE Transactions on Electromagnetic Compatibility* 62.4 (2020), pp. 1524–1533. DOI: [10.1109/TEM.2020.2996414](https://doi.org/10.1109/TEM.2020.2996414) (see p. 19).
- [168] Ratnakumar, B. V., Smart, M. C., Whitcanack, L. D., and Ewell, R. C.: *The impedance characteristics of Mars Exploration Rover Li-ion batteries*. In: *Journal of Power Sources* 159.2 (2006), pp. 1428–1439. DOI: [10.1016/j.jpowsour.2005.11.085](https://doi.org/10.1016/j.jpowsour.2005.11.085) (see pp. 19, 21, 29, 32).
- [169] Suresh, P., Shukla, A. K., and Munichandraiah, N.: *Temperature dependence studies of a.c. impedance of lithium-ion cells*. In: *Journal of Applied Electrochemistry* 32.3 (2002), pp. 267–273. DOI: [10.1023/A:1015565404343](https://doi.org/10.1023/A:1015565404343) (see p. 20).

- [170] Dickinson, E. J. and Wain, A. J.: *The Butler-Volmer equation in electrochemical theory: Origins, value, and practical application*. In: *Journal of Electroanalytical Chemistry* 872.186 A (2020), p. 114145. DOI: [10.1016/j.jelechem.2020.114145](https://doi.org/10.1016/j.jelechem.2020.114145) (see p. 20).
- [171] Ernst, S., Heins, T. P., Schlüter, N., and Schröder, U.: *Capturing the Current-Overpotential Nonlinearity of Lithium-Ion Batteries by Nonlinear Electrochemical Impedance Spectroscopy (NLEIS) in Charge and Discharge Direction*. In: *Frontiers in Energy Research* 7 (2019), p. 550. DOI: [10.3389/fenrg.2019.00151](https://doi.org/10.3389/fenrg.2019.00151) (see p. 20).
- [172] ANDRADE, E. N. D. C.: *The Viscosity of Liquids*. In: *Nature* 125.3148 (1930), pp. 309–310. DOI: [10.1038/125309b0](https://doi.org/10.1038/125309b0) (see p. 21).
- [173] Mehrer, H., ed.: *Diffusion in Solids: Fundamentals, Methods, Materials, Diffusion-Controlled Processes*. Vol. 155. Springer Series in Solid-State Sciences. Berlin, Heidelberg: Springer, 2007. ISBN: 978-3-540-71488-0 (see p. 22).
- [174] Spinner, N. S., Love, C. T., Rose-Pehrsson, S. L., and Tuttle, S. G.: *Expanding the Operational Limits of the Single-Point Impedance Diagnostic for Internal Temperature Monitoring of Lithium-ion Batteries*. In: *Electrochimica Acta* 174 (2015), pp. 488–493. DOI: [10.1016/j.electacta.2015.06.003](https://doi.org/10.1016/j.electacta.2015.06.003) (see pp. 22, 34, 36, 39, 123).
- [175] Uddin, K., Perera, S., Widanage, W., Somerville, L., and Marco, J.: *Characterising Lithium-Ion Battery Degradation through the Identification and Tracking of Electrochemical Battery Model Parameters*. In: *Batteries* 2.2 (2016), p. 13. DOI: [10.3390/batteries2020013](https://doi.org/10.3390/batteries2020013) (see pp. 23–25).
- [176] Zinth, V., Lüders, C. von, Hofmann, M., Hattendorff, J., Buchberger, I., Erhard, S., Rebelo-Kornmeier, J., Jossen, A., and Gilles, R.: *Lithium plating in lithium-ion batteries at sub-ambient temperatures investigated by in situ neutron diffraction*. In: *Journal of Power Sources* 271.9 (2014), pp. 152–159. DOI: [10.1016/j.jpowsour.2014.07.168](https://doi.org/10.1016/j.jpowsour.2014.07.168) (see p. 24).
- [177] Xu, H., Han, C., Li, W., Li, H., and Qiu, X.: *Quantification of lithium dendrite and solid electrolyte interphase (SEI) in lithium-ion batteries*. In: *Journal of Power Sources* 529 (2022), p. 231219. DOI: [10.1016/j.jpowsour.2022.231219](https://doi.org/10.1016/j.jpowsour.2022.231219) (see p. 24).
- [178] Wen, J., Yu, Y., and Chen, C.: *A Review on Lithium-Ion Batteries Safety Issues: Existing Problems and Possible Solutions*. In: *Materials Express* 2.3 (2012), pp. 197–212. DOI: [10.1166/mex.2012.1075](https://doi.org/10.1166/mex.2012.1075) (see pp. 24, 25).
- [179] Bhattacharyya, R., Key, B., Chen, H., Best, A. S., Hollenkamp, A. F., and Grey, C. P.: *In situ NMR observation of the formation of metallic lithium microstructures in lithium batteries*. In: *Nature materials* 9.6 (2010), pp. 504–510. DOI: [10.1038/nmat2764](https://doi.org/10.1038/nmat2764) (see p. 24).
- [180] MacNeil, D. D., Larcher, D., and Dahn, J. R.: *Comparison of the Reactivity of Various Carbon Electrode Materials with Electrolyte at Elevated Temperature*. In: *Journal of The Electrochemical Society* 146.10 (1999), pp. 3596–3602. DOI: [10.1149/1.1392520](https://doi.org/10.1149/1.1392520) (see pp. 24, 94).
- [181] Yuqin, C., Hong, L., Lie, W., and Tianhong, L.: *Irreversible capacity loss of graphite electrode in lithium-ion batteries*. In: *Journal of Power Sources* 68.2 (1997), pp. 187–190. DOI: [10.1016/S0378-7753\(96\)02549-9](https://doi.org/10.1016/S0378-7753(96)02549-9) (see pp. 24, 94).
- [182] Shim, J. and Striebel, K. A.: *The dependence of natural graphite anode performance on electrode density*. In: *Journal of Power Sources* 130.1-2 (2004), pp. 247–253. DOI: [10.1016/j.jpowsour.2003.12.015](https://doi.org/10.1016/j.jpowsour.2003.12.015) (see pp. 24, 94).

- [183] Gandoman, F. H., Jaguemont, J., Goutam, S., Gopalakrishnan, R., Firouz, Y., Kalogiannis, T., Omar, N., and van Mierlo, J.: *Concept of reliability and safety assessment of lithium-ion batteries in electric vehicles: Basics, progress, and challenges*. In: *Applied Energy* 251.5 (2019), p. 113343. DOI: [10.1016/j.apenergy.2019.113343](https://doi.org/10.1016/j.apenergy.2019.113343) (see p. 24).
- [184] Birkel, C. R., Roberts, M. R., McTurk, E., Bruce, P. G., and Howey, D. A.: *Degradation diagnostics for lithium ion cells*. In: *Journal of Power Sources* 341.1 (2017), pp. 373–386. DOI: [10.1016/j.jpowsour.2016.12.011](https://doi.org/10.1016/j.jpowsour.2016.12.011) (see pp. 24, 25).
- [185] Wu, Y., Keil, P., Schuster, S. F., and Jossen, A.: *Impact of Temperature and Discharge Rate on the Aging of a LiCoO₂/LiNi_{0.8}Co_{0.15}Al_{0.05}O₂ Lithium-Ion Pouch Cell*. In: *Journal of The Electrochemical Society* 164.7 (2017), A1438–A1445. DOI: [10.1149/2.0401707jes](https://doi.org/10.1149/2.0401707jes) (see p. 24).
- [186] Richard, M. N. and Dahn, J. R.: *Accelerating Rate Calorimetry Study on the Thermal Stability of Lithium Intercalated Graphite in Electrolyte. I. Experimental*. In: *Journal of The Electrochemical Society* 146.6 (1999), pp. 2068–2077. DOI: [10.1149/1.1391893](https://doi.org/10.1149/1.1391893) (see p. 24).
- [187] Maleki, H., Deng, G., Anani, A., and Howard, J.: *Thermal Stability Studies of Li-Ion Cells and Components*. In: *Journal of The Electrochemical Society* 146.9 (1999), pp. 3224–3229. DOI: [10.1149/1.1392458](https://doi.org/10.1149/1.1392458) (see p. 24).
- [188] Ashwin, T. R., McGordon, A., and Jennings, P. A.: *A mass transfer based variable porosity model with particle radius change for a Lithium-ion battery*. In: *Electrochimica Acta* 232.6 (2017), pp. 203–214. DOI: [10.1016/j.electacta.2017.02.129](https://doi.org/10.1016/j.electacta.2017.02.129) (see p. 24).
- [189] Orendorff, C. J.: *The Role of Separators in Lithium-Ion Cell Safety*. In: *Interface magazine* 21.2 (2012), pp. 61–65. DOI: [10.1149/2.F07122if](https://doi.org/10.1149/2.F07122if) (see p. 25).
- [190] Edström, K., Gustafsson, T., and Thomas, J. O.: *The cathode–electrolyte interface in the Li-ion battery*. In: *Electrochimica Acta* 50.2-3 (2004), pp. 397–403. DOI: [10.1016/j.electacta.2004.03.049](https://doi.org/10.1016/j.electacta.2004.03.049) (see p. 25).
- [191] Lei, B., Zhao, W., Ziebert, C., Uhlmann, N., Rohde, M., and Seifert, H.: *Experimental Analysis of Thermal Runaway in 18650 Cylindrical Li-Ion Cells Using an Accelerating Rate Calorimeter*. In: *Batteries* 3.4 (2017), p. 14. DOI: [10.3390/batteries3020014](https://doi.org/10.3390/batteries3020014) (see p. 25).
- [192] Ohsaki, T., Kishi, T., Kuboki, T., Takami, N., Shimura, N., Sato, Y., Sekino, M., and Satoh, A.: *Overcharge reaction of lithium-ion batteries*. In: *Journal of Power Sources* 146.1-2 (2005), pp. 97–100. DOI: [10.1016/j.jpowsour.2005.03.105](https://doi.org/10.1016/j.jpowsour.2005.03.105) (see p. 25).
- [193] Harris, O. C., Lee, S. E., Lees, C., and Tang, M.: *Review: mechanisms and consequences of chemical cross-talk in advanced Li-ion batteries*. In: *Journal of Physics: Energy* 2.3 (2020), p. 032002. DOI: [10.1088/2515-7655/ab8b68](https://doi.org/10.1088/2515-7655/ab8b68) (see p. 25).
- [194] Sahore, R., Dogan, F., and Bloom, I. D.: *Identification of Electrolyte-Soluble Organic Cross-Talk Species in a Lithium-Ion Battery via a Two-Compartment Cell*. In: *Chemistry of Materials* 31.8 (2019), pp. 2884–2891. DOI: [10.1021/acs.chemmater.9b00063](https://doi.org/10.1021/acs.chemmater.9b00063) (see p. 25).
- [195] Zhan, C., Wu, T., Lu, J., and Amine, K.: *Dissolution, migration, and deposition of transition metal ions in Li-ion batteries exemplified by Mn-based cathodes – a critical review*. In: *Energy Environ. Sci.* 11.2 (2018), pp. 243–257. DOI: [10.1039/C7EE03122J](https://doi.org/10.1039/C7EE03122J) (see p. 25).
- [196] Biensan, P., Simon, B., Pérès, J., Guibert, A. de, Broussely, M., Bodet, J., and Pertion, F.: *On safety of lithium-ion cells*. In: *Journal of Power Sources* 81-82 (1999), pp. 906–912. DOI: [10.1016/S0378-7753\(99\)00135-4](https://doi.org/10.1016/S0378-7753(99)00135-4) (see p. 25).

- [197] Ochida, M., Doi, T., Domi, Y., Tsubouchi, S., Nakagawa, H., Yamanaka, T., Abe, T., and Ogumi, Z.: *Effects of Electrolyte Additives on the Suppression of Mn Deposition on Edge Plane Graphite for Lithium-Ion Batteries*. In: *Journal of The Electrochemical Society* 160.2 (2013), A410–A413. DOI: [10.1149/2.021303jes](https://doi.org/10.1149/2.021303jes) (see p. 25).
- [198] Watanabe, S., Kinoshita, M., Hosokawa, T., Morigaki, K., and Nakura, K.: *Capacity fade of $\text{LiAl}_y\text{Ni}_{1-x-y}\text{Co}_x\text{O}_2$ cathode for lithium-ion batteries during accelerated calendar and cycle life tests (surface analysis of $\text{LiAl}_y\text{Ni}_{1-x-y}\text{Co}_x\text{O}_2$ cathode after cycle tests in restricted depth of discharge ranges)*. In: *Journal of Power Sources* 258 (2014), pp. 210–217. DOI: [10.1016/j.jpowsour.2014.02.018](https://doi.org/10.1016/j.jpowsour.2014.02.018) (see p. 25).
- [199] Schindler, M., Sturm, J., Ludwig, S., Durdel, A., and Jossen, A.: *Comprehensive Analysis of the Aging Behavior of Nickel-Rich, Silicon-Graphite Lithium-Ion Cells Subject to Varying Temperature and Charging Profiles*. In: *Journal of The Electrochemical Society* 168.6 (2021), p. 060522. DOI: [10.1149/1945-7111/ac03f6](https://doi.org/10.1149/1945-7111/ac03f6) (see p. 25).
- [200] Dubarry, M., Svoboda, V., Hwu, R., and Liaw, B. Y.: *Capacity loss in rechargeable lithium cells during cycle life testing: The importance of determining state-of-charge*. In: *Journal of Power Sources* 174.2 (2007), pp. 1121–1125. DOI: [10.1016/j.jpowsour.2007.06.185](https://doi.org/10.1016/j.jpowsour.2007.06.185) (see p. 25).
- [201] Ning, G., Haran, B., and Popov, B. N.: *Capacity fade study of lithium-ion batteries cycled at high discharge rates*. In: *Journal of Power Sources* 117.1-2 (2003), pp. 160–169. DOI: [10.1016/S0378-7753\(03\)00029-6](https://doi.org/10.1016/S0378-7753(03)00029-6) (see p. 25).
- [202] Savoye, F., Venet, P., Millet, M., and Groot, J.: *Impact of Periodic Current Pulses on Li-Ion Battery Performance*. In: *IEEE Transactions on Industrial Electronics* 59.9 (2012), pp. 3481–3488. DOI: [10.1109/TIE.2011.2172172](https://doi.org/10.1109/TIE.2011.2172172) (see p. 25).
- [203] Wang, J., Liu, P., Hicks-Garner, J., Sherman, E., Soukiazian, S., Verbrugge, M., Tataria, H., Musser, J., and Finamore, P.: *Cycle-life model for graphite- LiFePO_4 cells*. In: *Journal of Power Sources* 196.8 (2011), pp. 3942–3948. DOI: [10.1016/j.jpowsour.2010.11.134](https://doi.org/10.1016/j.jpowsour.2010.11.134) (see p. 25).
- [204] Mc Carthy, K., Gullapalli, H., Ryan, K. M., and Kennedy, T.: *Review—Use of Impedance Spectroscopy for the Estimation of Li-ion Battery State of Charge, State of Health and Internal Temperature*. In: *Journal of The Electrochemical Society* 168.8 (2021), p. 080517. DOI: [10.1149/1945-7111/ac1a85](https://doi.org/10.1149/1945-7111/ac1a85) (see pp. 25, 33).
- [205] Komsijska, L. et al.: *Critical Review of Intelligent Battery Systems: Challenges, Implementation, and Potential for Electric Vehicles*. In: *Energies* 14.18 (2021), p. 5989. DOI: [10.3390/en14185989](https://doi.org/10.3390/en14185989) (see pp. 25, 33).
- [206] Zhou, X., Huang, J., Pan, Z., and Ouyang, M.: *Impedance characterization of lithium-ion batteries aging under high-temperature cycling: Importance of electrolyte-phase diffusion*. In: *Journal of Power Sources* 426 (2019), pp. 216–222. DOI: [10.1016/j.jpowsour.2019.04.040](https://doi.org/10.1016/j.jpowsour.2019.04.040) (see p. 26).
- [207] Lohmann, N., Weßkamp, P., Haußmann, P., Melbert, J., and Musch, T.: *Electrochemical impedance spectroscopy for lithium-ion cells: Test equipment and procedures for aging and fast characterization in time and frequency domain*. In: *Journal of Power Sources* 273.12 (2015), pp. 613–623. DOI: [10.1016/j.jpowsour.2014.09.132](https://doi.org/10.1016/j.jpowsour.2014.09.132) (see p. 26).
- [208] Feng, X., Sun, J., Ouyang, M., He, X., Lu, L., Han, X., Fang, M., and Peng, H.: *Characterization of large format lithium ion battery exposed to extremely high temperature*. In: *Journal of Power Sources* 272.2 (2014), pp. 457–467. DOI: [10.1016/j.jpowsour.2014.08.094](https://doi.org/10.1016/j.jpowsour.2014.08.094) (see p. 26).

- [209] Waag, W., Käbitz, S., and Sauer, D. U.: *Experimental investigation of the lithium-ion battery impedance characteristic at various conditions and aging states and its influence on the application*. In: *Applied Energy* 102.1 (2013), pp. 885–897. DOI: [10.1016/j.apenergy.2012.09.030](https://doi.org/10.1016/j.apenergy.2012.09.030) (see pp. 26, 27, 29, 31, 32).
- [210] Barai, A., Uddin, K., Widanage, W. D., McGordon, A., and Jennings, P.: *A study of the influence of measurement timescale on internal resistance characterisation methodologies for lithium-ion cells*. In: *Scientific reports* 8.1 (2018), p. 21. DOI: [10.1038/s41598-017-18424-5](https://doi.org/10.1038/s41598-017-18424-5) (see pp. 26, 29, 31, 32).
- [211] Zappen, H., Ringbeck, F., and Sauer, D.: *Application of Time-Resolved Multi-Sine Impedance Spectroscopy for Lithium-Ion Battery Characterization*. In: *Batteries* 4.4 (2018), p. 64. DOI: [10.3390/batteries4040064](https://doi.org/10.3390/batteries4040064) (see pp. 26, 28).
- [212] Carkhuff, B. G., Demirev, P. A., and Srinivasan, R.: *Impedance-Based Battery Management System for Safety Monitoring of Lithium-Ion Batteries*. In: *IEEE Transactions on Industrial Electronics* 65.8 (2018), pp. 6497–6504. DOI: [10.1109/TIE.2017.2786199](https://doi.org/10.1109/TIE.2017.2786199) (see pp. 27, 34, 36, 39).
- [213] Ranieri, M., Alberto, D., Piret, H., and Cattin, V.: “Electronic module for the thermal monitoring of a Li-ion battery cell through the electrochemical impedance estimation.” In: *2016 22nd International Workshop on Thermal Investigations of ICs and Systems (THERMINIC)*. IEEE, 21.09.2016 - 23.09.2016, pp. 294–297. ISBN: 978-1-5090-5450-3. DOI: [10.1109/THERMINIC.2016.7749069](https://doi.org/10.1109/THERMINIC.2016.7749069) (see p. 27).
- [214] Schwarz, R., Semmler, K., Wenger, M., Lorentz, V. R. H., and Marz, M.: “Sensorless battery cell temperature estimation circuit for enhanced safety in battery systems.” In: *IECON 2015 - 41st Annual Conference of the IEEE Industrial Electronics Society*. IEEE, 09.11.2015 - 12.11.2015, pp. 001536–001541. ISBN: 978-1-4799-1762-4. DOI: [10.1109/IECON.2015.7392319](https://doi.org/10.1109/IECON.2015.7392319) (see pp. 27, 34, 36, 39).
- [215] Howey, D. A., Mitcheson, P. D., Yufit, V., Offer, G. J., and Brandon, N. P.: *Online Measurement of Battery Impedance Using Motor Controller Excitation*. In: *IEEE Transactions on Vehicular Technology* 63.6 (2014), pp. 2557–2566. DOI: [10.1109/TVT.2013.2293597](https://doi.org/10.1109/TVT.2013.2293597) (see p. 27).
- [216] Klotz, D., Schönleber, M., Schmidt, J. P., and Ivers-Tiffée, E.: *New approach for the calculation of impedance spectra out of time domain data*. In: *Electrochimica Acta* 56.24 (2011), pp. 8763–8769. DOI: [10.1016/j.electacta.2011.07.096](https://doi.org/10.1016/j.electacta.2011.07.096) (see p. 27).
- [217] Fasmin, F. and Srinivasan, R.: *Review—Nonlinear Electrochemical Impedance Spectroscopy*. In: *Journal of The Electrochemical Society* 164.7 (2017), H443–H455. DOI: [10.1149/2.0391707jes](https://doi.org/10.1149/2.0391707jes) (see p. 28).
- [218] Schweiger, H.-G., Obeidi, O., Komesker, O., Raschke, A., Schiemann, M., Zehner, C., Gehnen, M., Keller, M., and Birke, P.: *Comparison of several methods for determining the internal resistance of lithium ion cells*. In: *Sensors (Basel, Switzerland)* 10.6 (2010), pp. 5604–5625. DOI: [10.3390/s100605604](https://doi.org/10.3390/s100605604) (see pp. 28, 29, 32).
- [219] Roscher, M. A., Vetter, J., and Sauer, D. U.: *Characterisation of charge and discharge behaviour of lithium ion batteries with olivine based cathode active material*. In: *Journal of Power Sources* 191.2 (2009), pp. 582–590. DOI: [10.1016/j.jpowsour.2009.02.024](https://doi.org/10.1016/j.jpowsour.2009.02.024) (see p. 28).

- [220] Dubarry, M., Truchot, C., Cugnet, M., Liaw, B. Y., Gering, K., Sazhin, S., Jamison, D., and Michelbacher, C.: *Evaluation of commercial lithium-ion cells based on composite positive electrode for plug-in hybrid electric vehicle applications. Part I: Initial characterizations*. In: *Journal of Power Sources* 196.23 (2011), pp. 10328–10335. DOI: [10.1016/j.jpowsour.2011.08.077](https://doi.org/10.1016/j.jpowsour.2011.08.077) (see p. 28).
- [221] Anseán, D., García V.M., González, M., Viera, J. C., Blanco, C., and Antuña, J. L.: “DC internal resistance during charge: analysis and study on LiFePO₄ batteries.” In: *EVS27 International Battery, Hybrid and Fuel Cell Electric Vehicle Symposium*. Vol. 27. 2013 (see pp. 28, 29, 31).
- [222] Yue, Y., Li, S., Cheng, X., Wei, J., Zeng, F., Zhou, X., and Yang, J.: *Effects of temperature on the ohmic internal resistance and energy loss of Lithium-ion batteries under millisecond pulse discharge*. In: *Journal of Physics: Conference Series* 2301.1 (2022), p. 012014. DOI: [10.1088/1742-6596/2301/1/012014](https://doi.org/10.1088/1742-6596/2301/1/012014) (see p. 29).
- [223] Zhao, S., Wu, F., Yang, L., Gao, L., and Burke, A. F.: *A measurement method for determination of dc internal resistance of batteries and supercapacitors*. In: *Electrochemistry Communications* 12.2 (2010), pp. 242–245. DOI: [10.1016/j.elecom.2009.12.004](https://doi.org/10.1016/j.elecom.2009.12.004) (see pp. 29, 31, 32).
- [224] Christophersen, J. P., Hunt, G. L., Ho, C. D., and Howell, D.: *Pulse resistance effects due to charging or discharging of high-power lithium-ion cells: A path dependence study*. In: *Journal of Power Sources* 173.2 (2007), pp. 998–1005. DOI: [10.1016/j.jpowsour.2007.08.025](https://doi.org/10.1016/j.jpowsour.2007.08.025) (see pp. 29, 32).
- [225] Kindermann, F. M., Noel, A., Erhard, S. V., and Jossen, A.: *Long-term equalization effects in Li-ion batteries due to local state of charge inhomogeneities and their impact on impedance measurements*. In: *Electrochimica Acta* 185 (2015), pp. 107–116. DOI: [10.1016/j.electacta.2015.10.108](https://doi.org/10.1016/j.electacta.2015.10.108) (see p. 29).
- [226] Uddin, K., Picarelli, A., Lyness, C., Taylor, N., and Marco, J.: *An Acausal Li-Ion Battery Pack Model for Automotive Applications*. In: *Energies* 7.9 (2014), pp. 5675–5700. DOI: [10.3390/en7095675](https://doi.org/10.3390/en7095675) (see p. 32).
- [227] Rajmakers, L., Danilov, D. L., Eichel, R.-A., and Notten, P.: *A review on various temperature-indication methods for Li-ion batteries*. In: *Applied Energy* 240.1978 (2019), pp. 918–945. DOI: [10.1016/j.apenergy.2019.02.078](https://doi.org/10.1016/j.apenergy.2019.02.078) (see p. 33).
- [228] Beelen, H., Rajmakers, L., Donkers, M., Notten, P., and Bergveld, H. J.: *An Improved Impedance-Based Temperature Estimation Method for Li-ion*. In: *IFAC-PapersOnLine* 48.15 (2015), pp. 383–388. DOI: [10.1016/j.ifacol.2015.10.055](https://doi.org/10.1016/j.ifacol.2015.10.055) (see pp. 34, 36, 39).
- [229] Richardson, R. R. and Howey, D. A.: *Sensorless Battery Internal Temperature Estimation Using a Kalman Filter With Impedance Measurement*. In: *IEEE Transactions on Sustainable Energy* 6.4 (2015), pp. 1190–1199. DOI: [10.1109/TSSTE.2015.2420375](https://doi.org/10.1109/TSSTE.2015.2420375) (see pp. 34, 36, 39, 70, 71).
- [230] Sun, J., Wei, G., Pei, L., Lu, R., Song, K., Wu, C., and Zhu, C.: *Online Internal Temperature Estimation for Lithium-Ion Batteries Based on Kalman Filter*. In: *Energies* 8.5 (2015), pp. 4400–4415. DOI: [10.3390/en8054400](https://doi.org/10.3390/en8054400) (see pp. 34, 36, 39).
- [231] Richardson, R. R., Zhao, S., and Howey, D. A.: *On-board monitoring of 2-D spatially-resolved temperatures in cylindrical lithium-ion batteries: Part II. State estimation via impedance-based temperature sensing*. In: *Journal of Power Sources* 327 (2016), pp. 726–735. DOI: [10.1016/j.jpowsour.2016.06.104](https://doi.org/10.1016/j.jpowsour.2016.06.104) (see pp. 34, 36, 39, 70).

- [232] Zhu, J., Sun, Z., Wei, X., and Dai, H.: *Battery Internal Temperature Estimation for LiFePO₄ Battery Based on Impedance Phase Shift under Operating Conditions*. In: *Energies* 10.1 (2017), p. 60. DOI: [10.3390/en10010060](https://doi.org/10.3390/en10010060) (see pp. 34, 36, 39).
- [233] Haussmann, P. and Melbert, J.: *Internal Cell Temperature Measurement and Thermal Modeling of Lithium Ion Cells for Automotive Applications by Means of Electrochemical Impedance Spectroscopy*. In: *SAE International Journal of Alternative Powertrains* 6.2 (2017), pp. 261–270. DOI: [10.4271/2017-01-1215](https://doi.org/10.4271/2017-01-1215) (see pp. 34, 36, 39, 75).
- [234] Srinivasan, R., Demirev, P. A., and Carkhuff, B. G.: *Rapid monitoring of impedance phase shifts in lithium-ion batteries for hazard prevention*. In: *Journal of Power Sources* 405.14 (2018), pp. 30–36. DOI: [10.1016/j.jpowsour.2018.10.014](https://doi.org/10.1016/j.jpowsour.2018.10.014) (see pp. 34, 36, 39, 123).
- [235] Beelen, H., Mundaragi Shivakumar, K., Raijmakers, L., Donkers, M., and Bergveld, H. J.: *Towards impedance-based temperature estimation for Li-ion battery packs*. In: *International Journal of Energy Research* 44.4 (2020), pp. 2889–2908. DOI: [10.1002/er.5107](https://doi.org/10.1002/er.5107) (see pp. 34, 36, 39).
- [236] Xie, Y., Li, W., Hu, X., Lin, X., Zhang, Y., Dan, D., Feng, F., Liu, B., and Li, K.: *An Enhanced Online Temperature Estimation for Lithium-Ion Batteries*. In: *IEEE Transactions on Transportation Electrification* 6.2 (2020), pp. 375–390. DOI: [10.1109/TTE.2020.2980153](https://doi.org/10.1109/TTE.2020.2980153) (see pp. 34, 36, 39).
- [237] André, M.: *The ARTEMIS European driving cycles for measuring car pollutant emissions*. In: *The Science of the total environment* 334-335 (2004), pp. 73–84. DOI: [10.1016/j.scitotenv.2004.04.070](https://doi.org/10.1016/j.scitotenv.2004.04.070) (see p. 38).
- [238] Ludwig, S., Steinhardt, M., and Jossen, A.: *Determination of Internal Temperature Differences for Various Cylindrical Lithium-Ion Batteries Using a Pulse Resistance Approach*. In: *Batteries* 8.7 (2022), p. 60. DOI: [10.3390/batteries8070060](https://doi.org/10.3390/batteries8070060) (see pp. 41, 42, 70–73, 108).
- [239] Steinhardt, M., Gillich, E. I., Rheinfeld, A., Kraft, L., Spielbauer, M., Bohlen, O., and Jossen, A.: *Low-effort determination of heat capacity and thermal conductivity for cylindrical 18650 and 21700 lithium-ion cells*. In: *Journal of Energy Storage* 42 (2021), p. 103065. DOI: [10.1016/j.est.2021.103065](https://doi.org/10.1016/j.est.2021.103065) (see p. 42).
- [240] Efest: *IMR26650: 26650*. 18.01.2022. URL: <http://www.efestpower.com/index.php?ac=article&at=read&did=448> (visited on 01/18/2022) (see p. 42).
- [241] Wei, Y. and Agelin-Chaab, M.: *Experimental investigation of a novel hybrid cooling method for lithium-ion batteries*. In: *Applied Thermal Engineering* 136.9 (2018), pp. 375–387. DOI: [10.1016/j.applthermaleng.2018.03.024](https://doi.org/10.1016/j.applthermaleng.2018.03.024) (see p. 42).
- [242] Wei, Y. and Agelin-Chaab, M.: *Development and experimental analysis of a hybrid cooling concept for electric vehicle battery packs*. In: *Journal of Energy Storage* 25.9 (2019), p. 100906. DOI: [10.1016/j.est.2019.100906](https://doi.org/10.1016/j.est.2019.100906) (see p. 42).
- [243] Troxler, Y., Wu, B., Marinescu, M., Yufit, V., Patel, Y., Marquis, A. J., Brandon, N. P., and Offer, G. J.: *The effect of thermal gradients on the performance of lithium-ion batteries*. In: *Journal of Power Sources* 247 (2014), pp. 1018–1025. DOI: [10.1016/j.jpowsour.2013.06.084](https://doi.org/10.1016/j.jpowsour.2013.06.084) (see pp. 70, 71, 123).
- [244] Ludwig, S., Zilberman, I., Horsche, M. F., Wohlers, T., and Jossen, A.: *Pulse resistance based online temperature estimation for lithium-ion cells*. In: *Journal of Power Sources* 490.6 (2021), p. 229523. DOI: [10.1016/j.jpowsour.2021.229523](https://doi.org/10.1016/j.jpowsour.2021.229523) (see pp. 75, 76).

- [245] Ludwig, S., Zilberman, I., Oberbauer, A., Rogge, M., Fischer, M., Rehm, M., and Jossen, A.: *Adaptive method for sensorless temperature estimation over the lifetime of lithium-ion batteries*. In: *Journal of Power Sources* 521 (2022), p. 230864. DOI: [10.1016/j.jpowsour.2021.230864](https://doi.org/10.1016/j.jpowsour.2021.230864) (see pp. 76, 94, 107).
- [246] Zilberman, I., Ludwig, S., Schiller, M., and Jossen, A.: *Online aging determination in lithium-ion battery module with forced temperature gradient*. In: *Journal of Energy Storage* 28.9 (2020), p. 101170. DOI: [10.1016/j.est.2019.101170](https://doi.org/10.1016/j.est.2019.101170) (see p. 93).
- [247] Hannan, M. A., Lipu, M., Hussain, A., and Mohamed, A.: *A review of lithium-ion battery state of charge estimation and management system in electric vehicle applications: Challenges and recommendations*. In: *Renewable and Sustainable Energy Reviews* 78.9 (2017), pp. 834–854. DOI: [10.1016/j.rser.2017.05.001](https://doi.org/10.1016/j.rser.2017.05.001) (see p. 108).
- [248] Lipu, M. H., Hannan, M. A., Hussain, A., Hoque, M. M., Ker, P. J., Saad, M., and Ayob, A.: *A review of state of health and remaining useful life estimation methods for lithium-ion battery in electric vehicles: Challenges and recommendations*. In: *Journal of Cleaner Production* 205 (2018), pp. 115–133. DOI: [10.1016/j.jclepro.2018.09.065](https://doi.org/10.1016/j.jclepro.2018.09.065) (see p. 108).
- [249] Hossain Lipu, M. S., Hannan, M. A., Hussain, A., Ayob, A., Saad, M. H., Karim, T. F., and How, D. N.: *Data-driven state of charge estimation of lithium-ion batteries: Algorithms, implementation factors, limitations and future trends*. In: *Journal of Cleaner Production* 277 (2020), p. 124110. DOI: [10.1016/j.jclepro.2020.124110](https://doi.org/10.1016/j.jclepro.2020.124110) (see p. 108).
- [250] Tian, H., Qin, P., Li, K., and Zhao, Z.: *A review of the state of health for lithium-ion batteries: Research status and suggestions*. In: *Journal of Cleaner Production* 261.1 (2020), p. 120813. DOI: [10.1016/j.jclepro.2020.120813](https://doi.org/10.1016/j.jclepro.2020.120813) (see p. 108).
- [251] Yang, B., Wang, J., Cao, P., Zhu, T., Shu, H., Chen, J., Zhang, J., and Zhu, J.: *Classification, summarization and perspectives on state-of-charge estimation of lithium-ion batteries used in electric vehicles: A critical comprehensive survey*. In: *Journal of Energy Storage* 39.2 (2021), p. 102572. DOI: [10.1016/j.est.2021.102572](https://doi.org/10.1016/j.est.2021.102572) (see p. 108).
- [252] Yang, S., Zhang, C., Jiang, J., Zhang, W., Zhang, L., and Wang, Y.: *Review on state-of-health of lithium-ion batteries: Characterizations, estimations and applications*. In: *Journal of Cleaner Production* 314 (2021), p. 128015. DOI: [10.1016/j.jclepro.2021.128015](https://doi.org/10.1016/j.jclepro.2021.128015) (see p. 108).
- [253] Jocher, P., Steinhardt, M., Ludwig, S., Schindler, M., Martin, J., and Jossen, A.: *A novel measurement technique for parallel-connected lithium-ion cells with controllable interconnection resistance*. In: *Journal of Power Sources* 503.1 (2021), p. 230030. DOI: [10.1016/j.jpowsour.2021.230030](https://doi.org/10.1016/j.jpowsour.2021.230030) (see p. 123).
- [254] Kraft, L.: *Enhancing the Performance of Lithium-Ion Cells via New Active Materials and Improved Electrode and Cell Design*. PhD thesis. München: Technische Universität München, 31.08.2021 (see p. 149).

List of Figures

1.1	Projected global battery demand in GWh from 2020 to 2030 by application. [5]	1
1.2	BEVs and PHEVs sales by market: a) current figures from 2010 to 2021 and b) forecast for 2025 and 2030 compared to 2021. [8]	2
1.3	Scope and outline of this thesis structured by chapters and with indication on involved publications.	5
2.1	Scope of Chapter 2.	7
2.2	Schematic representation of the components of a lithium-ion cell and the current and ion flow during the discharge process. Above the cell, the structure of an anode particle made from graphite (left) and a cathode particle made from LiMO_2 (right) is illustrated. The SEI is shown only simplified at the interface between the anode and the separator.	8
2.3	Overview of common active materials for a) cathodes and b) anodes with regard to their approximate discharge potentials vs. Li/Li+ over the specific capacity. Derived from [62–69].	9
2.4	a) Stacking of a double-sided coated electrodes for anode and cathode isolated by separator layers. b) Winding methods for the stacked electrodes and c) integration in corresponding cell casings. Adapted from [96].	11
2.5	Exemplary voltage response of a LIB to a current pulse excitation and classification into the corresponding overpotentials. Below the approximate time intervals in which the overpotentials occur as well as the corresponding dependencies to temperature with reference to the associated equations. Based on [33; 118; 120].	15
2.6	Effects of low and high temperatures on the anode, cathode, and separator and their impact on the lifetime, safety, and performance of LIBs. Adapted from [18; 175].	23
2.7	a) Measurement principle for EIS and b) exemplary Nyquist diagram of a 18650 cell (see Table 3.1) between 10 mHz and 10 kHz at 20 °C and a SOC of 45%.	26
2.8	Example of discharge voltage curves to calculate the R_{VCD} with the voltage curve difference method. Based on [221].	29
2.9	Current and voltage profiles for the characterization of the resistance of a LIB with methods based on a direct current pulse. a) The four different current change types P_1 to P_4 suitable for resistance calculation and definition of the pulse duration t_p , pulse break t_b , and the duration Δt between current change and resistance calculation. b) Example of different base lines and Δt for resistance calculation and their relation to the overpotentials in Fig. 2.5. c) Voltage and current signals for the current switch method for determining the R_{DC} and the current change types P_5 and P_6	30
3.1	Scope of Chapter 3.	41

3.2	Results of the investigation on the relation of internal temperature gradients and the temperature determined by the resistance regarding the publication [238]. a) Example for the volume-related conductance of the 18650 cell at $SOC = 50\%$, the pulse type P_1 and $\Delta t = 100$ ms. Difference between the temperature T_p , determined with the volume-related conductance, and the volume average cell temperature $T_{\text{avg,vol}}$ for temperature gradients from ± 1 K to ± 6 K for b) the 18650, c) the 21700, and d) the 26650 cell. The circles mark the worst case scenario for the temperature gradients determined in [238].	72
4.1	Scope of Chapter 4.	75
4.2	Flowchart showing the development process for the temperature estimation method in [244]. From top to bottom: a) investigated pulse parameters; b) R_{DC} resistance calculation and other influence factors; followed by filters for method parametrization and validation; estimation method with examples for c) R_{DC} reference and d) estimation function; and finally the optimization of Δt with e) the calculation of the estimation error and f) the minimization of the estimation error. Adapted from [245].	76
5.1	Scope of Chapter 5.	93
5.2	a) Flowchart of aging procedure with boundary temperature conditions and evaluation of the checkups showing b) the capacity and the c) resistance in relation to the initial checkup. The resistance is the average value for $\Delta t = 120$ ms with the shaded areas as indication for the maximal spread of the different pulses used in the checkup. See Table 2 in [245] for details. Adapted from [245].	94
6.1	Scope of Chapter 6.	107

List of Tables

2.1	Resistivity ρ_M , conductivity σ_M , and temperature coefficient α for the reference temperature $T_0 = 20^\circ\text{C}$ for the current collector metals copper and aluminum.	16
2.2	Resistivity ρ_{CAM} and conductivity σ_{CAM} values of common cathode and anode active materials at 20°C	18
2.3	Ionic conductivity of lithium salt solution at 20°C . All samples referenced are 1 mol dm^{-3} solutions of their respective salts. Table adapted from [33].	19
2.4	State of the art impedance-based temperature estimation methods: Type of estimated temperature, utilized inputs, estimation method, and used impedance features.	34
2.5	State of the art impedance-based temperature estimation methods: Investigated LIB systems, temperature range, and consideration of aging effects.	36
2.6	State of the art impedance-based temperature estimation methods: Method validation and accuracy.	39
3.1	General information and parameters of the investigated cells. Adapted from [238].	42

Acknowledgment

The first time I was asked during my studies whether I could imagine doing a doctorate, I answered the question resolutely with: “No, I can’t imagine a few more years at university.” In the end it was another five years full of exciting projects, scientific discussions and new friendships. I am all the more grateful that I took this path and was able to spend an unforgettable and instructive time in the sworn “fellowship of batteries” at the [Institute for Electrical Energy Storage Technology \(EES\)](#).

I would like to thank a few people in particular. First of all, many thanks to Prof. Andreas Jossen, who made this path possible for me in the first place, by offering me the opportunity to do my PhD at the [EES](#) at the [Technical University of Munich \(TUM\)](#).

Special thanks go to my colleague and longtime [EES](#) roommate Ilya Zilberman, who introduced me to the institute and was always by my side with advice and support. He helped me to gain a foothold in science and at the institute since supervising my master’s thesis.

I am also grateful to the rest of team [BMS](#) and my other colleagues for the exciting, absurd, and mind-expanding (non)scientific exchange and the good time at the institute. With their help, I was not only able to expand my professional and scientific knowledge, but also acquired new skills that I would not want to do without in retrospect. Just to name two: During my time at the institute, I became a sought-after hat designer. I also had the privilege of bringing my mechanical engineering colleagues, in particular Johannes Sturm and Sven Friedrich, closer to the wonderful world of electrical engineering, whether I wanted to or not.

I would also like to thank our technicians Jens Dietrich and Korbinian Schmidt, who both helped me with advice and practical support. Whether as support during the internship “Schaltungsentwicklung für Batteriesysteme” or with various test setups and test preparations, I could always rely on both of them.

Dear Ludwig, I couldn’t put it better, that’s why I quote you: “Many thanks likewise go to my colleague and namesake ... Ludwig [Kraft] (the shared part of the name caused quite some confusion during our time at the EES), who was always available for a drink whenever necessary” [254].

Furthermore, I would like to thank my project partners from research and industry for the cooperation in the projects EVERLASTING and OSLiB, who gave me exciting insights into research and development of lithium-ion batteries in Germany and Europe. In this context, I would also like to thank Carolin Nierwetberg and Gudrun Rahn-Koltermann, who guided and supported me through all the organizational tangles of the [TUM](#), writing research proposals, and EU projects.

Finally, I want to express my special thanks to Barbara, my family, and friends for the time spent together, allowing me to keep my work-life-balance and thereby supporting me along the way through my time at the university.